Yale University

EliScholar – A Digital Platform for Scholarly Publishing at Yale

Yale Graduate School of Arts and Sciences Dissertations

Spring 2022

Jet to Event Activity Correlations in Small System Collisions at STAR

David J. Stewart
Yale University Graduate School of Arts and Sciences, ds.johnny@gmail.com

Follow this and additional works at: https://elischolar.library.yale.edu/gsas_dissertations

Abstract

Jet to Event Activity Correlations in Small System Collisions at STAR

David Stewart

2022

At sufficient energy densities, ultra-relativistic heavy ion collisions produce a quark gluon plasma (QGP), in which quarks and gluons are deconfined into an extended medium. High energy partons in the collision scatter at short time scales, may afterward interact with the QGP media, and ultimately hadronize into a collimated spray of particles. Experimentally, these particles are algorithmically clustered into jets, which are used as proxies for the initiating partons and therefore as probes of the QGP's properties.

This thesis presents jet measurements from $\sqrt{s_{\mathrm{NN}}} = 200\,\mathrm{GeV}$ p+Au collisions recorded by STAR at RHIC in 2015. These are the first reported semi-inclusive jet results for small system collisions (p/d/He+A or "s+A") at RHIC kinematics and are particularly timely because of an ongoing revolution in the field's perception of, and use for, small system collisions. Originally s+A collisions were of principal interest to serve as a QGP-free benchmark of cold nuclear effects, which was used to compare A+A collisions with pp collisions to quantify actual QGP effects. That paradigm began to shift with the discovery that most signals attributed to QGP formation are present, to some degree, in s+A collisions; however, as an exception, no jet quenching has been observed to date.

In 2015, the ATLAS and PHENIX collaborations reported event activity (EA) dependent modification of jet spectra in p+Au and p+Pb collisions, a possible jet quenching signal. Intriguingly, the ATLAS jet modification, in the p going direction, appears to scale with the "Bjorken-x_{p}" of the jets ($\approx 2E_{\mathrm{jet}}/\sqrt{s}$) for $x_{\mathrm{p}} \gtrsim 0.1$; at the same time, measurements of lower x_{p} jets from collisions at the same energy by the ALICE experiment found no EA jet spectra modification.

Jets at kinematics up to $x_{\mathrm{p}} \approx 0.5$ are reported in this thesis through their p_{T} spectra per

trigger (S), azimuthal distribution per trigger (A), and dijet p_T balance (A_J). There is significant EA dependent modification of S, and some of A. This modification is demonstrated by this thesis to result primarily, perhaps completely, from observed anti-correlations between EA and the energy of the trigger particle ($E_\mathrm{T}^\mathrm{trig}$). These EA-to-$E_\mathrm{T}^\mathrm{trig}$ anti-correlations are also presented. The A_J distribution is independent of EA, further supporting the conclusion that the EA dependence of the jet p_T spectra is a constraint imposed by the initial conditions of the x_p hard scattering and not a result of subsequent jet-QGP interactions. As a result, EA-to-$E_\mathrm{T}^\mathrm{trig}$ correlations are presented as an opportunity to further probe the initial stage conditions of high energy ion collisions.

Jet to Event Activity Correlations in Small System Collisions at STAR

A Dissertation
Presented to the Faculty of the Graduate School
of
Yale University
in Candidacy for the Degree of
Doctor of Philosophy

by
David Stewart

Dissertation Director: Professor Helen L. Caines

May 2022

This work is dedicated to Samantha

Without you support, optimisim and love,
I would have crossed neither the start
nor the finish line of this endeavor

To Jane, Jack, Fred, and Kate

For embarking with us on this adventure
and sticking it through to the end

To Anna and Rose

For enlisting mid-voyage
with all the confidence and chaos
that only comes in people so small

Acknowledgements

I am very grateful for the privilege of knowing many truly wonderful people who have selflessly helped me along my way. For whatever I amount to, it is built on foundations laid with the generous help of many hands. Here I mention just a few.

Helen, thank you for opportunity to spend several marvelous years working in your group doing what I love to do. Thank you for your knowledge, open door, pragmatic advice, tireless edits, interesting conversations and timely advice.

John, thank you for the privilege of joining this research community that you have brought to, and fostered, at Yale. Thank you for your insightful and clear feedback throughout my studies here.

Stephen & Raymond, thanks for all the help, both before and after you finished in our group. The probability that I will message you prior to finishing the final revisions in this thesis with yet another question is not insignificant...

Tong and Daniel, thanks for sharing an office in my pre-pandemic years in the group, for many shared memories and conveniences. Among many of which, thanks for a last minute transportation to Rhode Island as well as humoring my desire to take mass transit in Wuhan.

Hannah, Caitie, Raghav, Li, Mike, Michael, (and all the above!) thanks for all the help, the edits, the feedback, and the many, many, interesting lunch conversations. I will miss this working group very much. Also, Hannah, a special thank you for all the edits on this thesis; it is a better product for your thoughtful feedback.

Paula, I have never in my professional life had to deal so little, or so conveniently, with the administration that pertains to my work. Thank you so much! It's been an even greater privilege getting to know you.

To Lieutenant Commander Tony Duttera: Thanks for your teaching and support, during and after the Navy.

To Mike Nahorney: I have always admired your constant learning new practical knowledge that you apply in new and expanding ways. You were a great boss and your example has served me well.

To Mom, who has always had a higher-than-rational belief in me, and Dad, for many wonderful early mornings, conversations, and confidence.

Thanks to Jane, Jack, Fred, Kate, Anna & Rose for adding an abundance of balance to my life.

Above all, thanks to Samantha, for staying the course with me and supporting me in a thousand-and-one ongoing ways

Contents

List of Figures

List of Tables

Chapter 1

Introduction

1.1 Energy Scales and the Standard Model

The standard model (SM) of physics is a theory of three of the four known fundamental forces. It is not a physical theory of everything: it does not model gravity and makes no predictions regarding neutrino mass, baryon asymmetry, dark matter or dark energy. However, even with its 18 required input parameters [1], it is a stunningly efficient scaffolding with which to address observations ranging over about 44 orders of magnitude: ranging roughly, using natural units of $\hbar = c = 1$,[1] from the top quark Compton length (10^{-16} [2]) to the age of the universe (10^{28} [3, 4]). What is perhaps even more remarkable is that at almost any scale, significant and unique physics of interest emerge which can be locally studied.

1.2 Quantum Chromodynamics: Quarks, Gluons, Confinement & Freedom

Quantum Chromodynamics (QCD) models the strong (or "color") force and is the most recently developed component of the SM. It is a non-Abelian SU(3) theory [5, 6] which con-

---

1. Such that $[\text{energy}]^{-1} = [\text{mass}]^{-1} = [\text{length}] = [\text{time}]$

sists of quarks charged with three "colors", whose force exchanges are mediated via gluons. A fundamental feature of this theory is that gluons, unlike photons in QED, are also color charge carriers and can therefore self-interact. This means that the interaction coupling α_s "runs" with resolution scale: it decreases monotonically with increasing resolution.

The results of the running coupling $\alpha_s(Q)$, where Q is the four momentum transfer in an interaction, are profound. First, at high resolutions (within about $0.2\,\mathrm{fm}$ or $Q \sim 1\,\mathrm{GeV}$) QCD interactions are perturbatively calculable. Consequently, QCD in at these scales is referred to as perturbative QCD (pQCD). In this regime quarks are "asymptotically free" with growing Q: they are resolvable as individual partons with well modelled (by pQCD) scattering cross sections. On the other hand, at lower resolutions, $\alpha_s(Q)$ grows and results in nonperturbative QCD (npQCD). In this regime, higher order interaction terms do not converge, and QCD calculations are no longer perturbatively tractable.

Figure 1.1 displays one calculation for an effective $\alpha_s(Q)$ connecting the pQCD and npQCD regime.[2] Physically this means that as the distance between two interacting quarks increases, it becomes energetically favorable to "break the gluon string" connecting them with the pair production of two new quarks which couple with the original quarks. As such, individual quarks at low resolution are energetically forbidden and are confined to exist only paired with other quarks in color neutral objects.[3] This is referred to as confinement, or sometimes as "infrared (IR) slavery" at low resolutions, as opposed to "asymptotic freedom" in ultra-violet (UV) resolutions.

1.3 Quark Gluon Plasma: Motivation for Heavy-Ion Physics

QCD's introduction of confinement and asymptotic freedom explained the experimental puzzle why quarks, indirectly observed in deep inelastic scattering, were nevertheless never

---

2. Values of $\alpha_s(Q)$ diverge as $Q \to 0$. One way join the npQCD and pQCD regimes is to use an "effective charge" value for α_s which accounts for the npQCD divergences at small Q.

3. Hence the name "color" in QCD theory. It has nothing to do with color from light from QED; it was simply chosen as a useful mnemonic in which the three base colors (red, green, and blue) sum to a colorless composite.
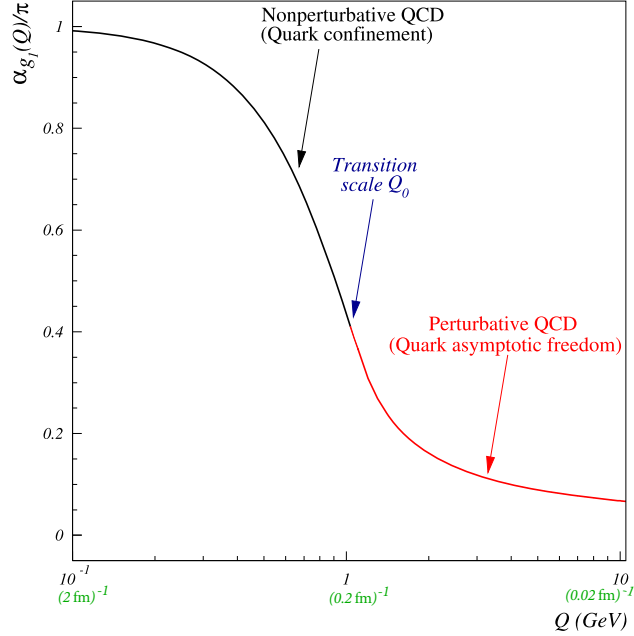
Figure 1.1: Unified strong effective coupling constant interpolated across perturbative and nonperturbative QCD regimes. In this method, non-perturbative processes have been absorbed into the definition of α_{g1} which by definition obeys the limit $\lim_{Q\to 0} \alpha_{g1}(Q) = \pi$. Refer to [7], from which the figure is taken (labels of fm^{-1} have been added).

observed as isolated product of particle collisions. It also explains that the order among the hadrons[4] results from their quark compositions. However, it also makes the prediction that at high enough density an entire ensemble of quarks can be mutually deconfined into a phase of matter governed by a QCD equation of state (EoS) [9, 10]. Due to the analogous state for free electrostatic charges in conventional plasmas, this new state of matter was named a Quark Gluon Plasma (QGP) starting in 1980 [11, 12]. Study of quarkonic media have applications in modeling the universe immediately following the Big Bang in cooler but dense systems, like neutron stars, and more recently in analyzing gravitational signals from neutron star mergers [13]. Refer to Figure 1.2.

Theory puts the QGP formation energy density on the order of $1\,\mathrm{GeV/fm}$ [15] which is above the expected achievable values for pp and p+A collisions.[5] As such, the experimental path to study the QGP in a laboratory is to accelerate heavy ions to near the speed of light

4. The observed "eightfold way" of the "particle zoo" of observations [8]

5. For a possible counterexample at top CERN energies in pp collisions see [16].
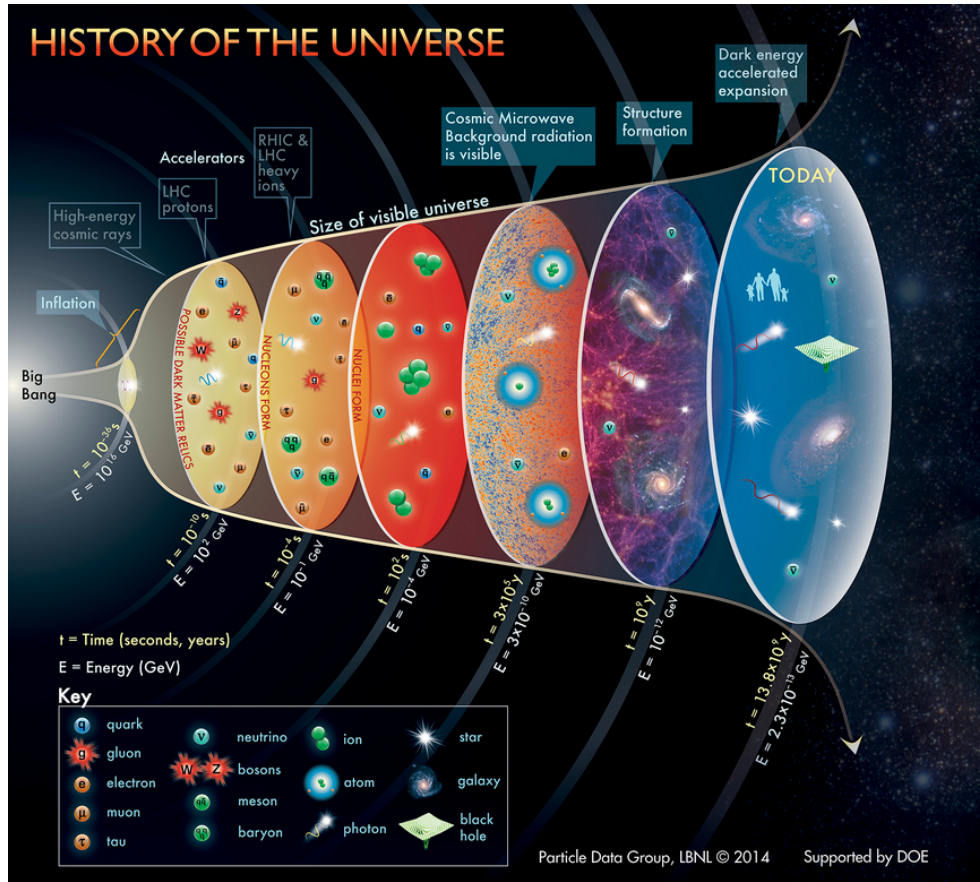
Figure 1.2: Cartoon of evolution of matter states in universe along with labels for LHC and RHIC collisions[14].

and collide them in detectors.

Under this motivation, the US Department of Energy (DOE) built the Relativistic Heavy-Ion Collider (RHIC), currently the world's largest dedicated heavy-ion collider, and the European Council for Nuclear Research (CERN) built the Large Hadron Collider (LHC) with the intention of colliding heavy ions along with the pp program. RHIC started in 1999 and collides a wide variety of ions, the heaviest being Au+Au at up to center of mass collision energies per nucleon ($\sqrt{s_{\mathrm{NN}}}$) of $200\,\mathrm{GeV}$, followed by the LHC in 2009 with Pb+Pb collisions reaching $\sqrt{s_{\mathrm{NN}}} = 5.02\,\mathrm{TeV}$.[6]

As expected, the results have been quite complex, and qualitatively different from particle physics (high or low energy) in the sheer scale of the system modeled, along with the stages of evolution from collision to final particles. Reinhard Stock, one of the experimental founders of the field,[7] noted that the proposition to collide heavy ions at first was compared, with some hilarity, to "smashing delicate Swiss watches against each other in order to find out how the rational of when they were built", while his colleague Arthur Poskanzer[8] remarked that "it was my background in chemistry that allowed me to look at these very complex reactions. My theory was that if reactions get very complicated, they become simple again" [20]. Refer to illustrations in Figure 1.3.

1.3.1 Musing: Very Complex to Simple Again

Poskanzer's idea that the very complex can become simple again is a good description of many aspects of this field of physics and also the research presented in this thesis. In general, factorization of QCD into calculable pQCD and non-tractable but at least measurable

---

6. There were preliminary heavy-ion collisions in modified runs in devices that had been purpose build for pp collisions at both the Brookhaven National Laboratory (BNL), home of RHIC, of $\sqrt{s_{\mathrm{NN}}} = 5\,\mathrm{GeV}$ Si and Au collisions at the Alternating Gradient Synchrotron (build for proton collisions) and at CERN with $\sqrt{s_{\mathrm{NN}}} = 7\,\mathrm{GeV}$ Si and Pb collisions [17]. Also of note is the Bevatron accelerator at the Lawrence Berkeley National lab, which in 1974 was joined with the SuperHILAC (Super Heavy Ion Linear Accelerator) to form a joint experiment called "Bevalac" to collide light ions, and was later modified in 1982 to collide heavy ions at about $\sim 1\,\mathrm{GeV}$ per nucleon [18, 19].

7. Who, from his retirement, still actively contributes to the field

8. A co-founder of experimental high energy heavy-ion physics who was also active in the field until he passed away this past June

npQCD, allows treatment and measurements in the face of large complexity [21]. Similarly, many QGP signals are the result of ensemble-level properties which are relatively clear even as we seek to probe and map out the underlying EoS and connecting physics that give rise to these signals. In a perhaps much more modest way, the simple fact that the SM creates all atoms alike, so that the several million p+A collision events are probing *exactly* the same distributions, allows measurements like this thesis to credibly observe semi-inclusive correlations, with real physical consequences, even in the face of tremendous underlying complexity.
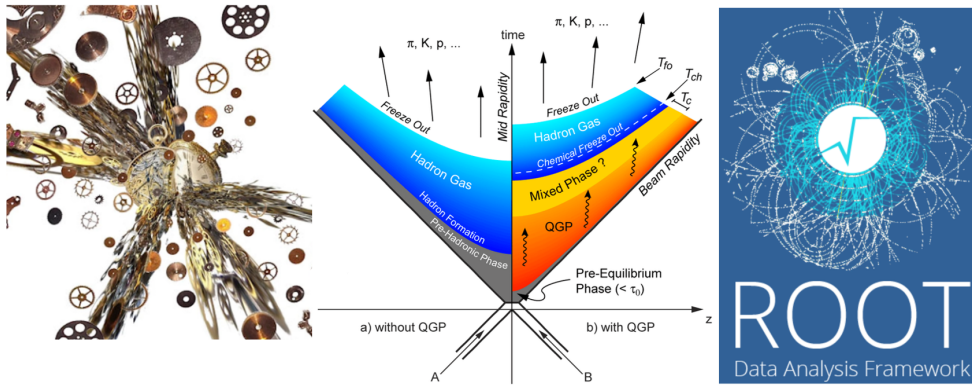
Figure 1.3: Cartoon of results of heavy-ion collisions. Left to right: (a) skeptics' view: cogs and gears from smashed watches [22], (b) theory: stages of evolving media [23], (c) actual data: files of collisions with lists of particle ϕ, η, E, ... [24].

1.4   QCD Phase Diagram and QGP Equation of State

A sketch of a QCD phase diagram in terms of temperature and baryon chemical potential (μ_{B}) is given in Figure 1.4. Zero μ_{B} is the limit at which matter and anti-matter are perfectly balanced. At this limit, lattice QCD[9] has calculated the phase transition temperature to be $\sim 156\,\mathrm{MeV}$ [25], with decreasing values as μ_{B} increases. Mapping the QCD diagram remains a major global endeavor of the high energy heavy ion field.[10]

Of necessity, the field has a very strong interplay between the theory and experiment communities in studying the QGP, with a primary goal to determine the QGP EoS. The exper-

---

9. In which QCD fields are discretized to a lattice in equilibrium.

10. NICA and FAIR, being build in Russia and Germany, respectively, are two of the major future colliders being built which will probe the QCD diagram at higher μ_{B} values.
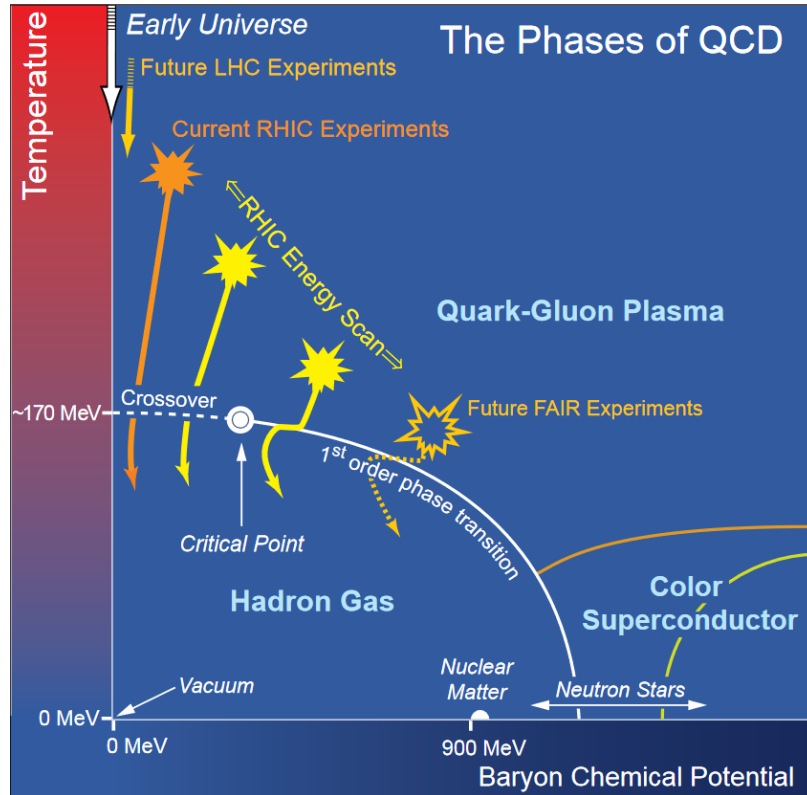
Figure 1.4: Sketch of the QCD phase diagram [26].

imental observables available to experiment are the final results of a complex evolution of various stages of each collision. As such, comparisons to theory are frequently only possible when theory is used to build statistical simulations which are then compared to experiment. At the same time, experiment is used to optimize model parameters (including those that characterize the QGP) so that simulations can improve in their predictive and discriminatory power. Given the number of parameters and processes involved, the field includes significant effort in recent years to include ways to optimize and constrain many parameters simultaneously, such as global Bayesian Analysis[11], or to better map high-dimensional observables at detectors to the underlying EoS, such as through machine learning.[12]

While there remains much to be done, one of the headline results of matching QGP fluid dynamics to data is the discovery that the shear viscosity to entropy density ratio (η/s)

---

11. For example, see [27].

12. For example, see [28].

value which best fits the data approaches and/or is $1/4\pi$ [29], which was also calculated as a theoretical minimum in 2003 [30].

1.5 Heavy-Ion Collisions: Framework for Measurements

1.5.1 Geometries of Colliding Heavy Ions and Detector Measurements

The left hand side of Figure 1.5 shows a cartoon of a heavy ion collision, which is parameterized by the impact parameter b, and the geometric plane defined by the vector $\vec{b}$ and the beam line direction $\vec{z}$. From that interaction, there is an evolution to many final state particles which are distributed in azimuth (ϕ), which may or may not be oriented relative to the reaction plane, and rapidity y[13] or pseudo-rapidity (η).[14] The figure also includes a cartoon of a flow mechanism in which gradients of pressure in a formed QGP translate to an asymmetry in the p_T[15] distribution of final state particles. The study of particle correlations which indicate collective motion/flow is one of the principle signals used in studying the QGP. This is done by comparing measured flow to flow simulated by hydrodynamic codes which use input from the QGP EoS predicted by QCD. The comparisons constrain the physical models and consequently our understanding of the nature of the QGP.

1.5.2 Collisions and pQCD: Jets and Heavy Flavor

Additionally, heavy-ion collisions are composed of many QCD scatterings. "Hard" (meaning high momentum transfer, Q), pQCD, scatterings are relatively rare and occur very early in the collisions.[16] The bulk of the collisions are governed by npQCD, and occur later.

To first order rare, hard-scattered partons result in back-to-back partons with equal and opposite p_T.[17] This make p_T a particularly convenient measurement parameter, because

---

13. Not to be confused with the Cartesian coordinate y, rapidity is defined as $y = \frac{1}{2} \ln \frac{E + p_\mathrm{T}}{E - p_\mathrm{T}}$ and is useful because $\Delta \eta$ is constant under boosts along the beam line direction z.

14. $\eta = -\ln \left[\tan \left(\frac{\theta}{2} \right) \right]$. Note that for any particle, $y \to \eta$ as $m/\vec{p} \to 0$.

15. Transverse momentum, the component of the momentum vector in the xy plane.

16. See Figure 1.1, where the length scales in fermi (10^{-15}m) are also the measurements of the time scale (the conversion is just time=length/c). Therefore pQCD starts at a distance and time resolution of ~ 0.2 fm.

17. Ignoring intrinsic initial partonic p_T, the original particle motion is purely in the z direction, such that
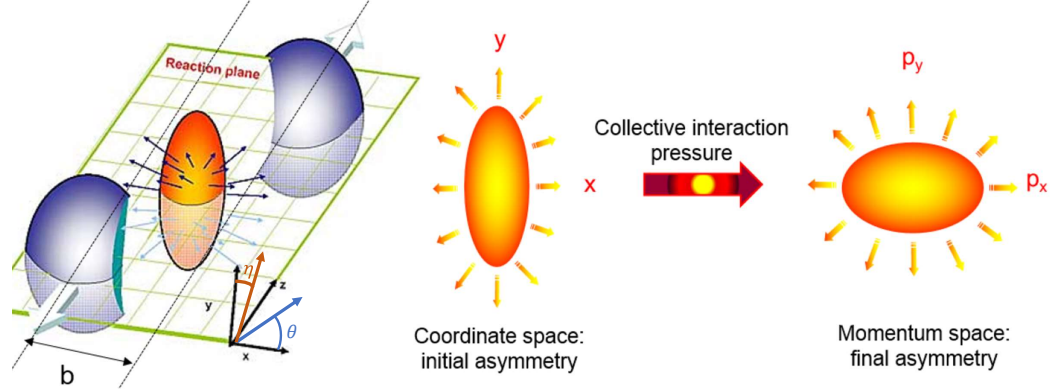
Figure 1.5: Left: Cartoon of geometry of a heavy-ion collisions. Center and right: Cartoon of pressure gradients in a QGP due to collision asymmetry leading to boosted asymmetry in final particle momenta distributions. Figure modified from [31].

the p_T balance can be studied independently of the kinematics of initially participating partons. Hadrons containing heavier quarks are also formed early in the process. Consequently, both "heavy flavor" objects and jets are formed in time to interact with any formed QGP. This is diagrammed in Figure 1.6. Also shown in Figure 1.6 is a "jet", which is an algorithmic grouping of several final state observed particles which are added together to approximate the kinematics of the initiating high-p_T parton. Jets are presented in more detail in Section 2.

Because jets are the best experimental approximation available of a hard scattered parton, it is natural to compare them to the Bjorken-x (x_B) of the parton, where x_B is the longitudinal momentum fraction that a hadron's constituent parton carries[18] [33]. The kinematics are more complicated than in electron+hadron deep inelastic scattering (DIS) experiments,[19] and the resolution of the final jets is experimentally limited.[20] Nevertheless, total jet energy

p_T must be conserved in scatterings, which in a $2 \rightarrow 2$ interaction, will be back-to-back. There are, in fact, Transverse Momentum Dependent (TMD) Parton Distribution Functions (PDFs), which are one of many things that the Electron Ion Collider (EIC), which will be build at the BNL, will be able to directly measure to much better precision with the well defined initial and final momentum of the scattered electrons.

18. In the limit of an infinite momentum frame, where mass is insignificant relative to the energy scale, and the parton's momentum is determined by an elastic scattering (such as DIS with an electron).

19. In a hadron collision both hard scatterers are partons separately sampled from nuclear parton distribution functions (nPDF's).

20. For this reason, it is very interesting to measure hard-γ scatterings, which are difficult to isolate and obtain with good statistics, but are also clear measurement of initial scatterings than jets.
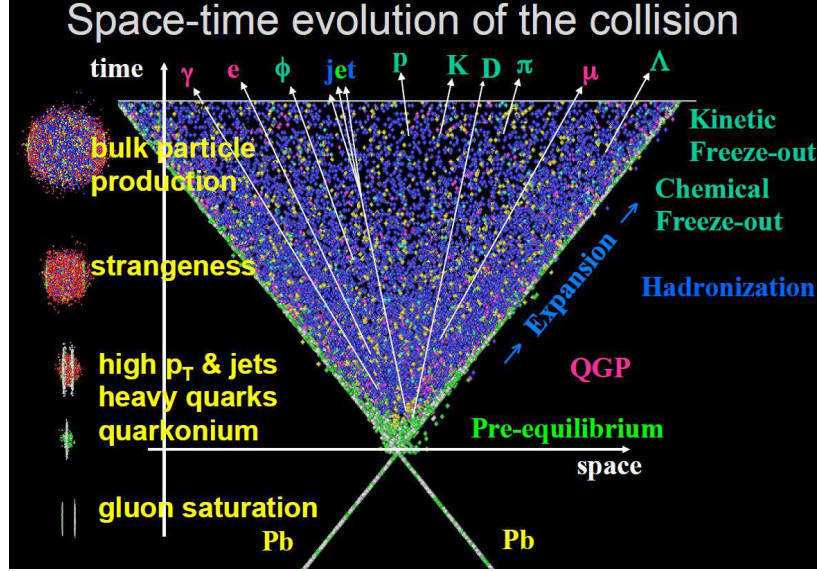
Figure 1.6: Cartoon of evolution of a heavy-ion collision. Note that high resolution objects produced early in the vertical timeline, prior to possible QGP formation and expansion. Figure from [32].

is a best measurement of $x_{\mathrm{B}} \times \sqrt{s_{\mathrm{NN}}}$. When referring specifically to the initiating longitudinal momentum fraction of the parton in the proton in p+Pb collisions, reference [34] uses the notation x_{p}. The STAR (Solenoidal Tracker At RHIC) data used in this thesis does not enjoy the same high-η coverage for jets in the p-going direction as ATLAS did in [34], however, this thesis adopts the same convention of using x_{p} for $2p_{\mathrm{T,jet}} \cosh(\eta)/\sqrt{s_{\mathrm{NN}}}$.[21]

1.5.3 Controls for QGP Effects in Heavy-Ion Measurements

Measurements of jets, heavy flavor, and flow open avenues to study the QGP. However, additional controls are also needed. Once a jet or heavy flavor observable has been measured, it is important to be able to compare it to some benchmark to be able to disentangle what parts of the signal, if any, are from a QGP. Observe, for example, the cartoon of processes in Figure 1.7.[22] Many effects can result from both the pre-equilibrium state and in the hadron gas phase which are shared in both versions of collision evolution – with or without a QGP – whose signals are not trivial to separate from QGP signals.

---

21. Or, for measurements at mid-rapidity where $2\cosh(\eta) \approx 1$, simply $2p_{\mathrm{T,jet}}/\sqrt{s_{\mathrm{NN}}}$.

22. A larger version of the middle cartoon in Figure 1.3.
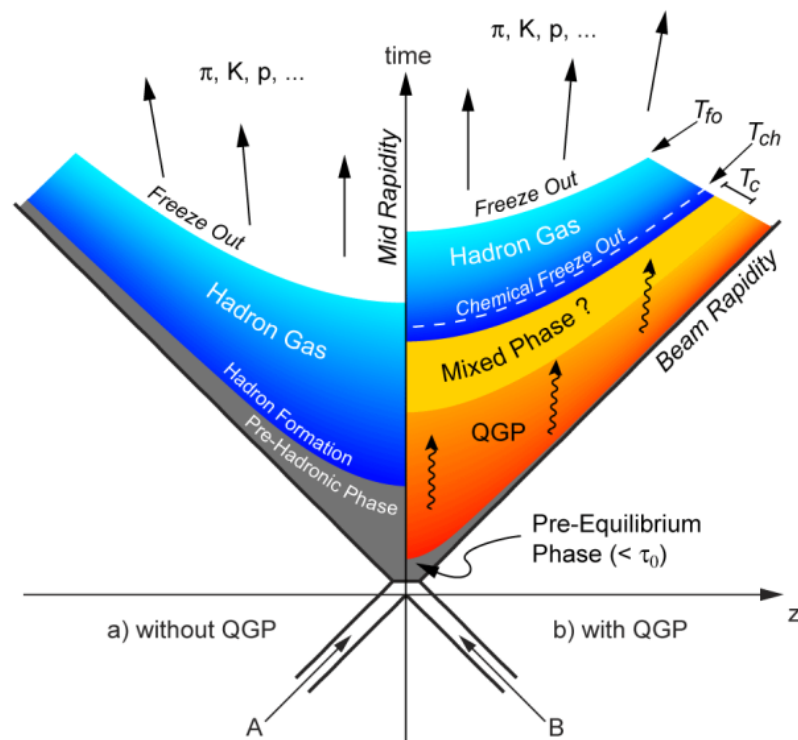
Figure 1.7: Cartoon of evolution of a heavy-ion collision with and without QGP formation. Figure obtained from [23].

One way to proceed experimentally is to vary the collision system size, with the expectation that in a smaller system QGP signals will "turn off". This can be done by differentially comparing A+A collisions in bins of varying impact parameters. In the field, this is labeled as "centrality" and usually demarcated by percentages of impact parameter b, from 0% being a perfectly head-on collisions, to 100% at which point the heavy ions do not collide. It can also be done by varying the size of the colliding ions, in which "small system" (pp and s+A, in which s stands for p, d, or He) collisions can be a control with little-to-no QGP formation. Whether small system collisions have any QGP formation is a topic of intense interest and ongoing research and provide a central motivation for this thesis.

1.5.4 Nucleon Scaling of Heavy Ions – Glauber Model

For many measurements and theory simulations, it is useful to model ion collisions (A+A or s+A) as superpositions of a collection of individual nucleon-nucleon collisions within the framework of the Glauber Model. This model assumes the independence of each individual nucleon-nucleon collision (i.e. ignoring any results of the binding of the nucleons in the ion nucleus, "Cold Nuclear Matter" effects), and applies the optical limit: at sufficiently high energies the colliding nuclei are undeflected [35, 36]. Given these limits, a "Monte Carlo Glauber" simulation can be run which generates distributions of the number of participating nucleons (N_{part}) and the number of binary nucleon-nucleon collisions (N_{coll}), as illustrated in the cartoon in Figure 1.8. A short, visual, explanation of the mechanics of Monte Carlo Glauber calculations are given here.

The ion nucleus A (with nuclear number A) is mapped to a given distribution of nucleons, typically a Fermi ([38] and references therein) or a Woods-Saxon distribution [39, 40]. Then, for each randomly sampled impact parameter b, the colliding $p/d/$A+A are projected through each other, and the total amount of overlap is calculated. This can be done differentially as shown schematically in Figure 1.9, which results in a nuclear thickness function $T_{\mathrm{AB}}(\mathbf{b}) = \int T_{\mathrm{A}}(\mathbf{s})T_{\mathrm{B}}(\mathbf{s}-\mathbf{b})\mathrm{d}^2 s$ [38]. Alternatively, a Monte Carlo calculation, as illustrated in Figure 1.8 and Figure 1.10, can simply count N_{part} and N_{coll}. Note that in p+A collisions, N_{part} is trivially equal to $N_{\mathrm{coll}} + 1$. This may be done either as an integer number of
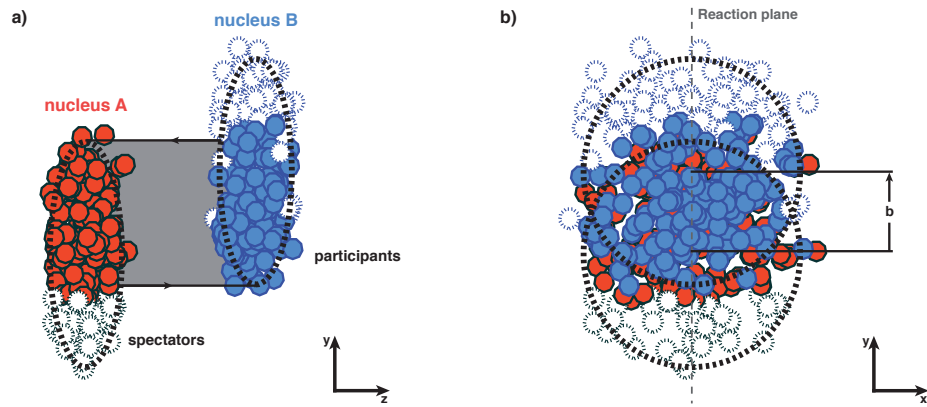
Figure 1.8: Illustration of the Glauber model used to calculate number of participating nucleons and pairs of collisions, N_{part} and N_{coll}. Figure adapted from [37].
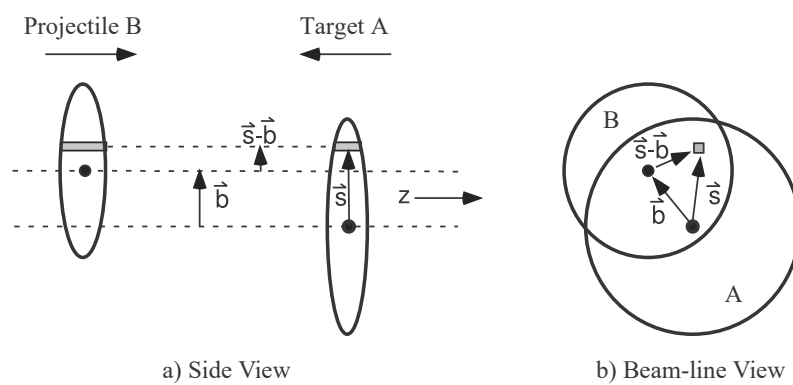
Figure 1.9: Schematic of differentially calculating nuclear overlap thicknesses [38].

nucleons which overlap in any degree (as shown in the cartoons), or weighted by each binary nuclear to nucleon impact parameter. The N_{part} and N_{coll} distributions from a Monte Carlo Glauber are displayed in Figure 1.11.
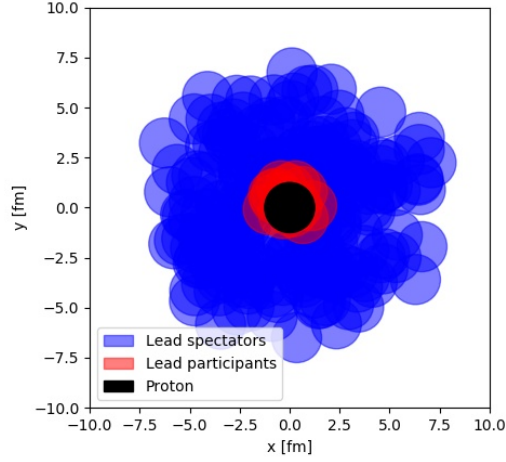
Figure 1.10: Illustration of the Glauber model in a p+Pb collision [41].
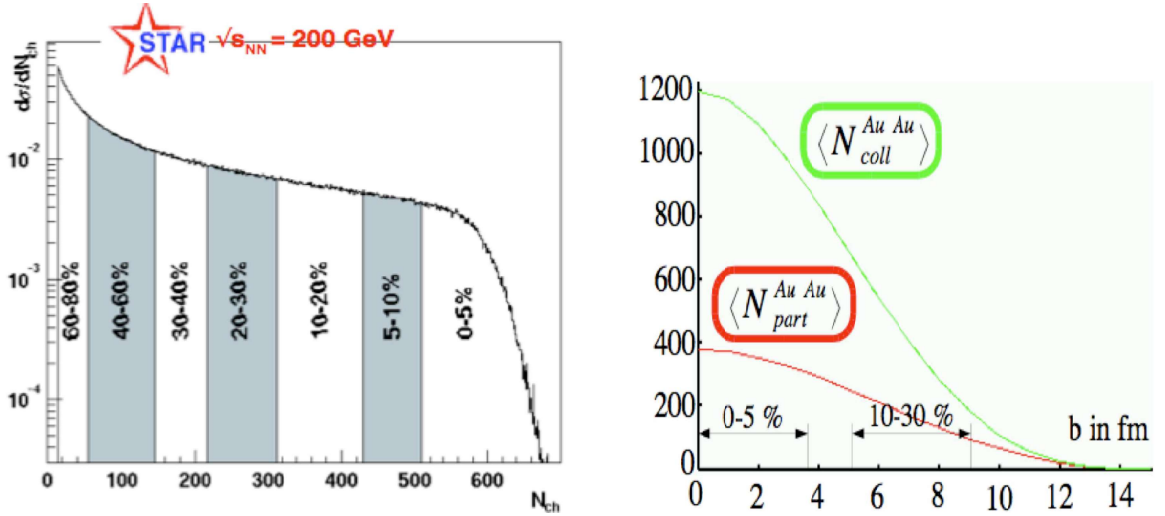
Figure 1.11: MC Glauber Distributions for Au+Au collisions from [42].

The cross sections of σ_{pp} and $\sigma_{p\mathrm{A}}$ are both experimentally measurable, and therefore the probability that any given nucleon in the heavy ion in a p+A collision is struck becomes $\sigma_{pp}/\sigma_{p\mathrm{A}}$, so that $\langle N_{\mathrm{part}} \rangle = A\sigma_{pp}/\sigma_{p\mathrm{A}} + 1$ (where A is the mass number of the ion, and the $+1$ accounts for the p). A large number of measurements going back to the 1970's have demonstrated that the average number of generated particles (a npQCD process)

scales approximately linearly with $\langle N_{\mathrm{part}} \rangle$ [43]. Therefore, soft particle production scales primary with system total size, from all the "wounded nucleons" (i.e. N_{part}, all participating nucleons). This linearity can be seen for a number of LHC and RHIC measurements in Figure 1.12.

To make these measurements, what has been done in practice is to read event activity (EA) of the collisions with one area of the detector (at a high $|\eta|$), sort those events into bins of EA, correlate the EA of each bin to a centrality decile through a Glauber distribution (left hand side of Figure 1.11) which are then associated with a given N_{part} and N_{coll}.
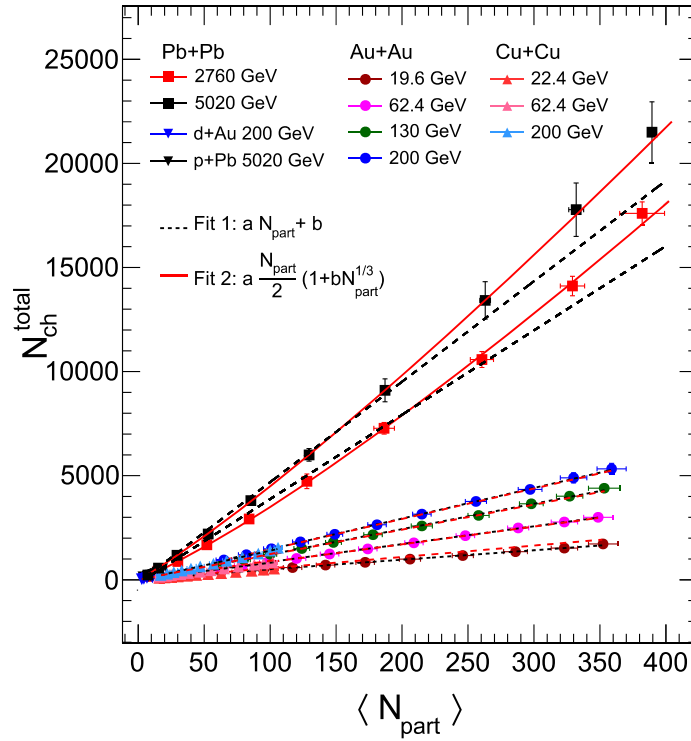
Figure 1.12: Total charged particle production in A+A and p/d+A collisions per $\langle N_{\mathrm{part}} \rangle$, from [44].

On the other hand, hard pQCD processes have very small cross sections, such that the probability to produce a hard scattering is approximately equal for each individual binary collision. Therefore hard scatterings are expected to scale with N_{coll}. A nice example of results from ATLAS[23] for Z bosons,[24] is shown in Figure 1.13.

---

23. Refer list of acronyms for experiment names, such as ATLAS, PHENIX, ALICE, and CMS

24. $m_Z = 91.2\,\mathrm{GeV}$
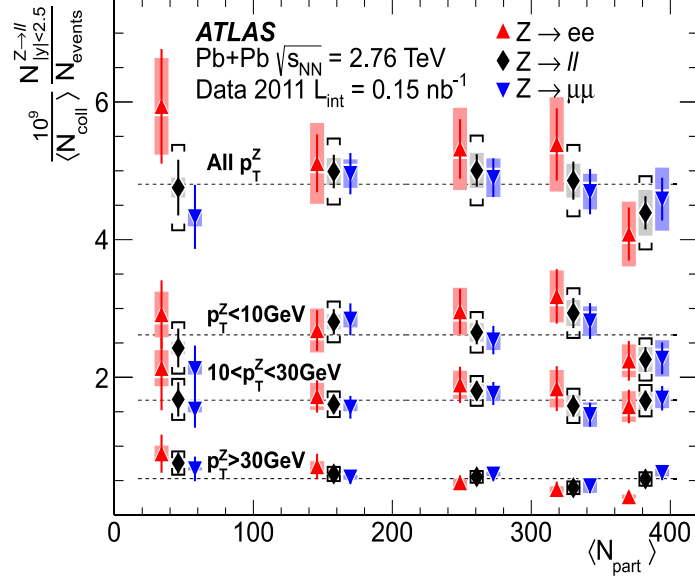
Figure 1.13: Scaled Z boson production per N_{coll} at various centralities [45].

1.6 Heavy-Ion Collisions: Experimental Signals of QGP

1.6.1 QGP and Parton/Jet Quenching

In 1982 J. D. Bjorken predicted that partons (quarks or gluons) propagating through the QGP would suffer energy loss.[46][25] He suggested that this quenching of partons with a long enough path in the QGP would form a signature of the QGP. Namely, pairs of hard scattered partons formed near the QGP surface could send one parton out through the surface unquenched but the other into the QGP volume where it would be quenched. The result would be a developed imbalance in p_{T} of hard scatterings. STAR observed a clear signal of this quenching of the recoil p_{T} correlation in Au+Au collisions in 2003 and 2004 as reported in the plots in Figure 1.14. In both figures, the trigger is the highest-p_{T} (i.e. "hardest") track, with only events with $p_{\text{T}}^{\text{trigger}} \in [4, 6]\,\text{GeV}$, and the relative azimuthal location of the remaining "associated" tracks ($\Delta\phi \equiv \phi_{\text{assoc.}} - \phi_{\text{trigger}}$]), which are all other tracks with $p_{\text{T}}^{\text{assoc.}} \in [2\,\text{GeV}, p_{\text{T}}^{\text{trigger}}]$. In the left-hand plot, the away-side associated particles are completely quenched for the Au+Au collisions, relative to the pp and d+Au collisions. In the right-hand plot the in-plane away-side peak is totally suppressed for out-of-plane triggers but only somewhat for in-plane triggers. Refer to Figure 1.5 for a cartoon of the

---

25. Original source quoted as unpublished with preprint number Fermilab-Pub-82/59-THY.

reaction plane and semi-central interaction region. In-plane triggers are those within $\pi/8$ in azimuthal of the reaction plane. The interpretation then, is that in-plane triggers are sending their recoil particles through the short axis of a QGP plasma volume (see middle cartoon of Figure 1.5) and therefore are not as quenched as those recoiling from out-of-plane triggers which pass through the long axis.
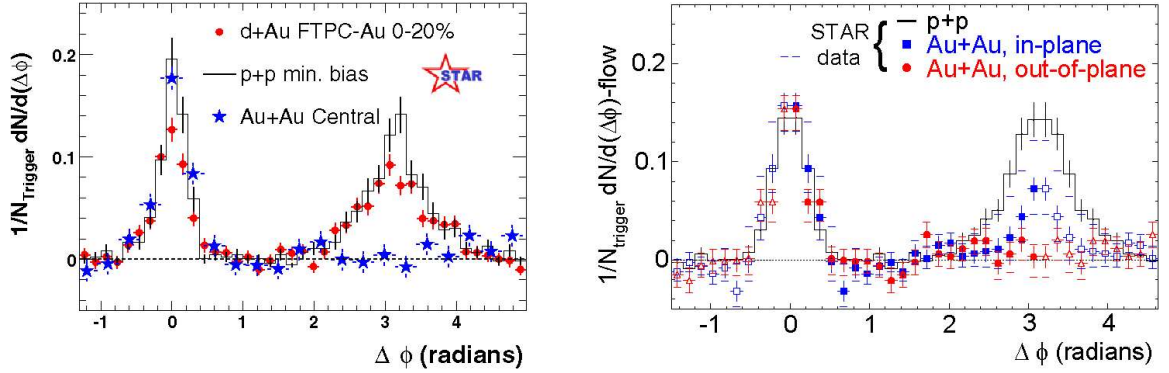
Figure 1.14: Measurements of azimuthal distribution of associated particles relative to highest p_T particles per event (p_T^{trigger}). Pedestal and flow has already been subtracted. Left: pp, central d+Au, and central Au+Au collisions. Right: Semi-central Au+Au collisions, divided by orientation of ϕ_{trigger} relative to the event-plane. Figure from [47].

These measurements are representative of many QGP quenching measurements. The fact that recoil particle p_T disappear for the Au+Au collisions but not the d+Au or pp suggest that the small systems are too small to form a QGP[26] and are therefore appropriate benchmarks to which to compare A+A collisions when seeking to separate QGP effects.

1.6.2 Dijet Asymmetry and QGP

Similar measurements have been made measuring jet[27] p_T^{jet} imbalance. Figure 1.15 shows the average imbalance of jet pairs at STAR and ATLAS.[28] In each case, $A_J = \frac{p_T^{\mathrm{trigger}} - p_T^{\mathrm{recoil}}}{p_T^{\mathrm{trigger}} + p_T^{\mathrm{recoil}}}$, and the recoil jets are the single highest recoil jet. The energy scales are different,[29] but the

---

26. Or at least a QGP large enough to have appreciable quenching

27. See Section 2

28. Both use $R = 0.4$ anti-k_T jets; STAR jets only use tracks, while ATLAS uses full jets. See Section 2 for introduction of jet terminology.

29. The p_T^{jet} lower cutoffs for RHIC trigger and recoil jets are $20\,\mathrm{GeV}$ and $10\,\mathrm{GeV}$, while for ATLAS they are $100\,\mathrm{GeV}$ and $25\,\mathrm{GeV}$

asymmetry is present for both ATLAS jets (relative to *pp* jets) and also for RHIC jets.[30]
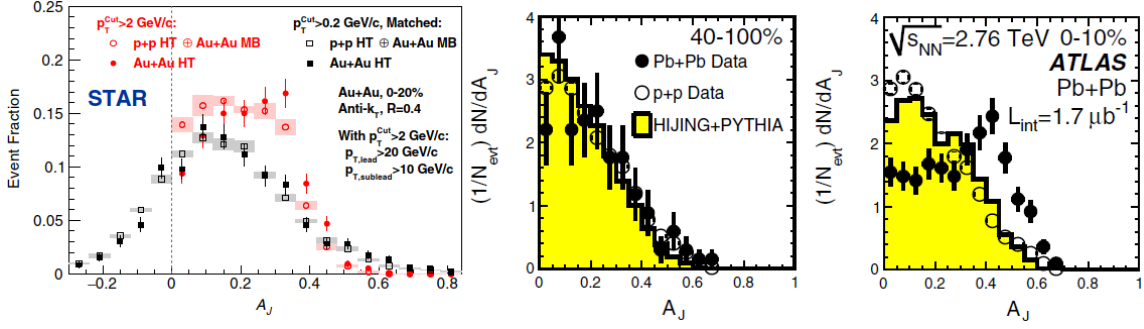
Figure 1.15: Measurements of dijet p_T imbalance (A_J) at STAR (left, from [48]) and ATLAS (middle and right, from [49]).

While the away side jet measurement shows jet quenching (the jets loose p_T or disappear entirely), jet measurements do not show that jets are significantly deflected in azimuth.[31] Two such examples are shown in Figure 1.16. In the STAR plot, the recoil spectra distribution about π does not appreciably broaden. In the ALICE plot, the jet azimuthal deflection becomes narrower (more peaked) around the directly recoiling direction.
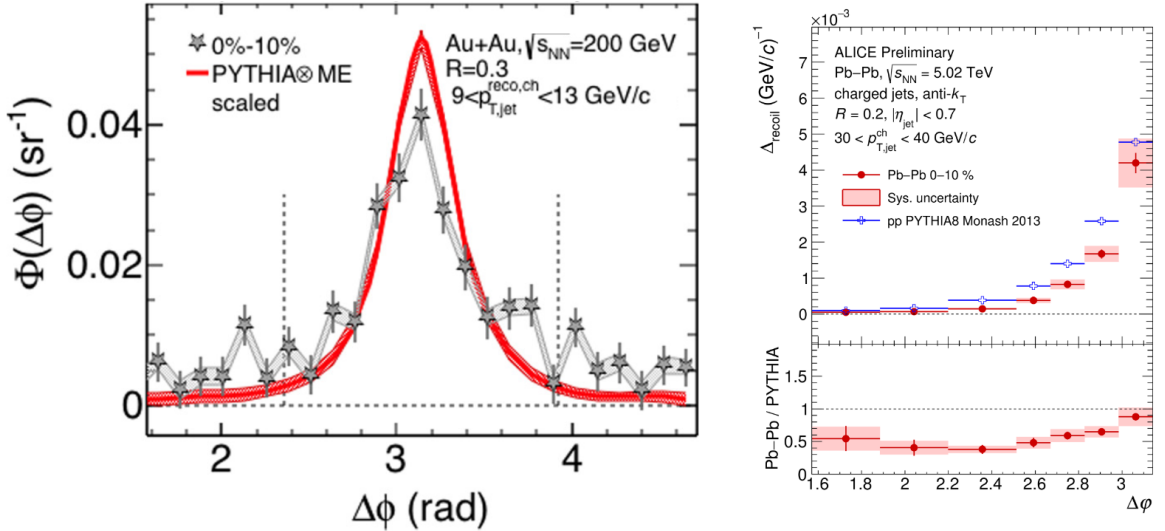
Figure 1.16: Measurements of recoil jet deflection azimuthal deflection in central Au+Au and Pb+Pb collisions. Left: STAR [50]. Right: ALICE [51].

---

30. When using particles at $2\,\mathrm{GeV}$ and above.

31. Note that the due to varying p_z of the initiating partons, η is *not* back-to-back, but rather has a distribution in which $\Delta\eta$ is higher at LHC kinematics than at RHIC kinematics

1.6.3 Nuclear Modification Factor as a QGP Signal

Once pp collisions are determined to not experience QGP quenching (see above), then it is natural to compare the production of pQCD observable "X" in s+A and A+A collisions in ratio to its production in pp collisions scaled by $\langle N_{\text{coll}} \rangle$.[32] This ratio is called the nuclear modification factor (R_{AA} generically for any collisions, but $R_{s\text{A}}$ specifically for small system collisions).

$$\text{if,} \quad \text{p/d/A} + \text{A} \rightarrow X + \dots \tag{1.1}$$

$$\text{then:} \quad R_{\text{p/d/A+A}}(X, p_{\text{T}}) = \frac{1}{\langle N_{\text{coll}} \rangle} \frac{\mathrm{d}^2 N/\mathrm{d}p_{\text{T}}\mathrm{d}X}{\mathrm{d}^2 \sigma_{pp \rightarrow X}/\mathrm{d}p_{\text{T}}\mathrm{d}X} \tag{1.2}$$

$$\text{or:} \quad R_{\text{p/d/As+A}}(X, p_{\text{T}}) = \frac{1}{\langle T_{p/d/A+A} \rangle} \frac{\mathrm{d}^2 N/\mathrm{d}p_{\text{T}}\mathrm{d}X}{\mathrm{d}^2 \sigma_{pp \rightarrow X}/\mathrm{d}p_{\text{T}}\mathrm{d}X} \tag{1.3}$$

Cold nuclear matter effects (CNM), such as shadowing and Cronin enhancement [35], are benchmarked by $R_{p/d+\text{A}}$. Once CNM are accounted for, then R_{AA} is a probe of how much X's production is modified by a QGP.

Some single-particle R_{AA} values from RHIC and LHC experiments are presented in Figure 1.17. Isolated photons and W and Z bosons are those which are not the result of decays (such as $\pi^0 \rightarrow 2\gamma$) but rather come from either the initial scattering or the QGP itself. Because they carry no color charge, they experience no final state effects, and $R_{\text{AA}}(\gamma)$ is anticipated to be unity, as confirmed in the right-hand plot. Existing measurements of jet R_{AA} in s+A collisions are particular motivations for this thesis and presented in Section 2.2, after jets algorithms have been introduced.

1.6.4 Collective Flow and QGP

Correlations in final state particles provide an experimental handle to reveal collective flow. These may be characterized for a given selection of events by the Fourier coefficients (v_n in

---

32. As shown in the equations, the nuclear thickness function can also be used. See Section 1.5.4.
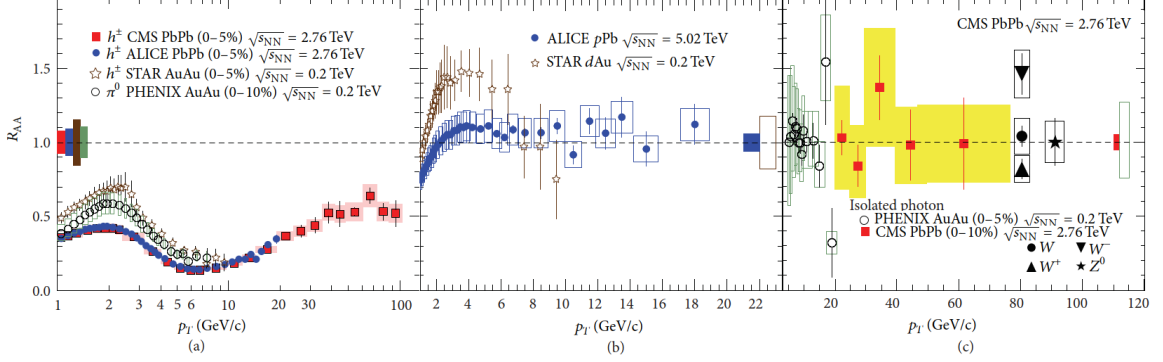
Figure 1.17: Nuclear modification factors from collisions at LHC and RHIC. Left: R_{AA} from central A+A collisions. Middle: $R_{p/dA}$, exhibiting Cronin enhancement (also called anti-shadowing). Right: R_{AA} for vector bosons. Figures from [52].

the literature) of the azimuthal particle probability distribution.[33] In this vocabulary, v_1 quantizes directed flow and v_2 elliptic flow. Elliptic flow may originate from pressure gradients generated by anisotropy the formed QGP volumes resulting from collision geometry, as illustrated in Figure 1.5.

However, interpretation of v_n as resulting from QGP flow must be complimented to account for the following effects: auto-correlations generated from subprocesses,[34] statistical fluctuations,[35] and possible momentum anisotropy resulting from the pre-equilibrium state and post-hadronization.[36] Regarding this final point, Figure 1.18 shows three starting (pre-equilibrium) energy distributions with different initial anisotropies. Additionally, the kinematics of particle interactions in non-fluid phase[37] converts (at least some) energy den-

---

33. Specifically $E\frac{d^3N}{dp^3} = \frac{d^2N}{2\pi p_T dp_T d\eta}\left(1 + 2\Sigma_{n=1}^{\infty} v_n(p_T,\eta)\cos\left(n(\phi - \Phi_n)\right)\right)$ in which Φ_n orients the reaction plane at each n. Values of v_n may be calculated from 2,4,6,..., particle correlation functions – and therefore often designated $v_n k$. This becomes important in systems with smaller numbers of particles. See [53] for a prescription.

34. Such as studying jets, where the jet constituents will add two-particle correlation whose importance in weighting increases with smaller systems

35. The degree of freedom in fitting each harmonic's event plane will automatically find *some* value of v_n just from particle number and distribution fluctuations. For symmetric collision systems, for example, v_3 must result entirely from such fluctuations.

36. Refer, again, to Figure 1.7, in which these are the phases on the left-hand size of the diagram which also sandwich the QGP on the right-hand side of the diagram.

37. Dependent principally on the number of mean free paths of interaction prior to kinetic freeze-out at which point the particles no longer interact but simply free-stream away from the collision site to the detector.

20

sity anisotropy into p_T anisotropy quantified by v_n. For example, a study in 2019 found that a third to a half of v_2 in heavy-ion collisions may result from kinematics requiring one mean free path of interaction length in a non-hydrodynamized system [54].
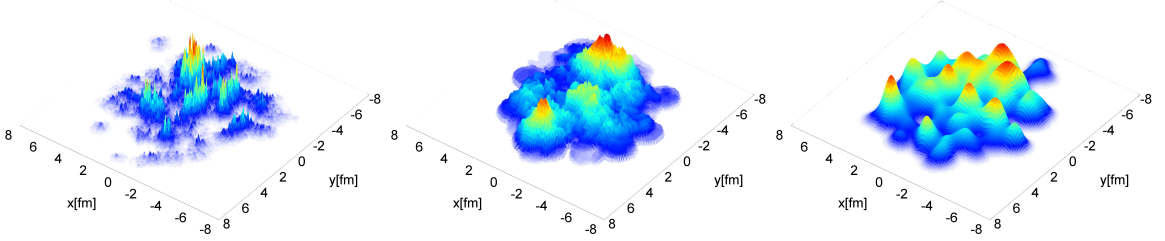
Figure 1.18: Energy density distributions (arb. units) from initial conditions in heavy-ion collisions using three different models. Left: IP-Glasma, in which the incoming nucleons are color glass condensates (CGC). The CGC is characterized by a system of saturated gluons with stochastically distributed large x color sources "frozen" by time dilation and coupled to the gluon fields which form "color flux tubes" [55] yielding the spiky distribution in the figure. Middle: MC-KLN model, also working with the CGC, but does not include fluctuations at the same length scale as IP-Glasma [56]. Right: MC-Glauber in which energy deposition is purely Gaussian for each binary collision. All figures from [56].

While investigations into v_2 from initial collision stages and hadronic interactions remain an ongoing and nuanced work, v_2 remains a strong signal for QGP formation in heavy-ion systems. A particularly convincing signal is the $v_2(\text{KE}_T)$ correlation per particle type as shown in Figure 1.19. Here, $\text{KE}_T \equiv \sqrt{p_T^2 + m^2} - m$ which is, at mid-rapidity and to leading order, equal to E_K, a universal scaling parameter for v_2 in perfect fluid dynamics [57, 58]. This mass ordered scaling, and universal scaling, is apparent from left to right in each of the two panels. The scaling by number of quarks (n_q) strongly suggests that the elliptic flow occurred at a quark level in a QGP which then hadronized with co-moving quarks in phase space into mesons and baryons. If the flow occurred at a molecular hadron level, then baryons would be boosted to comparable speeds as mesons on the same v_2 distribution and the hadrons' curves would move to the right of, and stay below, the mesons' curves, instead of exhibiting the crossover presented by the data.

1.6.5 Suppression of J/ψ and Quarkonia R_{AA} in QGP

Suppression of quarkonia (forms of $c\bar{c}$ and $b\bar{b}$ mesons) is an anticipated signal of the QGP. The mechanism is that Debye color screening in the QGP will cause the quarkonia to
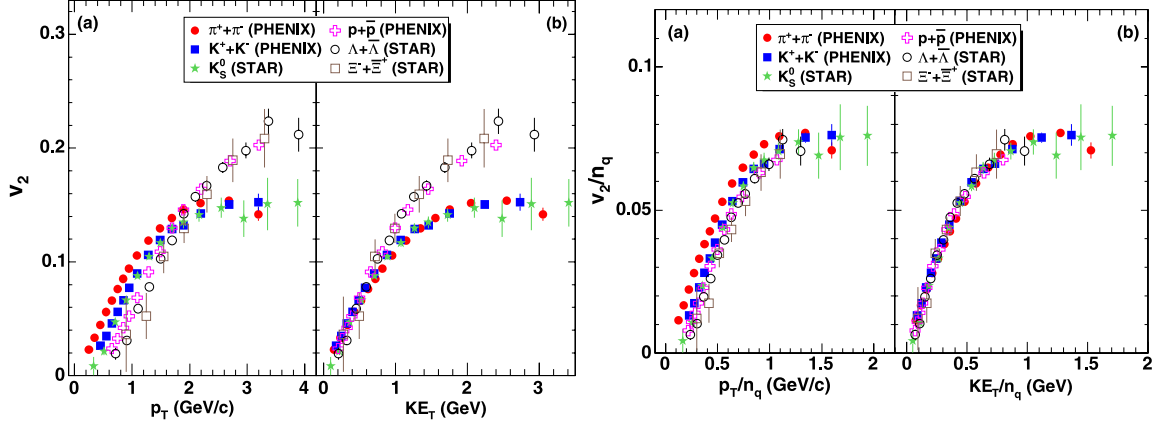
Figure 1.19: Elliptic flow for identified mesons ($n_q = 2$) and baryons ($n_q = 3$) at in $\sqrt{s_{\mathrm{NN}}} = 200\,\mathrm{GeV}$ Au+Au minimum-bias collisions at RHIC [58]. Left: v_2 per p_{T} & KE_{T}. Right: same as left while scaling v_2, p_{T}, and KE_{T}, by n_q.

dissociate (or "melt"). The effect of the screening should become more pronounced with the "size" of the meson – i.e. the interaction length of it's binding energy. There are complications because the QGP may also facilitate recombination. However, as shown in Figure 1.20, there is qualitative agreement of R_{AA} suppression of quarkonia ordered by binding energy.
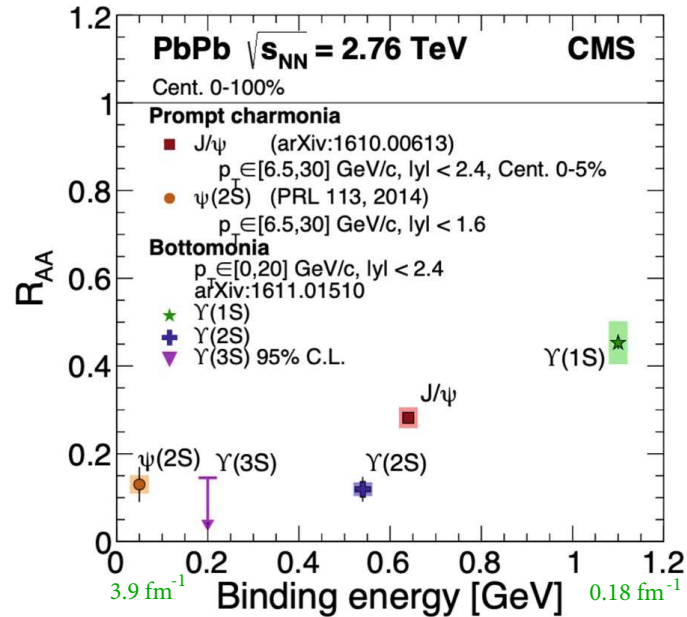
Figure 1.20: R_{AA} of quarkonium states vs binding energy on Pb+Pb collisions at $\sqrt{s_{\mathrm{NN}}} = 2.76\,\mathrm{TeV}$ CMS

1.7 Intrigue: QGP Signals in Small Systems

As presented, small system (pp, p/d/He+A) collisions are generally not expected to form a QGP, and therefore act as both qualitative and quantitative benchmarks for various QGP signals in A+A collisions. However, CMS published a result in 2010 observing a clear near-side ridge in the two particle correlation function for high multiplicity pp events – a signal of potential collective motion and flow [59], see Figure 1.21.

CMS N $\geq$ 110, 1.0GeV/c<p_T<3.0GeV/c
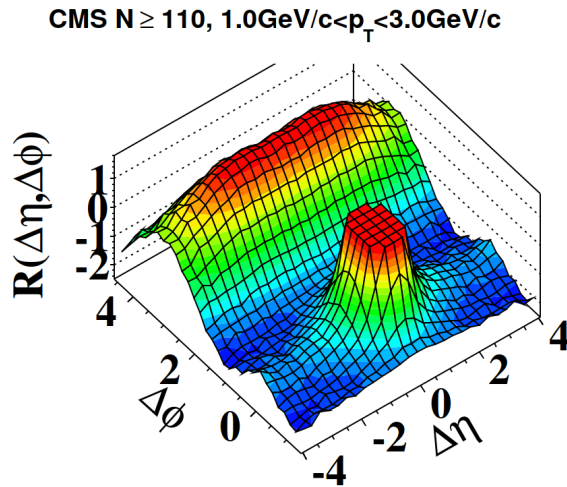
Figure 1.21: Two-particle correlation for high multiplicity $\sqrt{s_{NN}} = 7\,\mathrm{TeV}$ pp collisions at CMS.

This began a broad examination of small systems data looking for all the observables in A+A collisions which are interpreted as QGP signals. Many such QGP-like signals were found in small systems, including v_n signals, some particle ratios, and quarkonia suppression [60].[38] There is considerable ongoing research into understanding these signals and how much they result from, or in spite of, QGP formation. One example is the study of how much v_n is caused from initial energy anisotropies and hadronic scattering vs QGP flow (see Section 1.6.4).

This broader investigation into the (re-)study of small system collisions motivates jet studies in these collisions, including the new measurements presented in this thesis. A selection of existing small system jet results are presented in Section 2.2 both as motivation for this

---

38. Reference is a good bibliography of further references for pp, p+Pb, and Pb+Pb measurements.

thesis's measurements and for context in interpreting the import and meaning of these new results.

Chapter 2

Jets: Algorithms and Prior Measurements

2.1   Jet Definition

Chapter 1 motivated jets and heavy flavor as hard probes of the QGP. A jet is defined as an algorithmically selected group of particles (jet constituents) which are clustered together into a single object, typically by summing the constituents' four momenta.[1] This has the obvious advantage that it provides a better approximation of each jet's initiating hard-scattered parton, prior to the division of that parton through hard and soft splittings, and fragmentation. This is illustrated both in a cartoon of a dijet and an associated diagram of STAR's detector response to a dijet in Figure 2.1.

While beyond the scope of this thesis, jets have the further major advantage that the structure of the constituents (jet substructure) is expected to be modified by jet-medium and medium-jet interactions with the QGP, which provides a powerful set of additional observables to probe for QGP effects [61].[2]

---

1. In the data in this thesis, particles are unidentified and are therefore uniformly assigned the mass of a π_+ meson.

2. The figure of one such result is cited at the end of this thesis with Figure 7.1
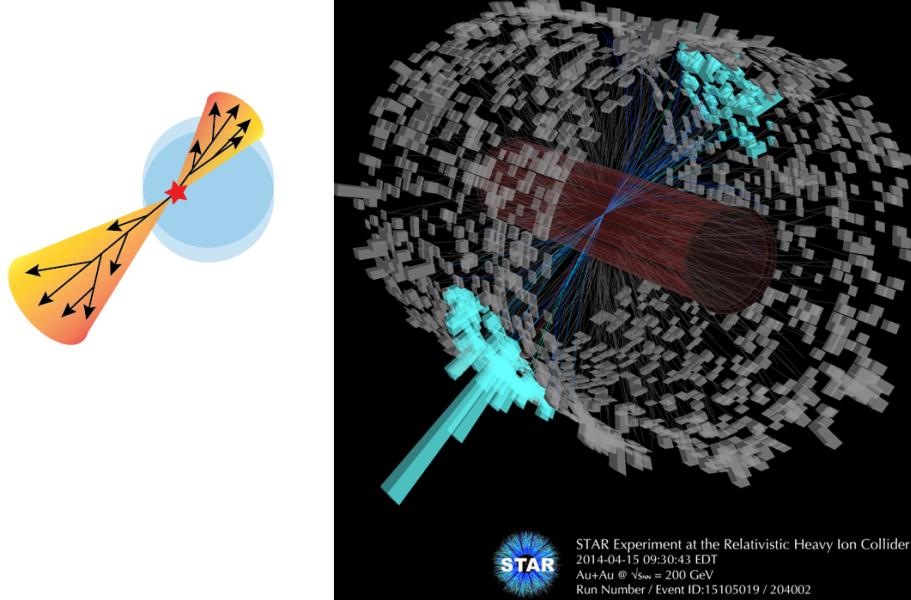
Figure 2.1: Left: Sketch of a dijet, to first order back-to-back in ϕ and balanced in p_{T} [62]. Right: An event display of all particles in a Au+Au collision event at STAR. Charged tracks and hits in calorimeters are shown, (refer to Chapter 3). The tracks and calorimeter hits clustered experimentally into a dijet are highlighted [63].

2.1.1 Jet Algorithm Requirements

The theory and experimental community set a series of requirements for jet algorithms in the 1990 Snowmass Accords[3] [64]. They are:

1. Simple to implement in experimental analyses

2. Simple to implement in theoretical calculations

3. Defined at any order of perturbation theory

4. Yield finite cross section at any order of perturbation theory

5. Yield a cross section that is relatively insensitive to hadronization

The first two points are accomplished through highly optimized, centrally distributed, and universally available software. Currently, this is provided predominately by the FastJet3 software libraries [65]. The third and fourth requirements may be recast as Infrared and Collinear (IRC) safety: In theory, this is defined in measurement functions V of n partons (V_n) of k momenta [61]:

---
3. named after Snowmass Colorado, the location of the 1990 Summer Study on High Energy Physics

$$\text{collinear safety:} \quad V_{n+1}(..., k_i, k_j, ...) \to V_n(..., k_i + k_j, ...) \quad \text{if } k_i || k_j$$

$$\text{infrared safety:} \quad V_{n+1}(..., k_i, ...) \to V_n(..., k_{i-1}, k_{i+1}, ...) \quad \text{if } k_i \to 0$$

In experiment, IRC safety simply means that the jet reconstruction should not be modified by collinear splittings or soft particle radiation. This also helps a jet measurement be robust to variations in experimental resolution: the same jet will be reconstructed whether or not two of its constituent particles' signals have already been merged into one in, for instance, a single calorimeter pad.

2.1.2   The anti-k_T, k_T, and Cambridge/Aachen Algorithms

The anti-k_T [66], k_T [67, 68], and Cambridge/Aachen [69, 70] algorithms are all IRC safe and are each in common use among all high energy experiments. Algorithmically, they differ only by a parameter (p below) which controls the relative clustering priority of particles by energy or distance. The algorithm is given here:

1. Setup:
   - Make an indexed list L_{input} of all particles, each of which is considered a "pseudo-jet" at all stages of the clustering. For purposes of clustering, each jet is defined only by its four-momenta.
   - Make an empty list L_{jets} of the reconstructed jets.
   - Set a jet resolution parameter R. R is roughly equivalent to the final jet radius in ϕ-η space.
   - For any pair of pseudojets i & j, define $\Delta_{ij} = \sqrt{(\phi_i - \phi_j)^2 + (\eta_i - \eta_j)^2}$ and $d_{ij} = \min(p_{T,i}^{2p}, p_{T,j}^{2p}) \frac{\Delta_{ij}^2}{R^2}$, where $p = -1$, 0, or 1 for anti-k_T, k_T, or Cambridge/Aachen jets, respectively.

2. Find the minimum d_{ij} for all pairs of i & j.

3. If $d_{ij} < \min(p_{T,i}^{2p}, p_{T,j}^{2p})$, combine pseudojets i and j into a single pseudojet entry in L_{input}. Otherwise, consider the pseudojet with the smallest value of p_T^{2p} as a final pseudojet; remove it from L_{input} and add it to L_{jets}.

4. Repeat Steps 2 and 3 until L_{input} is empty. Return L_{jets}.

The anti-k_T algorithm is particularly useful in heavy ion collisions because the jet shapes of hard scatterings are largely robust to the presence of large amounts of soft background particles.[4] It is therefore currently used almost ubiquitously to initially sort particles in groups of jet constituents.[5] In practice, it is common to add a distribution of particles with negligible p_T, called ghost particles, to an event over entire ϕ and η acceptance of the detector. When using the anti-k_T algorithm, these particles are simply clustered into the jets without influencing their calculated kinematics. The number of ghost particles per jet may then be used to quantify jet areas.

An example of the three jet algorithms is shown in Figure 2.2. There, a simulated dijet (from PYTHIA6) is embedded into a minimum bias collision.[6] The figure shows the results of using the anti-k_T, k_T, and Cambridge/Aachen algorithms. As can be seen in the example, the p+Au events are relatively sparse, and the PYTHIA dijet (in black in the diagram) clustering selects almost the same particles in each algorithm.[7] The background energy is very sparse, about $1\,\mathrm{GeV}$ of energy per unit of ϕ-η, or about $500\,\mathrm{MeV}$ per $R = 0.4$ jet.

---

4. This contrast to k_T jets can be clearly seen in Figure 2.2.

5. Once the jet constituents are identified, they are frequently then reclustered with other algorithms. For instance, the k_T produces jets whose areas who are not robust in the face of soft background, but in whom subjets have a good resolution [71]. The Cambridge/Aachen algorithm gives angle-ordered splittings within the jet and is also frequently used for jet sub-structure studies.

6. The embedding and event are taken from the those used in this thesis.

7. The tracks clustered into the leading dijet are identical, in the case shown, using the anti-k_T and Cambridge/Aachen algorithms. The k_T algorithm clusters one additional soft track to the dijet.
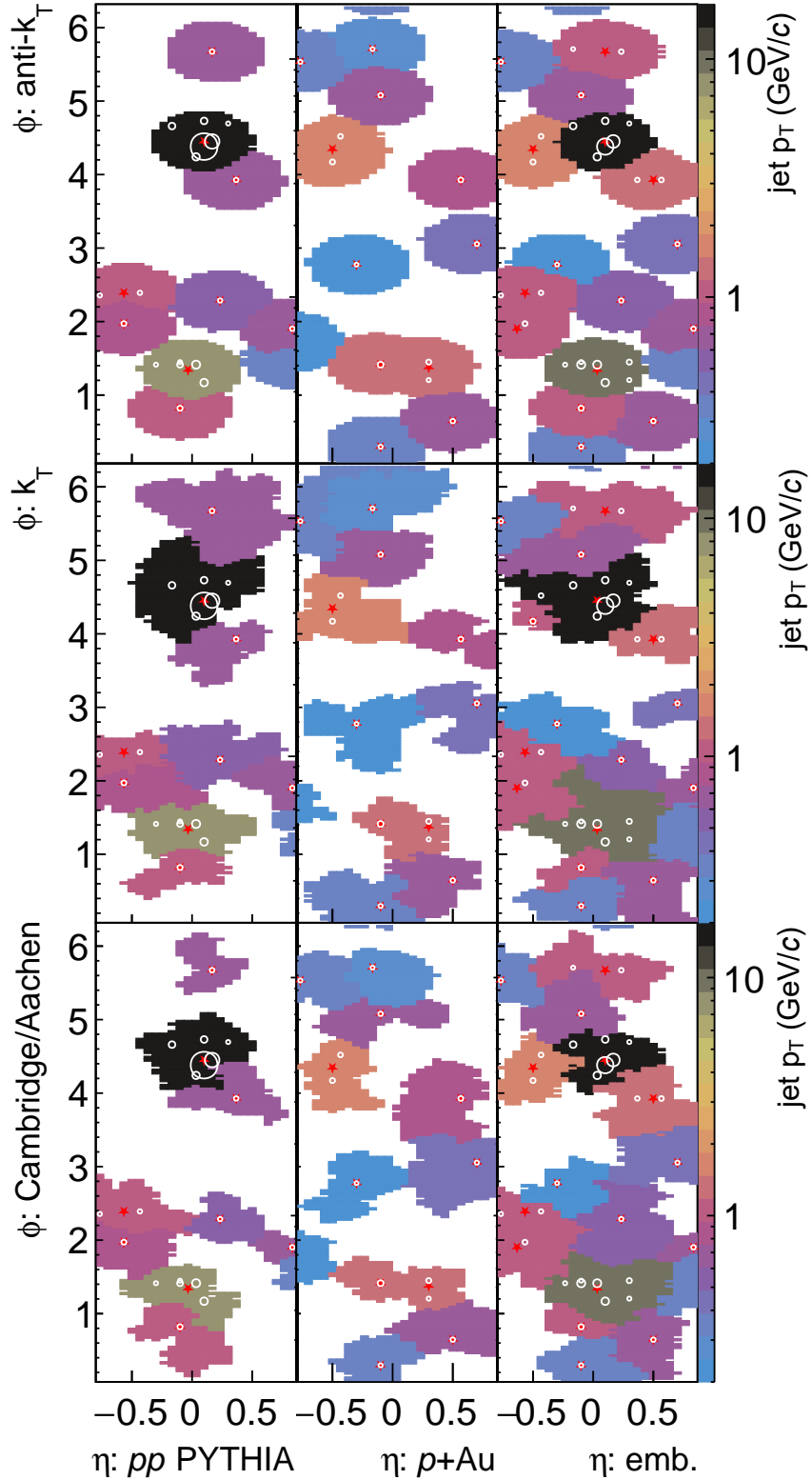
Figure 2.2: A PYTHIA6 pp dijet embedded into a p+Au minimum bias (MB) event. Only tracks shown (ergo, these are charged jets). Red stars are jet axes. White circles are jet tracks constituents; marker sizes scale with track p_T. 1st column: embedded PYTHIA6 tracks successfully reconstruction in simulation. 2nd column: tracks in p+Au MB event. 3rd column: 1st+2nd column's tracks combined.

2.2 Existing Jet Spectra Measurements in p/d+A Collisions

Inclusive R_{sA} jet measurements are the cleanest experimental starting place to look for jet quenching in small systems. It depends only on experimentally determined inclusive pp and s+A cross sections, and measured jet spectra from s+A collisions.[8] As such, a result of $R_{sA} \neq 1$ would make a very strong statement regarding jet quenching in those collisions. The contrapositive ($R_{sA} = 1 \Rightarrow \nexists$ QGP) is not necessarily true, as just how much quenching would result in s+A collisions' correspondingly smaller QGP volumes (if the QGP is present) is not yet settled. In any case, measurements at PHENIX, ALICE, CMS, and ATLAS all report R_{sA} equivalent to unity, as shown in Figure 2.3.
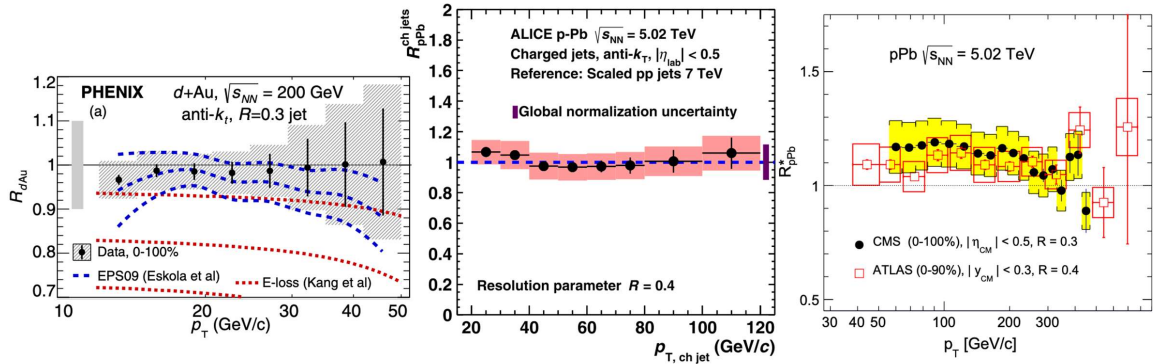
Figure 2.3: Inclusive R_{sA} consistent with unity. Left: Full jets at PHENIX in $\sqrt{s_{NN}} = 200\,\mathrm{GeV}$ collisions [72]. Middle: Charged jets at ALICE in $\sqrt{s_{NN}} = 5.02\,\mathrm{TeV}$ collisions [73]. Right: Full jets at CMS and ATLAS in $\sqrt{s_{NN}} = 5.02\,\mathrm{TeV}$ collisions [74].

ATLAS also measured EA at $\eta \in [-4.9, -3.2]$ (in the Pb-going direction) and used it to bin the $R_{p+\mathrm{Pb}}$ into centrality bins ($R_{p+\mathrm{Pb}}|_{\text{centality}}$), and surprisingly observed a significant suppression(enhancement) of the jet spectra in central(peripheral) p+Pb collisions. Refer to Figure 2.4. As noted in the bins in the figure, the jet modification is more pronounced at mid to high p-going rapidities.

The ATLAS paper makes one further tantalizing observation: the ratio of jet suppression between central and peripheral events (R_{CP}) in each of central-to-p-going centrality bins measured, are approximately identical when the jets are scaled by $\cosh(\langle y^* \rangle)$ (where $\langle y^* \rangle$ is the midpoint of each rapidity bin), as shown in Figure 2.5. The scaling factor converts jet

---

8. Refer to Section 1.5.4 for the trivial derivation for p+A collisions.

p_{T} into jet total momentum.[9] Given that this R_{CP} scaling appears to be only a function of jet energy, and only in the p-going direction over about three units of rapidity indicates that the R_{CP} modification is a x_{p} effect.
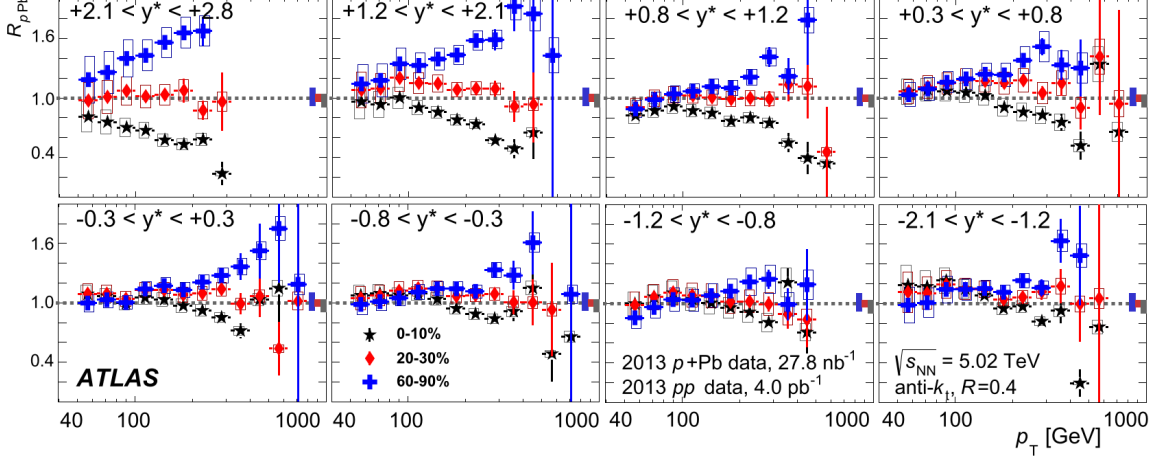
Figure 2.4: Centrality binned jet $R_{p+\mathrm{Pb}}$, plotted in frames of rapidity with most p-going at the top left to most Pb-going in bottom right [34]. Data exhibits clear suppression(enhancement) in central(peripheral) events at p-going rapidities and mid rapidities.
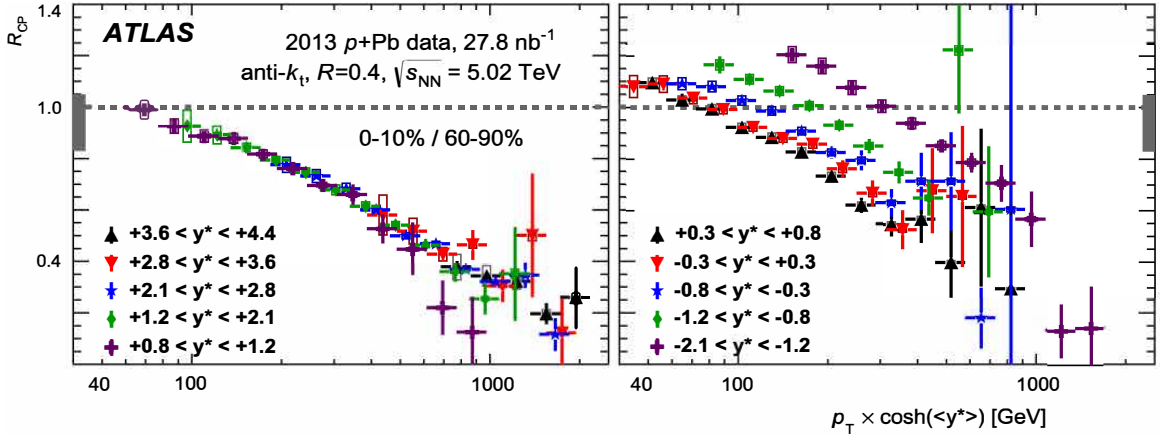
Figure 2.5: ATLAS ratio of central to peripheral $R_{p+\mathrm{Pb}}$ in rapidity bins with jets scaled to full energy [34] with the factor $p_{\mathrm{T}} \times \cosh\left(\langle y^* \rangle\right)$. Left: p-going rapidities. Right: central and Pb-going rapidities. Note strong agreement of all R_{CP} values in all p-going bins. $\langle y^* \rangle$ is the midpoint in each rapidity bin.

Subsequent to these ATLAS results, the ALICE collaboration produced two jet modification studies, also in $\sqrt{s_{\mathrm{NN}}} = 5.2\,\mathrm{TeV}$ $p+\mathrm{Pb}$ collisions. The first, released in 2016, was a nuclear modification factor measurement. Noting the inherent ambiguities in the centrality binning,

9. And therefore, approximately total jet energy, when $E_{\mathrm{jet}} \gg m_{\mathrm{jet}}$.

they labeled their final observed $Q_{p\text{Pb}}$. A plot with their central and peripheral results displayed with ATLAS's results is given in the left hand plot of Figure 2.6.

Two things should be noted regarding this result. First: the centrality binning in s+A collisions is more difficult than in A+A collisions. In A+A collisions, the EA signals are much larger than for pp collisions, such that the fluctuation to mean ratios are also much larger. For an example in p+Au collisions, see Figure 5.3. Second, like STAR, ALICE's rapidity is limited to central rapidities $|\eta| \leq 1$, and their kinematic acceptance for high-p_T hadrons is lower than ATLAS. Therefore, the x_p range sampled by ALICE is smaller than that by ATLAS. As shown in Figure 2.6, ATLAS also did not see $R_{p+\text{Pb}}|_{\text{centality}}$ modification within the x_p range probed by ALICE.

ALICE released a second jet spectra study in 2018 using a semi-inclusive method[75]. Instead of measuring jet spectra per N_{coll}, they instead collected events with a high p_T hadron called a "trigger", and measured the recoiling jet spectra per trigger. The data was further divided according to signal at high Pb-going rapidity into high and low EA bins. This is the same signal which in the $Q_{p\text{Pb}}$ analysis was used to assign centrality. However, in this analysis, it was not required to apply the Glauber model to count by $\langle N_{\text{coll}} \rangle$ per bin. Instead, it is enough to simply compare spectra-per-trigger at high and low EA, and observe the EA-dependence of the ratio. See right hand side of Figure 2.6.

The 2018 ALICE jet paper has a broader application than it's null result for directly observing jet spectra suppression in high EA events (which, given the prior result, they probably weren't expecting anyway). It also calculated the limit of how much out of jet cone energy transport (a means of jet quenching) that could have occurred and still be consistent with the measured recoil spectra. It furthermore found that the ATLAS jet modification, if attributed only to out of jet cone energy transport, would violate this limit [75].

These measurements are the principle motivation for the studies in this thesis. In summary:

- ATLAS observes EA dependence of $R_{p+\text{Pb}}|_{\text{centality}}$ at LHC scale energies, but the inclusive $R_{p+\text{Pb}}$ value is consistent with unity. Therefore, one or a combination of the
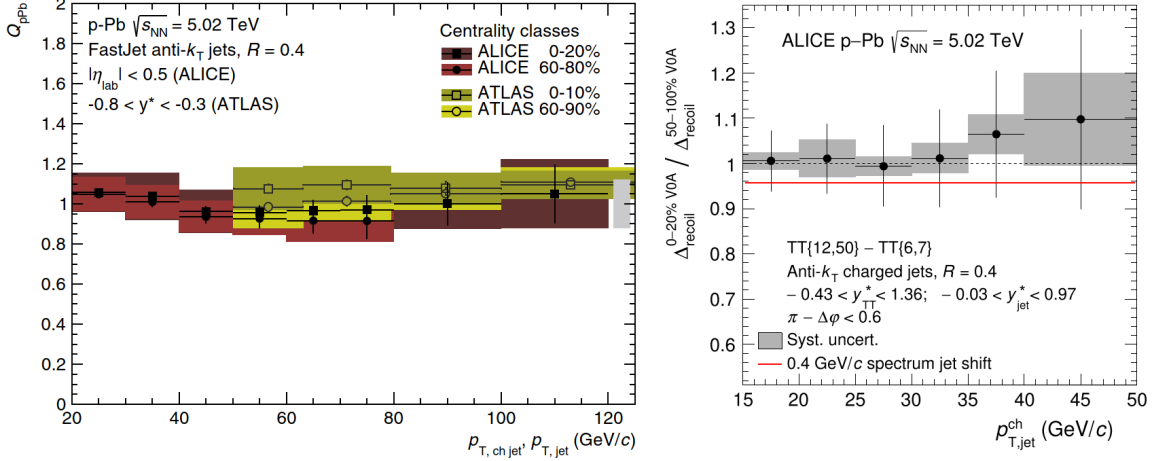
Figure 2.6: Left: ALICE $Q_{p\text{Pb}}$ values plotted against ATLAS $R_{p+\text{Pb}}$ values for most central and peripheral bins [76]. Note that ALICE jets use only charged constituents, whereas ATLAS used charged and neutral particles. Therefore, the x_p value of the ALICE jets are higher than shown relative to the ATLAS jets. Right: Ratio of high to low, corrected, semi-inclusive recoil jet spectra at ALICE [75]. The label Δ was chosen to represent the jet spectra in which the uncorrelated jet spectra had been subtracted from the triggers' correlated jet spectra.

two following processes must be true:

(1) There is an actual physical suppression and enhancement of the jets in the central and peripheral collisions respectively. This would be very exciting: the direct measurement of potentially hot nuclear effects on jets in $p+\text{A}$ collisions.

(2) Somehow, some events are mis-binned, such that high-yield central events are being normalized with lower $\langle N_{\text{coll}} \rangle|_{\text{periphral}}$ events (and are therefore "enhanced") with the opposite occurring with low-yield peripheral events being suppressed by the higher $\langle N_{\text{coll}} \rangle|_{\text{central}}$. This also would have important implications, some possibilities of which are introduced in Section 7.1.

- ATLAS observes that EA modification of R_{CP} scales with x_p.

- ALICE, at lower values of x_p, does not measure EA dependence in either inclusive or semi-inclusive measurements, and notes that limitations set on jet quenching at low x_p do not appear to apply at high x_p.

- Because x_p scales inversely with collision $\sqrt{s_{\text{NN}}}$, RHIC experiments can measure jets that are both lower in magnitude in p_T and also comparable in x_p values to ATLAS. They are ideally suited to verify if it is a x_p result independent of energy scale.

• No semi-inclusive jet spectra measurement has been made at RHIC energy scales.

Along with their inclusive R_{dAu} jet measurement, PHENIX also released measurements of EA binned R_{dAu} and corresponding R_{CP} values. This year (2021) they released a statement that they would update those results with an erratum in the publication. The initial results showed a very clear $R_{dAu}|_{\text{centrality}}$ suppression for the most central bins, which evolves monotonically to a decided enhancement for the most peripheral bin, with the corresponding R_{CP} signal. The trends in the values plotted in the erratum also show a hint of monotonically decreasing R_{CP} with x_p, but are must less distinct. The text of the erratum is not yet published, so perhaps more can be said later. Both the currently published and the proposed amended figures are given in Figure 2.7.
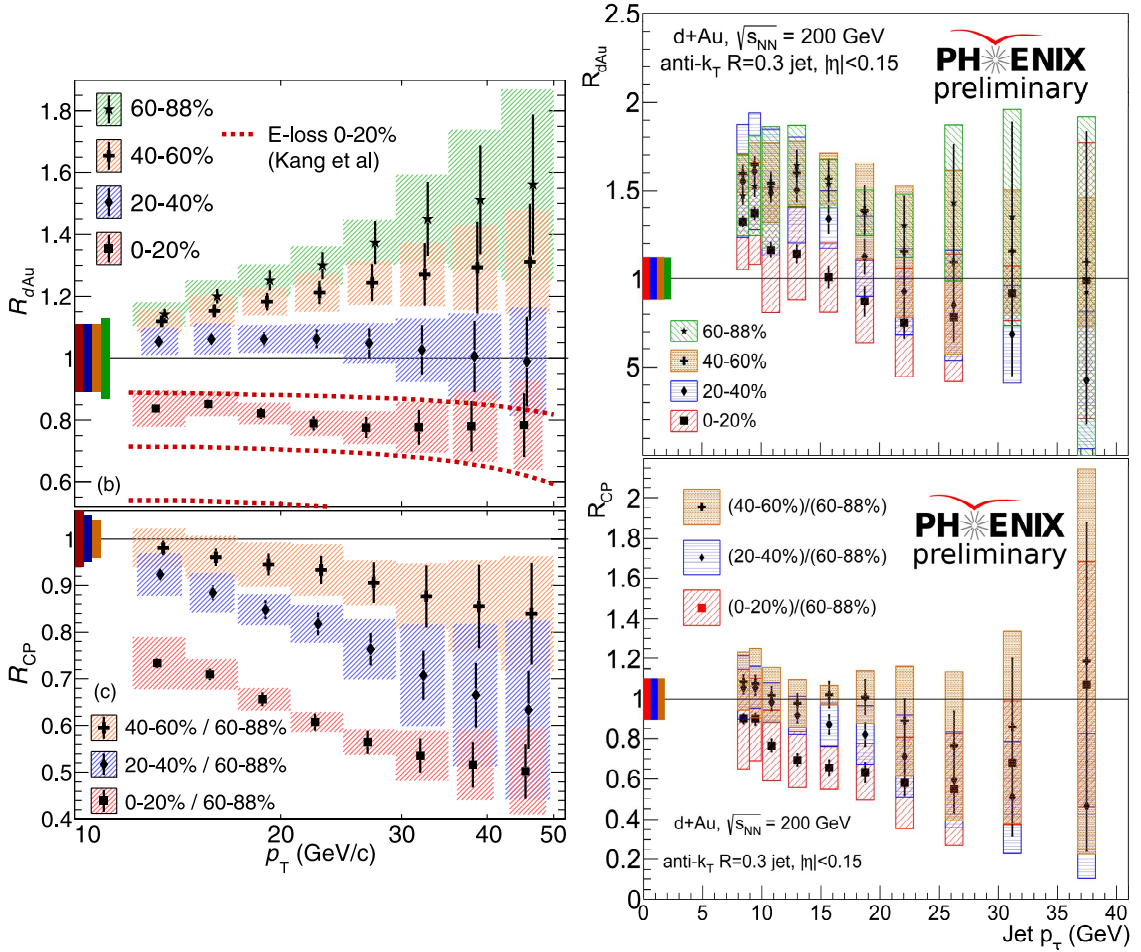
Figure 2.7: Plots of PHENIX full jet $R_{dA}|_{\text{centrality}}$ and R_{CP}. Left: published plots [72]. Right: proposed erratum (not yet published) [77].

In light of the prior version of the result, a driving motive for this thesis was to take the first semi-inclusive small system measurement at high x_{p} (at either RHIC or LHC energy). With the added ambiguity in the PHENIX result, it is also an important confirmation, or clarification, if there is EA dependence of jet spectra at RHIC energies in p+Au collisions.

Chapter 3

Experimental Setup

3.1 Relativistic Heavy Ion Collider

RHIC, built at the Brookhaven National Laboratory (BNL), is the largest dedicated heavy-ion collider in the world. It has two rings 3833 m in circumference with 1740 Helium cooled superconducting magnets [78]. The maximum beam energy available is limited by the ability of the magnets to bend the beam, as determined by the charge-to-mass ratio of the ions in the beam. The maximum value for 197 $_{79}$Au ions is 100 GeV per nuclean, while the maximum value for pp collisions is a corresponding 2.5 times higher (250 GeV).[1]

This thesis presents measurements of $\sqrt{s_{\mathrm{NN}}} = 200$ GeV p+A collisions in the STAR experiment. The paths taken by the $^{197}_{79}$Au and p ions in RHIC are highlighted in yellow and red respectively in Figure 3.1, where the paths in common – as well as both the clockwise blue ring and counterclockwise yellow RHIC ring – are highlighted in blue. For the $^{197}_{79}$Au ions, the process is as follows: gold ions are sputtered off a gold source in the Tandem Van de Graaff and passed through two stripping targets (one in the Van de Graaff, one upon exiting). Around 6% of the ions exit the Van de Graaff with a charge of 32 e at 1 MeV[2]

---

1. As designated in the RHIC design overview [79], and first reached in pp collisions in 2009. In 2012, the actual maximum of 255 GeV was first reached [80].

2. All energies quoted are per nucleon.

[79, 81]. Ions are passed into the Booster Synchrotron, accelerated to 95 MeV and passed through a stripping target on exit to a charge of 77 e with an efficiency of about 45%. The ions are passed into the Alternating Gradient Synchrotron (AGS) and boosted to 8.86 GeV; the final two electrons are stripped when the ions exit the AGS at about 50% efficiency. The ions in the AGS are grouped into bunches of 10^9 ions and 56 bunches total are passed into the RHIC yellow ring [79].[3,4]

The protons originate from a proton source,[5] are accelerated through the linear accelerator (LINAC) to 2.46 GeV and then to 24.3 GeV in the AGS, then transfered to the blue RHIC beam line [82] in groups called "buckets". The proton buckets contain about 1×10^{11} ions, about two orders of magnitude higher than for Au+Au collisions, and consequently four orders of magnitude higher in luminosity ($\mathcal{L}_{pp}$). This is largely offset by a comparable offset in cross sections for pp and Au+Au, such that the overall reaction rates are of the same order of magnitude.[6]

RHIC has six locations where the two beams can be diverted into nearly head-on collisions, of which STAR takes the 6 o'clock position (see Figure 3.1). It can hold beams for up to 10 hours and in practice will abort beams to refill depending on luminosity and beam conditions. Conditions making it desirable to dump a beam fill and recommence with a new fill include a drop in luminosity as beam ions are consumed or lost, or an increase in ions hitting the walls of the pipe (which are called pile-up (PU) events) as the beam loses focus. The fills used for the p+A collisions in this thesis were 7 hours long [85]. The swing in luminosity in the p+A collision runs is representative, with an average starting luminosity (L_{init}) of $88 \times 10^{28} \, \text{cm}^{-2}\text{sec}^{-1}$ compared to a store average of about half of that

3. For reference, that's 56×10^9 gold ions in the ring, from about 4.4×10^{12} ions initially sputtered off the source. That's about 1.43×10^{-9} g of gold (double that if filling both blue and yellow beams for Au+Au collisions). At the going price of data and gold ($10/Gb and $58.30 per gram), this is about the same cost in gold as to send a 16 character text via an app.

4. This is the actual configuration of RHIC for the p+A collisions used in this thesis. The beam lines are versatile, and RHIC could just have easily put Au ions in the blue ring and protons in the yellow ring. Other collisions at RHIC include Copper, Ruthenium, Zirconium, Helium, and Uranium.

5. Optically pumped ion source (OPPIS)[82].

6. Reaction rate R is $\mathcal{L}\sigma$. Total cross sections of pp and Au+Au collisions at $\sqrt{s_{\text{NN}}} = 200 \, \text{GeV}$ are: $\sigma_p = 54.67 \, \text{mb}$ and $\sigma_{\text{AuAu}} = 218.5 \, \text{b}$ [83, 84].
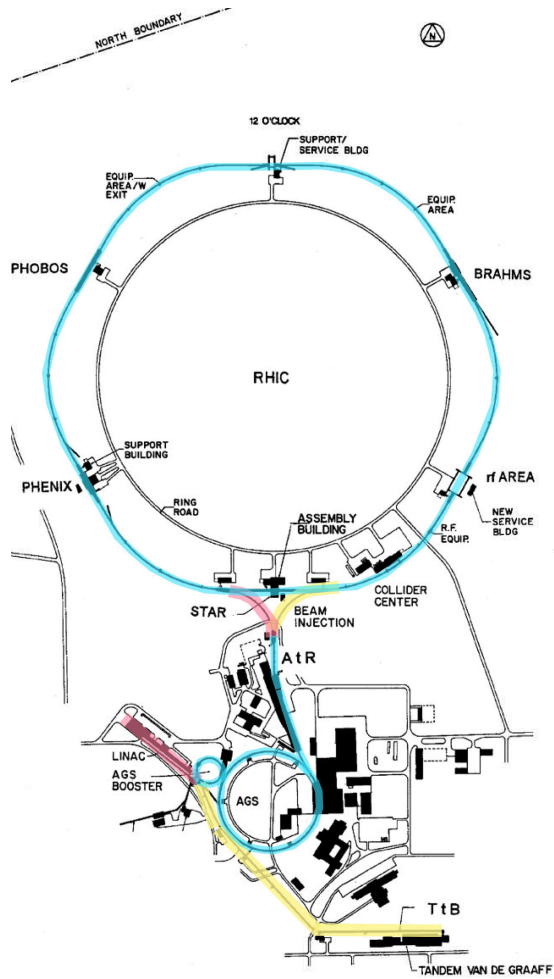
Figure 3.1: Schematic of particle accelerators that make up the RHIC complex. Accelerators and beams are highlighted as follows: yellow for heavy ions, red for p's, blue for both. The RHIC beam line contains two beam line rings: blue is clockwise and yellow is counterclockwise. In this figure they are mutually colored blue. Original figure from [79].

at $45 \times 10^{28}\,\mathrm{cm}^{-2}\mathrm{sec}^{-1}$ [86]. For convenience of the data file size, internally STAR broke up recording events into "runs" of about 30 minutes.[7]

3.2   STAR Detector

The STAR experiment is located at the "6 o'clock" interaction point in the RHIC ring (using north as 12 o'clock), see Figure 3.1. This thesis uses data primarily from the STAR subsystems detailed in Table 3.1, most of which are shown in the schematic in Figure 3.2.

---

7. See to Figure A.1.

As indicated by its name, STAR is located inside of a solenoid magnet; the magnet has an inner diameter of 5.26 m and a length of 6.2 m (see Figure 3.2) [87]. The magnet can deliver fields of 0.25–0.5 T with deviations in field uniformity less than 1000 ppm [88]. For the p+A collisions in this thesis, the full field value of 0.5 T was used.
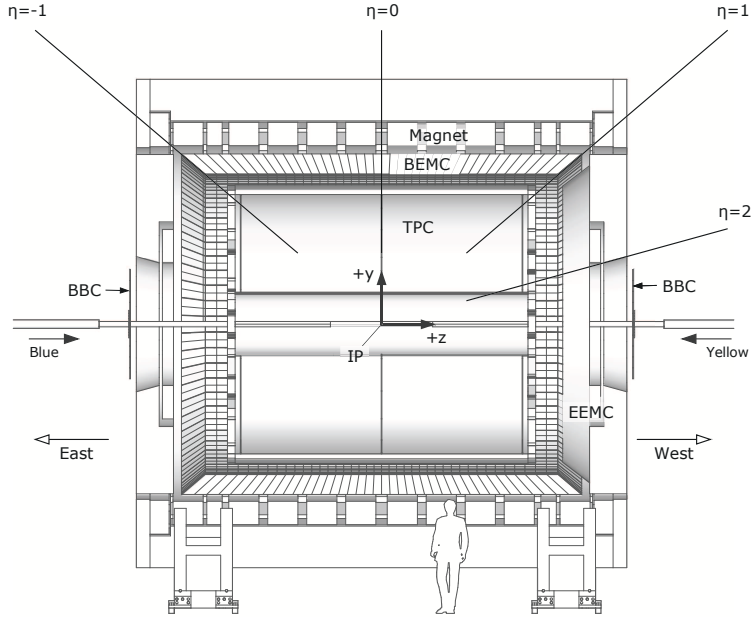
Figure 3.2: Schematic of the STAR detector. In collisions in this thesis, the p and Au going ions are in the blue and yellow beams respectively. Even though it is labeled here, the Endcap Electromagnetic Calorimeter (EEMC), is not used in this thesis. For other acronyms, refer to Table 3.1. Figure from [89].

Table 3.1: Principle STAR detector subsystems used to produce data used in this thesis.

Name	Acronym	Section
DETECTORS		
Time Projection Chamber	TPC	3.2.1
Barrel Electromagnetic Calorimeter	BEMC	3.2.2
Time of Flight	TOF	3.2.3
Beam Beam Counters	BBC	3.2.4
Zero Degree Calorimeter	ZDC	3.2.5
Vertex Position Detector	VPD	3.2.6
TRIGGERS & EVENT RECONSTRUCTION		
Trigger System		3.2.7
Track & Vertex Reconstruction		3.2.8

3.2.1 Time Projection Chamber

The Time Projection Chamber is the principle subsystem of the STAR detector. It consists primarily of a empty cylinder of gas volume of inner to outer radius of 50 to 200 cm by 4.2 m in length. It is divided into two halves by a positively charged central membrane, which is the cathode of an 135 V/cm electric field parallel to the length of the TPC and paired with two anodes, one at each end of the cylinder. Refer to Figure 3.3. The TPC is filled with P10 (90% Argon, 10% Methane) gas, which is ionized by charged particles passing through the TPC. Electrons from the ionization are amplified at the end caps and read by 136,608 read out pads, which are distributed into 12 inner and 12 outer sectors at each end cap [90].[8]
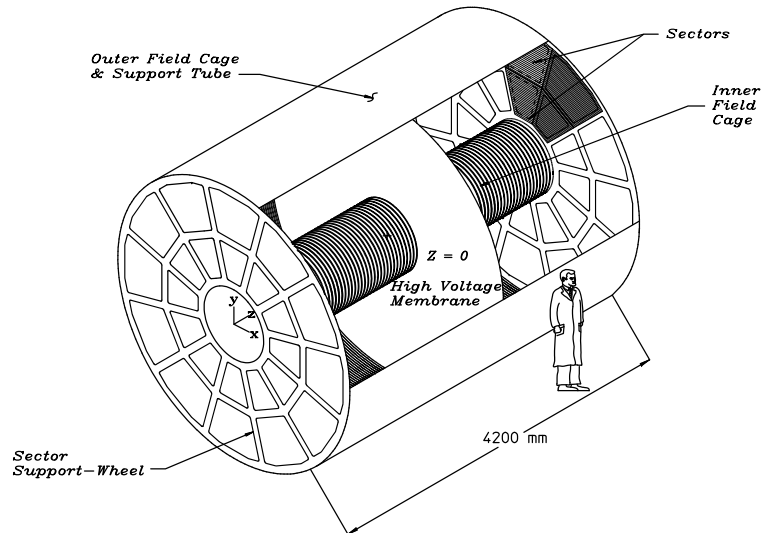
Figure 3.3: Schematic of overall structure of TPC [90].

The magnetic and electric fields in the TPC are designed to be uniform and parallel so that ionization electrons travel straight paths along the length of the TPC to the endcaps and readout pads. Small deviations may occur due to field non-uniformities, field non-alignment, and geometry effects from endcap non-flatness. These effects typically are less than 0.1 cm, are corrected for as best possible, and effect track reconstruction resolution. The combination of hits in the readout pads are reconstructed geometrically into tracks, with information

---

8. Reference provides all values in this paragraph and following paragraph.

regarding the track transverse momentum (p_{T}) from the track curvature, and also ionization energy per distance travelled ($\mathrm{d}E/\mathrm{d}x$) which is a tool for particle identification (PID) for differentiation of particle type.[9]

The drift velocity of electrons from gas ionization is $5.45\,\mathrm{cm}/\mu\mathrm{s}$ along a maximum drift distance of $210\,\mathrm{cm}$ [90], resulting in a maximum drift time of $38.53\,\mu\mathrm{sec}$. This limits time resolution of TPC measurements to a "slow detector" relative to calorimetric or luminosity measurements.[10]

The TPC also sets the geometry reference points for analysing collisions. In Cartesian and ϕ-η coordinates, the z axis is taken to be parallel to the beam-line, with $z = 0$ set at the physical mid-point of the TPC.

3.2.2 Barrel Electromagnetic Calorimeter

The Barrel Electromagnetic Calorimeter consists of 4800 calorimeters encompassing the outer radius of the TPC; see Figure 3.2. It has an inner radius of $220\,\mathrm{cm}$, has full azimuthal coverage, and like the TPC, has rapidity coverage of $|\eta_{\mathrm{BEMC}}| < 1$. The towers are arranged such that each tower subtends ~ 0.05 units of $\Delta\phi$ and $\Delta\eta$.[11] Each calorimeter is composed of $10\,\mathrm{cm}$ of lead divided into 20 layers, interspersed with $10.7\,\mathrm{cm}$ of Kuraray scintillator[12] [91].

Each BEMC tower signal from the scintillators is fed to photomultiplier tubes (PMTs) and summed for a scaler value from each tower. This signal scales linearly with the transverse energy deposited (E_{T}). As such, interpreting the towers signals requires two parameters: a pedestal and a gain value. These can initially be estimated for a tower from a relatively small set of measurements because about 30-40% of relativistic charge hadrons deposit about 20–$30\,\mathrm{MeV}$ in the BEMC towers regardless of hadron species or momentum [92].

---

9. This thesis uses all charged tracks together without PID; it does however, use π, K and p specific embedded tracks for tracking efficiency and unfolding purposes.

10. i.e. BEMC and BBC

11. Radians in ϕ and rapidity in η.

12. This is the same scintillator material used in the BBC, see Section 3.2.4.

These interactions are referred to as Minimum Ionizing Particles (MIPs), and provide a common MIP peak for all towers. In practice, the gain for each tower is relatively stable, and was calibrated for the $p+$A collisions with data from preceding pp collisions. The pedestal values are less stable and were frequently updated between fills while there was no beam (typically several times a day).

3.2.3 Time of Flight Detector

The time of flight detectors are located between the TPC and the BEMC with the same coverage: full azimuth and $|\eta| < 1$. It consists of multigap resistive plate chambers (MR-PCs). The modules consist of an anode and cathode separated by a series of five electrically floating glass plates separated by fishing line. An electrical field of about $100 \, \text{kV/cm}$ is applied and ionizing particles generated avalanches in the gas in the gaps [93]. The resulting signals are very small, but the resolution is very high. As suggested by the name, the TOF is a fast detector, with timing resolution on the order of $90 \, \text{ps}$ [94]. This is important for STAR in general for PID.

3.2.4 Beam Beam Counter

The beam beam counters are located outside of the TPC at $3.7 \, \text{m}$ along z (the beamline direction) from the collision point. They consist of $1 \, \text{cm}$ thick hexagonal scintillator (Kuraray) tiles arranged in an inner and outer annulus [95] as shown in Figure 3.4. The inner hexagonal tiles have $5.57 \, \text{cm}$ sides and the larger tiles have sides four times as large ($22.28 \, \text{cm}$) [96]. The annuli are located at $|\eta_{\text{BBCinner}}| \in [3.4, 5]$ and $\eta_{\text{BBCouter}} \in [2, 3.4]$. The signals are converted by PMT's. The BBC is a fast detector, and used in many of STAR's triggers.[13]. In this thesis, the sum of activity from the Au-going inner BBC tiles is used as a high-rapidity indication of event activity (EA).

---

13. For a good overview, see [97]
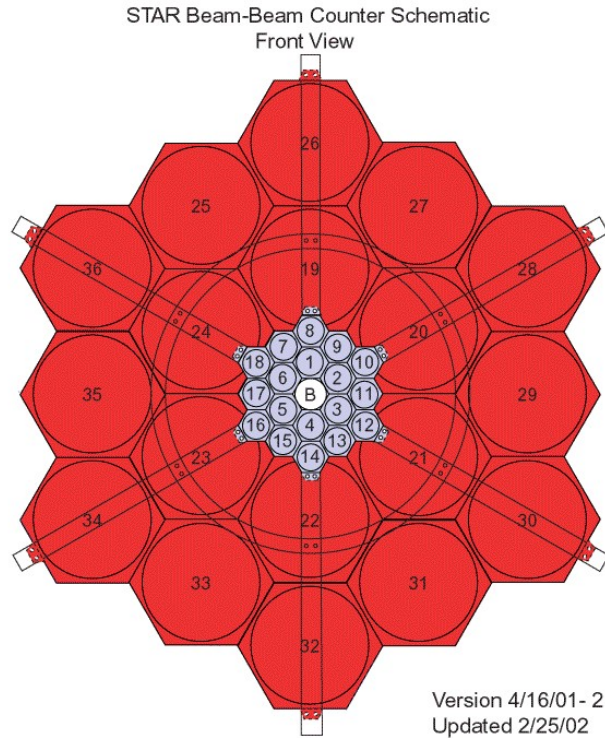
[Schematic of Beam Beam Counter]

Figure 3.4: Schematic of Beam Beam Counter [98]. Small and large hexagons are 5.57 cm and 22.28 cm on edge, respectively.

3.2.5 Zero Degree Calorimeter

STAR's Zero Degree Calorimeters (ZDC's) consist of a tungsten (W) plate with a layer of fiber optic wires which collect Cherenkov radiation from the plates and feed the signal to PMTs. There are three identical ZDC units on each end of the STAR detector 18 m from the interaction point in z [99]. As indicated by the name, the ZDC is located directly in the path of the beam direction, but just after the charged constituents of the beam have been steered away by a dipole magnet, as shown in Figure 3.5. As such, it detects primarily free neutrons generated in the collision events. This allows correlated readings in both ZDC's to indicate a collision.[14] The ZDC is also part of the scaler system, in which signal bits from

---

14. Primarily for A+A collisions; a coincidence of a hit in pp collisions in both ZDC's is not an effective trigger

the ZDC are read at a high frequency, and the frequency of the bits occupation is read as a scalar, the "ZDCx" rate. ZDCx is often used as a luminosity measurement, in which high luminosity is directly correlated with higher amounts of PU events.
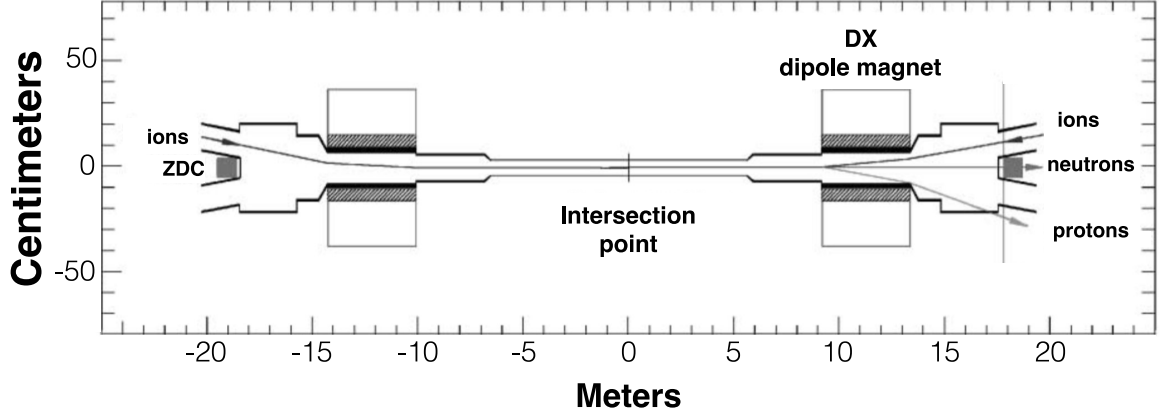
Figure 3.5: Schematic of ZDC location relative to beam line and experiment collision point [100].

3.2.6 Vertex Position Detector

STAR has two Vertex Position Detectors (VPD's), one each located immediately around the beam pipe $4.5\,\mathrm{m}$ on the East and West of the collision point [101][15] and are reflection symmetric for the beams traveling in both directions. Each consists of an arrangement 19 detector assemblies which collectively cover about half of full azimuthal coverage in rapidity $|\eta| \in [4.24, 5.1]$ [102]. The timing resolution of each individual assembly is similar to the TOF (order $100\,\mathrm{ps}$), but collectively the VPD resolution scales by $1/\sqrt{N}$,[16] which in Au+Au collisions results in a resolution on the order of $1\,\mathrm{cm}$[17] and about 2.5 times larger for pp collisions [102].

In practice the VPD frequently serves three separate but similar purposes, all of which are used in the data in this thesis:

1. As a signal to the triggering system that an event occurred

---

15. STAR is at the 6 o'clock position of RHIC, with 12 o'clock being north. Consequently, the beam line runs East and West in STAR.

16. N is number of assemblies triggered in a given measurements

17. i.e. a few tens of ps

2. As a specific requirement in some trigger configurations that the z-axis location of the VPD signal ($V_{\mathrm{z,VPD}}$) is within a required range

3. An analysis specific event level cut requiring that the reconstructed vertex be within a given distance of $V_{\mathrm{z,VPD}}$

3.2.7 Trigger System

The STAR Trigger System is responsible for determining when the STAR Data Acquisition system (DAQ) should read all applicable detectors and record a collision event to file. To do this, a set of logic conditions (called "triggers") are provided to define when an event of interest has occurred. These triggers are selected specific to the type of physics desired, and each is given a "prescale" value. The primary triggers used in this analysis are a minimum bias (MB) and a high tower (HT) trigger. A short, high-level, overview of the STAR Trigger System is given here using these two triggers,[18] the subsystems listed in Table 3.1 and reference [97].[19]

RHIC provides beam bunch crossings in the center of the STAR experiment at 9.37 MHz. For comparison, data buffering in the output limits the rate to less than 3 kHz and the TPC itself can only read events at less than 1.8 kHz. The outputs of the VPD, BBC, and ZDC are small and fast and are sent to the Trigger System in their entirety ("trigger only detectors" in Figure 3.6). The BEMC and TOF, also quite fast, send summary data, and the TPC only reports it's state ("summary data from DAQ detectors" in Figure 3.6). This data is read by the Trigger System every bunch crossing and compared to the triggers. The MB trigger requires an indication from the VPD that there was a collision.[20] The HT trigger requires a VPD measured collision with $|z| \leq 30\,\mathrm{cm}$ in addition to a hard hit in the

18. For reference, this analysis' "MB" trigger number is 500004 and "HT" trigger number is 500206. Refer to Section 4.1.

19. For consistency with the rest of the text, the present tense is used although the data were taken in the summer of 2015.

20. Other MB triggers used the BBC, and many also required the determined vertex to be within a given z-axis range.

BEMC.[21]

For each trigger if, (1) the trigger conditions are met, (2) the required detectors are available, and (3) the DAQ has available tokens, then the Trigger System will check the trigger prescale value. In the $p+A$ data taken, the MB trigger requires only the VPD East-West signal timing to indicate that a collision has occur. To limit the MB data to the desired rate, a large prescale (averaging about 11,800 over all runs) was applied, such that a MB event was measured only once out of every 11,800 times times it was available. The HT events have a much smaller cross section (and are a priority of this data) so they had a prescale of 1, such that every HT event available was recorded. If conditions (1)-(3) were met, and the prescale value agrees, the Trigger System will (a) instruct the DAQ to record the event (while also passing all the trigger data and information from the VPD, BBC, ..., so that it can be recorded with the event), (b) receive a token from the DAQ, and (c) send a message to the slow detectors to digitize and record the event.
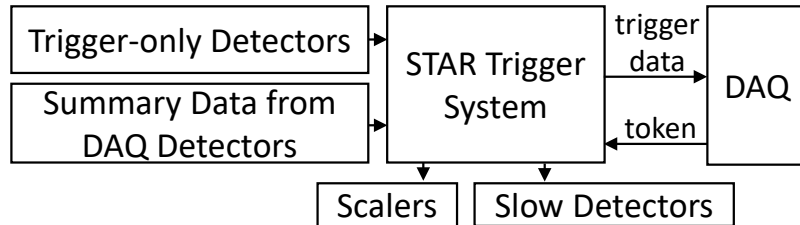
Figure 3.6: STAR Trigger System basic input-output schematic. Simplified from [97]

3.2.8 Track & Vertex Reconstruction

When the DAQ receives instructions from the Trigger System to record an event, it builds an `StEvent` object recorded in a software `ROOT` file using all requested detector subsystems [103]. One of the most computationally intensive tasks is reconstructing hits in the TPC into charged tracks and determining the locations of the primary vertex (PV). The general process is shown in Figure 3.7. The track reconstruction uses a Kalman Filter [104], also referenced in Figure 3.7, which uses a physics model of the TPC similar to, but simpler than, `GEANT`.[22]

---

21. The signal threshold required is equivalent to about 2.6 GeV

22. The software used to simulate particle interactions with the STAR subsystems

After all tracks have been reconstructed without any references to vertices (i.e. "Global Tracks"), they are used in conjunction with the BEMC and Endcap ElectroMagnetic Calorimeters (EEMC) to determine the most likely collision vertex location(s), which are then ranked from most to least likely [105]. The tracks are then refit as "Primary Tracks" relative to each vertex, with their paths forced to pass through the vertex. The data in this thesis uses the best ranked vertices (as algorithmically determined by STAR's event reconstruction) as input, and proceeds with further quality cuts on the vertices and tracks.
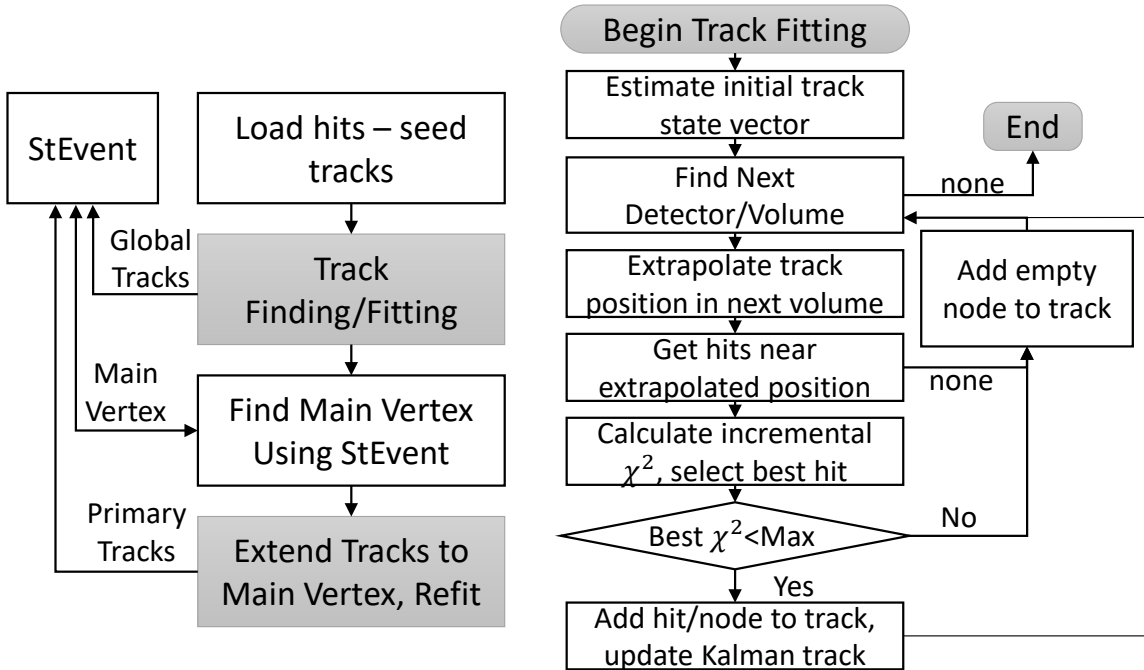
Figure 3.7: Logic process of TPC event reconstruction. Simplified from [104].

Chapter 4

Data Selection and Embedding

The STAR subsystems used in the measurements reported in this thesis have been presented in Chapter 3 along with some details on the event reconstruction and storage. The STAR collaboration processed the data, with some quality assurance cuts, into the files that are the input stream for the analyses in this thesis.[1] The quality assurance process and cuts which are specific to this thesis are presented here. This is done in four stages:

1. Selecting STAR runs

2. Selecting BEMC towers

3. Selecting events

4. Selecting tracks and towers hits

4.1   STAR Runs Selection

RHIC provided p+Au beam for $\sqrt{s_{\mathrm{NN}}} = 200\,\mathrm{GeV}$ collisions in fills that averaged 7 hours. STAR divided these fills into "runs" of data taking lasting about 30 minutes. There are two triggers used in this thesis:

---

1. In STAR's database: `SL20a picoDst` reconstruction of `st_physics` data stream of the `P16id MuDST` files.

- Minimum bias (MB) trigger:[2] This trigger requires signal in both the East and West VPD in correlation with the timing of a bunch crossing. This trigger saturates quickly and has a correspondingly high prescale value.[3]

- High Tower (HT) trigger:[4] Requires a hard hit in a BEMC tower (an online ADC value of 11, which translates to about $2.5\,\mathrm{GeV}$) as well as the online VPD primary vertex measurement of $|V_{z,\mathrm{VPD}}| < 30\,\mathrm{cm}$.

There were 1067 STAR data runs which had events selected with the MB trigger. Runs with short times are frequently the result of a run being restarted to address either detector or beam abnormal conditions. Therefore as a simple heuristic, runs lasting less than $10\,\mathrm{minutes}$ are removed from further consideration. This removes 159 runs, and about 2.4% of the events. Additionally, runs with less than 2000 events are also cut, removing a negligible[5] number of events.

For all remaining runs, fourteen different run averaged parameters ($\langle X \rangle|_{\mathrm{run}}$) from the subsystems of interest are measured. Runs which are outliers in one or more $\langle X \rangle|_{\mathrm{run}}$ are cut in order to minimize variations in beam and detector conditions in the analysis. The criteria labels and the percentage of events removed with any individual cut are given in Table 4.1. The correlation of which runs were cut by which X criteria can be seen in Figure 4.1. All together, the cuts remove about 5.5% of the data. The distribution of cut runs per number of MB events in each run is shown in Figure 4.2.

The criteria X measured for $\langle X \rangle|_{\mathrm{run}}$ are as follow, and are also tabulated in Table 4.1, which lists the event cut statistics and the figure(s) associated with each criteria.

- Track kinematics: ϕ, η, mean and total p_{T} ($\langle p_{\mathrm{T,tracks}} \rangle$ & $\Sigma p_{\mathrm{T,tracks}}$)

- $\mathrm{DCA_{3D}}$ and $\mathrm{DCA_{2D}}$: distance of closest approach between the track's path and the primary vertex in either xyz space or projected into the xy plane

---

2. STAR trigger ID `500004`

3. The prescale value was adjusted from run to run, but averaged 11836.

4. STAR trigger ID `500206`

5. Less than 0.015%

49

- N_{hits}/N_{poss}: ratio of total hits in the TPC associated with a track to the total possible number of hits the track's path could have had

- N_{tracks}^{BEMC} and N_{tracks}^{TOF}: number of tracks whose projected paths match a corresponding hit in the BEMC or TOF

- $N_{tracks,good}^{primary}$: number of tracks that pass track quality cuts (see Section 4.4)

- $N_{tracks}^{primary}$: total number of primary tracks

- $\Sigma BBC_{East\,Small}$: summed signal from the inner tiles of the east BBC. Refer to Section 3.2.4.

- $V_{z,VPD}$ and $V_{z,TPC}$: the locations of the primary vertex in the beam-line direction (z) according to the VPD and the TPC respectively.

- Trigger rate: total number of MB triggered events per second in run

- ZDCx: frequency of occupation of signal bits from the ZDC (refer to Section 3.2.5). This is a measurement of how much activity is occurring in the detector. Increased collision rates due to beam intensity, as well as beam interactions with the beam-pipe, contribute to higher ZDCx rates. The correspondence between ZDC and luminosity can be clearly seen in the event average ZDC per run in Figure A.17. RHIC provides the highest beam luminosity at the beginning of the fill, which then monotonically decreases to the end of the fill, which is the same pattern in the run averaged ZDCx values ($\langle ZDCx \rangle$) recorded by STAR for each fill.

The values of $\langle X \rangle |_{run}$ were calculated for each criteria X for each run using all the MB in that run. The resulting bad runs list is used for analysis of *both* MB *and* HT triggered events. This is reasonable because both triggers were taken concurrently in the same runs, as shown in Figure 4.3, and are both affected by the same variations in detector and beam conditions. In the figure, the effects of saturation and prescaling are also evident. The HT trigger does not saturate, and therefore the number of HT triggered events (N_{HT}) follows the $\langle ZDCx \rangle |_{run}$ pattern of high-to-low for each RHIC fill. The MB trigger saturates even at low luminosity, and therefore doesn't follow the ZDCx pattern. The lower panel also gives the ratio of HT to MB (in which the high MB prescale suppresses $N_{MB\,events}$ relative to $N_{HT\,events}$) along with which runs where cut. This ratio is also plotted scaled by

Table 4.1: Run Consistency Cuts

Subsystem	Parameter X	No. Runs Cut	% Events Cut	Figures
Preliminary Cuts		†		
	$< 10\,\text{min}$	159	2.44	A.1
	$< 2\text{k Events}$	15	0.01	A.2
$\langle X \rangle_{\text{event}}$ Cuts*		‡		
TPC	ϕ_{tracks}	10	2.21	A.3
TPC	η_{tracks}	5	0.44	A.4
TPC	$\langle p_{\text{T,tracks}} \rangle$	8	1.03	A.5
TPC	$\Sigma p_{\text{T,tracks}}$	9	1.15	A.6
TPC	DCA_{3D}	7	0.44	A.7
TPC	DCA_{2D}	5	0.39	A.8
TPC	$\text{N}_{\text{hits}}/\text{N}_{\text{poss}}$	9	0.86	A.9
TPC & BEMC	$\text{N}_{\text{tracks}}^{\text{BEMC}}$	7	0.24	A.10
TPC & TOF	$\text{N}_{\text{tracks}}^{\text{TOF}}$	5	0.39	A.11
TPC	$\text{N}_{\text{tracks,good}}^{\text{primary}}$	6	0.42	A.12
TPC	$\text{N}_{\text{tracks}}^{\text{primary}}$	14	0.99	A.13
BBC	$\Sigma\text{BBC}_{\text{East Small}}$	13	1.07	A.14
VPD	$\text{V}_{\text{z,VPD}}$	5	0.39	A.15
TPC	$\text{V}_{\text{z,TPC}}$	8	0.66	A.16
ZDC	ZDCx	2	0.09	A.17
Trigger	event/sec	4	0.31	A.18
All $\langle X \rangle_{\text{event}}$ Cuts		46	5.52	4.1 & 4.2

† Out of all runs

* These cuts are for outliers of event averages per run of each parameter X

‡ Out of runs that pass preliminary cuts

$\langle \langle \text{ZDCx} \rangle |_{\text{run}} \rangle / \langle \text{ZDCx} \rangle |_{\text{run}}$; as seen, the scaling mostly removes the luminosity dependence in the ratios.

An example of $\langle X \rangle |_{\text{run}}$ is given for $X = \Sigma\text{BBC}_{\text{East Small}}$ in Figure 4.4. The plots for all 16 conditions of X are given in Appendix A.1 (as listed and references in Table 4.1). As seen in the figure, cutoffs are made for $\pm 3\sigma$ of the binned data of run averages.
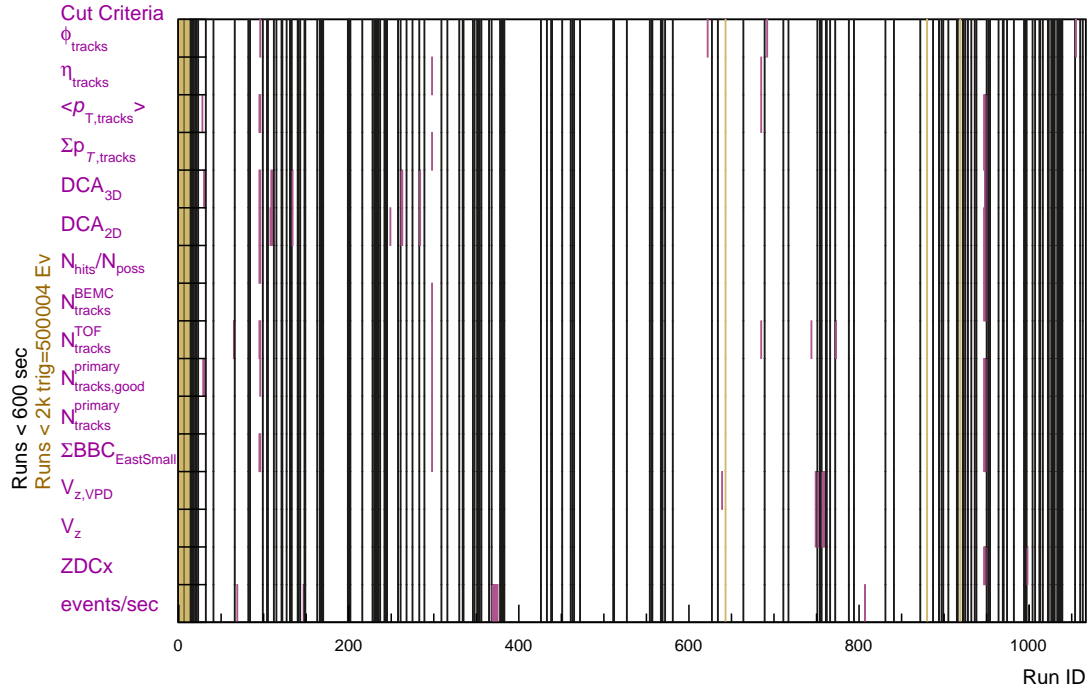
Figure 4.1: Runs cut by QA criteria. Runs are first cut for duration and number of events (they must last at least 10 minutes and have at least 2000 events). These are runs indicated by the black and tan stripes, and are removed before the mean value of each X criteria ($\langle X \rangle |_{\mathrm{run}}$) are calculated. The criteria are listed along the y-axis, and each outlier value for each $\langle X \rangle |_{\mathrm{run}}$ are plotted in magenta. Each run that has an outlier in any criteria is cut. Refer to Table 4.1.
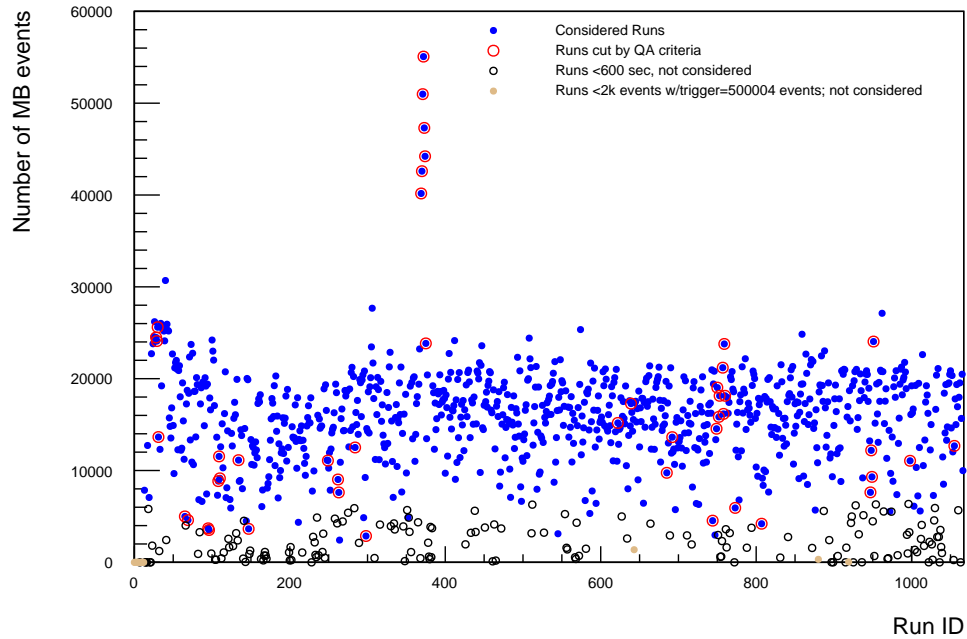
Figure 4.2: Number of MB events per run, and which runs were cut and why; namely, black: too short, tan: too few events, red: $\langle X \rangle |_{\mathrm{event}}$ outlier, blue (without red): not cut.
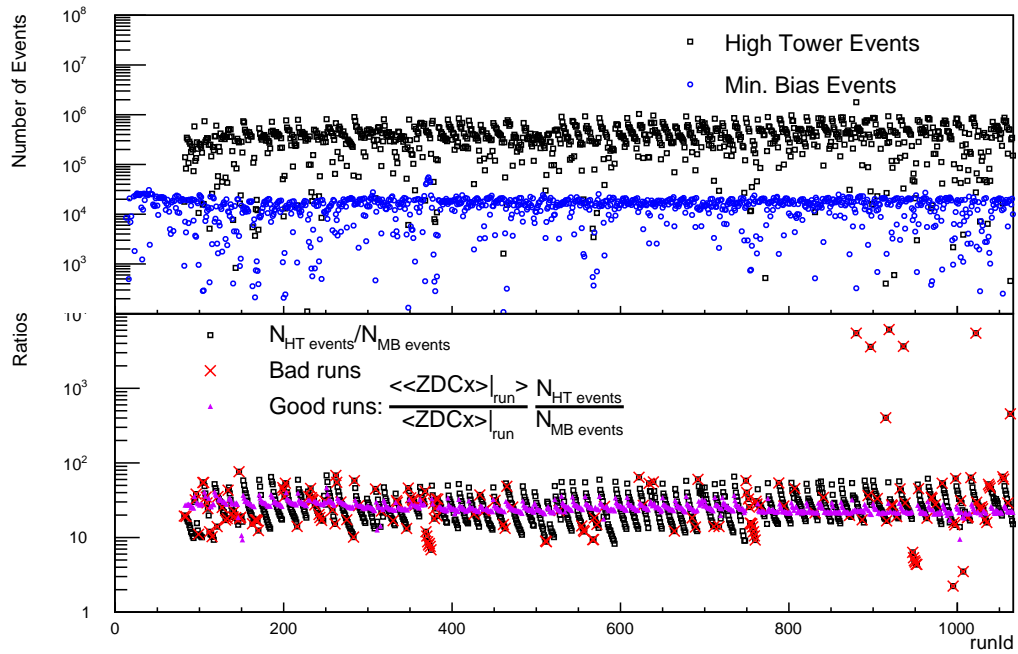
Figure 4.3: Top: Number of MB and HT events per run. Bottom panel: ratio of $N_{HT\ events}$ to $N_{MB\ events}$. The prescales of the HT and MB triggers are 1 and around 12k (It was adjusted run-to-run, but averaged 11836) respectively. Bad runs are crossed out in red. The ratios of numbers of good HT to good MB events (one data point per run) are also plotted divided by the corresponding run's average luminosity scaled by the mean value of all runs' average luminosities; these are the magenta dots.
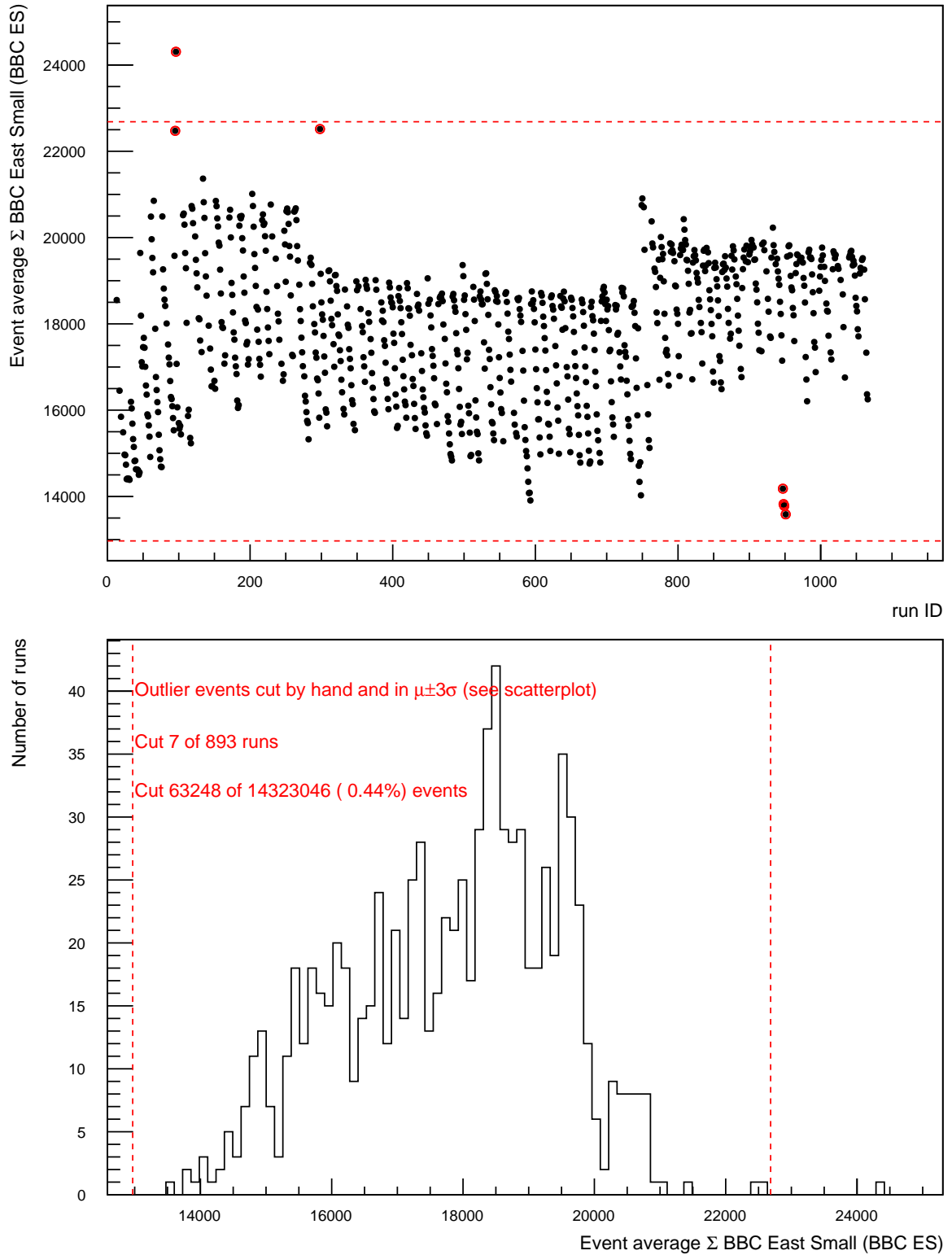
Figure 4.4: Event averaged $\Sigma\text{BBC}_{\text{East Small}}$ (sum of inner tile signal in the BBC, see Section 3.2.4) per run (top), and distribution of averages (bottom). Outliers cut at $\pm 3\sigma$ of distribution (red dotted lines) and/or by hand. Runs circled in red (in top figure) are cut.

54

4.2   BEMC Tower Cuts

The BEMC consists of 4800 towers. It is a fast detector and provides a summary signal of its values to the STAR triggering system for every bunch crossing; this signal is used in the HT trigger requirement. Towers can get stuck in error conditions, such as a hot tower which always signals high and could saturate the HT triggers. Consequently, individual towers can be masked out during the data taking. The STAR collaboration conducts general quality assurance of the BEMC tower signals off line, diagnosing statuses such as stuck bits, bad pedestals, or generally hot or cold towers [106]. The statuses assigned to towers during the data taking were generally consistent throughout the 36 days[6] of data taking, with only a few changes in a minority of the towers.

There were 229 towers which were masked out as bad towers for all runs. This thesis work excludes an additional 89 towers for having an abnormally high frequency of hits in either the HT or MB runs. The frequency of hits above the minimum threshold used in this analysis (200 MeV) was examined in HT and MB runs separately. Additionally, the frequency of hits above 10 GeV was examined for HT runs. The number of hits per tower per event is plotted in Figure 4.5. For each of the three frequencies measured, any tower above the mean $+ 3\sigma$ was removed as a bad tower.[7] The means and standard deviations were recalculated with the first round of bad towers removed, and the cut was applied again to the remaining towers. A map of all 229 initially removed bad towers and the additional 89 removed for this thesis work, is shown in Figure 4.6.

For the final publication, outliers will be selected based on binning in η, which results in approximately the same bad tower selection for $> 10\,\text{GeV}$ tower hits, but a more extensive bad tower list for $> 200\,\text{MeV}$ tower hits. In any case, the bad tower selection is used when quantifying detector response efficiencies by measuring simulated jets embedded into real events.[8]   Therefore, while these moderate changes in bad tower selection may somewhat

---

6. May 4 to June 8, 2015

7. Two very hot towers identified by their $> 10\,\text{GeV}$ frequencies were removed first before calculated the mean and standard deviation.

8. More detail is given in Section 4.7.

smear the resolution of the p_T^{jet} unfolding, it will only very minimally influence the mean p_T^{jet} unfolded values.
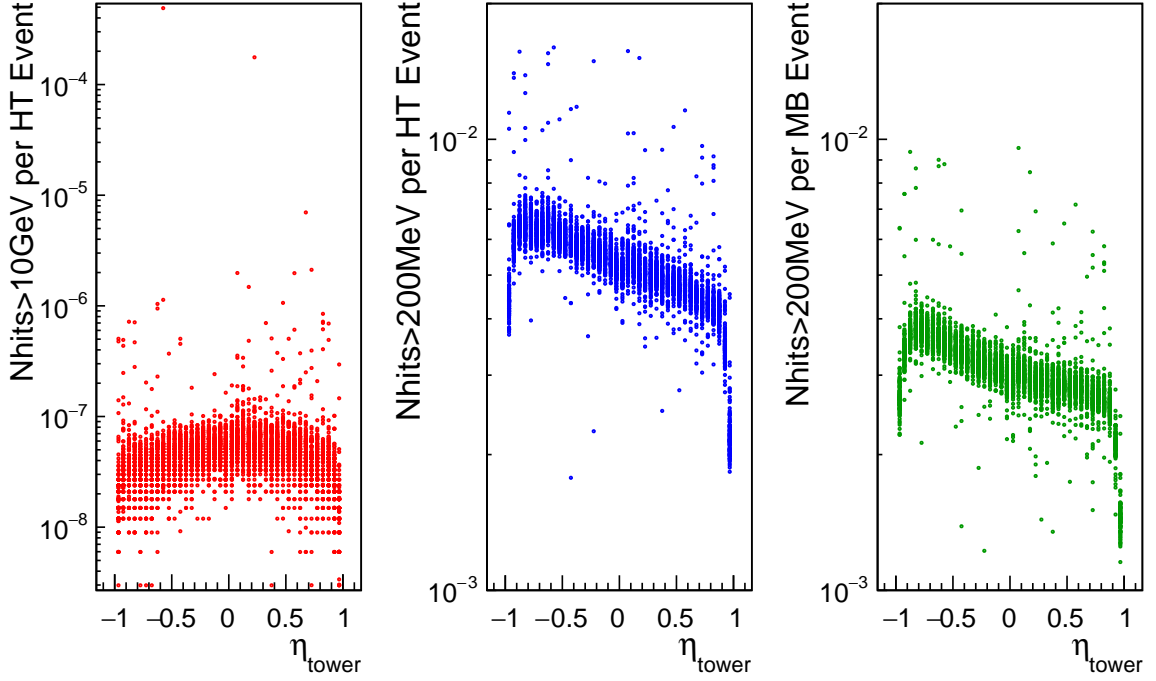
Figure 4.5: Average number of hits per event (N_{hits}/event) for each BEMC tower. Left: N_{hits}/event $> 10\,\text{GeV}$ hits in HT events; note the two very hot towers. Center: N_{hits}/event $> 200\,\text{MeV}$ in HT events. Right: N_{hits}/event $> 200\,\text{MeV}$ in MB events. The asymmetry of the p+Au collisions is apparent, with about 25% more soft hits in the Au-going ($\eta < 0$) half of the BEMC.
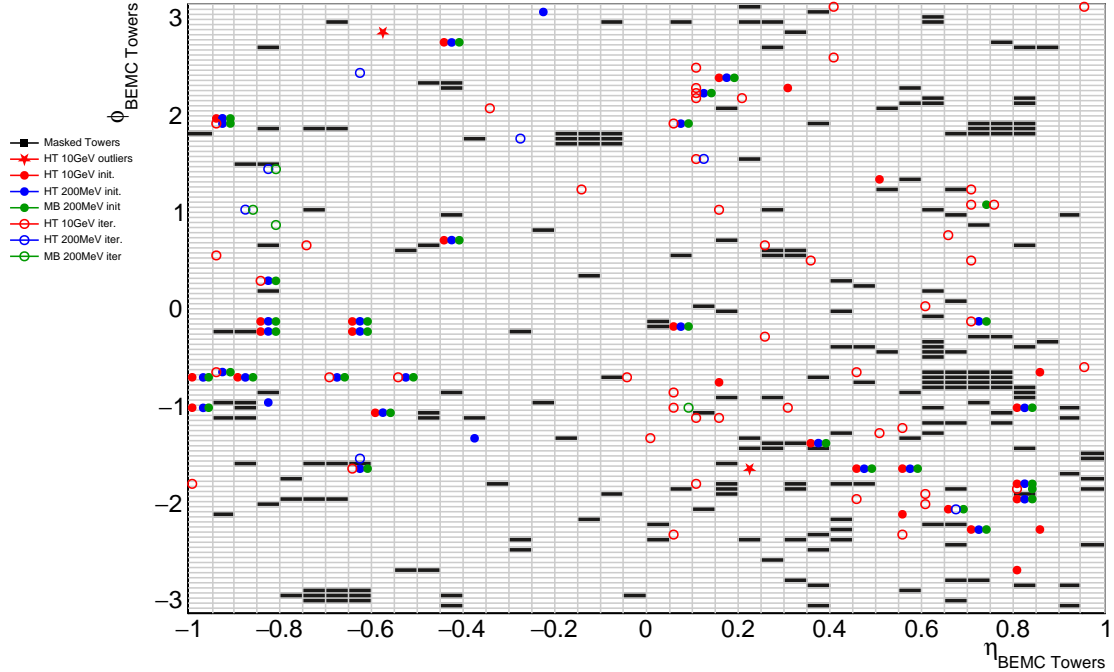
Figure 4.6: Locations of BEMC towers in ϕ and η (relative to $z = 0$) of excluded BEMC towers. Cells in black were masked by the STAR collaboration. The two red full stars (located in ϕ-η at $(-0.575, 2.85)$ and $(0.225, -1.65)$) indicate the very hot, high-frequency $> 10\,\text{GeV}$ hit outliers. The 89 towers with circles are masked for being 3σ above the mean as calculated using either all non-masked towers (the first cut, full circles), or as calculated after removing the first cut (second cut, open circles). Red indicates cuts for hits $> 10\,\text{GeV}$ in HT events, blue and green for hits $> 200\,\text{MeV}$ in HT and MB events, respectively.

4.3 Event Selection

Event z vertex locations (V_z) are required to be within $10\,\text{cm}$ of the center of the TPC. This thesis uses the additional requirement that the VPD determination of the z vertex ($V_{z,\text{VPD}}$) agrees with V_z within $6\,\text{cm}$. The agreement between $V_{z,\text{VPD}}$ and V_z is approximately Gaussian with $\sigma = 2.2\,\text{cm}$ on top of a broader background, such that the cut removes about 10% of events, as shown in Table 4.2 and Figure 4.7, in which effects of the trigger definitions are visually apparent. The events displayed for the MB, which doesn't have a V_z requirement in the trigger, has a much flatter distribution in V_z with a standard deviation of $\sigma(V_z) = 26\,\text{cm}$, whereas for the HT events, which does have a trigger V_z requirement, $\sigma(V_z) = 17\,\text{cm}$. That the VPD should be slightly more efficient in the HT events, 90% vs 88% for MB events, is expected due to the increased activity (and therefore larger signals) of the HT events.

Table 4.2: V_z and $V_{z,\mathrm{VPD}}$ Event Cuts

Cumulative Cuts[†]	Min. Bias. Trigger		High Tower Trigger	
	$N_{\mathrm{events}}\times 10^6$	Ratio Events	$N_{\mathrm{events}}\times 10^6$	Ratio Events
$|V_z| < 50\,\mathrm{cm}$	8.15	1.00	294	1.00
$|V_z - V_{z,\mathrm{VPD}}| < 6\,\mathrm{cm}$	7.16	0.88	264	0.90
$|V_z| < 10\,\mathrm{cm}$	1.74	0.21	102	0.35

† Each of the cuts is in addition to the ones above it
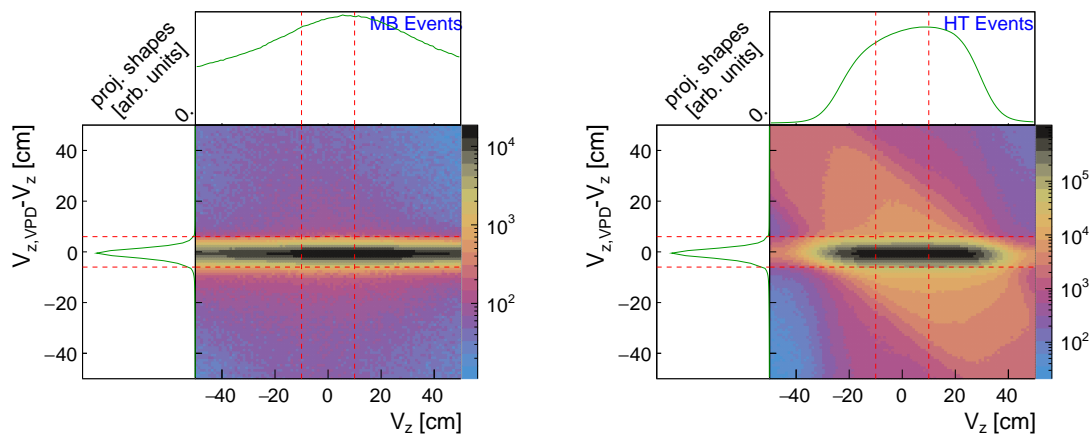
Figure 4.7: All events at $(V_z, |V_{z,\mathrm{VPD}} - Vz|) \leq 50\,\mathrm{cm}$ for Minimum Bias (left) and High Tower triggered (right) events. Color scale is for total number of events. The event cuts are: $|V_z| < 10\,\mathrm{cm}$ and $|V_{z,\mathrm{VPD}} - V_z| < 6\,\mathrm{cm}$, as shown by the red dotted lines.

4.4 Track Selection

Quality cuts for tracks are provided at the collaboration software level, keeping only tracks with a $\mathrm{DCA_{2D}}$ within $3\,\mathrm{cm}$ of the primary vertex. This analysis also enforces the $\mathrm{DCA_{3D}}$ to fall within $3\,\mathrm{cm}$.[9] It is also required that the tracks have $p_\mathrm{T} \in [0.2, 30]\,\mathrm{GeV}/c$, beyond which STAR's TPC track p_T resolution suffers due to the small curvature of the tracks. The tracks are also required to have a minimum number of pads used ("hits" in the TPC, $\mathrm{N_{Hits,Fit}}$) as well as a minimum ratio of "hits" to possible pads ($\mathrm{N_{Hits,Fit}}/\mathrm{N_{Hits,Possible}}$) according to the reconstructed track path. Table 4.3 and Figure 4.8 list the track hit cuts and hit ratio cuts for all used events.

9. The addition of this to the $\mathrm{DCA_{2D}}$ cut removes a small amount (less than 0.34%) of tracks.

Given that DCA cuts force the tracks to pass within a few centimeters of the vertex of the event, which itself must take place in the beam pipe (which is radially in the center of the TPC), then most tracks will have trajectories that cross most of the 45 TPC pads rows with a correspondingly large number of $N_{Hits,Possible}$[10] ($N_{Hits,Possible} \geq 38$ for more than 90% of tracks). The reconstruction efficiency of these possible number of hits is good, with the 90th percentile at $N_{Hits,Fit} \geq 20$.

Table 4.3: Track TPC Hit Cuts for All Used Events

Cumulative Cuts†	Min. Bias. Trigger		High Tower Trigger	
	$N_{tracks} \times 10^6$	Ratio Tracks	$N_{tracks} \times 10^9$	Ratio Tracks
Base Cuts‡	30.1	1.00	2.29	1.00
$N_{Hits,Fit} \geq 15$	28.8	0.96	2.19	0.96
$N_{Hits,Fit}/N_{Hits,Possible} \geq 0.52$	27.1	0.90	2.05	0.90

† Each of the cuts is in addition to the ones above it

‡ $p_T \in [0.2, 30] \mathrm{GeV}/c$, $DCA_{3D} < 3\,\mathrm{cm}$, $|\eta| < 1$
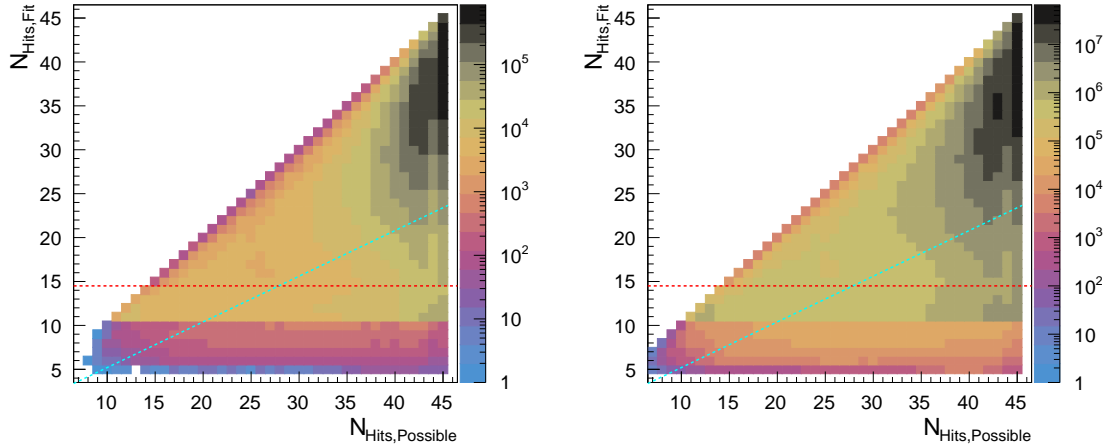
Figure 4.8: Cuts made on tracks associated with the primary vertices of all events which pass event cuts (see Table 4.2) for (left) Minimum Bias and (right) High Tower trigger events. Color scale is for total number of tracks. The track cuts are: $N_{Hits,Fit} \geq 15$ (red dotted line) and $N_{Hits,Fit}/N_{Hits,Possible} \geq 0.52$ (cyan dotted line).

10. Exceptions may occur when a track runs along a sector boundary.

4.5 Tower Matched-Track p_T Correction

When clustering charged jets, only track p_T are used; when clustering full jets, E_T from hits in the BEMC are clustered with the tracks. Some of the BEMC calorimeter signals result from the same charged particles which are also reconstructed as tracks in the TPC, and therefore may be double counted. Ultimately, the jet p_T spectra are corrected by unfolding embedded jets;[11] however, the double-counted energy in the detector level jets results in a smearing of the Jet Energy Resolution (JER). Minimizing the double-counting of charged particles correspondingly minimizes this smearing of the JER. This is done by projecting the charge particle trajectories from their tracks to the BEMC to see if there is a "matched tower." Particles may leave a variable amount of energy in the matched towers, varying from a MIP to their full energy.[12] In prior analyses STAR has corrected BEMC tower energies by subtracting both the MIP energy for towers matched to tracks, and also using the full p_T of the matched tracks, and determined that the later subtraction choice smears the JER less [107]. This analysis therefore does the same; it corrects towers but subtracting the full energies of all matched tracks.[13] Any resulting ener gy (E) scaled by $1/\cosh(\eta)$ (in order to get E_T) with values less than the threshold of $E_\mathrm{T} < 200\,\mathrm{MeV}$ are dropped. The effect on the BEMC E_T spectra in both MB and HT is shown in Figure 4.9.

By construction, tower hits with E_T close to $200\,\mathrm{MeV}$ must be cut whenever they are matched because previously applied track have already removed tracks with $p_\mathrm{T} < 200\,\mathrm{MeV}$. Hence, the hit elimination ratio for matched towers (red squares in Figure 4.9) must start at unity at $200\,\mathrm{MeV}$. Also, as expected, the ratio of tower hits matched at low E_T is comparable in both MB and HT events. As tower hits increase in energy, it becomes increasingly less likely that a track will deposite only a MIP instead of its full energy in the BEMC. This results in the modest falling of the $\mathrm{N_{cut}}/\mathrm{N_{matched}}$ ratio. Combined with the decrease in matching probability, this results in the correction becoming increasing less

---

11. Refer to Section 4.7

12. See Section 3.2.2

13. The track energies are calculated using π^+ meson masses.

important for higher E_T in the BEMC tower E_T spectra (the bottom panels in Figure 4.9).
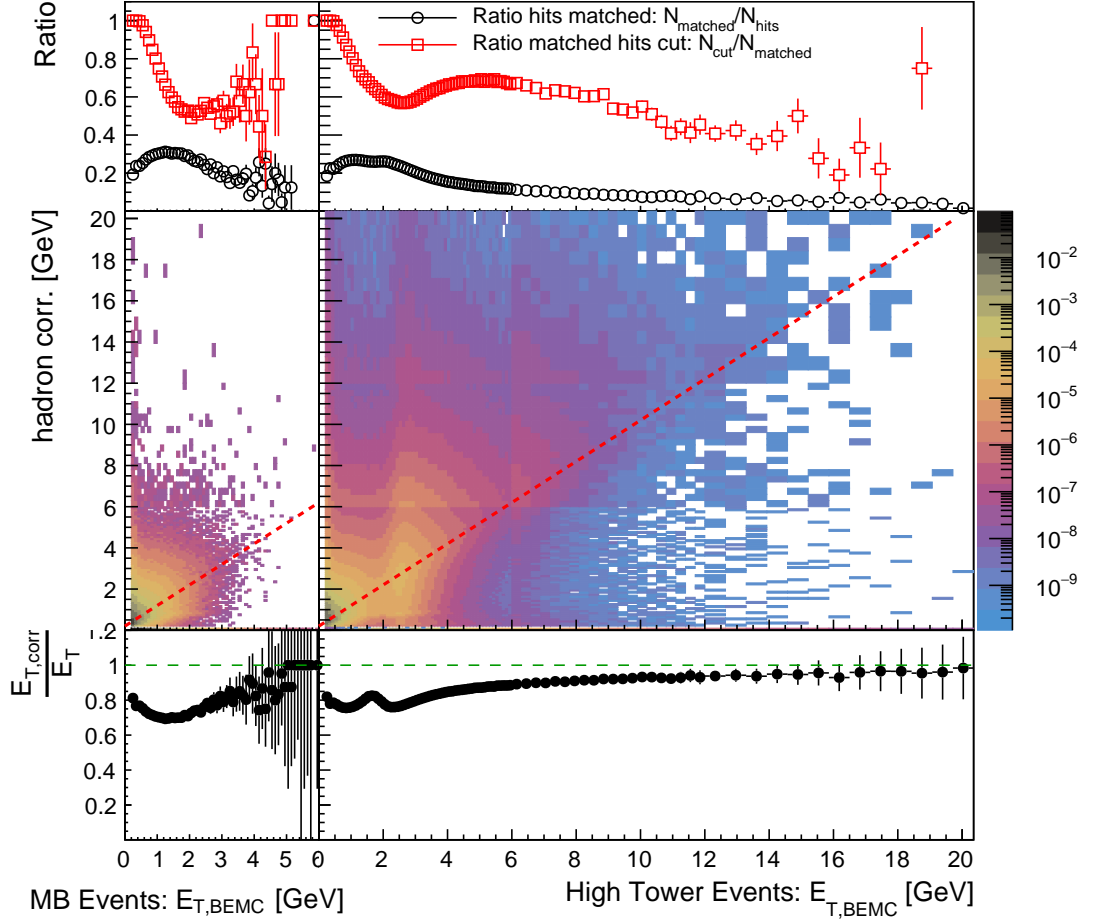
Figure 4.9: Results on tower hit E_T values when subtracting the full energy of all matched tracks. Left column: MB events, right column: HT events. Top row: ratio BEMC hits which have matched track(s) (black circles) & ratio of towers with matches whose correction eliminates the hit (because $E_\mathrm{T,corrected} < 200\,\mathrm{MeV}$ and therefore discarded) (red circles). Middle row: probability distribution of tower hits vs track correction (note that the bin sizes change at $6\,\mathrm{GeV}$ and $12\,\mathrm{GeV}$). All points above the dotted red lines are tower hits which are eliminated by the track matching correction. Bottom row: Ratio of E_T corrected to uncorrected.

4.6   STAR Track Embedding

When STAR's DAQ processes events, it saves the ADC values from various subsystems (including the TPC and BEMC) for a subset of the recorded collisions. These events can then be used for "embedding" additional simulated particles. When this is done, STAR simulates the additional instrumentation responses from the embedded particles' interactions

with the detectors materials and geometries using the Monte-Carlo `GEANT3` code [108]. The instrumentations' embedded responses are combined with the ADC data from the actual events; this combined response is then processed by STAR as if it were an entirely real measurement. In this manner, STAR can embed "particle level" (also called "truth level") tracks into actual events and match them to "detector level" (also called "measured") results. The correspondence between truth and detector level allows the tracking efficiency and resolution to be simulated.

In order to calculate the tracking efficiency and resolution, STAR embedded 260k each of $\pi^{\pm}$, $K^{\pm}$, p, and $\bar{p}$ into minimum bias p+Au collisions.[14] As shown in Figure 4.10, the track reconstruction efficiency approaches about 87% by a few GeV/c for all tracks. At lower energies, the Kaon reconstruction efficiencies are lower because of decays[15] (and consequently shorter path lengths and fewer TPC hits), as seen in top panel of Figure 4.10. The same is true of $\bar{p}$ tracks at low p_{T} due to the higher likelihood of the $\bar{p}$ annihilating.

As track p_{T} grows, it becomes increasingly difficult to measure due to the small track curvature, as attested by decreasing resolution of the reconstructed tracks in panel 3 of Figure 4.10, which results in a total relative resolution of the reconstructed tracks around 3-5%. However, by a few hundred MeV, the mean measured track p_{T} ($p_{\mathrm{T}}^{\mathrm{M}}$) is very close to the truth-level embedded track p_{T} ($p_{\mathrm{T}}^{\mathrm{T}}$), as seen in panel 2 of the figure.

In order to use the track embedding to correct the detector-level track p_{T} spectrum, it is necessary to weight the embedded $p_{\mathrm{T}}^{\mathrm{T}}$ spectrum to match an assumed prior. This prior is important, because it determines bin migration. The dominant effect is that the more low-momentum $p_{\mathrm{T}}^{\mathrm{T}}$ tracks will be reconstructed in higher $p_{\mathrm{T}}^{\mathrm{M}}$ bins (this "bin migration" caused by the limited reconstruction momentum resolution seen in panel 3 of Figure 4.10) than will migrate from the more sparsely populated high-momentum $p_{\mathrm{T}}^{\mathrm{T}}$ bins done to lower measured $p_{\mathrm{T}}^{\mathrm{M}}$ bins. In order to construct the unidentified track prior, it is necessary have a prior for each embedded species, including the relative weighting between them. In $\sqrt{s_{\mathrm{NN}}} = 200\,\mathrm{GeV}$

---

14. Internal STAR embedding request 20180601.

15. Mean proper lifetime: $c\tau_{K^{\pm}} = 371.1\,\mathrm{cm}$ [109].
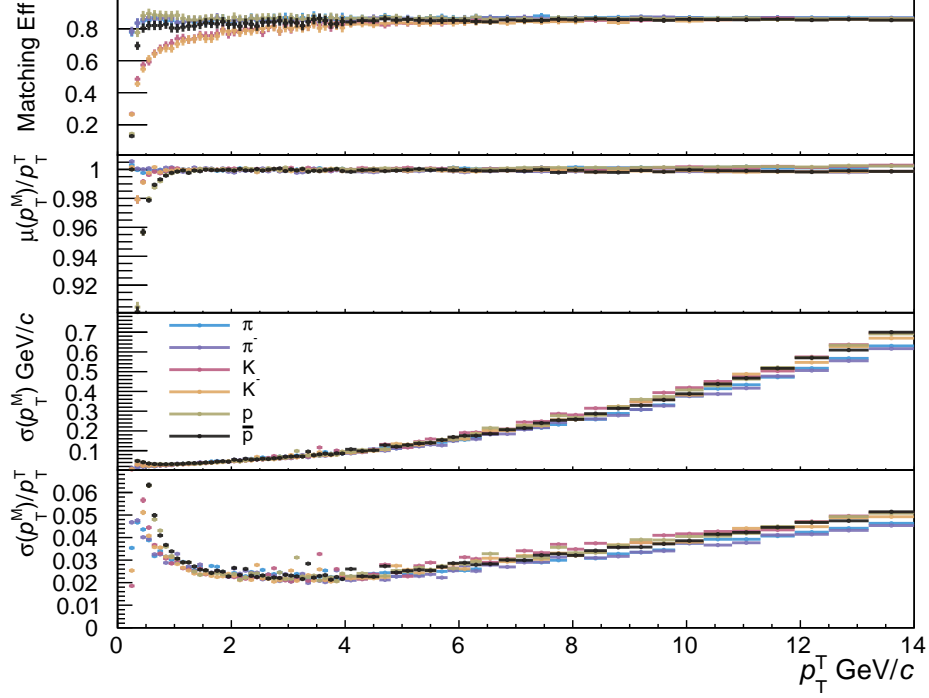
Figure 4.10: Track matching efficiencies and resolution for $\pi^{\pm}$, $K^{\pm}$, p, and $\bar{p}$. 1st panel: efficiency (probability) of matching an embedded track to a reconstructed track. 2nd panel: mean measured p_T (p_T^M) per embedded p_T (p_T^T). 3rd panel: reconstructed track momentum resolution. 4th panel: reconstructed momentum resolution normalized by p_T^T.

data, the following particle spectra data have been measured:

- STAR has measured p, $\bar{p}$, and $\pi^{\pm}$, up to $p_T \sim 10\,\mathrm{GeV}/c$ in pp and d+Au collisions [110].

- STAR has also measured K_S^0 up to $p_T \sim 5\,\mathrm{GeV}/c$ in pp collisions [111].

- PHENIX has measured K^+ up to $p_T \sim 2.3\,\mathrm{GeV}/c$ in d+Au collisions [112].

There are no minimum bias measurements of hadron p_T spectra for p+Au spectra at $\sqrt{s_{NN}} = 200\,\mathrm{GeV}$; however, it is not expected that the relative ratios of the hadrons are significantly different from either pp or d+Au events. Therefore, the spectra from pp collisions are used for priors in this analysis, and the differences resulting from using spectra from d+Au collisions as priors instead is included in the systematic uncertainties.[16]

In order to extend the spectra out to $15\,\mathrm{GeV}/c$, the experimental spectra are fit with a

---

16. The added relative uncertainty, for example, in Figure 5.11 is rarely more the 0.1%

Levy function of the form:

$$\frac{\mathrm{d}^2\mathrm{N}}{2\pi p_\mathrm{T}\mathrm{d}p_\mathrm{T}\mathrm{d}y} = \frac{B}{(1 + (m_\mathrm{T} - m_0)/nT)^n} \tag{4.1}$$

$$\text{where } m_\mathrm{T} = \sqrt{p_\mathrm{T}^2 + m_0^2} \tag{4.2}$$

where B, n, and T are fitted constants and m_0 is the rest mass of the hadron [110].[17] As reported in the references, the measured Kaon spectra scale with m_T multiplied by a factor of two. Using this, the $\pi^\pm$ spectra can be scaled for use in place of the $\mathrm{K}^\pm$ spectra. Therefore, within a given rapidity y, a measured set of points mapped by $\mathrm{N}_i/p_{\mathrm{T},i} = f(p_{\mathrm{T},i})$ can be converted from π to K spectra. For each set of points i:

$$m_{\mathrm{T,K}} = m_{\mathrm{T},\pi} \Rightarrow p_{\mathrm{T,K}}^2 + m_\mathrm{K}^2 = p_{\mathrm{T},\pi}^2 + m_\pi^2 \tag{4.3}$$

$$\Rightarrow p_{\mathrm{T,K}} = \sqrt{p_{\mathrm{T},\pi}^2 + m_\pi^2 - m_\mathrm{K}^2} \tag{4.4}$$

Remembering the factor of $p_{\mathrm{T},i}$ in the denominator on the left-hand side of Eq. 4.1, and the scaling factor of 2, then:

$$N_\mathrm{K} = \frac{1}{2}N_\pi \frac{p_{\mathrm{T,K}}}{p_{\mathrm{T},\pi}} \tag{4.5}$$

The results of m_T scaling from $\pi^\pm$ to K's in pp and $p/d+$A collisions are shown in Figure 4.11 where the scaled $\pi^\pm$ spectra are plotted along with available K data.

The ratios of tracks that are each of the six particle species are plotted in Figure 4.12; the top panel showing the results when derived from pp collision data (which are the ratios used in this thesis) and what the differences are if using results are instead derived using the $d+$Au collision data. Not surprisingly, the biggest differences are found at higher p_T value where the yield values are extrapolated with the Levy function fit.

The ratios of track spectra – measured to matched truth and measured to all embedded – are shown in Figure 4.13. The plots show the small (generally sub-percentile) uncertainty introduced by the $d+$Au prior (which only become significant for high p_T tracks). The ratios were also calculated an additional four times; once each using tracks from high and low

---

17. Also see [113] contained in reference.
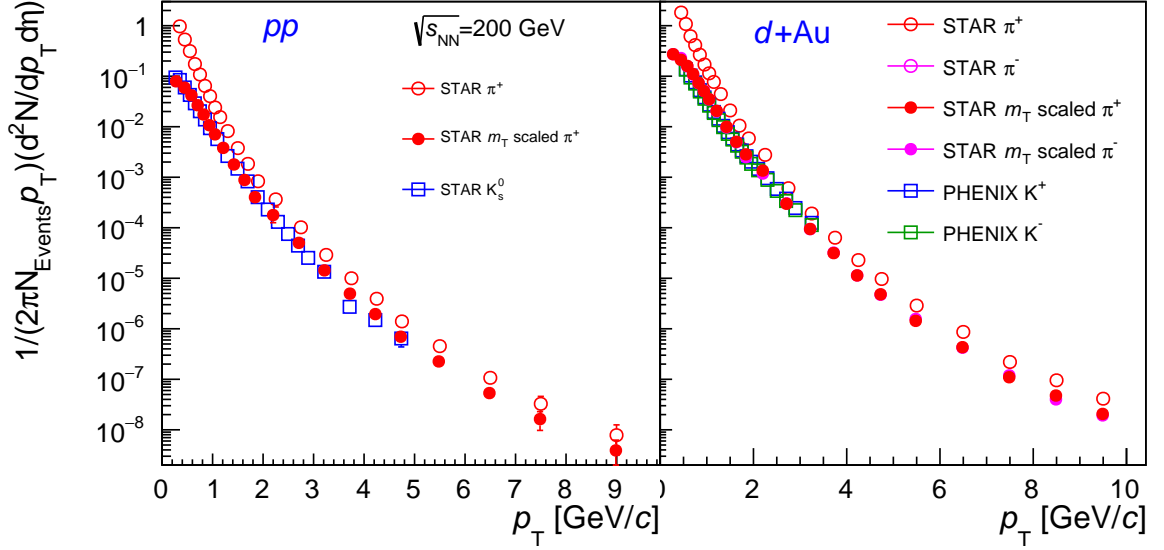
Figure 4.11: Plots of experimental K and $\pi^{\pm}$ spectra along with $\pi^{\pm}$ spectra m_{T} scaled to K masses in $\sqrt{s_{\mathrm{NN}}} = 200\,\mathrm{GeV}$ collisions. Left: *pp* collisions with STAR data. Right: *d*+Au collisions with $\pi^{\pm}$ data from STAR and K$^{\pm}$ data from PHENIX. Measured $\pi^{\pm}$ and K$^{\pm}$ spectra from [110–112].

luminosity events, and once each using tracks from high and low EA$_{\mathrm{BBC}}$ events. The results determine the corresponding systematic uncertainties. As shown in plots, the luminosity uncertainty dominates.

The track embedding data is used to unfold spectra in different bins of p_{T}, which is then used to calculated average number of tracks and mean track p_{T} density (Section 5.5 and Figure 5.9). In those measurements, the softer tracks (along with their errors) dominate.
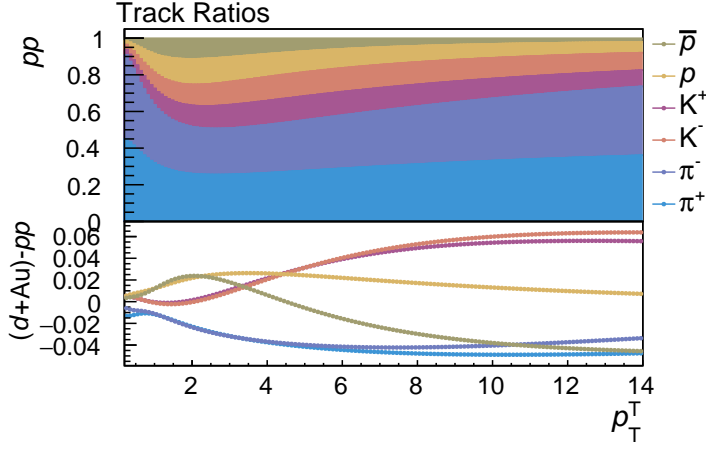
Figure 4.12: Ratios of tracks priors in which tracks are estimated to consist entirely of $\pi^\pm$, $K^\pm$, p, and $\bar{p}$. Levy functions are fit to existing data points to extrapolate to all p_T. $K^\pm$ in the pp data are extrapolated from K_s^0 values; in $d+Au$ data they extrapolated from m_T scaled $\pi^\pm$ data. Top panel: track particle ratio composition derived from pp collision measurements. Bottom panel: Change in particle ratios compositions if derived from $d+Au$ collision data.
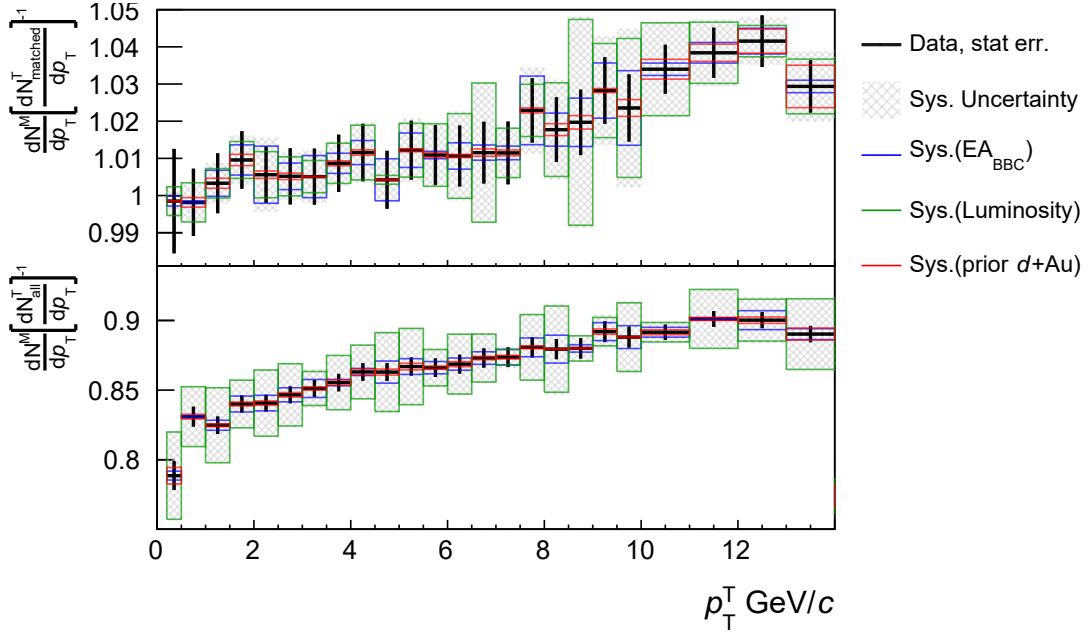
Figure 4.13: Track reconstruction efficiencies. Top panel: ratio of reconstructed track p_T spectra to matched-embedded track p_T spectra. Bottom panel: Ratio of reconstructed track p_T spectra to total embedded track p_T spectra (essentially the top plot decreased by the matching efficiency). Luminosity effect dominated uncertainties. The efficiency growth with increasing p_T is due to bin migration from low p_T^T to higher p_T^M.

4.7 Jet Embedding

In order to calculate and correct jet energy spectra (JES) and jet energy scale (JES) – collectively the "jet performance" – `PYTHIA6` jets were embedded into p+Au MB events.[18] This serves to populate unfolding matrices are used to correct jet spectra measured at the detector level to the actual "particle-level" (also called truth-level) jets. This simulates the closest condition available to a triggered HT event in which we know the truth-level jet details in a p+Au environment. Because STAR has tunned `PYTHIA6` to closely simulate jets in 200 GeV collisions, the particle production weightings of the jet constituents of the `PYTHIA6` jets are used as-is.

The MB trigger is experimentally designed to sample the total distribution of scattering energies (Q) which occurred in the STAR detector. Jet events are the small high-Q tail of that distribution, experimentally selected with the HT trigger. This triggering is necessary, because otherwise it would require an infeasibly large number of MB triggered events to collect sufficient high-Q events to conduct jet studies.[19] In an analogous way, `PYTHIA6` is designed to sample the true ("MB") spectra including the high-Q jet tail, but it is not tractable to populate that tail by simple generating the enormous number of events necessary to eventually populate the tail. Therefore, `PYTHIA` has a feature, similar to a HT trigger, that allows the user to request to run in different $\hat{p}_\mathrm{T}$ bins. In each bin, `PYTHIA`, early in the simulation, determines if a sufficiently hard interaction has occurred, as required by the input $\hat{p}_\mathrm{T}$ range. It if it has not, as is usually the case for MB events, then the simulation terminates the loop early and tries again. `PYTHIA6` keeps statistics for the total cross section for each $\hat{p}_\mathrm{T}$ bin set of events, such that the results of the runs in each ith $\hat{p}_\mathrm{T}$ bin can be weighted by $1/\left(N_{bin\,i}^\mathrm{events}\sigma_{\mathrm{bin}\,i}\right)$ for the appropriate relative weighting. The summation of the weighted bins of jets therefore becomes the prior: the best estimate of the actual high-Q tail of the MB spectra. This weighting is essential because it determines significant effects in the unfolding, such as bin migration in jet p_T.

---

18. Internal STAR embedding request 20184801.

19. See Figure 5.7 for an example, in which the MB upper tail in leading tower E_T essentially runs out of statistics by 5 GeV, well below the 8 GeV cut applied for many of the rest results reported in this thesis.

Sufficient events were embedded such that the resolution on the unfolding spectra would be limited by the statistics of the experimental sample, rather than the statistics of the embedded events. The number of embedded events requested is given in Table 4.4. In data, a $30\,\text{GeV}/c$ cut is applied to the maximum track p_T or tower energy in any event; otherwise the event is discarded.[20] The same cut is applied in simulation as in data which, not surprisingly, removes about a quarter of the PYTHIA events generated in the maximum $\hat{p}_\text{T}$ bin of 55-65.

Table 4.4: Embedded Pythia Events by $\hat{p}_\text{T}$ Bin

Low $\hat{p}_\text{T}$ [GeV]	High $\hat{p}_\text{T}$ [GeV]	$N_\text{events} \times 1000$	σ [mb]	% cut by $30\,\text{GeV}$ Limit[†]
5	7	375.7	1.075×10^{-1}	
7	9	217.7	1.910×10^{-2}	
9	11	110.7	4.752×10^{-3}	
11	15	168.8	1.988×10^{-3}	
15	25	517.8	3.613×10^{-4}	
25	35	176.4	9.655×10^{-6}	1
35	45	57.6	4.711×10^{-7}	4
45	55	53.0	2.684×10^{-8}	12
55	65	45.1	1.382×10^{-9}	25

† Any events with $p_\text{T}^\text{track} > 30\,\text{GeV/c}$ or $E_\text{T}^\text{tower} > 30\,\text{GeV}$ are cut.
  (Numbers in third column are post cut.)

The work for this thesis reconstructed the truth-level (as displayed in Figure 4.14) and detector-level jets and matched them in a process analogous to the charged particle track embedding discussed above in Section 4.6. Both the truth level PYTHIA6 jets and the embedded events were reconstructed using the anti-k_T algorithm with jet resolution $R = 0.4$. At the truth level, all neutral and charged particles were clustered. On the reconstructed level, tracks and towers were clustered together. The exact same cuts and corrections were applied as for jets in the HT events. These are:

- Track p_T cuts. See Section 4.4.

- Tower cuts, including the bad tower list. See Section 4.2.[21]

---

20. Refer to Section 4.4

21. Note that because the bad tower selection is the same in both the data and in the simulation used
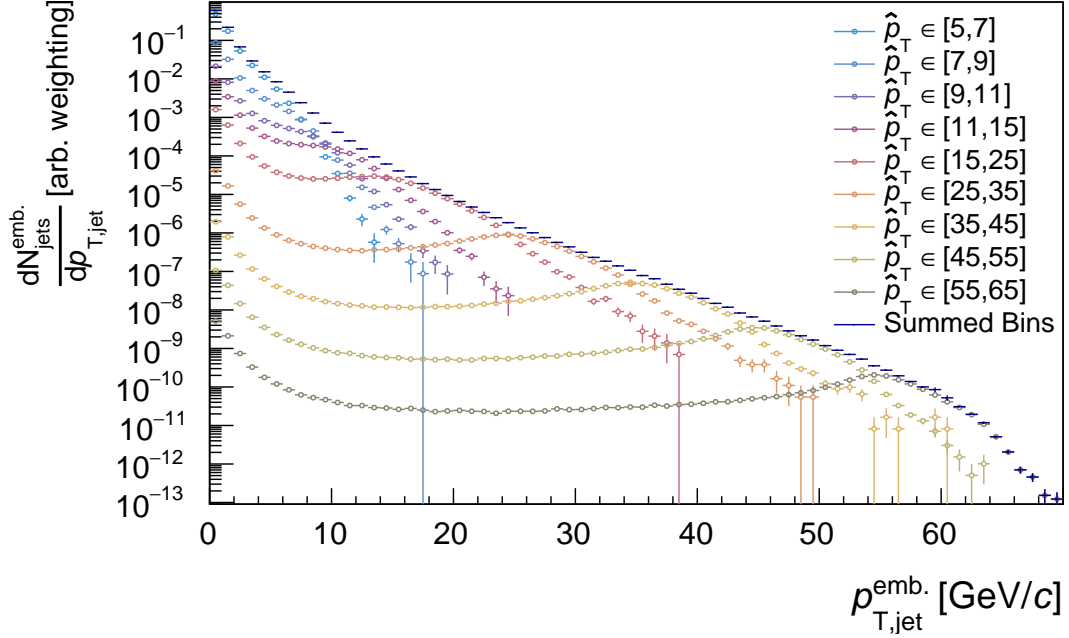
Figure 4.14: Spectra of the embedded anti-k_T $R = 0.4$ full jets from `PYTHIA6` events in $\hat{p}_T$ bins given in Table 4.4. Jets from each ith embedding $\hat{p}_T$ bin are weighted by $1/\left(N_{\text{events}}^i \sigma^i\right)$, which brings it close to a minimum bias spectra. For the purposes of this thesis, only the relative weighting is required, such that the overall cross section is arbitrary.

- Tower matched-track correction. See Section 4.5.

- Jet cuts: in order to minimize jet-boundary effects, a fiducial cut is made that discards all jets within 0.4 units (the jet resolution parameter) of the edge of the TPC ($|\eta_{\text{jet}}| \leq$ 0.6).

For each embedded event, two lists of jets clustered are produced: Truth, and Measured. A simple algorithm is used to correlate the two lists:

1. Sort the both the truth-level and detector-level jet lists by p_T from high to low

2. Prepare output four histograms of jet p_T:[22]

   i. 1D histogram of truth spectra, filled with the Truth list

   ii. 1D histogram of the measured spectra, filled with the Measured list

   iii. 1D histogram of "missed" jets: the subset of truth jets that are not matched to

---

to correct the data to truth-level jets, then variations in the bad-tower list would primarily smear the JER, but not change the mean of the unfolded values (the JES).

22. In practice, these histograms were contained inside `RooUnfoldResponse*` objects from the `RooUnfold` software package. See more information below.

any measured jets

v. 2D response matrix of all matched jets

3. Loop through the truth-level jet list in order. For each truth-level jet, conduct an inner loop comparing it to each unmatched detector-level jet[23] in ϕ-η distance as $\Delta \equiv \sqrt{\left(\eta_{\mathrm{jet}}^{\mathrm{M}} - \eta_{\mathrm{jet}}^{\mathrm{T}}\right)^2 + \left(\phi_{\mathrm{jet}}^{\mathrm{M}} - \phi_{\mathrm{jet}}^{\mathrm{T}}\right)^2}$. The compared jet is a match if $\Delta < R$. For a match:

   i Terminate the inner loop

   ii Fill the response matrix with the matched truth-level and detector-level jets

   iii Mark the detector-level jet in the list as "matched" so that it will be skipped in all subsequent iterations of the inner loop.[24]

   If the truth-level jet does not match any detector-level jet, then fill the histogram for missed jets with the truth-level jet.[25]

The embedded jet spectra are plotted in Figure 4.14. The resulting pairing of matched jets is plotted in Figure 4.15. When using the response matrix's data, outlier bins outlier bins with low statistics were dropped. These outliers come from the tails of the embedded and/or matching distributions. The outliers that are especially problematic are from the low-$\hat{p}_{\mathrm{T}}$ bins, which are therefore weighted with a high cross section. These outliers can create strong off-diagonal elements in the response matrix which create difficulties in the unfolded procedure. If there were enough statistics to smoothly populate the tails of the low-$\hat{p}_{\mathrm{T}}$ bins out to, and including, these outliers, then they would no longer be outliers, and would not be a problem.

---

23. All jets start unmatched

24. This brute-force two loop algorithm is not optimized for efficiently geometrically matching a large number of items in a 2D map. It is, however, adequate for the small numbers of jets in these events. For applications which have many items to matched, there are highly optimized libraries available, such as the CGAL library [114], which is used by FastJet, but is "relevant mainly if you expect to have N > 15000" [115]; the p+Au events studied in this thesis rarely have more than 20 jet-like objects in either the truth- or detector-level lists to match.

25. Note that matching by the ordering, which is ranked by high p_{T} to low p_{T}, has the benefit of prioritizing high p_{T} jets to match first, while subsequent $\Delta(\phi, \eta) < R$ cut enforces the correlation in locality.
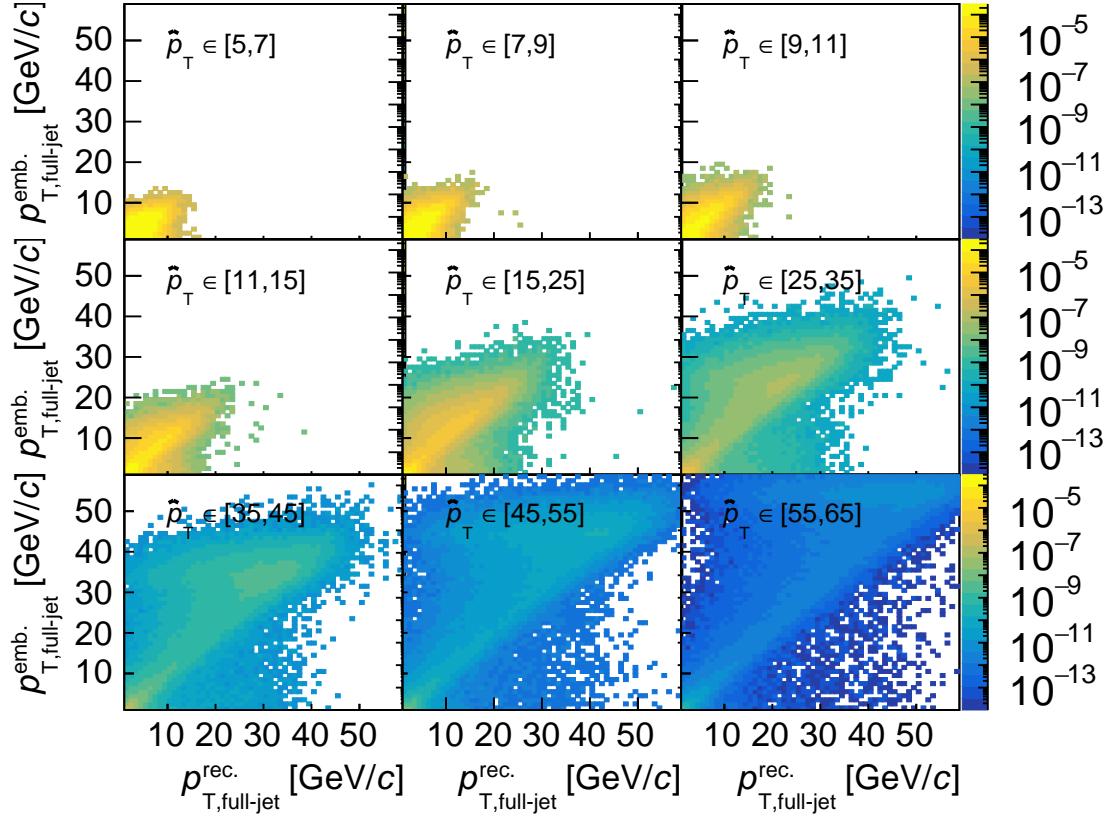
Figure 4.15: Truth to reconstructed `PYTHIA6` full jet matching histogram for each of the nine $\hat{p}_{\mathrm{T}}$ embedding bins listed in Table 4.4. The actual response histogram used for correcting data (in conjunction with the overall truth spectra from Figure 4.14, fakes, and missed spectra) is the sum of all nine histograms shown here.

4.7.1 Jet Energy Scale and Resolution

The jet matching process yields a distribution of measured-jet p_{T} ($p_{\mathrm{T}}^{\mathrm{M}}$) for each bin of true-jet p_{T} ($p_{\mathrm{T}}^{\mathrm{T}}$) which is roughly Gaussian combined with a long left-hand-side tail. This tail represents when jet's leading particle was not reconstruction and/or when a jet is mismatched with a softer background combinatorial "jet" from the embedded MB event. The jet matching efficiencies and resolutions can then be calculated analogously to those for tracks, as shown in Figure 4.13. The most common reported metric is the JES (the difference in mean reconstructed jet value) and the JER (the spread on that resolution). These values were taken from Gaussian fits over the 35th-100th percentile the distribution of measured-level jets matching each truth-level jet bin, as shown in Figure 4.16 and listed in Table 4.5.
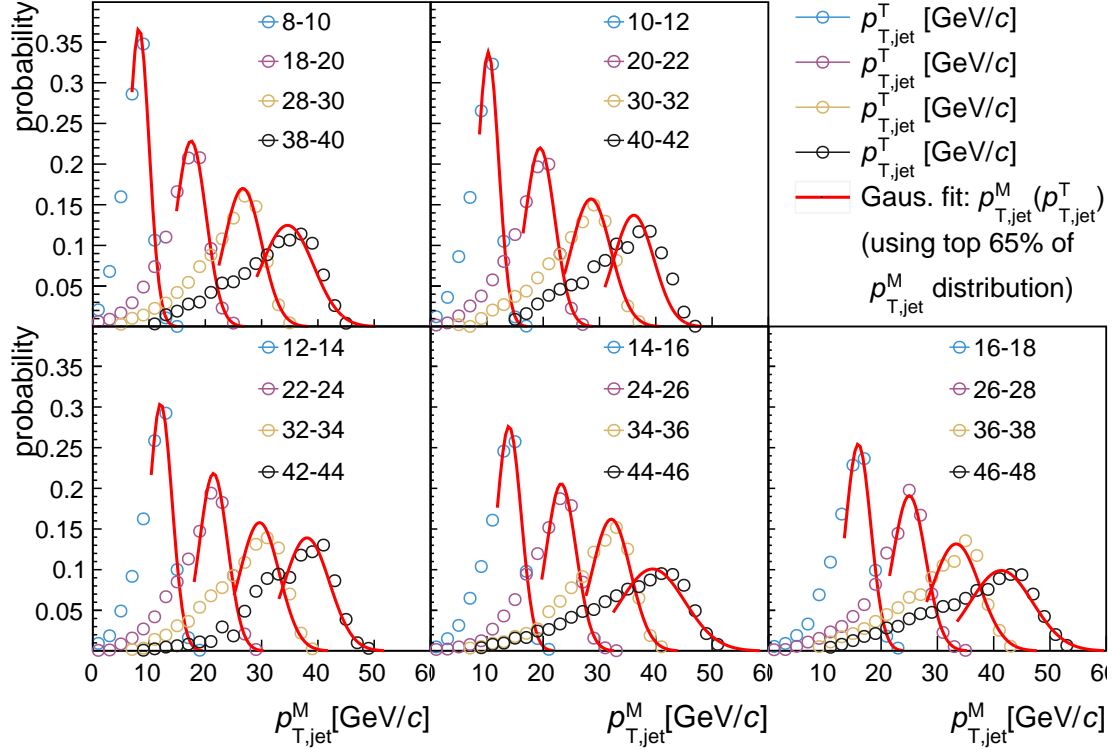
Figure 4.16: Jet Energy Scale and Jet Energy Resolution for `PYTHIA6` jets embedded into p+Au $\sqrt{s_{\mathrm{NN}}} = 200\,\mathrm{GeV}$ MB events. Truth-level jets are divided into $p_{\mathrm{T}}^{\mathrm{T}}$ bins $2\,\mathrm{GeV}/c$ wide. The resulting matched measurement-level jet $p_{\mathrm{T}}^{\mathrm{M}}$ spectra for each $p_{\mathrm{T}}^{\mathrm{T}}$ is plotted. The 35th-100th percentile of each $p_{\mathrm{T}}^{\mathrm{M}}$ spectrum is fit to a Gaussian; the offset of the Gaussian's mean to $p_{\mathrm{T}}^{\mathrm{T}}$ is the JES, and the σ is the JER.

4.7.2 Bayesian Unfolding

The response matrices for the track and jets are used in conjunction with the data for missed and fake track/jets in order to unfold the measured spectra via the Bayesian unfolding algorithm [116] implemented in the `RooUnfold` library [117, 118]. The number of iterations used in the unfolding procedure is one of the (very minor) uncertainties added into the systematic uncertainties of the final results.

Table 4.5: Jet Energy Spectra and Resolution

$p_{\mathrm{T,full}}^{\mathrm{True}}$ [GeV/c]	JES [GeV/c]	JER [GeV/c]
[8, 10]	-0.77 ± 0.02	1.80 ± 0.01
[10, 12]	-0.76 ± 0.03	1.85 ± 0.02
[12, 14]	-0.93 ± 0.04	2.03 ± 0.02
[14, 16]	-1.08 ± 0.05	2.18 ± 0.03
[16, 18]	-1.06 ± 0.06	2.24 ± 0.03
[18, 20]	-1.53 ± 0.04	2.65 ± 0.03
[20, 22]	-1.57 ± 0.04	2.64 ± 0.03
[22, 24]	-1.54 ± 0.05	2.50 ± 0.02
[24, 26]	-1.81 ± 0.06	2.64 ± 0.03
[26, 28]	-1.99 ± 0.07	2.91 ± 0.04
[28, 30]	-2.34 ± 0.05	3.33 ± 0.04
[30, 32]	-2.52 ± 0.07	3.53 ± 0.05
[32, 34]	-3.36 ± 0.08	3.51 ± 0.04
[34, 36]	-2.90 ± 0.10	3.41 ± 0.06
[36, 38]	-3.66 ± 0.10	4.21 ± 0.07
[38, 40]	-4.38 ± 0.11	4.60 ± 0.08
[40, 42]	-4.90 ± 0.13	3.57 ± 0.05
[42, 44]	-4.94 ± 0.15	4.01 ± 0.08
[44, 46]	-5.56 ± 0.10	5.70 ± 0.08
[46, 48]	-5.64 ± 0.12	5.55 ± 0.09

JES and JER calculated from the mean (μ) and standard deviation (σ) values of Gaussians shown in Figure 4.16. JES = $\mu - p_{\mathrm{T,full}}^{\mathrm{True}}$. JER = σ.

Chapter 5

Event Activity and Correlations with Measurements

5.1 Event Activity, From Heavy Ion and Small System Collisions

As introduced in Section 1.5.4, EA in A+A collisions scales primarily with N_{part}. Hard scatterings are rare, and the relative degree their constituents perturb EA binning due to the activity of the jets themselves is minor. This makes the Glauber model powerful and useful in which EA is monotonically, and positively, related to the impact parameter b. This is also the origin of the convention in which centrality/EA percentiles are ranked from the 0th percentile as the most central, and 100th percentile the most peripheral. This same convention has been kept in the literature for EA in s+A[1] collisions, and is used in this thesis: In this thesis, 0-30% is the "high" EA bin and 70-100% the "low" EA bin.

The conditions in A+A collisions, in which EA is an independent measure of centrality, simply are not true of s+A collisions. This is illustrated nicely in a p+Pb study in Figure 5.1, where the strong correlation from experimentally measured EA (the multiplicity on the

---

1. In which s is $p/d/\mathrm{He}^3$

y-axis of the bottom plots) maps cleanly in the right-hand column to N_{part} and b for Pb+Pb, but not so in the left-hand column for p+Pb. The degree to which the mapping is clean is also indicated visually in an Au+Au study in Figure 5.2, where selecting on the highest/lowest 30% EA events on the left, result in bins clearly separated in b with no significant overlap on the right.

Contrast the A+A situation with Figure 5.3 which shows a similar mapping in the p+Au events presented in this thesis. In the figure, the EA is measured as the sum of signals in the inner Au-going BBC tiles (see following section (5.2) and Figure 3.4 for details), and is compared to multiplicity of tracks in the TPC (N_{ch}). The left-hand plot shows the N_{ch} distributions of events binned by $\mathrm{EA}_{\mathrm{BBC}}$ in the high/lowest 30th percentiles (along with the middle 40%), and on the right-hand plot shows the $\mathrm{EA}_{\mathrm{BBC}}$ distributions binned by N_{ch} percentiles. In both plots, solid lines show distribution median values, and dotted lines are at one standard deviation above the means. Notably, there is clear monotonic increase of the mean of each distribution; however, all means are also within a single standard deviation of each other.

So, then, what *is* EA in s+A collisions? As a most general statement, it is a scale of the "violence" of a collision, of the entropy generated. In a semi-inclusive analysis, as in this thesis, it is measured in a separate ϕ-η region than the observables in order to avoid trivial autocorrelations; it is then used as a benchmark to ask if the observables (in the case of this thesis, jet production) are evolving and/or are correlated with EA. The answer of this thesis's investigation, as well as many other concurrent and recent studies[2] is a resounding "yes – there are clear EA correlations for hard scatterings". These correlations in s+A collisions make interpreting the hard scattered data and comparing them to pp collisions much more difficult then in A+A collisions, but are themselves probes that may be used to refine our understanding of the initial stages of heavy-ion collisions.

---

2. Including the ATLAS measurement [34] presented previously, and a high-multiplicity pp study looking at jet acoplanarity [119].
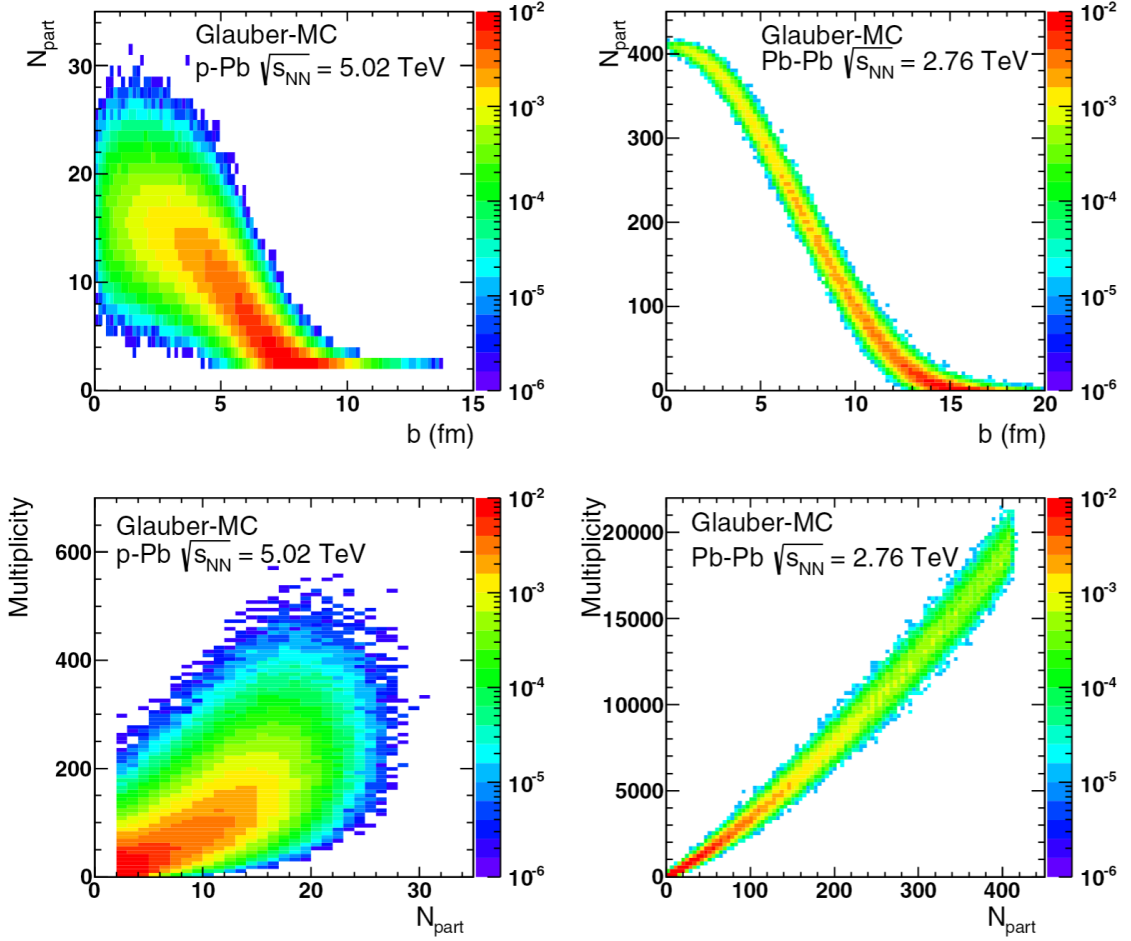
Figure 5.1: Glauber study of impact parameter, multiplicity, and N_{part} correlations in p+Pb and Pb+Pb collisions [120]. Note the relative linearity and separation of b for the high and low percentiles of N_{part}, and a similar separation for N_{part} for bins of multiplicity in the Pb+Pb collisions.
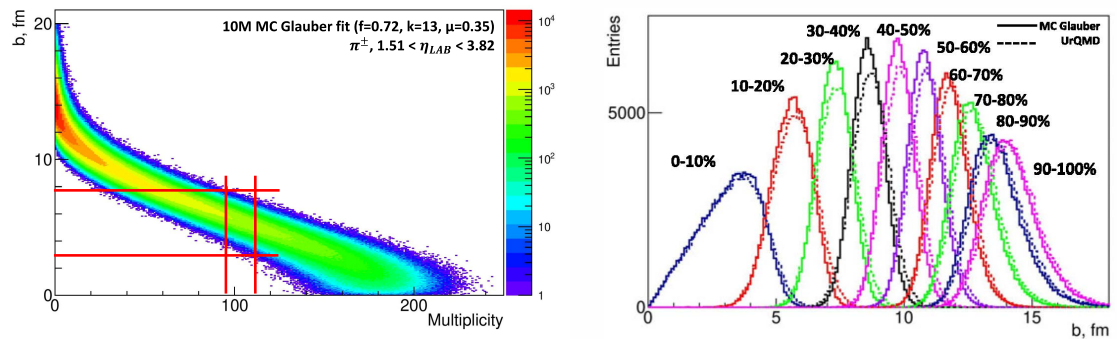
Figure 5.2: Left: Glauber modelled relationship of $\pi^{\pm}$ multiplicity at $\eta \in (1.51, 3.82)$ in Au+Au collisions. Right: distribution (and overlap) of centrality bins as selected by multiplicity. Plots from [121].
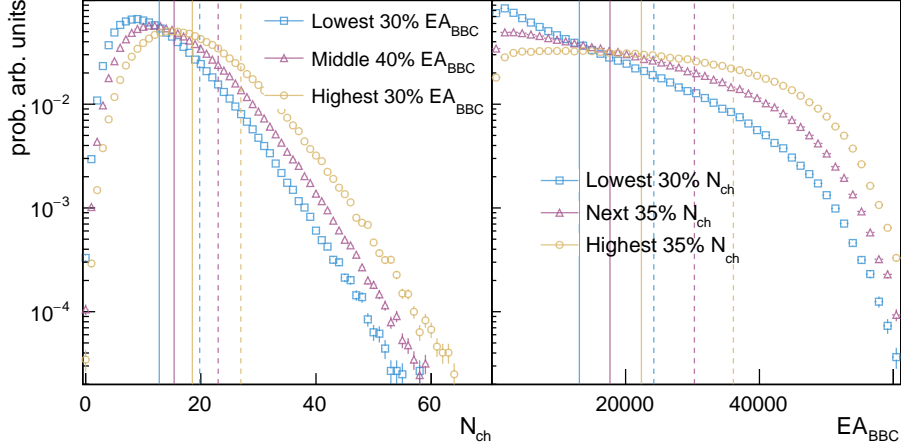
Figure 5.3: Relationship between $\mathrm{EA_{BBC}}$ and measured track multiplicity (N_ch) the TPC as measured in MB $\sqrt{s_\mathrm{NN}} = 200\,\mathrm{GeV}$ p+Au collisions at STAR. Left: Distribution of N_ch in bins of $\mathrm{EA_{BBC}}$. Right: Distribution of $\mathrm{EA_{BBC}}$ in bins of N_ch. Solid and dotted lines represent the mean and the mean+1σ of the correspondingly colored distributions. (Note: the bin boundary in N_ch is of necessity an integer; therefore, it was not possible to bin events by N_ch into exactly a middle 40% and highest 30% bin in the figure on the right.)

5.2   Event Activity Measurements

EA in this thesis is defined by two definitions, as illustrated in Figure 5.4. They are:

1. $\mathrm{EA_{BBC}}$: Sum of signal from the BBC east[3] inner tiles. These have full azimuthal coverage at $\eta \in [-5, -3.4]$.

2. $\mathrm{EA_{TPC}}$: The density of track p_T in the TPC in ϕ-η space. For MB triggered events, the full acceptance of the TPC is used. In HT events, only the acceptance of the TPC within $\pm\pi/8$ of being perpendicular in azimuth to the triggering tower is used. The triggering tower is defined as the tower with the greatest E_T.[4] This cut on ϕ is required so that the EA definition is not trivially autocorrelated with the tracks associated with jet production. Therefore:

$$\mathrm{EA_{TPC}}\big|_{\text{MB events}} \equiv \frac{\int p_\mathrm{T} \mathrm{d}\eta \mathrm{d}\phi}{\int \mathrm{d}\eta \mathrm{d}\phi} = \left.\frac{\Sigma p_\mathrm{T}|_\mathrm{TPC}}{4\pi}\right|_{\text{MB events}} \tag{5.1}$$

$$\mathrm{EA_{TPC}}\big|_{\text{HT events}} \equiv \frac{\int p_\mathrm{T} \mathrm{d}\eta \mathrm{d}\phi_\perp}{\int \mathrm{d}\eta \mathrm{d}\phi_\perp} = \left.\frac{\Sigma p_\mathrm{T}|_{\Delta\phi_\perp}}{\pi}\right|_{\text{HT events}} \tag{5.2}$$

---

3. East is the Au-beam going direction

4. Because towers on the bad tower list are excluded, this does not always match the tower that triggered the event in the STAR Trigger System.

where $\Delta\phi_\perp \equiv |\phi_{\text{track}} - \phi_{\text{trig}}|$ when $|\phi_{\text{track}} - \phi_{\text{trig}}| \in [3/8, 5/8]$.

There are, of course, also jets in MB triggered events. However, the steeply falling jet spectrum means that the effect of these jets on the shape of the MB EA spectra is negligible.[5]
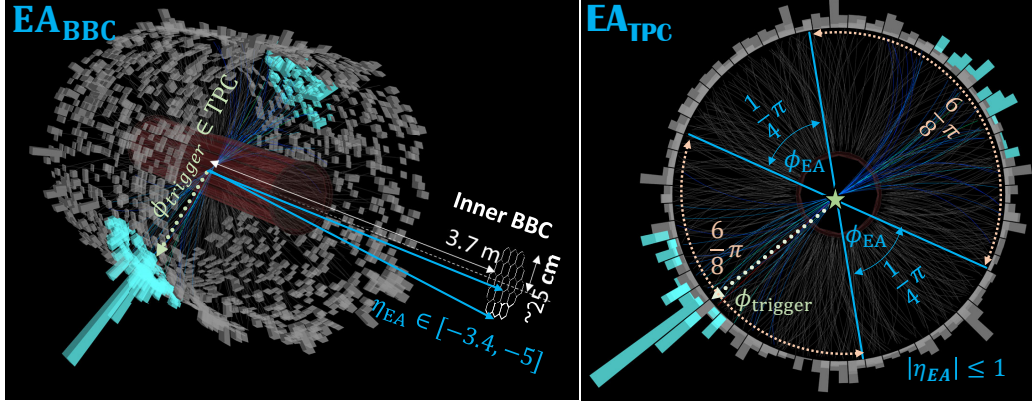
Figure 5.4: Cartoon of definition of EA_{BBC} (left) and EA_{TPC} (right). As shown, EA_{TPC} is for triggered events; in MB events, the full azimuthal acceptance of the TPC and BEMC are used.

5.3 Event Activity and Jet Autocorrelation

To be useful in sorting jet events, EA must be free of trivial autocorrelations with jets in events with a hard scattering. To first order, jets are produced back-to-back in ϕ with equal and opposite p_T,[6] the pair of which are referred to as "dijets", in which the one with the greater measured p_T is the "leading" jet and the recoil partner the "sub-leading" jet. Because trijets are rare at $\sqrt{s_{\text{NN}}} = 200\,\text{GeV}$ kinematics, the azimuthally transverse EA of EA_{TPC} is not anticipated to be influenced from leading dijet constituents. This can also be seen in the dijet $|\Delta\phi| = \eta_{\text{lead}} - \eta_{\text{sub}}$ measurement described later and shown in Figure 6.8.

While essentially directly recoiling in azimuth from the conserved p_T, the p_z (momentum in the beam-line direction) of dijet pairs is determined by the variable energies of the initiating partons. This results in an "η swing" ($\Delta\eta = \eta_{\text{leading}} - \eta_{\text{sub-leading}}$) distribution which

5. Refer to Figure 5.7, in which E_T^{trig} is a good proxy for jets.

6. This ignores the intrinsic p_T distribution of the partons in the colliding nuclei pre-collisions, whose contributions are, in any case, relatively small.

depends on beam energy. If the η swing were large enough that a pair of jets could have one partner in the TPC and the other hit the BBC then there *would be* an autocorrelation between jets and $\mathrm{EA_{BBC}}$. This would occur as follows:

1. Tower trigger $E_\mathrm{T}^\mathrm{trig}$ requires jet at mid-η; otherwise the event is not counted.

2. Each time a recoil jet misses the TPC acceptance due to a high η-swing, it is not counted, and the jet spectra is decreased

3. If recoil jets could hit the inner ring of the BBC, then $\mathrm{EA_{BBC}}$ would increase in correlation with a decrease in the jet spectra due to those same jets not being counted in the TPC.

As seen in Figure 5.5, in a `PYTHIA` pp simulation at $\sqrt{s_\mathrm{NN}} = 200\,\mathrm{GeV}$, when there is a $8\,\mathrm{GeV}$ neutral particle in the BEMC at RHIC kinematics, then dijet partners are rarely found in the outer BBC acceptance and (within the precision of the 1.5 million triggered events of the study) never within the inner BBC acceptance.
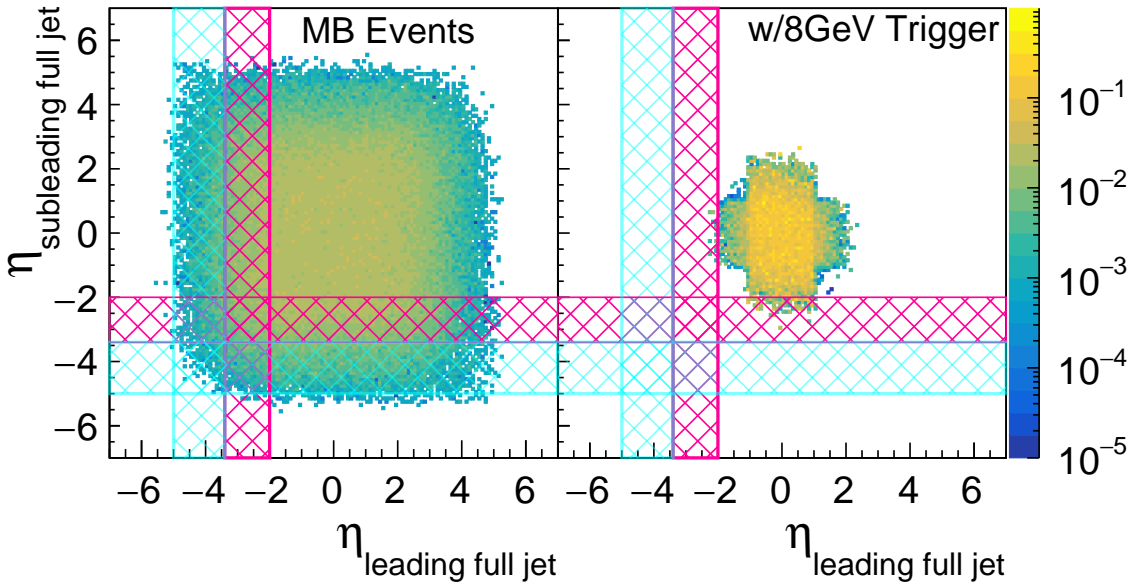
Figure 5.5: Probability distribution of η of leading and subleading jet pairs in `PYTHIA8` $\sqrt{s_\mathrm{NN}} = 200\,\mathrm{GeV}$ pp collisions using $R = 0.7$ anti-k_T full jets. Acceptance of the inner and outer BBC (in the Au-going direction) indicated in cyan and magenta, respectively. Left: 10.8×10^6 Min Bias events; 30% (10%) events have at least one jet-like object (in MB these objects are mostly low-p_T) in the outer (inner) BBC. Right: 1.47×10^6 Events triggered by a neutral particle at $|\eta| \leq 0.6$ with $E_\mathrm{T} \geq 8\,\mathrm{GeV}$; 3.2% events have one jet in the outer BBC, and no events have a jet in the inner BBC.

5.4 Event Activity and Jet Energy Scale Correlation

Another kind of correlation could occur in measurement if EA and the JES and/or JER were both strongly correlated by a common third parameter, such as luminosity. To first order, a high luminosity could add background tracks and neutral particles in both the TPC and BBC acceptance, such that the EA would become artificially high and the jet p_{T} values would increase (the JES's negative value would become larger in magnitude). If not corrected for in the unfolding, then high-EA jet spectra would be artificially enhanced relative to lower jet spectra. However, there is relatively little background energy in these events. As shown in Figure 5.6, the JES and JER are modified only modestly between high and low $\mathrm{EA_{BBC}}$ events.
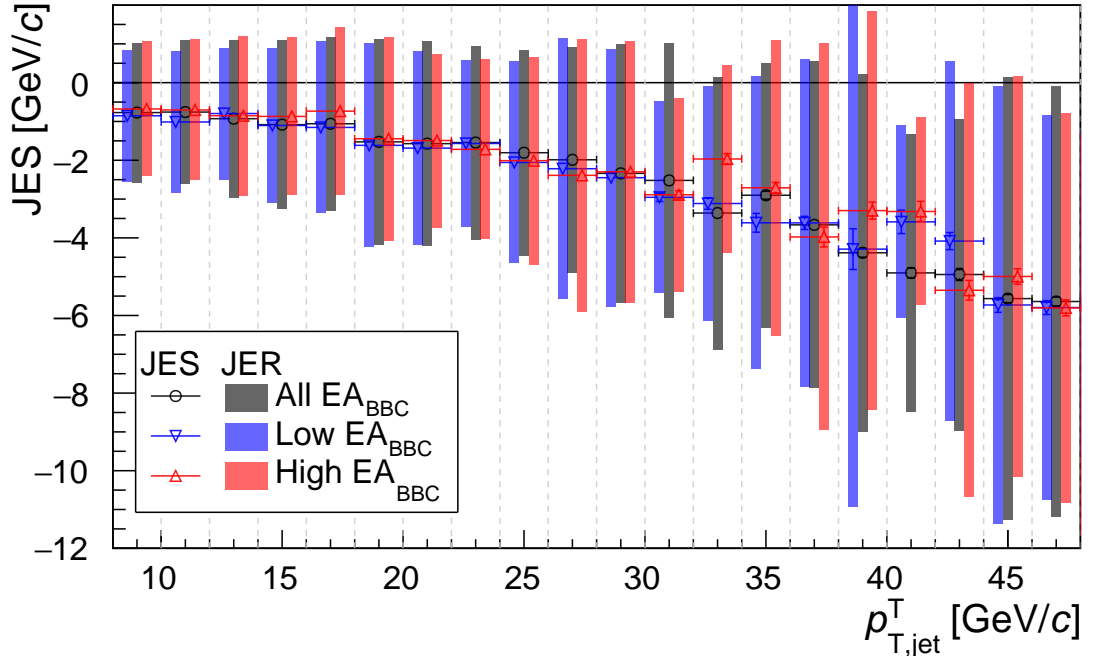
Figure 5.6: Plot of jet energy scale (JES) and resolution (JER) using all embedding events (in gray) only events with $\mathrm{EA_{BBC}}$ below 1σ of the mean of the $\mathrm{EA_{BBC}}$ distribution of embedded events (in blue), and above 1σ of the mean of the $\mathrm{EA_{BBC}}$ distribution (in red). The values of JES and JER for all data were determined as documented in Section 4.7.1, which also contains a plot, Figure 4.16, of the Gaussian fits used determine JES and JER and a table, Table 4.5. Corresponding plots for the high and low $\mathrm{EA_{BBC}}$ data are provided in the appendix and Figures A.21 and A.22, and Tables A.1 and A.2.

5.5 Measured Event Activity Distributions

The distribution of leading tower energies (E_T^{trig}), EA$_{BBC}$, and EA$_{TPC}$, in MB and HT events is shown in Figure 5.7. The autocorrelation between jet production and EA in the full TPC can be seen by comparing the MB curve for events with a 8 GeV hit in the BEMC with HT events with 4-8 GeV hits. The EA$_{TPC}$ for MB includes the full TPC acceptance, and the corresponding increase in EA$_{TPC}$ is apparent in the HT events (which exclude the azimuthal region of the dijets themselves). However, the steeply falling spectrum of the triggers also mean that there are less than 0.02% of the MB events with this autocorrelated energy. Therefore, the autocorrelation occurs only in a tail which is a very small percentile of the overall spectra. Therefore, the MB events can use the entire acceptance of the TPC as a "jet-less" baseline for the EA$_{TPC}$ distribution.[7]

The two EA definitions are positively, but not strongly, correlated, with correlation factors of 0.29 and 0.20 for MB and HT events respectively. The distributions and mean trends of each EA in bins of the other are shown in Figure 5.8. It is likely that there are at least two competing effects. First, it is expected that there is a mutual positive correlation between both EA definitions with the overall $\langle N_{part} \rangle$. Secondly, the relatively small signal in s+A collisions is inherently less smoothly distributed than in A+A collisions, which negatively correlates high energy densities in one fiducial volume with another.[8]

The black dotted lines added to figures Figure 5.7 show the locations of 30th and 70th percentiles of the EA$_{TPC}$ and EA$_{BBC}$ distributions in the MB events. These same EA$_{TPC}$ and EA$_{BBC}$ values are chosen as the upper and lower bounds for the low and high EA bins for the HT events. The percentages of events in each bin are shown on the plot and also given in Table 5.1 for convenience. As shown, adding the trigger requirement basically pushes 8%

---

7. This is convenient because there isn't a preferred direction in MB events to orient which way to look for transverse energy, because there isn't a hard trigger. Picking the highest energy particle in events with only soft particles would, on the other hand, strongly suppress EA$_{TPC}$ because it would always be biased away from some of the few soft particles present.

8. Basically the energy is distributed into fewer particles, and therefore is inherently less isotropic but more "lumpy": if its few particles particles are lumped into one volume, they cannot simultaneously be in another.
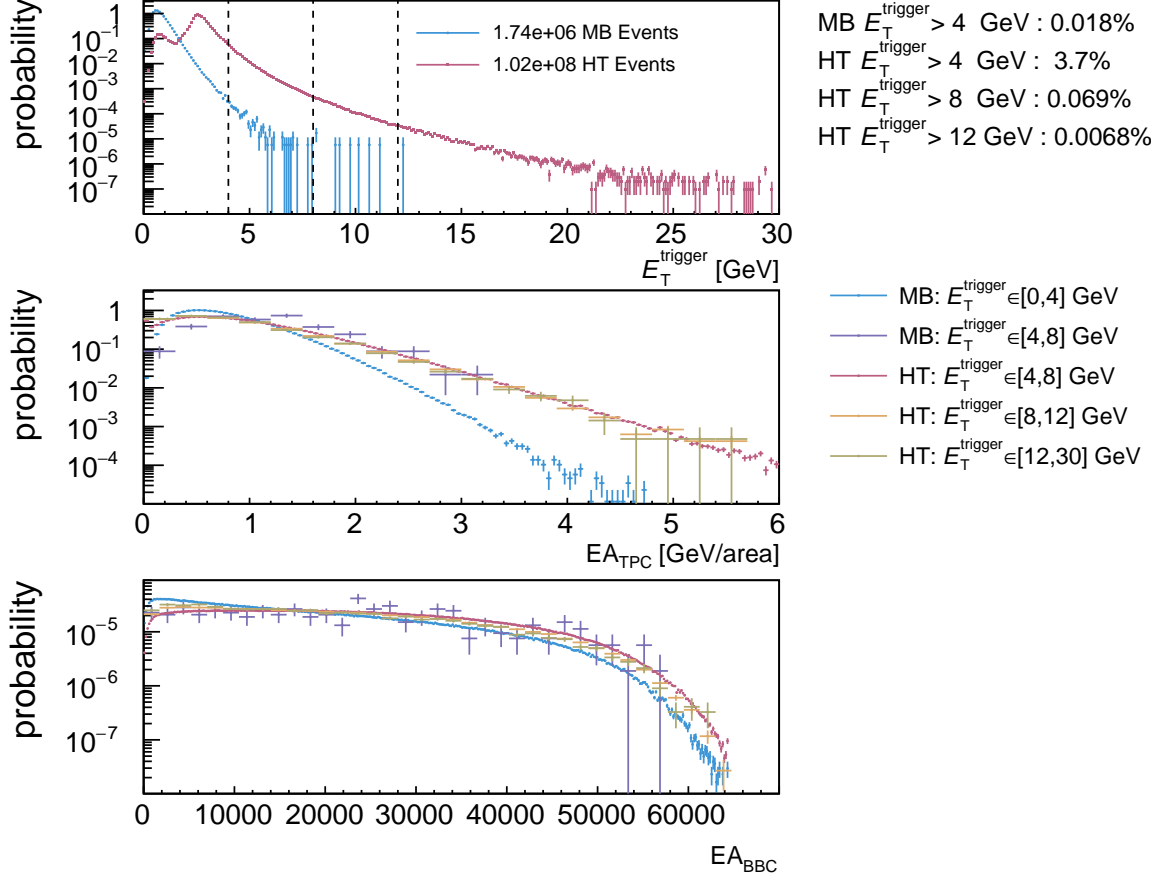
Figure 5.7: Probability distributions in MB and HT events. Top panel: $E_{\mathrm{T}}^{\mathrm{trig}}$ (which here refers to just the highest energy BEMC hit in the event). Middle and bottom panels: $\mathrm{EA_{BBC}}$ and $\mathrm{EA_{TPC}}$ distributions for MB and HT plotted in bins of $E_{\mathrm{T}}^{\mathrm{trig}}$.

more events into the high-EA bin; while shrinking the middle/low bin in $\mathrm{EA_{TPC}/EA_{BBC}}$. Nevertheless, the total number of events in the diagonal bins actually shrinks moderately from 43% to 39.5% instead of growing (as naively one would expect by simply pushing more events into the mutually highest activity bin). This is perhaps an indication of the negative correlation of limited energy being found in one or the other acceptance, but not both, and is an interesting avenue for further study.

5.6   EA Correlation to Energy of $E_{\mathrm{T}}^{\mathrm{trig}}$

In the following chapter, results of the jet spectra normalized per trigger (S) will be presented in the bins of high and low EA shown in Figure 5.8 and Table 5.1. The correlation of the hardness of the trigger ($E_{\mathrm{T}}^{\mathrm{trig}}$) to EA is an essential detail for that normalization. For
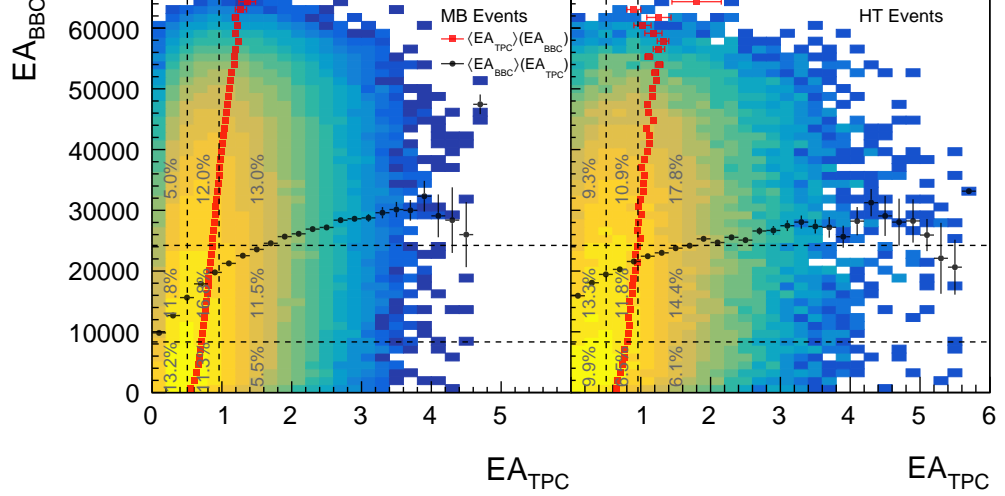
Figure 5.8: Relationship between EA_{TPC} and EA_{BBC} in MB events (left panel) and HT events with at least an $8\,GeV$ tower (right panel). Plotted circles(squares) are mean values of EA_{BBC} and EA_{TPC} when binned by the other EA definition. Error bars are uncertainties on the mean. Dotted lines are draw at the 30th and 70th percentiles of the MB distribution; these values are used for both MB and HT events as the binning for high & low EA_{BBC} and EA_{TPC}. Numbers in each of the nine regions represent the percentage of events contained in the region. These values are also given in Table 5.1.

example, the EA dependence of S will be presented as:

$$S \equiv \frac{1}{N_{\text{trig}}} \frac{\mathrm{d}N_{\text{jet}}}{\mathrm{d}p_{\text{T}}} \tag{5.3}$$

$$\Rightarrow \frac{S_{\text{EA}}^{\text{high}}}{S_{\text{EA}}^{\text{low}}} = \frac{S_{\text{EA}(0-30\%)}}{S_{\text{EA}(70-100\%)}} = \frac{N_{\text{trig}}|_{\text{EA}(70-100\%)}}{N_{\text{trig}}|_{\text{EA}(0-30\%)}} \frac{\mathrm{d}}{\mathrm{d}p_{\text{T}}} \frac{N_{\text{jet}}|_{\text{EA}(0-30\%)}}{N_{\text{jet}}|_{\text{EA}(70-100\%)}} \tag{5.4}$$

For the sake of illustration, assume that high-p_{T} jets only come from $E_{\text{T}}^{\text{trig}}$ above a given threshold value, $E_{\text{T}}^{\text{threshold}}$, but that the events collected are triggered from $E_{\text{T}}^{\text{trig}} > E_{\text{T}}^{\text{min}}$ where $E_{\text{T}}^{\text{threshold}} > E_{\text{T}}^{\text{min}}$. Since the trigger spectra are steeply falling (see top panel of Figure 5.7), then the normalization ratio:

$$\frac{N_{\text{trig}}|_{\text{EA}(70-100\%)}}{N_{\text{trig}}|_{\text{EA}(0-30\%)}}\Bigg|_{E_{\text{T}}^{\text{trig}} > E_{\text{T}}^{\text{min}}} \tag{5.5}$$

$$= \frac{N_{\text{trig}}|_{\text{EA}(70-100\%)}\big|_{E_{\text{T}}^{\text{trig}} \in [E_{\text{T}}^{\text{min}}, E_{\text{T}}^{\text{threshold}}]} + N_{\text{trig}}|_{\text{EA}(70-100\%)}\big|_{E_{\text{T}}^{\text{trig}} > E_{\text{T}}^{\text{threshold}}}}{N_{\text{trig}}|_{\text{EA}(0-30\%)}\big|_{E_{\text{T}}^{\text{trig}} \in [E_{\text{T}}^{\text{min}}, E_{\text{T}}^{\text{threshold}}]} + N_{\text{trig}}|_{\text{EA}(0-30\%)}\big|_{E_{\text{T}}^{\text{trig}} > E_{\text{T}}^{\text{threshold}}}} \tag{5.6}$$

$$\approx \frac{N_{\text{trig}}|_{\text{EA}(70-100\%)}}{N_{\text{trig}}|_{\text{EA}(0-30\%)}}\Bigg|_{E_{\text{T}}^{\text{trig}} \in [E_{\text{T}}^{\text{min}}, E_{\text{T}}^{\text{threshold}}]} \tag{5.7}$$

Table 5.1: Percentages of MB and HT Events per EA$_{\text{TPC}}$ and EA$_{\text{TPC}}$ Bin

	EA$_{\text{TPC}}$	70-100% Low	30-70% Medium	0-30% High	0-100% All
EA$_{\text{BBC}}$					
	MB	13.2	11.3	5.5	30.0
70-100%	HT	9.9	6.5	6.1	22.5
Low	Δ	-3.3	-4.8	0.6	-7.5
	MB	11.8	16.8	11.5	40.0
30-40%	HT	13.3	11.8	14.4	39.5
Medium	Δ	1.5	-4.9	2.9	-0.5
	MB	5.0	12.0	13.0	30.0
0-30%	HT	9.3	10.9	17.8	37.9
High	Δ	4.3	-1.1	4.7	7.9
0-100%	MB	30.0	40.0	30.0	100.0
All	HT	32.5	29.2	38.3	100.0
	Δ	2.5	-10.8	8.3	0.0

All values are percentages. MB and HT values are the percentages of events that call in each EA$_{\text{TPC}}$-EA$_{\text{BBC}}$ region, and are also also printed on the plots in Figure 5.8. EA percentiles run from lowest at 100% to highest at 0%.

At the same time, by assumption, the high-p_{T} jet spectra appears only in events at $E_{\text{T}}^{\text{trig}} > E_{\text{T}}^{\text{threshold}}$:

$$\frac{\mathrm{d}}{\mathrm{d}p_{\text{T}}} \frac{\left. N_{\text{jet}}^{\text{high}-p_{\text{T}}}\right|_{\text{EA}(0-30\%)}}{\left. N_{\text{jet}}^{\text{high}-p_{\text{T}}}\right|_{\text{EA}(70-100\%)}}\Bigg|_{E_{\text{T}}^{\text{trig}} > E_{\text{T}}^{\text{min}}} = \tag{5.8}$$

$$\frac{\mathrm{d}}{\mathrm{d}p_{\text{T}}} \frac{\left. N_{\text{jet}}^{\text{high}-p_{\text{T}}}\right|_{\text{EA}(70-100\%)}\Big|_{E_{\text{T}}^{\text{trig}} \in [E_{\text{T}}^{\text{min}}, E_{\text{T}}^{\text{threshold}}]}^{\,0} + \left. N_{\text{jet}}^{\text{high}-p_{\text{T}}}\right|_{\text{EA}(70-100\%)}\Big|_{E_{\text{T}}^{\text{trig}} > E_{\text{T}}^{\text{threshold}}}}{\left. N_{\text{jet}}^{\text{high}-p_{\text{T}}}\right|_{\text{EA}(0-30\%)}\Big|_{E_{\text{T}}^{\text{trig}} \in [E_{\text{T}}^{\text{min}}, E_{\text{T}}^{\text{threshold}}]}^{\,0} + \left. N_{\text{jet}}^{\text{high}-p_{\text{T}}}\right|_{\text{EA}(0-30\%)}\Big|_{E_{\text{T}}^{\text{trig}} > E_{\text{T}}^{\text{threshold}}}} \tag{5.9}$$

$$= \frac{\mathrm{d}}{\mathrm{d}p_{\text{T}}} \frac{\left. N_{\text{jet}}^{\text{high}-p_{\text{T}}}\right|_{\text{EA}(0-30\%)}}{\left. N_{\text{jet}}^{\text{high}-p_{\text{T}}}\right|_{\text{EA}(70-100\%)}}\Bigg|_{E_{\text{T}}^{\text{trig}} > E_{\text{T}}^{\text{threshold}}} \tag{5.10}$$

Therefore, the high-p_{T} jets are collected with a relatively small number of high-E_{T} triggers, but are normalized by the much more numerous lower-E_{T} triggers:

$$\frac{S^{\text{high}-p_{\text{T}}}_{\text{EA}(0-30\%)}}{S^{\text{high}-p_{\text{T}}}_{\text{EA}(70-100\%)}} \approx \frac{N_{\text{trig}}\big|_{\text{EA}(70-100\%)}}{N_{\text{trig}}\big|_{\text{EA}(0-30\%)}}\Bigg|_{E_{\text{T}}^{\text{trig}}\in[E_{\text{T}}^{\text{min}},E_{\text{T}}^{\text{threshold}}]} \frac{\text{d}}{\text{d}p_{\text{T}}} \frac{N_{\text{jet}}^{\text{high}-p_{\text{T}}}\big|_{\text{EA}(0-30\%)}}{N_{\text{jet}}^{\text{high}-p_{\text{T}}}\big|_{\text{EA}(70-100\%)}}\Bigg|_{E_{\text{T}}^{\text{trig}}>E_{\text{T}}^{\text{threshold}}}$$

$$(5.11)$$

In the idealized case of Eq. 5.11, if the ratio of triggers between low and high EA changes between the $E_{\text{T}}^{\text{trig}}$ range of $[E_{\text{T}}^{\text{min}}, E_{\text{T}}^{\text{threshold}}]$ and $> E_{\text{T}}^{\text{threshold}}$, then the per-trigger normalization of the jets will be affected by that same ratio. This is true even if the actual per-trigger production of jets at each p_{T} is not EA-dependent. Therefore, it is essential to look at the dependence of EA on various trigger bins. These are shown for EA_{BBC} in Figure 5.9 and EA_{TPC} in Figure 5.10.
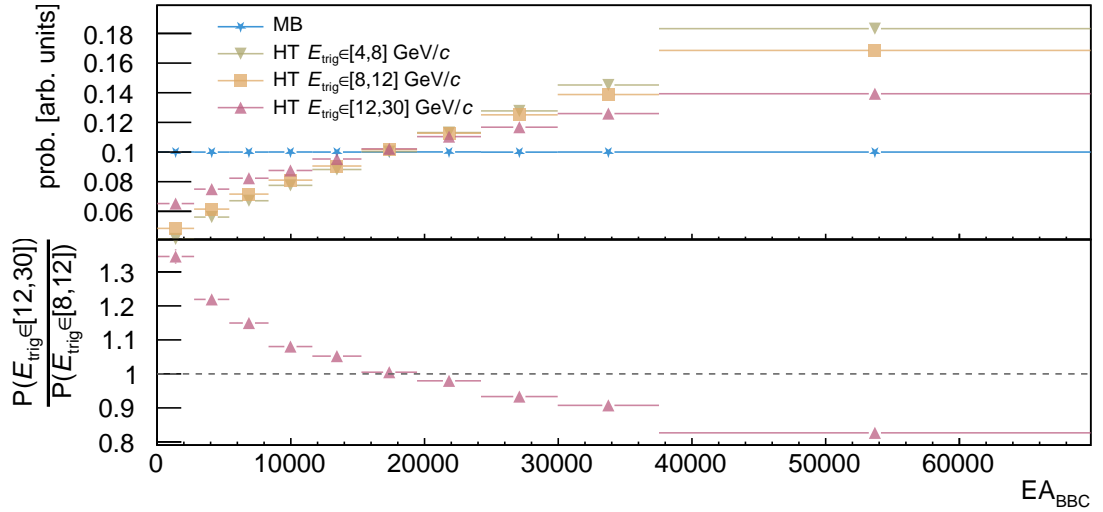
Figure 5.9: Top: Distribution of HT triggered events based on $E_{\text{T}}^{\text{trig}}$ into deciles of MB EA_{BBC} (in which bins edges are selected to contain 10% of MB events in each bin). Bottom: Ratio of probabilities of events with $E_{\text{T}}^{\text{trig}} \in [12, 30]\,\text{GeV}/c$ events with $E_{\text{T}}^{\text{trig}} \in [8, 12]\,\text{GeV}/c$.

In the EA_{BBC} data, there is a positive correlation between selecting events with harder triggers and higher EA. This is as one would expect from a Glauber model in which hard scatterings scale with $\langle N_{\text{coll}} \rangle$ that increases monotonically with $\langle N_{\text{part}} \rangle$. The fact that the slope itself is changing with different $E_{\text{T}}^{\text{trig}}$ ranges means that Eq. 5.11 predicts that the semi-inclusive spectra ratio in high-to-low EA_{BBC} will be suppressed due to the bias in the semi-inclusive normalization of the high-p_{T} jets.[9] (The statistics are too limited in higher

---

9. Of course, only to the degree that the assumptions of Eq. 5.11 apply

Table 5.2: Trigger Probabilities and Ratios in EA_{BBC} Bins

$E_{\text{T}}^{\text{trig}}$ Range [GeV/c]	$P\left(\text{EA}_{\text{TPC}}|_{70-100\%}\right)$	$P\left(\text{EA}_{\text{TPC}}|_{0-30\%}\right)$	$\frac{P\left(\text{EA}_{\text{TPC}}|_{70-100\%}\right)}{P\left(\text{EA}_{\text{TPC}}|_{0-30\%}\right)}$
$[8, 12]$	0.18	0.43	0.42
$[12, 30]$	0.22	0.38	0.58
ratio $[8, 12]$:$[12, 30]$	0.81	1.13	0.72

Table 5.3: Trigger Probabilities and Ratios in EA_{TPC} Bins

$E_{\text{T}}^{\text{trig}}$ Range [GeV/c]	$P\left(\text{EA}_{\text{TPC}}|_{70-100\%}\right)$	$P\left(\text{EA}_{\text{TPC}}|_{0-30\%}\right)$	$\frac{P\left(\text{EA}_{\text{TPC}}|_{70-100\%}\right)}{P\left(\text{EA}_{\text{TPC}}|_{0-30\%}\right)}$
$[8, 12]$	0.28	0.42	0.67
$[12, 30]$	0.32	0.38	0.84
ratio $[8, 12]$:$[12, 30]$	0.87	1.11	0.79

$E_{\text{T}}^{\text{trig}}$ to see if there is an actual turnover to a negative correlation at some point.) In order to quantify the effect, let $E_{\text{T}}^{\text{min}} = 8\,\text{GeV}$ and $E_{\text{T}}^{\text{threshold}} = 12\,\text{GeV}$. The ratio of triggers are just the ratio of probabilities of the first and last three bins. The numbers are given in Table 5.2.

Therefore, any jets which appear *only* in events with a $E_{\text{T}}^{\text{trig}} > 12\,\text{GeV}$, will experience a per-trigger normalization suppression (in ratio of high-to-low EA) by a factor of 0.72. Of course, the triggers are predominately single particles, and a step-function cutoff is not expected for any p_{T} range of jets; however, the effect is expected to increase for jets with increasing p_{T} values. For example, a PYTHIA8 study for $p_{\text{T}} > 30\,\text{GeV}/c$ jets found the ratio to be 0.84 (see Section 5.7).

Figure 5.10 and Table 5.3 give the analogous information for EA_{TPC} as was given for EA_{BBC} in Figure 5.9 and Table 5.2. The overall trigger normalization suppression is predicted to be somewhat less than when using EA_{BBC}.

The EA_{TPC} decile correlation to $E_{\text{T}}^{\text{trig}}$ is also different from the EA_{BBC} correlation in that the probabilities for all $E_{\text{T}}^{\text{trig}}$ are nearly constant for about the 30th to 60th decile, and then increase at both ends of the distribution. Two competing effects that can create this horseshoe shape are, first, at very low EA, a selection bias will anti-correlate jets, which
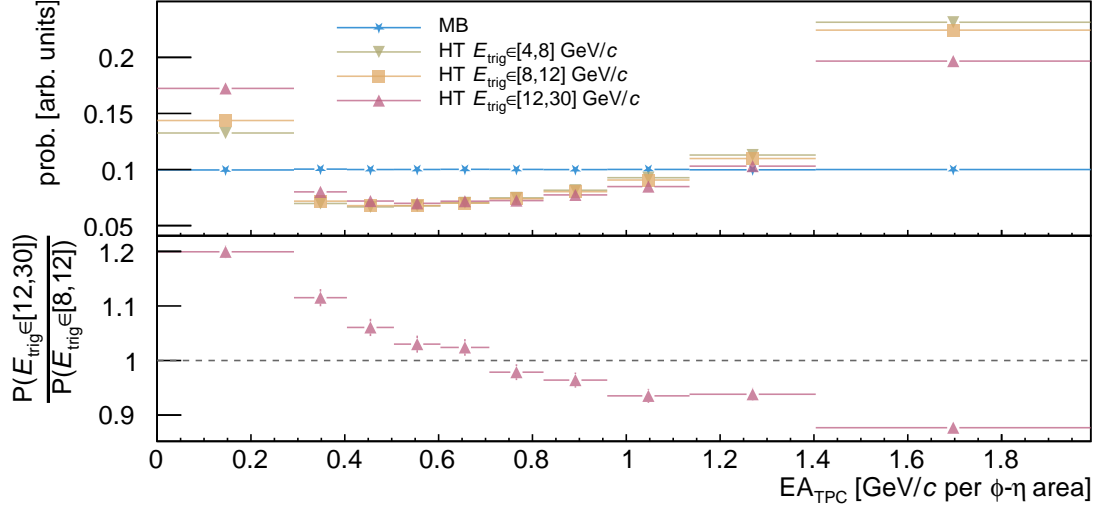
Figure 5.10: Distribution of HT triggered events based on E_T^{trig} into deciles of MB EA_{TPC} (in which bin edges are selected to contain 10% of MB events in each bin). Note that the upper boundary of the final bin has been truncated to 2 for convenience of presentation. Bottom: Ratio of probabilities of events with $E_T^{\text{trig}} \in [12, 30]\,\text{GeV}$ to events with $E_T^{\text{trig}} \in [8, 12]\,\text{GeV}$.

catch the few particles, and those that don't (i.e. the distribution in EA for $p+$Au collisions is lumpy, and if the lump is with the jet then it's not elsewhere). This would increase the probabilities of binning HT events at low EA, and may contribute to the left-hand side of the horseshoe. The right-hand side of the horseshoe is most likely from the positive correlation between $\langle N_{\text{coll}} \rangle$ and $\langle N_{\text{part}} \rangle$. The probability of finding a jet scales with $\langle N_{\text{coll}} \rangle$, and the corresponding $\langle N_{\text{part}} \rangle$ pushes up EA.

The interplay between triggers, EA_{BBC}, and EA_{TPC}, is also shown in Figure 5.11. Like Figure 5.9, it uses MB EA_{BBC} decile boundaries to bin events. The average number of tracks (per unit $\phi - \eta$) is plotted, as well as those same track's summed p_T per unit $\phi - \eta$ (which is EA_{BBC}).[10]

Figure 5.10 also showed that, outside of the lowest EA_{TPC} valued events, there is a positive correlation between EA_{TPC} and probability of having a hard scattering, but that that correlation decreases for increasingly hard E_T^{trig} cuts. That result is seen in Figure 5.11, in which within fixed bins in EA_{BBC}, there is an anticorrelation between average EA_{TPC} and

10. Note that the mean value of EA_{BBC} per EA_{TPC} is also shown in Figure 5.8, and that the values are a bit larger there than they are in Figure 5.11. This is because Figure 5.8 is uncorrected data and, more importantly, uses all tracks down to $p_T = 200\,\text{MeV}$.
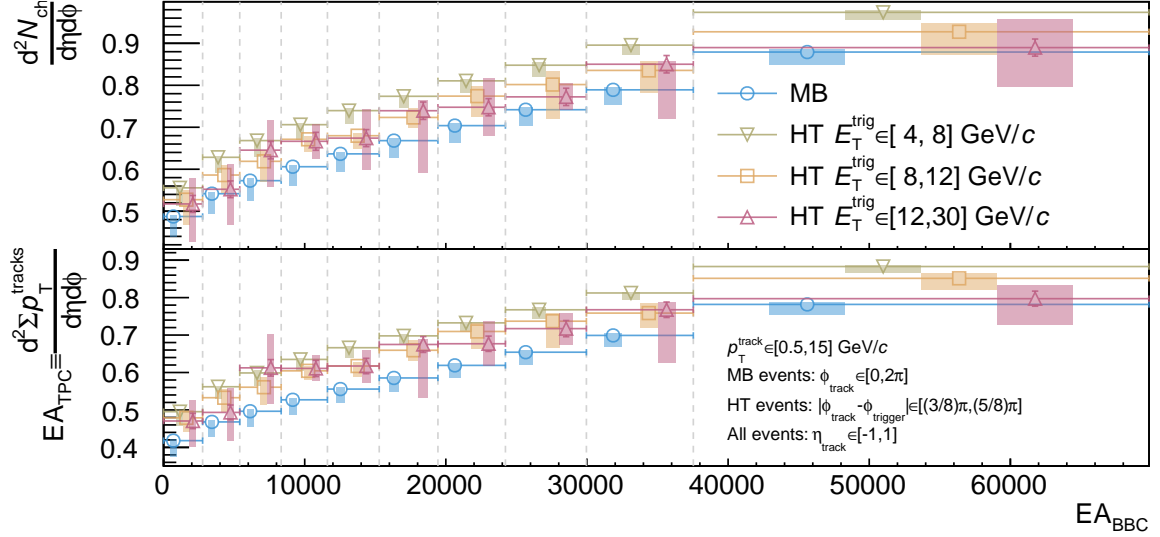
Figure 5.11: Density per unit ϕ and unit η of number of tracks (top panel) and summed track p_T (bottom panel). For MB events, all tracks in TPC are used. For HT events, tracks that transverse to the trigger ($|\phi_{\text{track}} - \phi_{\text{trigger}}| \in [(3/8)\pi, (5/8)\pi]$) are used. Values corrected for tracking efficiency and detector acceptance. Systematic uncertainty (shown in shaded boxes), the largest component of which accounts for pileup tracks. Within each EA_{BBC} bin, the x-axis locations of markers, and x-axis ranges of uncertainty boxes, have been selected for visual clarity and are not otherwise meaningful.

the hardness of the trigger.[11] This anticorrelation is such that in the highest EA_{BBC} bin the mean EA_{TPC} value in an event with $E_T^{\text{trig}} > 12\,\text{GeV}$ approaches the MB value (with the caveat, of course, that the systematic uncertainty on that measurement is large).

Again, at least two effects are present: asking for more EA_{BBC} results in more tracks in the TPC (top of Figure 5.11) and a better opportunity to find a jet (Figure 5.9). Therefore, in the Glauber picture, EA_{BBC} is positively correlated to $\langle N_{\text{coll}} \rangle$ and $\langle N_{\text{part}} \rangle$, and is a "good" EA estimator. However, if jets scale directly with N_{coll} and underlying event tracks with N_{part}, then the relationship breaks down as harder jets correlate with less (N_{part}). As noted, this may be partially due to the small system size – the tracks counted in the jet (with N_{part}) and counted in a different region than those counted in EA_{TPC} or EA_{BBC}, so they are in one or the other place, but not both. It may also be total energy conservation. Or, event more exciting, it may indicate some other physics process correlating hard and soft scatterings (as discussed in Section 7).

---

11. The uncertainties on the highest E_T^{trig} in many bins are large, but the trend is consistent.

5.7 MC and Phase Space Suppression

`PYTHIA8` has been used to model $\sqrt{s_{\mathrm{NN}}} = 200\,\mathrm{GeV}$ p+Au collisions, the results of which are clustered into anti-k_{T} jets with $R = 0.4$. The simulation quantified $\mathrm{EA_{BBC}}$ as the total number of charged particles produced in each collision in the acceptance of STAR's BBC. A plot of this simulated $\mathrm{EA_{BBC}}$ vs the leading (highest p_{T}) jet in the $|\Delta\phi| > (7/8)\pi$ bin is shown in Figure 5.12.
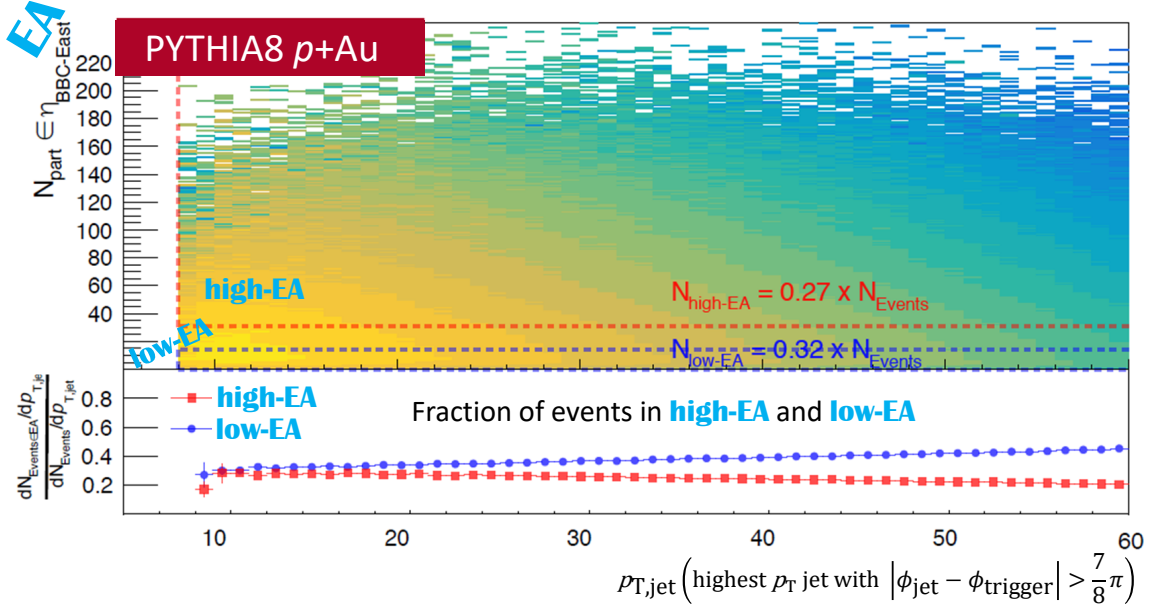

Figure 5.12: `PYTHIA8` simulation of p+Au $\sqrt{s_{\mathrm{NN}}} = 200\,\mathrm{GeV}$ events. Top panel: The number of particles the Au-going BBC acceptance is defined as the simulated $\mathrm{EA_{BBC}}$. The N_{part} for the 32th and 63rd percentiles are shown plotted (it wasn't possible to get exactly one-third of the distribution in either bin because of the integer count definition of the EA) as defined for all events are shown. The x-axis is the leading p_{T} full jet. The bottom panel shows the ratio of events for each jet-p_{T} bin that are in the $\mathrm{EA_{BBC}^{High}}$ and $\mathrm{EA_{BBC}^{Low}}$ bins.

The simulated value for ratio of EA-binned semi-inclusive jet spectra is:

$$\frac{S_{\mathrm{EA_{BBC}^{High}}}}{S_{\mathrm{EA_{BBC}^{Low}}}} = \frac{\dfrac{N_{\mathrm{jets}}^{\mathrm{EA_{BBC}^{High}}}}{N_{\mathrm{triggers}}^{\mathrm{EA_{BBC}^{High}}}}}{\dfrac{N_{\mathrm{jets}}^{\mathrm{EA_{BBC}^{Low}}}}{N_{\mathrm{triggers}}^{\mathrm{EA_{BBC}^{Low}}}}} = \frac{N_{\mathrm{triggers}}^{\mathrm{EA_{BBC}^{Low}}}}{N_{\mathrm{triggers}}^{\mathrm{EA_{BBC}^{High}}}} \frac{N_{\mathrm{jets}}^{\mathrm{EA_{BBC}^{High}}}}{N_{\mathrm{jets}}^{\mathrm{EA_{BBC}^{Low}}}} \qquad (5.12)$$

The EA definition is for all events, as mentioned above. The ratio of triggers is:

$$\frac{N_{\text{triggers}}^{\text{EA}_{\text{BBC}}^{\text{Low}}}}{N_{\text{triggers}}^{\text{EA}_{\text{BBC}}^{\text{High}}}} = \frac{32\%}{27\%} \approx 1.2. \tag{5.13}$$

In the simulation, we have the luxury of binning each event by the leading recoil jet value, and plotting only the entry for the lead recoil jet such that there is exactly one entry per trigger and jet. Therefore, that ratio of 1.2 is also the ratio of the total number of jets $> 8\,\text{GeV}/c$ in the low to high EA_{BBC} bins:

$$\left.\frac{S_{\text{EA}_{\text{BBC}}^{\text{High}}}}{S_{\text{EA}_{\text{BBC}}^{\text{Low}}}}\right|_{\text{All jets}} = \frac{N_{\text{triggers}}^{\text{EA}_{\text{BBC}}^{\text{Low}}} \, N_{\text{jets}}^{\text{EA}_{\text{BBC}}^{\text{High}}}}{N_{\text{triggers}}^{\text{EA}_{\text{BBC}}^{\text{High}}} \, N_{\text{jets}}^{\text{EA}_{\text{BBC}}^{\text{Low}}}} = 1.2 \times \frac{1}{1.2} = 1.0 \tag{5.14}$$

$$\text{with } E_{\text{T}}^{\text{trig}} \in [8, 30]\,\text{GeV}/c \ \& \ p_{\text{T}}^{\text{jet}} > 8\,\text{GeV}/c \tag{5.15}$$

However, one can see by eye, that the simulation has a negative correlation between the average lead recoil jet p_{T} and the EA. At $p_{\text{T,jet}} \approx 30\,\text{GeV}/c$ the ratio of events (and/or jets) is about 1.4, such that:

$$\left.\frac{S_{\text{EA}_{\text{BBC}}^{\text{High}}}}{S_{\text{EA}_{\text{BBC}}^{\text{Low}}}}\right|_{\text{Jets with } p_{\text{T}} \approx 30\,\text{GeV}/c} = \frac{N_{\text{triggers}}^{\text{EA}_{\text{BBC}}^{\text{Low}}} \, N_{\text{jets}}^{\text{EA}_{\text{BBC}}^{\text{High}}}}{N_{\text{triggers}}^{\text{EA}_{\text{BBC}}^{\text{High}}} \, N_{\text{jets}}^{\text{EA}_{\text{BBC}}^{\text{Low}}}} = 1.2 \times \frac{1}{1.4} = 0.86 \tag{5.16}$$

Hence, the `PYTHIA8` simulation predicts an anti-correlation between EA_{BBC} and jets at mid-rapidity, and a consequent suppression of $\sim 14\%$ of $30\,\text{GeV}/c$ jets recoiling from a trigger that turns on with $8\,\text{GeV}/c$ recoiling jets.

5.8 Measurement Indications of Jet Suppression

Before presenting the jet spectra measurements in the following chapter (Chapter 6), it is already clear that some jet spectra suppression to EA correlation is to be expected from the EA-to-trigger correlation, independent of any actual possible jet quenching. Just how much suppression is expected? It depends on the ratio of each jet p_{T} to each trigger E_{T}. From the qualitative arguments made above, strong suppression is expected for harder jets mixed with softer triggers.

The ratios of total number of full jets produced per number of triggers in high EA to low EA events are presented in Figure 5.13 (using EA_{BBC}) and Figure 5.14 (using EA_{TPC}). Each figure has four sub panels, each for a separate $10\,\mathrm{GeV}/c$ sub set of the overall jet range of $[10,50]\,\mathrm{GeV}/c$. The color in each panel represents the overall enhancement or suppression of jets per trigger, in which the trigger range runs from a lower bound (indicated by the x-axis location of the bin) to the upper bound (indicated by the y-axis location of the bin).

The relative distribution of jets among an overall set of ranges from the lower bound to the maximum upper bound ($30\,\mathrm{GeV}/c$) is indicated by circles (squares) in each bin for high (low) EA. The larger the circle or square, the higher percentage of the jets within that bin. (For example, the bin at ($E_T^{LB} \in [14, 15]$ & $E_T^{UB} \in [18, 19]$) has a circle (square) whose size represents the number of jets from events with triggers in the range $[18,19]\,\mathrm{GeV}/c$ divided by those in the entire column (i.e. jets from events with triggers in the range $[14,30]\,\mathrm{GeV}/c$).

Triggers in the range $E_T^{trig} > 25\,\mathrm{GeV}$ have been omitted from Figures 5.14 and 5.13 to simply allow more room to display the information in the range $E_T^{trig} \in [8, 25]\,\mathrm{GeV}$. As shown in Figure 5.7, there are very few triggers with $E_T^{trig} > 25\,\mathrm{GeV}$ such that the omission of these few high E_T^{trig} events on the plots is not significant.[12]

The expectation presented in argument in Section 5.6 is that the EA suppression of hard jets should result from having a large trigger range $E_T^{trig} \in [E_T^{LB}, E_T^{UB}]$, and that the high-EA events simply starve the population of hard triggers (and therefore indirectly hard jets) near the upper bound (E_T^{UB}) relative to the much larger population of jets near the lower bound (E_T^{LB}). In this scenario, there should be stronger suppression for hard jets for larger ranges of E_T^{trig} (i.e. the phase space represented by bins higher-above the diagonal turn-on where $E_T^{UB} = E_T^{LB} + 1\,\mathrm{GeV}$). The data plotted in Figures 5.13 & 5.14 only partially support this theory. It is true that higher suppression occurs for harder jets in conjunction with softer triggers. However, it is not generally shown that for a given low-value E_T^{LB} that raising the value of E_T^{UB} appreciably increases the suppression ratio of hard jets. Instead,

---

12. Besides which, it is evident in the figures themselves that the suppression is already stable by the upper bound of $E_T^{trig} = 25\,\mathrm{GeV}$ when using a lower bound less than about $E_T^{trig} \approx 18\,\mathrm{GeV}$. Also refer to Figure 5.15.

Figure 5.13: Using EA_{BBC}: Ratio of $N_{jets}^{High.EA}/N_{triggers}^{High.EA}$ to $N_{jets}^{Low.EA}/N_{triggers}^{Low.EA}$ gives color for each bin. Each panel is for jets in a separate p_T range, starting with $[10,16]\,GeV/c$ (top left), to $[28,34]\,GeV/c$ (bottom right). Jets are anti-k_T, $R = 0.4$, full jets, selected to be within $\pi/8$ radians of recoiling from the trigger. Each bin is for a different selection of events based the upper and lower bound of the trigger energy (marked as E_T^{LB} and E_T^{UB} on the x/y axes). The relative distribution of jets per E_T^{trig} bin in each column is given by sizes of circles (for low-EA events) and squares (for high-EA events).

the suppression is already largely determined by the first bin on the diagonal, and doesn't get stronger moving up from the diagonal.

A plot of the values of the first column in each of the p_T^{jet} quadrants in Figures 5.13 & 5.14 is given in Figure 5.15, in which the spectra are clearly not universally falling for all the harder jets. The falling trend fits best for jets at $p_T^{jets} \in [22, 28]\,GeV/c$ using EA_{TPC}.
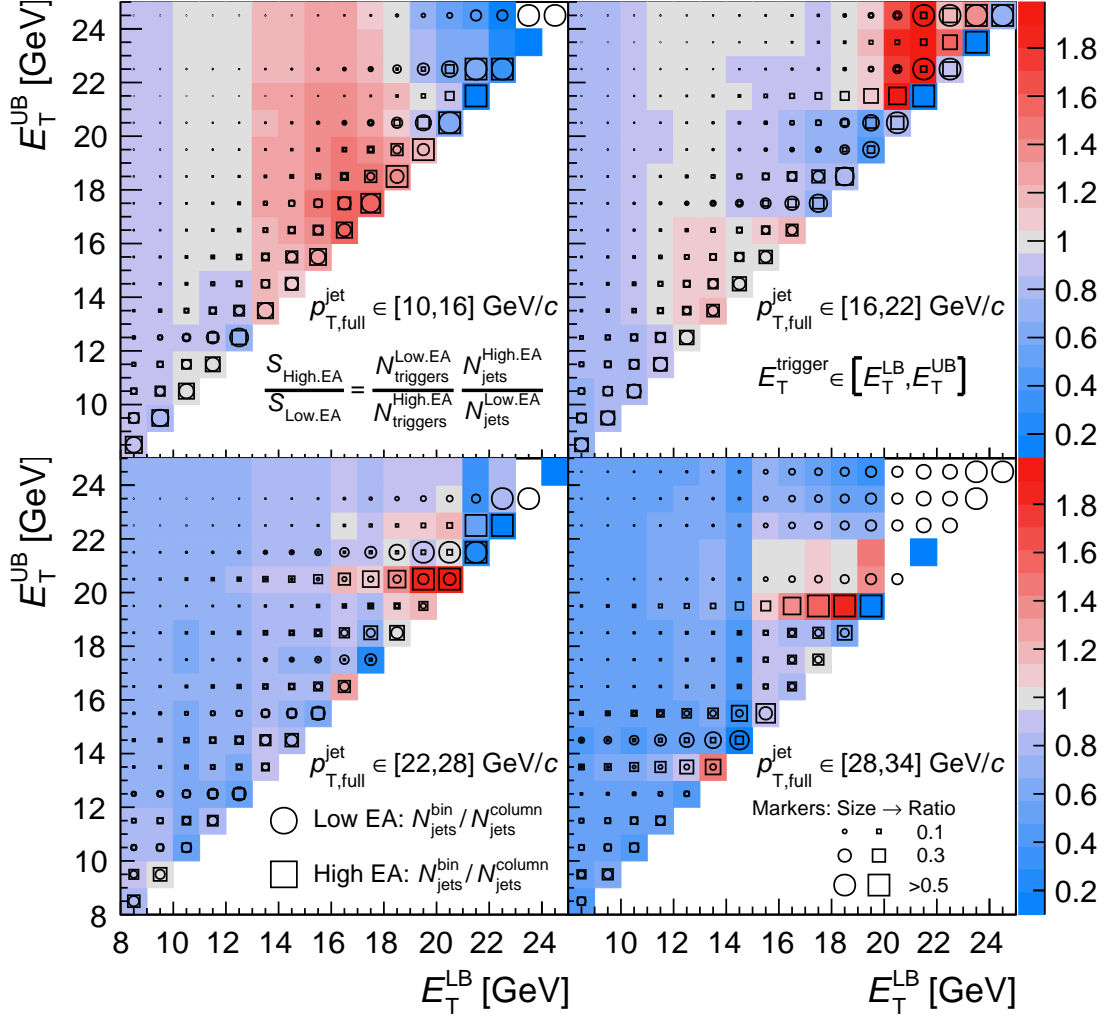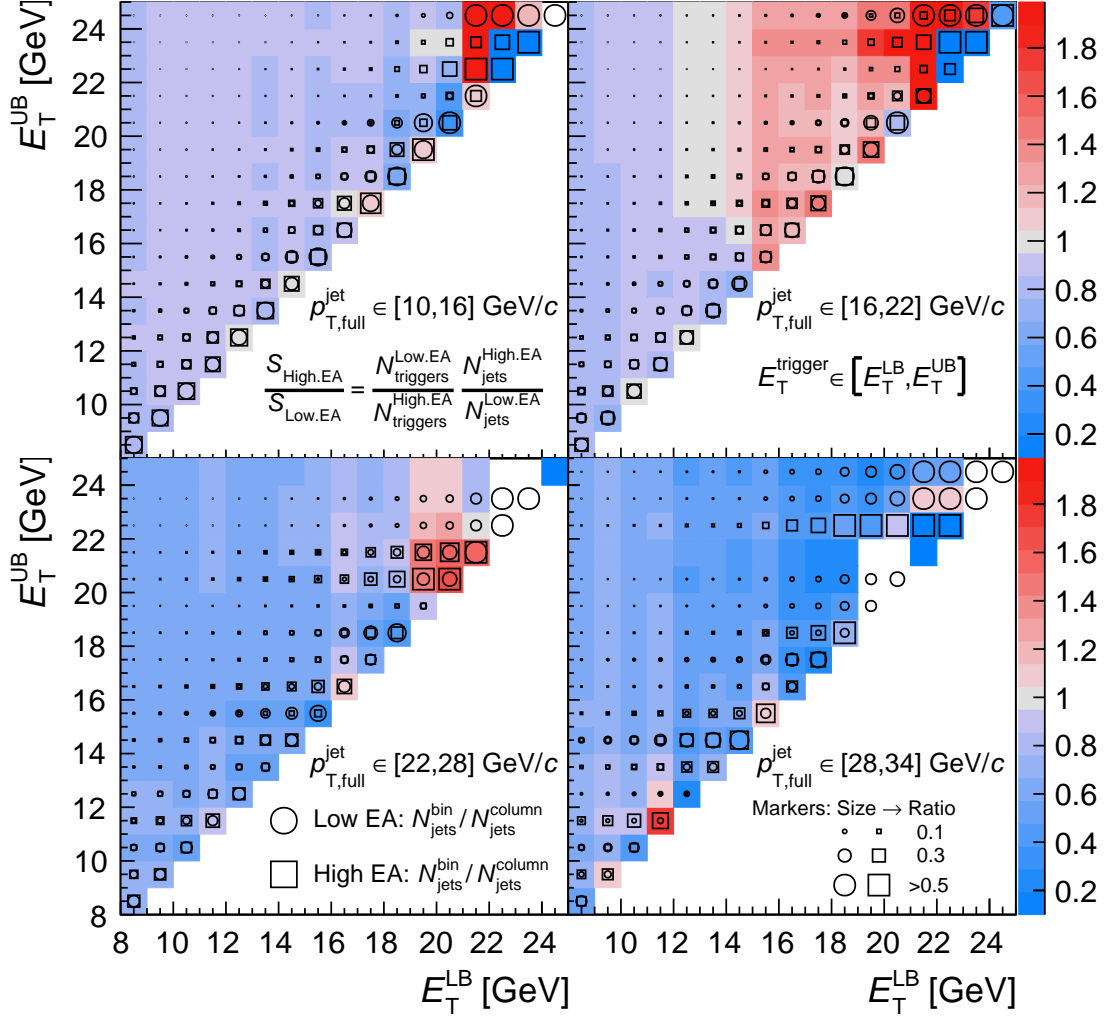
Figure 5.14: Using EA$_{\text{TPC}}$: Ratio of $N_{\text{jets}}^{\text{High.EA}}/N_{\text{triggers}}^{\text{High.EA}}$ to $N_{\text{jets}}^{\text{Low.EA}}/N_{\text{triggers}}^{\text{Low.EA}}$ gives color for each bin. Each panel is for jets in a separate p_{T} range, starting with $[10,16]\,\text{GeV}/c$ (top left), to $[28,34]\,\text{GeV}/c$ (bottom right). Jets are anti-k_{T}, $R = 0.4$, full jets, selected to be within $\pi/8$ radians of recoiling from the trigger. Each bin is for a different selection of events based the upper and lower bound of the trigger energy (marked as E_{T}^{LB} and E_{T}^{UB} on the x/y axes). The relative distribution of jets per $E_{\text{T}}^{\text{trig}}$ bin in each column is given by sizes of circles (for low-EA events) and squares (for high-EA events).

The discrepancy highlights the difference between the PYTHIA8 study in Figure 5.12 and the data. In the PYTHIA8 study, the events were divided cleanly by the leading recoil jet (which in that example case acted as the trigger). In reality, there is quite a bit of smearing between the trigger E_{T} and the jet p_{T}.[13] This is compounded by the steeply falling spectra

---

13. For instance, about 30% of all events with a 20 GeV leading jet and a 10 GeV recoil jet, when considering trigger range 4 GeV and up, fall in the range $E_{\text{T}}^{\text{trig}} \in [4, 5]\,\text{GeV}$.

of the E_T^{trig} distribution itself, so that a soft bin of triggers multiplied by a small cross section to generate hard recoil jets, can still generate more hard recoil jets than a much smaller, harder bin of triggers with their associated larger cross section for generating hard jets. Whether there is a more complicated relation between EA and E_T^{trig}, is a promising avenue for further study.
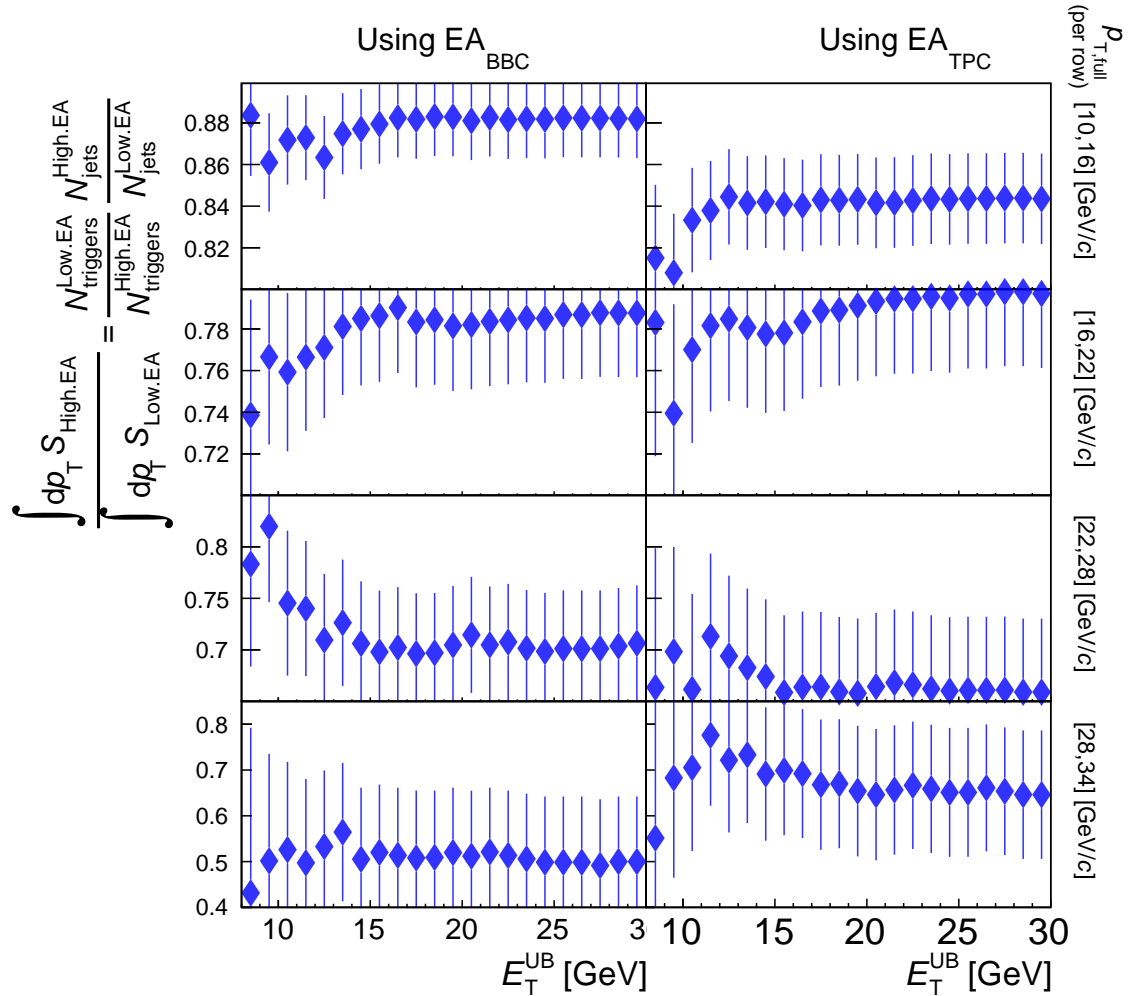

Figure 5.15: Suppression of jets-per-trigger in EA to jets-per-trigger in low EA, for both EA_{BBC} and EA_{TPC}. The jets are selected from events ranging from $8\,\mathrm{GeV}$ to the E_T^{UB} (the x-axes). Four different jet p_T ranges are binned, as indicated on the right-hand side of each row.

Chapter 6

Jet Measurements and Results

6.1 Overview of Jet Measurements

This chapter presents jet measurements using the events, tracks, and tower signals presented in Chapter 4. The tracks and towers are clustered with the anti-k_T algorithm using jet resolution parameter $R = 0.4$. To avoid boundary effects on the jet clustering, no jets are used with axes within R of the boundary of the TPC acceptant (i.e. $|\eta_\mathrm{jets}| \leq 0.6$).

Two populations of jets are presented. The first population comes from events which have a trigger, defined as the energy and location of the BEMC tower with the highest energy hit, which must fall within a certain range.[1] These jet distributions are normalized per trigger. The normalization makes these spectra semi-inclusive. That is, the spectra are measuring the cross section ratio $\sigma^{\mathrm{jet+trigger}}/\sigma^{\mathrm{trigger}}$ (or the conditional probability $P(\mathrm{jet|trigger})$) from $p+\mathrm{Au} \to \mathrm{trigger+jet}+X$ reactions.[2] Therefore the terms "semi-inclusive" and "per-trigger" are used interchangeably.

The semi-inclusive jets are binned by p_T and $|\Delta\phi| \equiv |\phi_\mathrm{jet} - \phi_\mathrm{trigger}|$. When presented as a

---

1. $E_\mathrm{T}^\mathrm{trig} \in [8, 30]\,\mathrm{GeV}$ for most measurements, but also $E_\mathrm{T}^\mathrm{trig} \in [4, 6]\,\mathrm{GeV}$ whose results are used for comparison.

2. Inclusive measurements quantify the full cross section (σ^jet) from $p+\mathrm{Au} \to \mathrm{jet} + X$. These include the ATLAS, PHENIX, and CMS measurements discussed in Chapter 2 [72–74].

p_T spectrum, the p_T bins are made as fine as possible, limited by JER (see Section 4.7) and bin statistics. These spectra are labeled:

$$S \equiv= \frac{1}{N_\text{triggers}} \frac{\mathrm{d}N_\text{jet}}{\mathrm{d}p_\text{T}^\text{jet}} \tag{6.1}$$

It is also binned by EA and taken in high EA to low EA ratio to observe EA dependence. The EA labels used are: $\text{EA}_\text{BBC}^\text{High}$ (or $\text{EA}_\text{TPC}^\text{High}$) S: $S_{\text{EA}(0-30\%)}$; $\text{EA}_\text{BBC}^\text{Low}$ (or $\text{EA}_\text{TPC}^\text{Low}$) S: $S_{\text{EA}(70-100\%)}$. Finally, S are binned by $|\Delta\phi|$ into eight spectra, with markers and colors as shown in Figure 6.1. The trigger and recoil spectra are of special interest, as they contain the dijets. The two transverse bins ($|\Delta\phi| \in [(3/8)\pi, (5/8)\pi]$) contain the acceptance of the EA_TPC measurement.
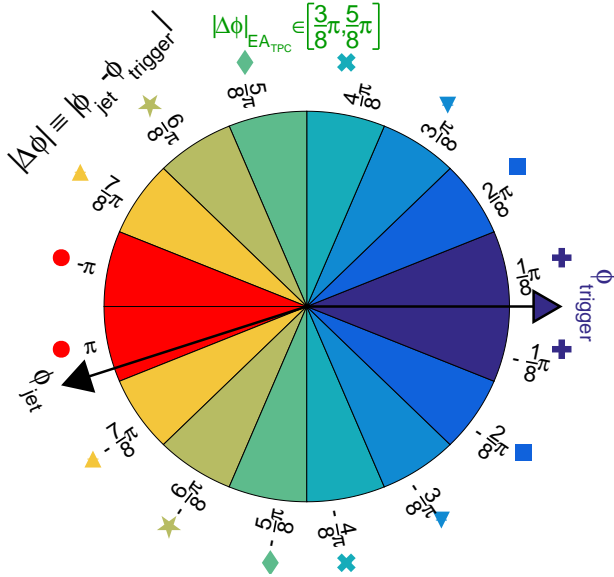

Figure 6.1: Markers and colors for bins of $\phi_\text{jet} - \phi_\text{trigger}$ used for semi-inclusive jet measurements. Each bin is in $|\Delta\phi|$ as indicated (the numerical labels on the cartoon are the upper bin boundaries).

Following presentation of S, the semi-inclusive jet population is also presented as spectra of $|\Delta\phi|$, with bin width limited principally by statistics. These include all jets with $p_\text{T} > 10\,\text{GeV}/c$, and were generated to see if there is a broadening of the recoil distribution, which is a measurement of acoplanarity and another signal for jet quenching.

In the final section (Section 6.10) a measurement of the dijet p_T balance is presented. This is a shape distribution normalized per dijet and uses all events with $E_\text{T}^\text{trig} \geq 4\,\text{GeV}$.

6.2 Uncorrected Measurement of Semi-Inclusive Jet Spectra

The jet spectra per trigger (S) are plotted in eight bins of $|\Delta\phi|$ in Figure 6.2. In order to plot the spectra continuously down toward zero, the spectra in the figure are detector-level; they have not been unfolded to particle level. This is because at low momenta the effects of the underlying events and limited JER become dominant. This is also to say that at low momenta the "jets" are really just jet objects generated by the clustering, and are not necessarily the product of a hard scattering.
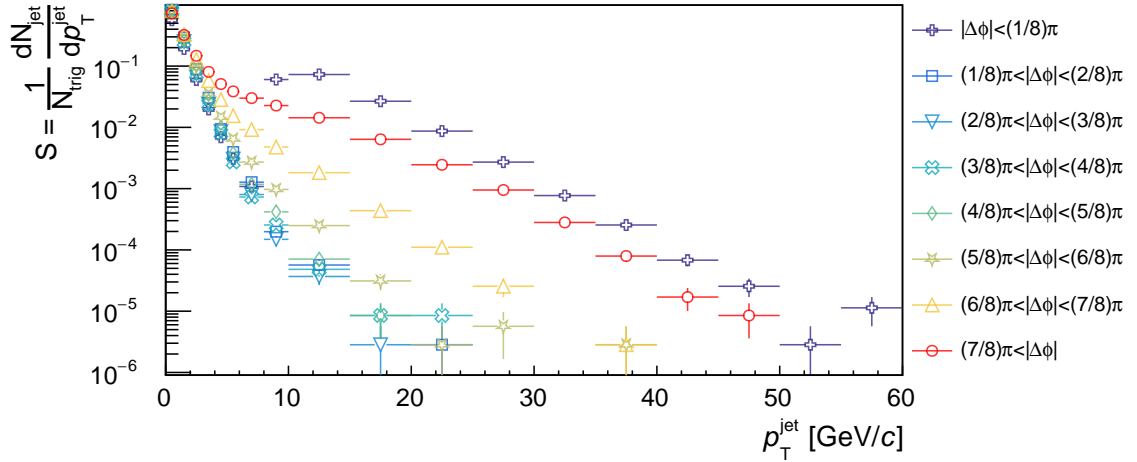

Figure 6.2: Detector-level (i.e. uncorrected), semi-inclusive full jet spectra (S) binned by $|\Delta\phi|$. Jets are anti-k_T, $R = 0.4$, full jets with $|\eta_\mathrm{jet}| < 0.6$. Jets are taken from all HT events with $E_\mathrm{T}^\mathrm{trig} > 8\,\mathrm{GeV}$.

The spectra in Figure 6.2 have several features of interest:

- The trigger bias in the $|\Delta\phi| < (1/8)\pi$ bin:
  - The turn-on of the required $8\,\mathrm{GeV}$ tower is obvious in the S spectra in the $|\Delta\phi| \in [0, (1/8)\pi]$ bin. Every event has a high energy BEMC hit, and unless the hit occurs such that the jet containing the hit is at $|\eta| > 0.6$, then there is a jet with $p_\mathrm{T} \geq 8\,\mathrm{GeV}/c$ in the $|\Delta\phi|$ trigger bin.
  - The $|\Delta\phi|$ bins are 1.6 units of rapidity by $\sim$0.79 radians $(\pi/4)$. There is room for more than one jet of radius $R = 0.4$ in each $|\Delta\phi|$ bin in each event. Therefore, there are some jets with $p_\mathrm{T} < 8\,\mathrm{GeV}/c$ in the trigger-side bin, composed presumably from underlying event (UE) activity. These jets must be farther away than

97

~0.4 in ϕ-η from the trigger tower, otherwise they would be clustered with the trigger tower into a jet with $p_T > 8\,\text{GeV}/c$. Therefore the trigger-side $|\Delta\phi|$ bin has the smallest amount of π-η in which to collect UE jets, which explains why it has the smallest spectra of S at $p_T < 8\,\text{GeV}/c$ out of all the $|\Delta\phi|$ bins.[3]

- The trigger-side S is markedly higher than the recoil-side S, spectra. There are at least two trends present:

  (a) The trigger-side jet normally contains the trigger itself, and in those events, the trigger-side jet is essentially 100% efficient on containing a $8\,\text{GeV}$ constituent.[4] This is a bias which pushes the trigger-side S curve to the right relative to the recoil-side S curve which has no such trigger bias.

  (b) The trigger itself biases the leading jet of the collision to be found, and dijet η swing between the leading and subleading jets frequently pushes the other jet out of the TPC's jet η acceptance of $|\eta_{\text{jet}}| \leq 0.6$. This bias can be seen from the PYTHIA8 generated pp collisions at $\sqrt{s_{\text{NN}}} = 200\,\text{GeV}$ pp collisions used to plot Figure 5.5. In those collisions, when there is an $8\,\text{GeV}$ neutral particle in the BEMC acceptance (and therefore, due to perfect reconstruction of jets in simulation, at least one $8\,\text{GeV}/c$ jet in the event) the leading or subleading jet is found within $\eta_{\text{jet}} \leq 0.6$ 77% of the time. In those events, both the leading and subleading fell within $|\eta| \leq 0.6$ only 28% of the time. Of course, when only one dijet misses the jet acceptance, sometimes that is the jet in the trigger-side jet $|\Delta\phi|$ bin (particularly when the tower trigger is at $|\eta_{\text{trig}}| > 0.6$). Therefore, the suppression ratio of 0.28 is a reasonable upper-bound for suppression due to η-swing kinematics.

The interplay of these two effects, along with effects such as fragmentation bias between the two sides, is of interest for further study.

- There is very little background, as indicted by the very low yield and steeply falling spectra of S transverse to the dijet axis (bins in $|\Delta\phi| \in [(1/8)\pi/(7/8)\pi]$). At jet p_T

---

3. The $[6, 8]\,\text{GeV}/c$ p_T bin in the $|\Delta\phi|$ bin at $[(3/8)\pi, (4/8)\pi]$ is the only exception, and it is only ~4% lower than that p_T bin's value in the trigger-side $|\Delta\phi|$ bin.

4. Due to the track-tower hadronic correction, it may be a track, tower or mix.

above about $10\,\text{GeV}$, the spectra S in $|\Delta\phi| \in [(2/8)\pi, (5/8)\pi]$ are two or more orders of magnitude smaller than the trigger- and recoil-side S.

- S in the three $|\Delta\phi|$ bins in the range $[(2/8)\pi, (5/8)\pi]$ all have comparable jet spectra, and as such appear to be uniformly representative of combinatoric jets from the isotropic underling event activity (UE).

- S in the next two transverse bins ($|\Delta\phi| \in [(5/8)\pi, (6/8)\pi]$ and $|\Delta\phi| \in [(5/8)\pi, (7/8)\pi]$) have small but clear increases over the prior S at $|\Delta\phi| \in [(2/8)\pi, (5/8)\pi]$, indicating some broadening of activity aligned with the recoil jets. The $|\Delta\phi|$ distribution of the jets will be discussed further in Section 6.9.

6.3   Uncorrected Semi-Inclusive Jet Spectra Binned in EA_{BBC}

The semi-inclusive spectra S binned by selecting events from high and low EA_{BBC} events are plotted for $p_{\text{T}} \in [0, 20]\,\text{GeV}/c$ in Figure 6.3 for all $|\Delta\phi|$ bins. As this presents jets below p_{T} that can be unfolded, these are also uncorrected values.

As already seen in Figure 5.11, higher-EA_{BBC} corresponds with higher background activity. This is seen clearly in the ratio in Figure 6.3: soft, combinatoric jets are enhanced at higher EA, with the effect being the most dramatic for the most transverse bins.

6.4   Corrected Semi-Inclusive Jet Spectra Binned in EA_{BBC}

The corrected jet spectra in the trigger- and away-side $|\Delta\phi|$ bins are plotted in Figure 6.4 for jets at $[8,50]\,\text{GeV}/c$ for both high and low EA_{BBC}. The bottom panel gives the ratio of $\text{EA}_{\text{BBC}}^{\text{High}}$ to $\text{EA}_{\text{BBC}}^{\text{Low}}$ spectra. The trend is monotonic suppression in S binned by $\text{EA}_{\text{BBC}}^{\text{High}}$ relative to S binned by $\text{EA}_{\text{BBC}}^{\text{Low}}$.

In each figure with corrected S, or ratios of corrected S, (Figures 6.4, 6.5, 6.6, A.19, and A.20), the jet spectra is unfolded for detector reconstruction efficiency and resolution, as discussed in Section 4.7. The S distributions were unfolded again with variations in the truth-level to detector-level $p_{\text{T}}^{\text{jet}}$ matching in order to account for uncertainties in tower calibration resolution, track reconstruction efficiency, hadronic correction fraction, and number
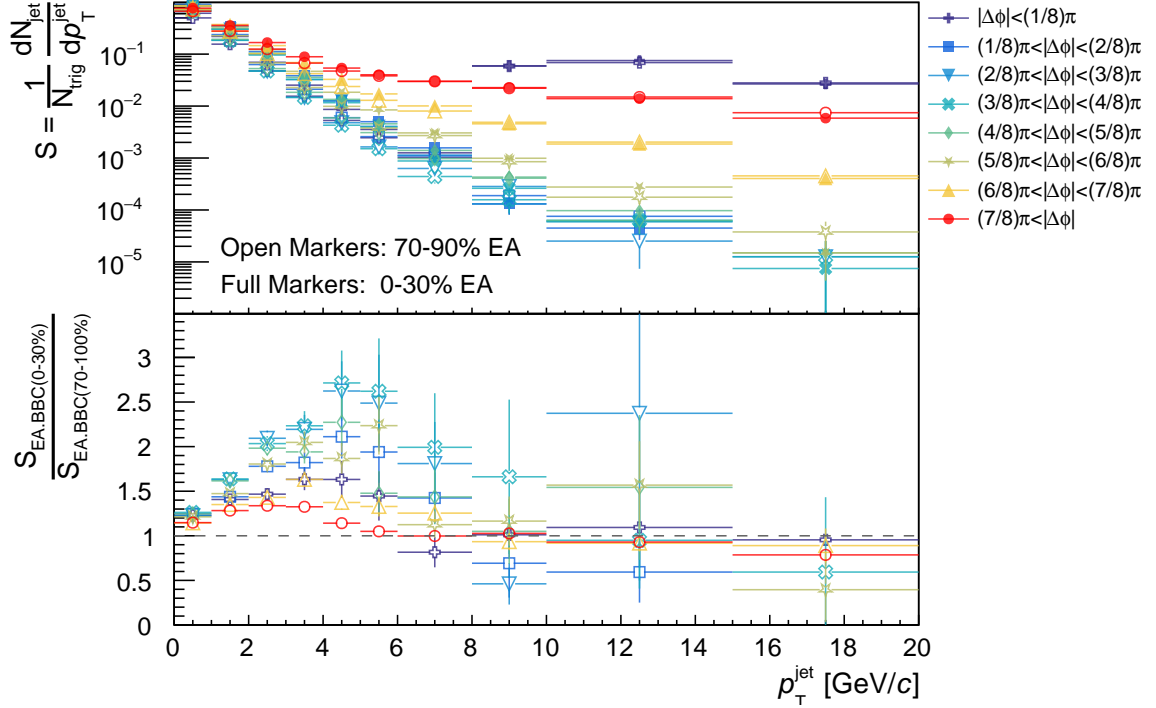
Figure 6.3: Top panel: Detector-level (i.e. uncorrected), full-jet, anti-k_T, $R = 0.4$, $|\eta_\mathrm{jet}| < 0.6$ spectra per trigger (S) binned by $|\phi_\mathrm{jet} - \phi_\mathrm{trigger}|$ and highest and lowest 30% $\mathrm{EA_{BBC}}$ from all HT events with $E_\mathrm{T}^\mathrm{trig} > 8\,\mathrm{GeV}$. Bottom panel: ratio of S binned by $\mathrm{EA_{BBC}^{High}}$ to $\mathrm{EA_{BBC}^{Low}}$.

of iterations in the Bayesian unfolding procedure.[5] With the exception of uncertainties in the unfolding stability, most variation in the spectra for high-EA and low-EA S distributions cancel in the ratios.

6.5 Event Activity Binned S Ratios with Varying $E_\mathrm{T}^\mathrm{trig}$

A naive expectation of the EA to trigger correlation[6] is that the jets associated with higher $E_\mathrm{T}^\mathrm{trig}$ will be more suppressed when normalized by events that include softer triggers. Figure 6.5 plots the suppression ratios for the trigger- and recoil-side $\Delta\phi$ bins for $E_\mathrm{T}^\mathrm{trig}$ bins in the ranges of $[8,30]\,\mathrm{GeV}$,[7] $[8,10]\,\mathrm{GeV}$, $[10,30]\,\mathrm{GeV}$, $[8,12]\,\mathrm{GeV}$, and $[12,30]\,\mathrm{GeV}$.

---

5. As provided by the `RooUnfold` library [117, 118]

6. As discussed in Section 5.6

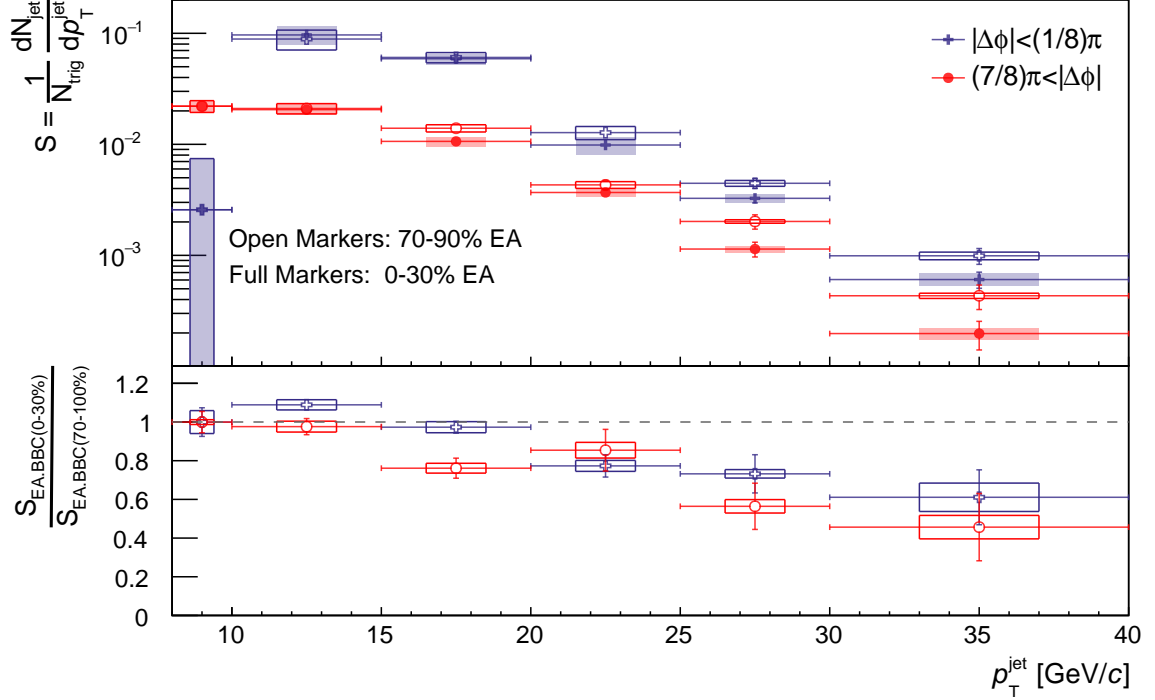7. This is the whole range, also plotted in Figure 6.4, although with different p_T binning.

Figure 6.4: Corrected full-jet, anti-k_{T}, $R = 0.4$, $|\eta_{\mathrm{jet}}| < 0.6$ spectra per trigger (S), binned by $|\phi_{\mathrm{jet}} - \phi_{\mathrm{trigger}}|$ to select near-side and recoil jets, and highest and lowest 30% $\mathrm{EA_{BBC}}$ from all HT events with $E_{\mathrm{T}}^{\mathrm{trig}} > 8\,\mathrm{GeV}$. Systematic uncertainties are given in boxes, statistical uncertainties as error bars. Top panel: S distributions. Bottom panel: ratios of $S_{\mathrm{EA_{BBC}^{High}}}$ to $S_{\mathrm{EA_{BBC}^{Low}}}$.

The statistics are limited and therefore the bins are quite large. The resulting suppression ratios of S are quite close together. Although the ordering of the suppression (most to least) is consistent between the first two bins of the top panel (trigger side) and all three bins in the bottom panel (recoil side), the differences are all within statistical, and often systematic, uncertainties. Therefore the data does not support any definitive statement about whether the predicted dependence of S suppression on the range of $E_{\mathrm{T}}^{\mathrm{trig}}$ is observed.

6.6 Semi-Inclusive Jet Spectra Binned in $\mathrm{EA_{BBC}}$ & $\mathrm{EA_{TPC}}$

The correlation between $\mathrm{EA_{TPC}}$ and $\mathrm{EA_{BBC}}$ has already been presented in Section 5.5. The percentages of events in the top/bottom 30% of events of each EA definition, the binning intersections $\mathrm{EA_{BBC}^{High}} \cap \mathrm{EA_{TPC}^{High}}$ and $\mathrm{EA_{BBC}^{Low}} \cap \mathrm{EA_{TPC}^{Low}}$, and the off-diagonal intersections $\mathrm{EA_{BBC}^{High}} \cap \mathrm{EA_{TPC}^{Low}}$ & $\mathrm{EA_{BBC}^{Low}} \cap \mathrm{EA_{TPC}^{High}}$, are given in Table 5.1. These final two intersections
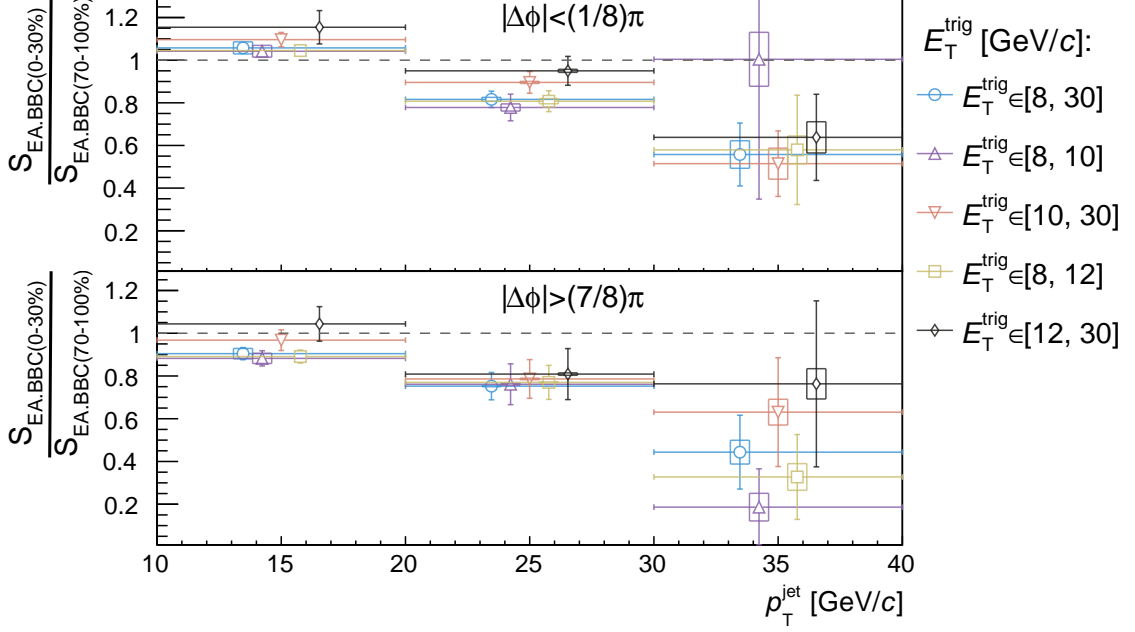
Figure 6.5: Ratios of corrected $S_{\mathrm{EA}_{\mathrm{BBC}}^{\mathrm{High}}}/S_{\mathrm{EA}_{\mathrm{BBC}}^{\mathrm{Low}}}$ for events collected with various ranges of $E_{\mathrm{T}}^{\mathrm{trig}}$. Top: jets in trigger-side ($|\Delta\phi| < (1/8)\pi$) bin, bottom jets in recoil-side ($|\Delta\phi| > (7/8)\pi$) bin. The horizontal offsets of the figure markers in the bins are for convenience only. Systematic (statistical) uncertainties plotted as boxes (error bars).

each contain only $\sim 5\%$ of the events and would seem pathologically bad as an EA-definition, but are one way of seeing if one EA definition is dominant in the EA-binned S dependence. The corresponding EA-binned S ratios are plotted in Figure 6.6, where the following points are clear.

- The $S_{\mathrm{EA}(0-30\%)}/S_{\mathrm{EA}(70-100\%)}$ is comparably suppressed using both $\mathrm{EA_{BBC}}$ (red circles) and $\mathrm{EA_{TPC}}$ (blue squares).

- Within the given binning[8] the suppression monotonically increases with increasing $p_{\mathrm{T}}^{\mathrm{jet}}$.[9]

- Using the intersections $\mathrm{EA_{BBC}^{High}} \cap \mathrm{EA_{TPC}^{High}}$ and $\mathrm{EA_{BBC}^{Low}} \cap \mathrm{EA_{TPC}^{Low}}$ (black stars) strengthens the suppressions.

- Using the contrary intersections $\mathrm{EA_{TPC}^{High}} \cap \mathrm{EA_{BBC}^{Low}}$ and $\mathrm{EA_{TPC}^{Low}} \cap \mathrm{EA_{BBC}^{High}}$ (brown dia-

---

8. The lack of statistics of higher p_{T} jets make bin values sensitive to the choice of $p_{\mathrm{T}}^{\mathrm{jet}}$ boundaries

9. This already follows from the above point combined with the same observation for EA-suppression of the jet spectra using $\mathrm{EA_{BBC}}$ in Figure 6.4

monds), within the limited available statistics, cancels the suppression, as would be naively expected if the two definitions of EA have equal effects on event selection.
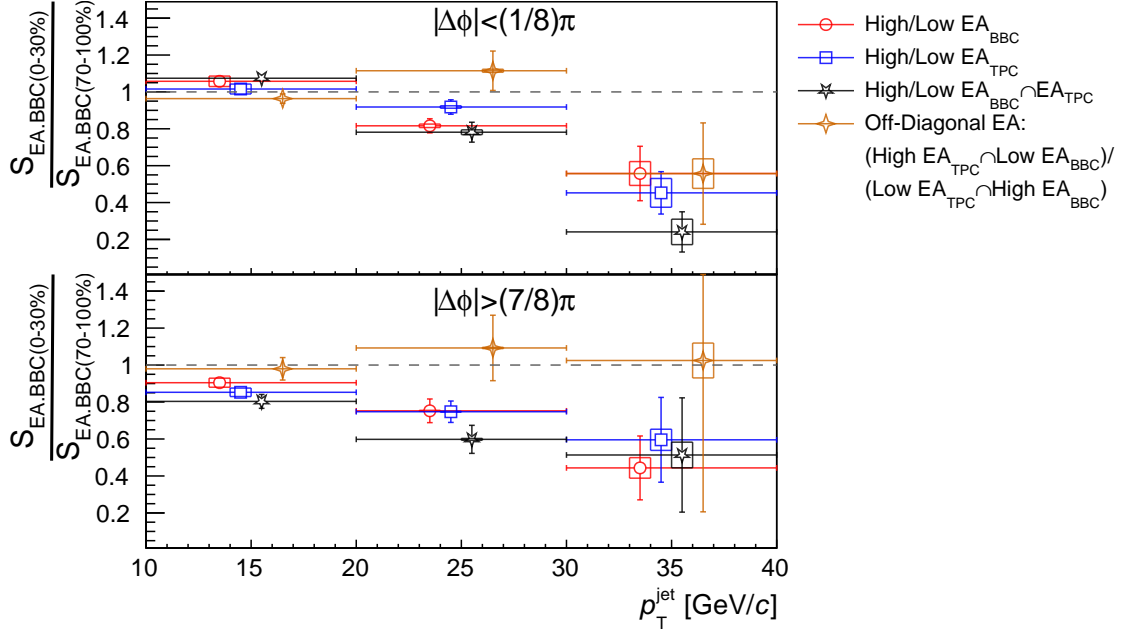

Figure 6.6: Ratios of high-to-low EA binned S, where EA is defined as $\mathrm{EA_{BBC}}$, $\mathrm{EA_{TPC}}$, and combinations thereof. Top: jets in trigger-side ($|\Delta\phi| < (1/8)\pi$) bin, bottom jets in recoil-side ($|\Delta\phi| > (7/8)\pi$) bin. Systematic (statistical) uncertainties plotted as boxes (error bars).

6.7 Semi-Inclusive Jet Spectra Binned in $\mathrm{EA_{TPC}}$

The semi-inclusive jet spectra S are plotted for high and low $\mathrm{EA_{TPC}}$ in Figure 6.7. This is analogous to the plot for the same parameters, but using $\mathrm{EA_{BBC}}$ (instead of $\mathrm{EA_{TPC}}$) in Figure 6.3. While Figure 6.6 has already demonstrated that the trigger- and recoil-side $|\Delta\phi|$ bins of S are comparably suppressed in high-to-low EA ratio using $\mathrm{EA_{BBC}}$ and $\mathrm{EA_{TPC}}$, $\mathrm{EA_{TPC}}$ is defined by the activity in the two transverse $|\Delta\phi| \in [(4/8)\pi, (5/8)\pi]$ and $|\Delta\phi| \in [(4/8)\pi, (5/8)\pi]$ bins. This autocorrelation is clearly visible in the top panel of Figure 6.7 where bins azimuthally transverse to the trigger (teal X's and olive-green diamonds) show a very strong suppression of the low-EA data (represented by open markers) relative to the high-EA data (represented by the full markers). It is also of note that the adjacent $|\Delta\phi|$ bins ($|\Delta\phi| \in [(3/8)\pi, (4/8)\pi]$ and $|\Delta\phi| \in [(5/8)\pi, (6/8)\pi]$) see what appears to be carryover effect of adjacent activity enhancement not present in the $\mathrm{EA_{BBC}}$ plot in
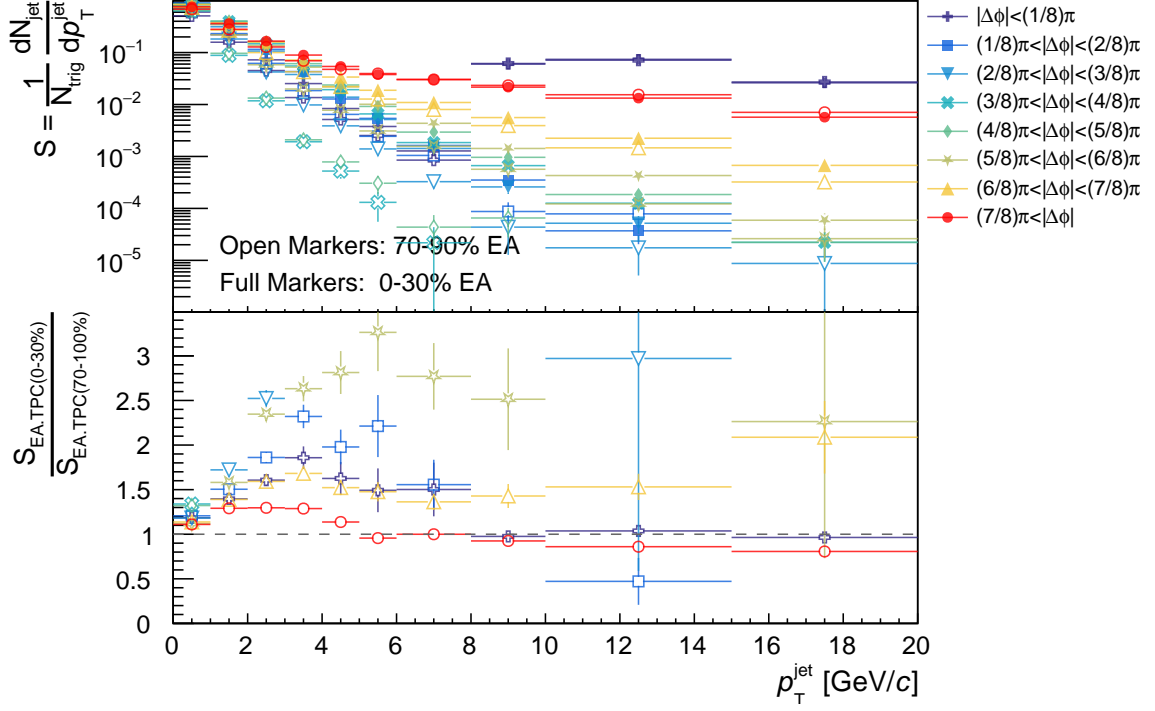
Figure 6.3

Figure 6.7: Uncorrected, full-jet, anti-k_T, $R = 0.4$, $|\eta_\mathrm{jet}| < 0.6$ semi-inclusive jet p_T spectra per trigger (S) binned by $|\phi_\mathrm{jet} - \phi_\mathrm{trigger}|$ and $\mathrm{EA_{TPC}}$. Top panel: S spectra. Bottom panel: ratio of S in $\mathrm{EA_{TPC}^{High}}$ events to S in $\mathrm{EA_{TPC}^{Low}}$ events.

6.8 Semi-inclusive Jet Spectra S Compared at $\mathrm{EA_{TPC}^{High}}$ to $\mathrm{EA_{TPC}^{Low}}$

Plots of the semi-inclusive jet spectra S for trigger- and recoil-side $|\Delta\phi|$ bins in ratio for $\mathrm{EA_{TPC}^{High}}$ to $\mathrm{EA_{TPC}^{Low}}$ are placed in the appendix as figures Figure A.19 and Figure A.20 for reference. Their characteristics are qualitatively identical to the same measurements, but using $\mathrm{EA_{BBC}}$ for EA binning which have already been presented as Figure 6.3 and Figure 6.4.

6.9 Semi-Inclusive Acoplanarity

Jet modification of a QGP medium can be probed not only via $p_\mathrm{T}^\mathrm{jet}$, but also by deflection of the dijet azimuth's from being directly back-to-back at exactly $|\Delta\phi| = \pi$. Broadening of large angle scattering (acoplanarity) beyond the amount normally produced from initial and final state radiation (ISR and FSR) is a proposed signature of a QGP due to scattering of individual particles in the QGP (Molière scattering) [122]. The same jets used to probe

the EA dependence of the semi-inclusive $p_\mathrm{T}^\mathrm{jet}$ spectra (S) reported in Sections 6.2-6.7 are used to present $\mathrm{EA_{BBC}}$[10] binned measurements of $|\Delta\phi|$ spectra.

The effects of combinatoric jets from UE activity are mitigated in two ways. First, only jets with $p_\mathrm{T} > 10\,\mathrm{GeV}/c$ are used; as seen in Figure 6.2 there is very little background at those energies. Second, jets from a second set of collisions with a softer trigger tower requirement, $E_\mathrm{T}^\mathrm{trig} \in [4, 6]\,\mathrm{GeV}$, are also measured. The same UE jet objects should be equally present for harder and for softer triggers.[11] Therefore, if the soft-trigger acoplanarity spectra is subtracted from the hard-trigger acoplanarity spectra, the UE should be removed, and whatever remains should be associated with a hard trigger.[12]

The $|\Delta\phi|$ distributions are plotted in Figure 6.8, binned by $\mathrm{EA_{BBC}^{High}}$ and $\mathrm{EA_{BBC}^{Low}}$, and also by events with $E_\mathrm{T}^\mathrm{trig} \in [4, 6]\,\mathrm{GeV}$ and $E_\mathrm{T}^\mathrm{trig} \in [8, 30]\,\mathrm{GeV}$. The distributions are of full jets with $p_\mathrm{T}^\mathrm{jet} > 10\,\mathrm{GeV}/c$ and labelled as $A\left(|\Delta\phi|\right)$.
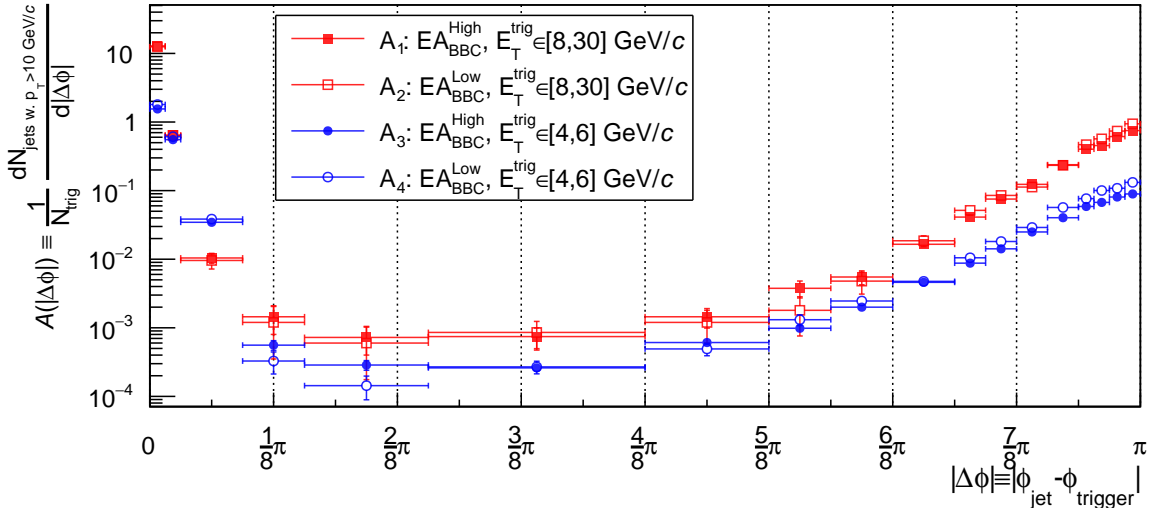

Figure 6.8: Azimuthal distribution of full jets, with $p_\mathrm{T}^\mathrm{jet} > 10\,\mathrm{GeV}/c$, relative to the azimuth of the trigger in the BEMC, normalized per the number of triggers. Distributions are for events binned by $\mathrm{EA_{BBC}}$, and for two different ranges of jets.

In order to quantify the broadening of the distribution, the cumulative distribution (CD)

---

10. $\mathrm{EA_{TPC}}$ is not used for the obvious reason that it is defined by the activity at $|\Delta\phi| \in [(3/8)\pi, (5/8)\pi]$.

11. The underlying event, UE, is by definition the activity not associated with the hard scattering.

12. See [75] for a prior application of this method for semi-inclusive jet p_T spectra in p+Pb collisions.

of each $|\Delta\phi|$ distribution from $|\Delta\phi| = \frac{\pi}{2}$ to $|\Delta\phi| = \pi$ is used. For convenience, these distributions CD($|\Delta\phi|$) are normalized to unity. In the continuous case, CD($|\Delta\phi|$) would be:

$$\mathrm{CD}(|\Delta\phi|) \equiv \frac{\int_{\pi/2}^{|\Delta\phi|} \frac{\mathrm{d}N_{\mathrm{jets}}}{\mathrm{d}|\Delta\phi|'}\mathrm{d}|\Delta\phi|'}{\int_{\pi/2}^{\pi} \frac{\mathrm{d}N_{\mathrm{jets}}}{\mathrm{d}|\Delta\phi|}\mathrm{d}|\Delta\phi|} \quad \text{where:} \ |\Delta\phi| \equiv |\phi_{\mathrm{jet}} - \phi_{\mathrm{trig}}| \tag{6.2}$$

The CD($|\Delta\phi|$) term is just the running sum of the fraction of jets "away from" the away-side peak of $|\Delta\phi| = \pi$. Therefore, at any value of $|\Delta\phi|$, it is the fraction of jets that are yet farther away from the recoil peak. As noted, the naive idealized back-to-back dijet scattering (in which CD($|\Delta\phi|$) $= \delta(|\Delta\phi| - \pi)$) is broadened at the parton-level by ISR and FSR. It is also broadened on the detector level by estimating the trigger-side ϕ_{parton} with ϕ_{trigger},[13] and by smearing between each recoil-side ϕ_{parton} and ϕ_{jet} due both to UE activity added into the jet's clustering, and actual constituents missed by the jet's clustering due to detector inefficiencies.

The values of CD($|\Delta\phi|$) for each of the four $A(|\Delta\phi|)$ distributions of Figure 6.8 (hard and soft triggered, high and low EA$_{\mathrm{BBC}}$) are plotted in the upper panel of Figure 6.9. Additionally, the CD($|\Delta\phi|$) values of two additional distributions are plotted: $A_6 \equiv A_1 - A_3$ (which is the "hard-trigger" $A(|\Delta\phi|)$ minus "soft-trigger" for EA$_{\mathrm{BBC}}^{\mathrm{High}}$ $A(|\Delta\phi|)$ from Figure 6.8) and $A_6 \equiv A_2 - A_4$ (which are the hard- minus soft-trigger, $A(|\Delta\phi|)$ distributions for EA$_{\mathrm{BBC}}^{\mathrm{Low}}$ events).

From the top panel of Figure 6.9, it is obvious that the soft-trigger ($E_{\mathrm{T}}^{\mathrm{trig}} \in [6, 8]\,\mathrm{GeV}$) data has a broadening in acoplanarity – the blue markers are higher earlier in the CD($|\Delta\phi|$) distribution. The CD($|\Delta\phi|$) from subtracting the blue from red $A(|\Delta\phi|)$ in Figure 6.8 yields the green star markers. The naive expectation is that this will remove the soft, isotropic, UE activity – which is what most wide-angle radiation should consist of. This effect is apparent in the top panel of Figure 6.9, where the softer-triggered CD($|\Delta\phi|$) distribution away from the recoil peak ($|\Delta\phi| < (6/8)\pi$) is higher by a factor of ~ 2 than the harder-triggered data (blue higher than red), and the EA$_{\mathrm{BBC}}^{\mathrm{High}}$ distributions are also consistently higher than the

---

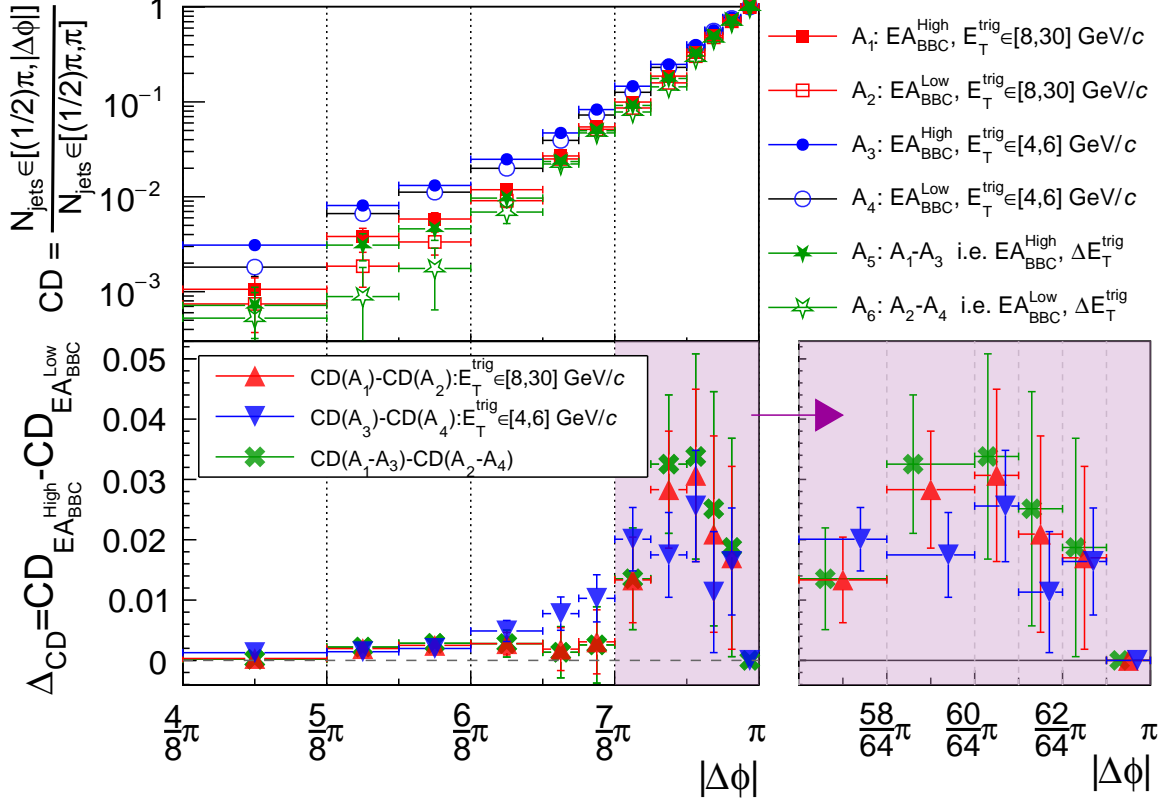13. As opposed to a jet that contains the trigger in its clustering

Figure 6.9: Top panel: Normalized cumulative distributions $(CD(|\Delta\phi|))$ of $A(|\Delta\phi|)$ (semi-inclusive distribution of raw, full jets, with $p_{\mathrm{T}} > 10\,\mathrm{GeV}/c$ normalized to "hard" and "soft" triggers) from Figure 6.8. The value of $CD(|\Delta\phi|)$ at any $|\Delta\phi|$ is the ratio of all jets in the range $[(1/2)\pi, |\Delta\phi|]$ relative to all jets azimuthally away from the trigger $(|\Delta\phi| \in [(1/2)\pi, \pi])$. (Therefore these values are 0 at $|\Delta\phi| = \pi/2$ and unity at $|\Delta\phi| = \pi$ by construction). The $CD(|\Delta\phi|)$ of the hard- minus soft- triggered distributions for both $\mathrm{EA}_{\mathrm{BBC}}^{\mathrm{High}}$ and $\mathrm{EA}_{\mathrm{BBC}}^{\mathrm{Low}}$ are also plotted (in full and open green stars. Bottom-left panel: The $CD(|\Delta\phi|)|_{\mathrm{EA}_{\mathrm{BBC}}^{\mathrm{High}}} - CD(|\Delta\phi|)|_{\mathrm{EA}_{\mathrm{BBC}}^{\mathrm{Low}}}$ for each pair of distributions in the upper panel. Bottom-right panel: blow-up box of bottom-left panel for $|\Delta\phi| \in [(7/8)\pi, \pi]$. The markers' horizontal offsets in each bin in the bottom-right panel are for visual convenience only.

$\mathrm{EA}_{\mathrm{BBC}}^{\mathrm{Low}}$ distributions for both hard and softer triggered events (full markers higher than open markers).

From the bottom panel of Figure 6.9, there is essentially no EA broadening past $|\Delta\phi| < (7/8)\pi$, while for the soft triggers the broadening extends out another eighth π to $|\Delta\phi| = (6/8)\pi$. There is, however, a maximum $\mathrm{EA}_{\mathrm{BBC}}$ broadening at about $|\Delta\phi| = (60/64)\pi$, which, when the soft triggered data is subtracted, actually slightly increases (the green star markers), but due to limited statistics, is hard to determine confidently. Noting that the jet

resolution parameter is $R = 0.4 \approx \pi/8$, then the broadening is within a single jet "radius" and the broadening peak is at about half a jet radius.

As discussed in Chapter 5, a correlation between EA_{BBC} (and EA_{TPC}) and the hardness of the trigger is expected to bias the semi-inclusive jet spectra S through generating softer jet spectra per trigger. An avenue to further study acoplanarity broadening is to differentiate in p_T^{jet} bins and see if the softer jets do have a correlating broader acoplanarity.[14]

_____

14. Although, it appears likely that such a search would be statistically limited given the current data size.

6.10   Dijet p_T Balance Measurement

The jet populations from these p+Au collisions can be probed for EA modification independently of EA-to-trigger correlations via the shape of the dijet p_T balance, A_J:

$$A_\mathrm{J} \equiv \frac{p_\mathrm{T}^\text{lead} - p_\mathrm{T}^\text{sub}}{p_\mathrm{T}^\text{lead} + p_\mathrm{T}^\text{sub}} \tag{6.3}$$

In which p_T^lead is the jet with the greatest p_T in the event, and p_T^sub is the jet with the greatest p_T recoiling from the leading jet, as defined in the criteria below. A maximum of one dijet per event is allowed. Dijets are selected according to the following criteria:

1. Leading jet: $p_\mathrm{T}^\text{lead} \geq 20\,\mathrm{GeV}/c$

2. Sub-leading jet: $p_\mathrm{T}^\text{sub} \geq 10\,\mathrm{GeV}/c$ and $|\phi_\text{lead} - \phi_\text{sub}| \geq (\pi - R)$, where R is the jet resolution parameter.[15]

3. Event trigger tower: $E_\mathrm{T}^\text{trig} \geq 4\,\mathrm{GeV}/c$.

The trigger requirement for the A_J events is softer than the requirements in the jet p_T spectra and acoplanarity measurements; the $20\,\mathrm{GeV}/c$ and $10\,\mathrm{GeV}/c$ lead and sub-leading jet requirements themselves ensure a hard scattering.[16]

The effects the E_T^trig required trigger value on A_J events collection is given in Figure 6.10. As shown, there are competing effects:

(a) Higher E_T^trig events are more likely on average to meet the A_J event requirements. This can be seen by the green stars in the 2$^\text{nd}$ panel of Figure 6.10: the ratio of events that meet the A_J requirements start at about 0.11% at $E_\mathrm{T}^\text{trig} = 4\,\mathrm{GeV}$, and rise to around 30% by $E_\mathrm{T}^\text{trig} = 20\,\mathrm{GeV}$.

(b) The E_T^trig spectra falls steeply

(c) The probability of finding a matching sub-leading jet in an event with a leading jet is

---

15. Incidentally, the value of R, 0.4, is within 0.01 rad of $\pi/8$; therefore, functionally the sub-leading jet's $|\Delta\phi|$ requirement is simply that is it in the "recoil-bin" used in the measurements of S, but where $|\Delta\phi|$ is measured with respect to the leading jet instead of a trigger.

16. Indeed, there is a trigger requirement at $4\,\mathrm{GeV}$ only to stay above the turn-on effects of the high tower trigger itself; refer to Figure 5.7.

constant around 40%.[17](This is seen from the constant ratio of star to square markers in the middle panel of Figure 6.10).

Effect (b) is much stronger than (a), as seen in the bottom panel of Figure 6.10: The softest trigger bin ($E_{\mathrm{T}}^{\mathrm{trig}} \in [4, 5]\,\mathrm{GeV}$) already contains 30% of all available dijet events with triggers above $4\,\mathrm{GeV}$. The running percentage is 73% at $E_{\mathrm{T}}^{\mathrm{trig}} = 8\,\mathrm{GeV}$ which is the percentage of dijets which would have been omitted if the same $8\,\mathrm{GeV}$ trigger value from the S measurement had been used.
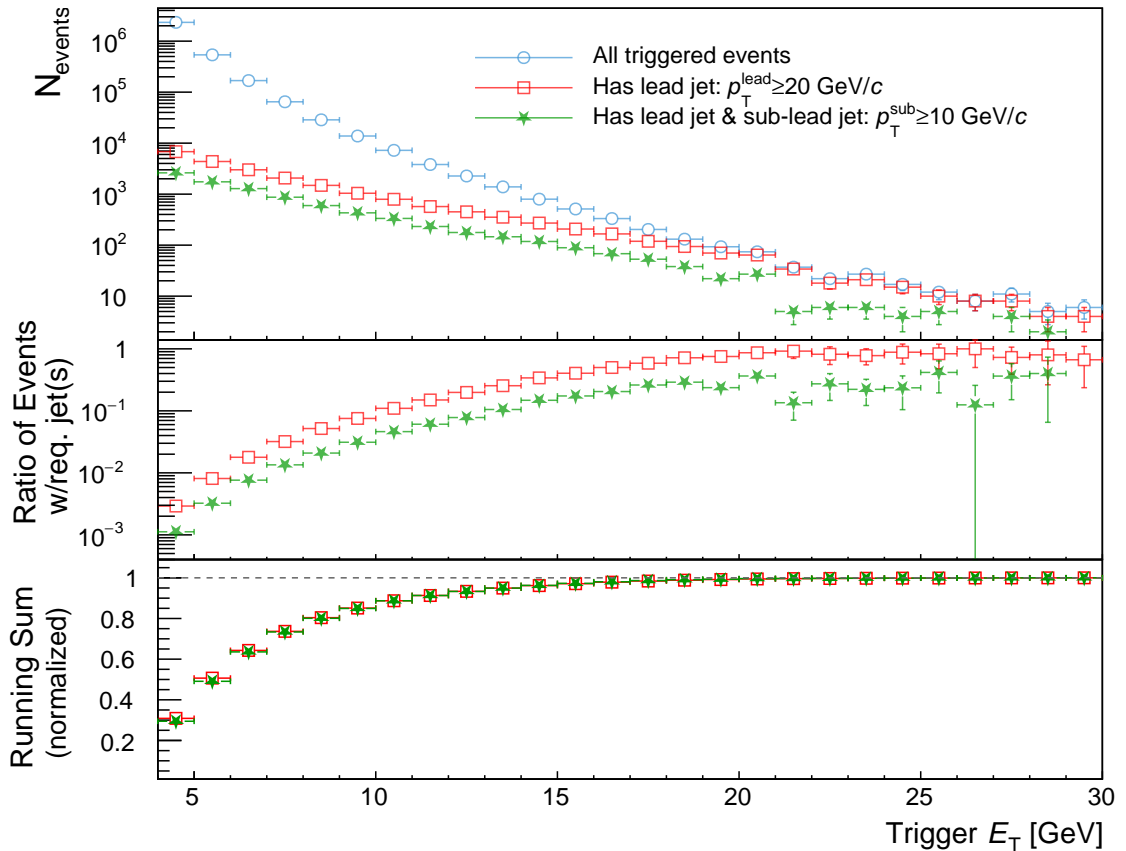
Figure 6.10: Top panel: Number of events at each $E_{\mathrm{T}}^{\mathrm{trig}}$ threshold, number of those events which also have a full "leading" jet with $p_{\mathrm{T}} \geq 20\,\mathrm{GeV}$, and number of the events with a leading jet which also have a $10\,\mathrm{GeV}$ "matching" recoil jet (such that $|\phi_{\mathrm{jet}}^{\mathrm{leading}} - \phi_{\mathrm{jet}}^{\mathrm{matching}}| > \pi - 0.4$) with $p_{\mathrm{T}} \geq 10\,\mathrm{GeV}$. Middle panel: Ratio of triggered events with leading, and leading & matching jets. Bottom panel: Ratio of all events accumulated by $E_{\mathrm{T}}^{\mathrm{trig}}$, out of all possible events from $4\,\mathrm{GeV}$ to $30\,\mathrm{GeV}$.

The normalized distribution of A_{J} for high and low EA (using both $\mathrm{EA_{BBC}}$ and $\mathrm{EA_{TPC}}$)

---

17. Otherwise the sub-leading jet is most likely lost due to the dijet η swing, as discussed in Section 6.2.

is plotted in Figure 6.11, along with the corresponding ratios. The values are raw (not corrected for detector effects); however, there is very little background, and the JES and JER do not depend appreciably on EA, such that the ratio should be only minimally affected. The ratios of the A_{J} distribution shapes are consistent with unity, which is to say, no jet-by-jet modification is observed in this measurement within current uncertainties.
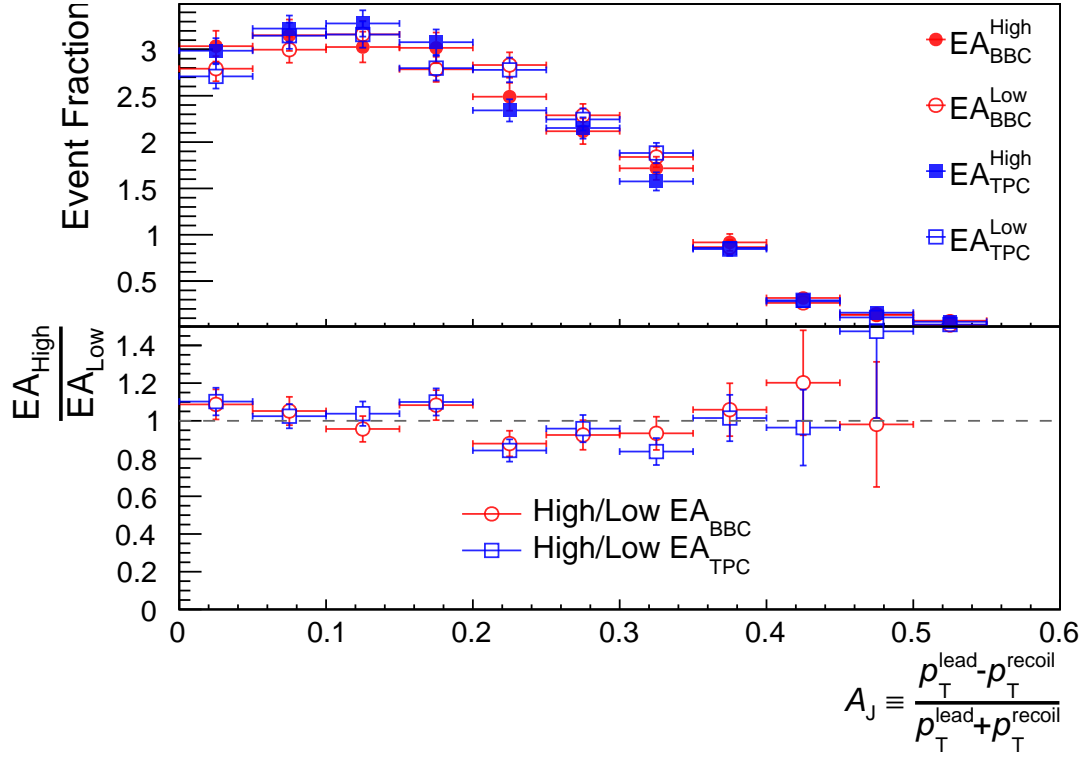

Figure 6.11: Top panel: dijet balance (A_{J}) binned both by high and low $\mathrm{EA}_{\mathrm{BBC}}$ and $\mathrm{EA}_{\mathrm{TPC}}$. Within statistical uncertainties, both definitions of EA yield the same results. Bottom panel: Ratios of A_{J} binned by high and low EAs. No EA-dependence is observed.

Chapter 7

Summary and Conclusion

7.1 Summary

In the last few years, the position of small system collision studies within experimental and theoretical high energy physics has evolved dramatically. Within the context of probing the QGP in A+A collisions via jets, a relatively simple paradigm using the optical limit in the Glauber model, with $\langle N_{\text{part}} \rangle$ EA scaling and $\langle N_{\text{coll}} \rangle$ jet scaling, was a powerful method to sort out QGP signatures from the complex signals that are A+A collision measurements. However, application of the same methodology to p/d+A collisions through inclusive measurements at ATLAS [34] and PHENIX [72], and then subsequent semi-inclusive measurements by ALICE [75, 76] presented surprising results, which motivated, and contextualized, the results presented in this thesis.

To leading order in p+A collisions, jets may be associated with the Bjorken-x of the hard scattered parton in the proton as $x_{\text{p}} \approx 2E_{\text{jet}}/\sqrt{s}$ [123]. These studies reveal that x_{p} of the jets is a useful metric in comparing results at different energy scales. This separates the ALICE measurements, whose maximum recorded charged jet p_{T} values are at a little under $x_{\text{p}} \approx 0.1$; from ATLAS which reaches values on the order of $x_{\text{p}} \sim 0.4$, and RHIC measurements at PHENIX and STAR at $x_{\text{p}} \sim 0.5$.

In small system collisions, the previous results indicate:

1. In the measurements of high x_p jets, when not binned by EA, the overall jet production is consistent with Glauber scaled pp values.

2. At high x_p, jet spectra EA dependence appears to scale monotonically with increasing jet x_p [34].

3. At low x_p values, the measured semi-inclusive and inclusive jet spectra has had no measurable EA dependence [75, 76].

4. If the low x_p jet quenching limit (from ALICE) is extended to the high x_p range, and jet quenching is assumed to be the cause of the modification, then a tension with the ATLAS results is observed [75].

The STAR results presented in this thesis are the first semi-inclusive, small system jet results, at RHIC kinematics (and therefore, also at high x_p). They show a significant suppression of the semi-inclusive jet p_T spectra, S binned by high-EA events relative to S binned by low-EA events. It is demonstrated that this EA dependence does not result from a trivial autocorrelation in which the jet activity itself (or lack of it) directly influences the EA measurements. Rather, it is shown that at high x_p values, there is a very definite correlation between EA and E_T^{trig}, and therefore presumably x_p. This complicates the question of asking about jet modification via EA itself, but also indicates that this is a good opportunity to use these $p+$A collisions to better probe the initial stages of the collision itself. This may be done through looking for the mechanism that (anti)correlates EA with x_p. Some possibilities are:

- Perhaps the x_p-to-EA correlation is a result of fluctuating proton configurations. Such initial state fluctuations are already of interest to potentially explain collective motion signals in small systems (see Figure 1.18, also [124]). They may also explain the EA to jet-x_p dependence. If the presence of a high-x_p parton reduces the proton cross section, such as by decreasing the average number of other partons available for interactions, then the $\langle N_{\mathrm{part}} \rangle$ in $p+$A collisions would decrease in correlation with the

presence of higher x_p partons [125]. EA scales with the softer $\langle N_\mathrm{part} \rangle$, and thereby be anti-correlated with the x_p scale of jet production.

- Perhaps it is a result energy conservation constraints on the successive collisions of the high-x_p proton with the nucleons in the heavy ion. How does the energy depletion affect the wave function and how is that communicated? Is there perhaps a kind of color-force transparency with results similar to a shrinking proton [126]?

Because the EA-to-$E_\mathrm{T}^\mathrm{trig}$ anticorrelation is observed, then high-to-low EA S suppression is expected and, as reported in this thesis, is observed. The degree of suppression on the azimuthal side of the event recoiling from the trigger appears to scale monotonically with p_T and therefore x_p.[1]

Studies of the relationship between $p_\mathrm{T}^\mathrm{jet}$ range, $E_\mathrm{T}^\mathrm{trig}$ range, and EA induced semi-inclusive spectra suppression have also been presented. The naive picture that $E_\mathrm{T}^\mathrm{trig} \in [E_\mathrm{T}^\mathrm{LB}, E_\mathrm{T}^\mathrm{UB}]$ should monotonically result in more suppression of hard jets with a fixed E_T^LB and increasing E_T^LB is not observed.[2] The argument was that the suppression should occur because the EA-correlation is strongest with higher x_p triggers toward E_T^UB, but the spectra are normalized by the dominant number of softer triggers from events toward E_T^LB. The discrepancy is likely due to the steeply falling spectrum of the triggers, such that even soft-triggers produce a dominant number of the higher x_p jets, thereby minimizing the $E_\mathrm{T}^\mathrm{trig}$ range's effect. This effect could be better probed by replacing the trigger towers with full jets whose clustering includes the trigger towers; this would remove some of the smearing between trigger and jet spectra.[3]

The results have also been used to check for semi-inclusive acoplanarity broadening. The study reveals a slight broadening within about 0.4 radians, peaking at about 0.2 radians. The S spectra dependency on EA is expected as a direct result of the EA-to-trigger cor-

---

1. Note that the conversion between $p_\mathrm{T}^\mathrm{jet}$ and $E_\mathrm{T}^\mathrm{jet}$ for the jets in this thesis is approximately linear. The maximum correction factor at the boundary of the jet rapidity acceptance $\eta_\mathrm{jet} = \pm 0.6$ is ~ 1.19.

2. Specifically, see Figures 5.13, 5.14, 5.15.

3. See Figure 6.10 for an indication of the degree of this smearing.

relation because of the per-trigger normalization. The acoplanarity result is a jet shape distribution with no such direct dependency on per-trigger normalization. As such, the expected relationship to the EA-trigger bias is not clear and this result is a promising venue for further study. While these measurements are not corrected for detector efficiency, there is very little background, particularly for jets with $p_\mathrm{T} > 10\,\mathrm{GeV}/c$, and the JES and JER are relatively independent of EA. As such, results in ratio to EA are not anticipated to change.

Finally, the dijet p_T balance is reported at high and low EA (as measured by both the BBC and TPC). The measurements are normalized per dijet, and are thereby not influenced by any per-trigger normalization bias from the EA-to-x_p correlation. The results see no EA-dependency on the dijet balance. They indicate the EA-modification of the S spectra does not result from jet quenching, but instead results from correlations formed prior to jet formation. This interpretation is reinforced by recent STAR measurements of the p+Au jet mass distribution, conducted concurrently with this research, as shown in Figure 7.1. There, jet mass is defined as $M \equiv |\Sigma_{i\in\mathrm{jet}}p_i| = \sqrt{E^2 - \mathbf{p}^2}$ where $\mathbf{p}$ is the three momentum of the jet [127] and is sensitive to jet substructure evolution and possible interaction with a QGP. As seen, there is no EA dependence on the M distribution. As in the case with the acoplanarity measurements, the A_J results are not corrected for detector effects; however, the same arguments for these jets at $10\,\mathrm{GeV}/c$ and $20\,\mathrm{GeV}/c$ apply as for the acoplanarity measurement. Therefore, the EA ratios of the results are not anticipated to change.

7.2   Conclusion and Outlook

These measurements at STAR show that EA-to-trigger correlations result in significant EA correlation in per-trigger normalized jet p_T spectra. Per-dijet normalized observables, such as the dijet p_T balance reported in this thesis, and the jet mass distribution concurrently measured at STAR and recently reported, show no EA dependence. This suggests that the EA-to-trigger correlation is fully responsible for the EA dependency of the jet spectra, and that there is no quenching of jet p_T by a QGP in p+Au collisions after jet formation. The small but observable broadening of the azimuthal distribution of jets away from the triggers

115
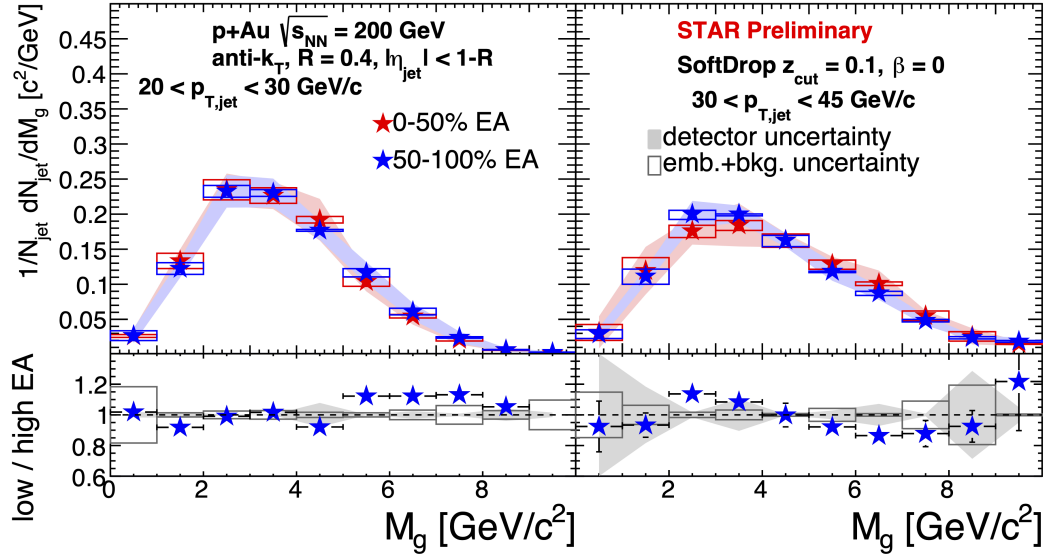
Figure 7.1: Jet mass distribution based on jet substructure. [128]

in high-EA events cannot be trivially explained in terms of the EA-to-trigger correlation, could possibly result from jet-medium interactions which are too weak to quench jet p_{T}, remain an intriguing result that is not fully understood, and worthy of further investigation.

For reasons reported in this thesis, it is an exciting time to be studying jets in small systems in high energy physics. The field's understanding of initial collisions in these systems is evolving quickly, and jets are a central feature of that field. As shown in this thesis, while phase space constraints of EA to x_{p} correlations cannot be ignored when interpreting small system jet p_{T} spectra, these correlations themselves offer a window to probe the initial stages of an event.

Within the precision of the A_{J} and S measurements (and supported by concurrent jet mass distribution results), jet quenching is not observed in p+Au collisions at RHIC kinematics. The outlook to further advance the field with this data lies primarily in what constraints the measured jet/trigger-x_{p} to EA correlations may apply to the initial stages of collisions. There is concurrent work at STAR looking at the long-range rapidity correlation of the activity within the $\mathrm{EA_{TPC}}$ to the rapidity of the triggers and jets, which will likely add an-

other dimension to the observables. An important next step to actually motivate, constrain, or eliminate the physics cause(s) is to compare the performance of simulations with the encoded physics relative to these results. Such encoded physics may include those touched on in this thesis, including simple phase space constraints from energy conservation,[4] a fluctuating proton through x_{p} state configuration, possibly other cold nuclear matter effect(s), or even a more detailed cause from an IP Glasma simulation.

---

4. Even here, there is some room for variation in the application of how that conservation across multiple p to Au-nucleon scatterings is communicated.

Appendix A

Supporting Material and Figures

A.1   Run QA Figures: $\langle X \rangle_{\mathrm{run}}$

This sections shows the plots of 16 run averaged parameters X, listed in Table 4.1, which were used to identify runs as outliers to exclude from the analysis. Each parameter used is explained in Section 4.1, which also lists how many runs and events where eliminated with each cut.
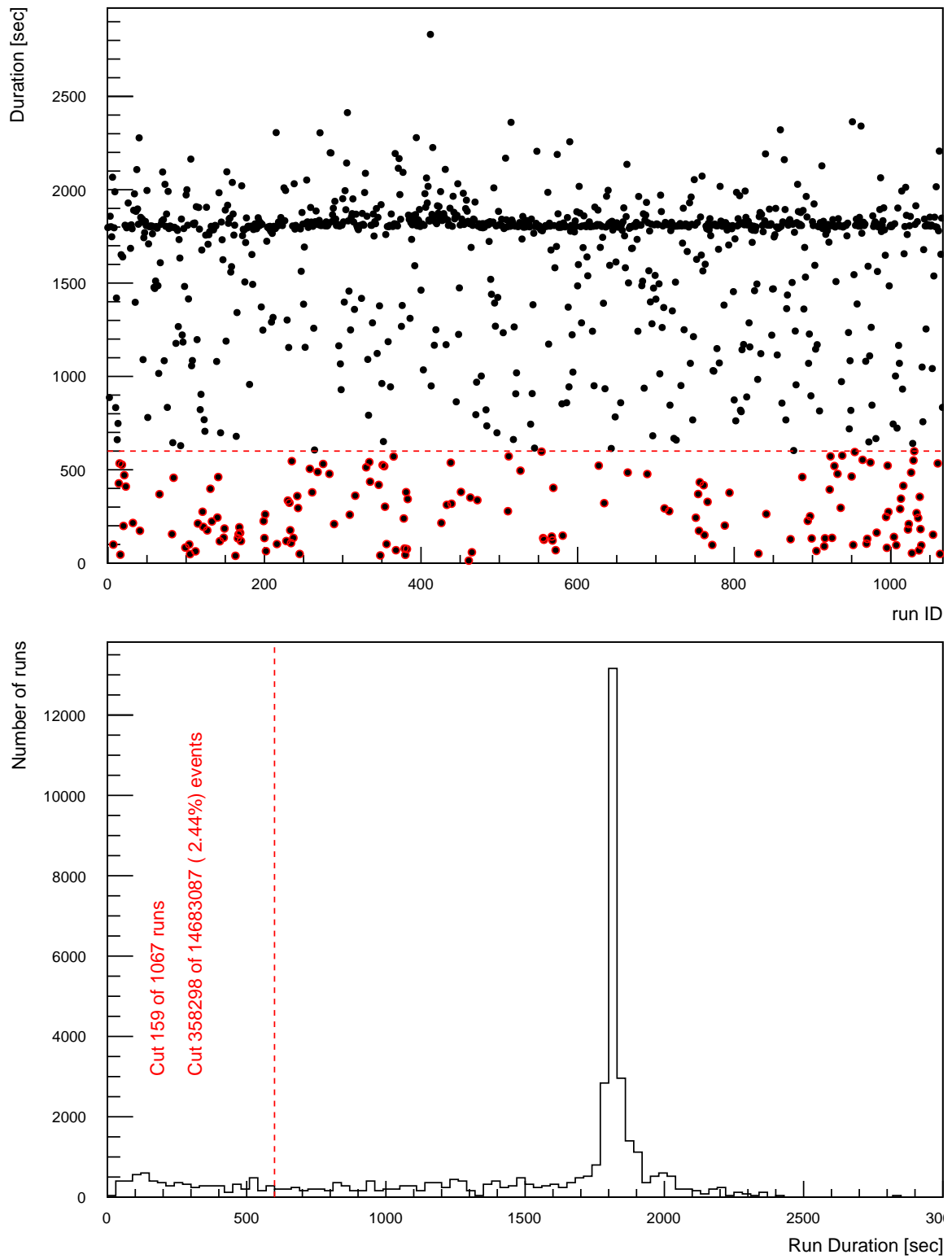
Figure A.1: Duration of each run (top), and distribution of run durations (bottom). Runs with less than 10 minutes cut (red dotted line). Runs circled in red (in top figure) are cut.
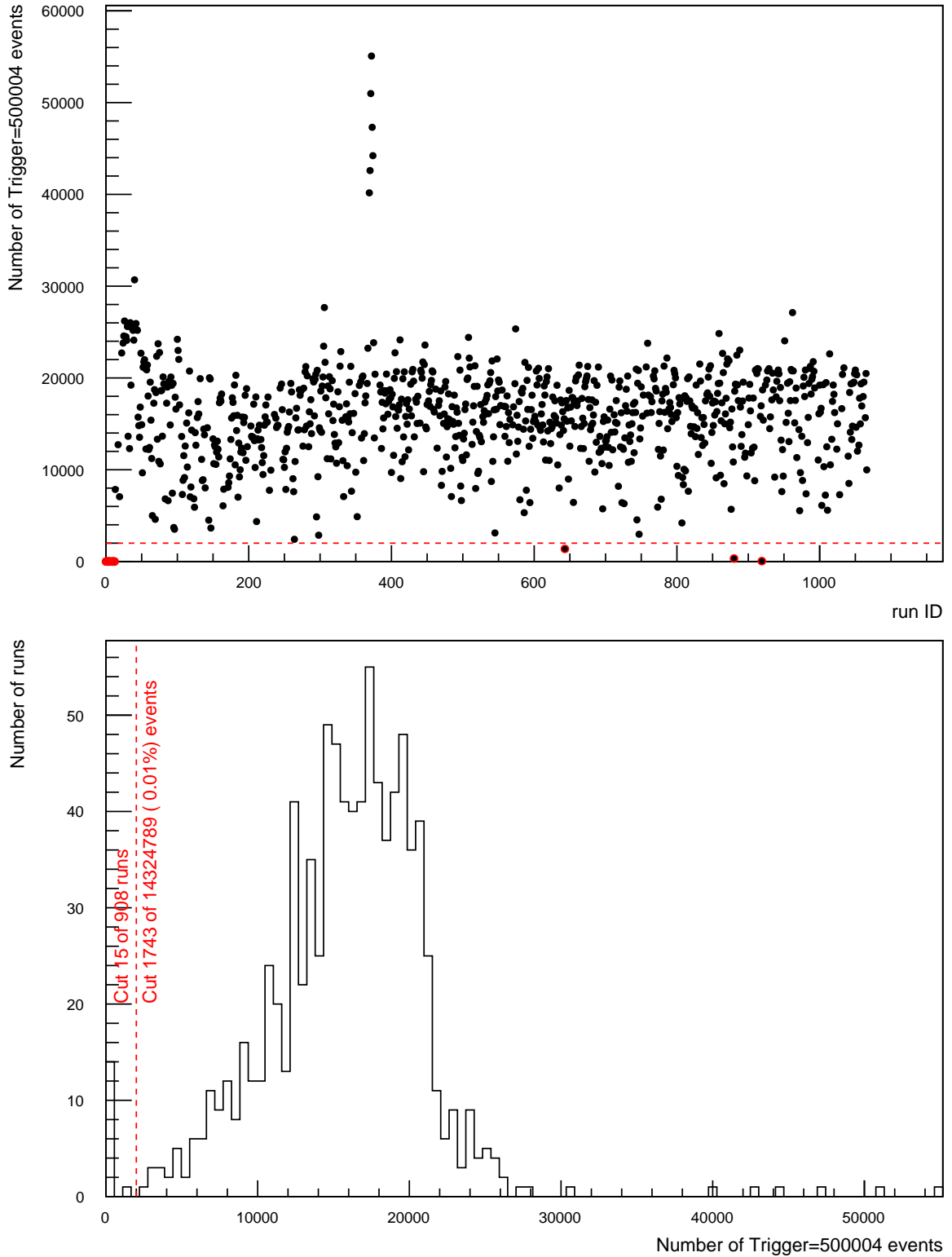
Figure A.2: Number of Minimum Bias events in each run (top) and distribution of run event numbers (bottom). Runs with less than 2000 events cut (red dotted line). Runs circled in red (in top figure) are cut.
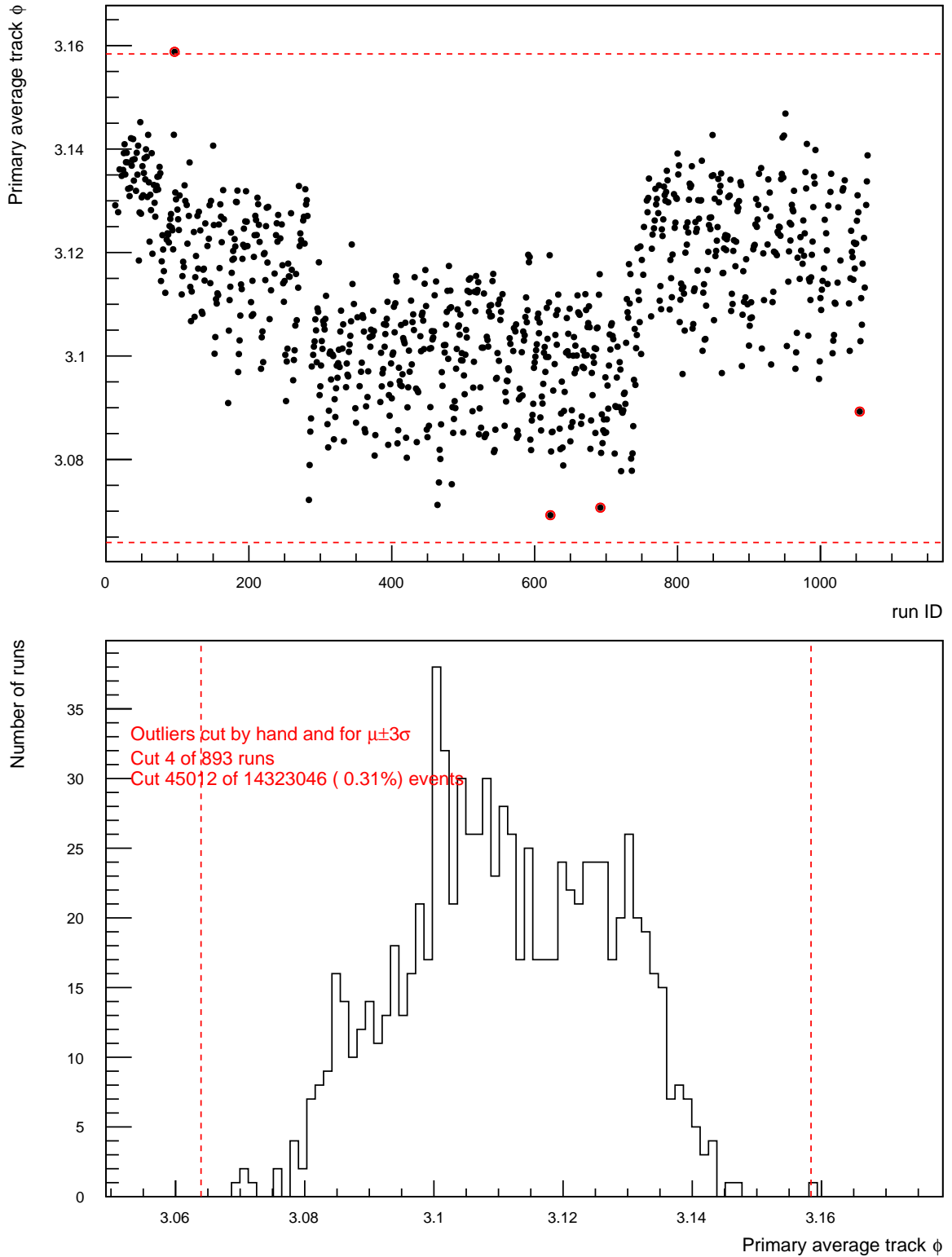
Figure A.3: Event averaged ϕ_{tracks} per run (top), and distribution of averages (bottom). Outliers cuts at $\pm 3\sigma$ of distribution (red dotted lines) and by hand. Runs circled in red (in top figure) are cut.
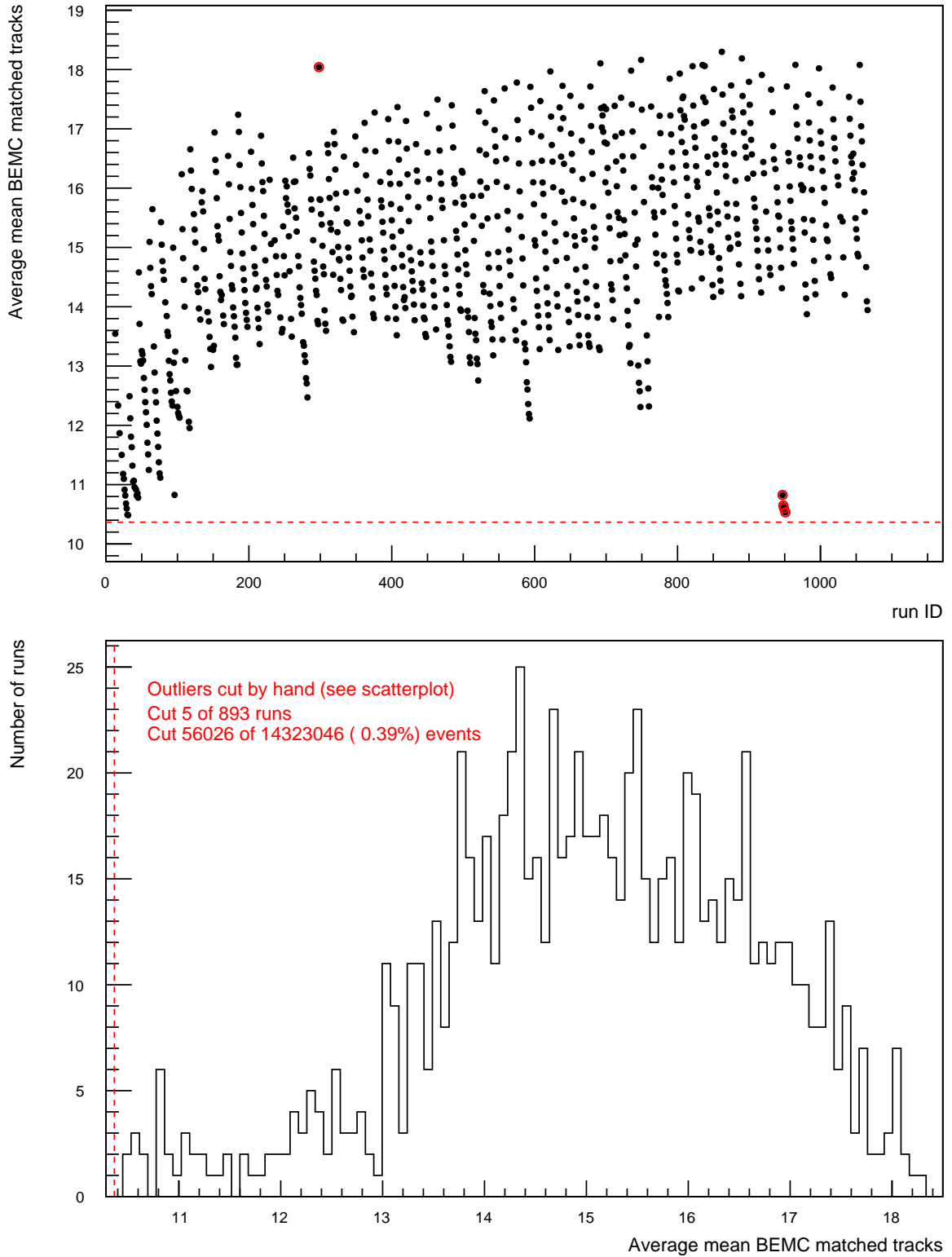
121
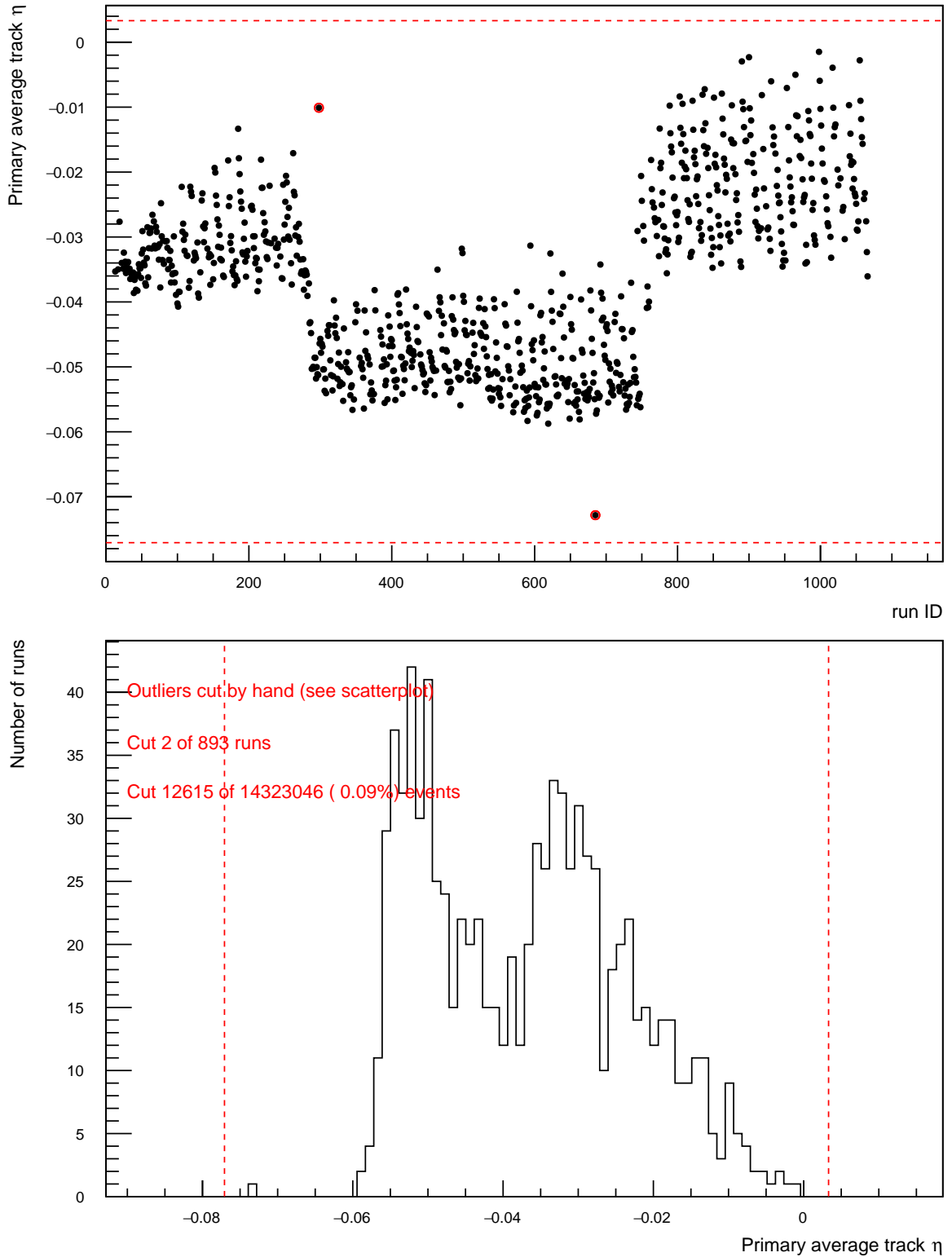
Figure A.4: Event averaged η_{tracks} per run (top), and distribution of run averages (bottom). Outliers cuts at $\pm 3\sigma$ of distribution (red dotted lines) and by hand. Runs circled in red (in top figure) are cut.
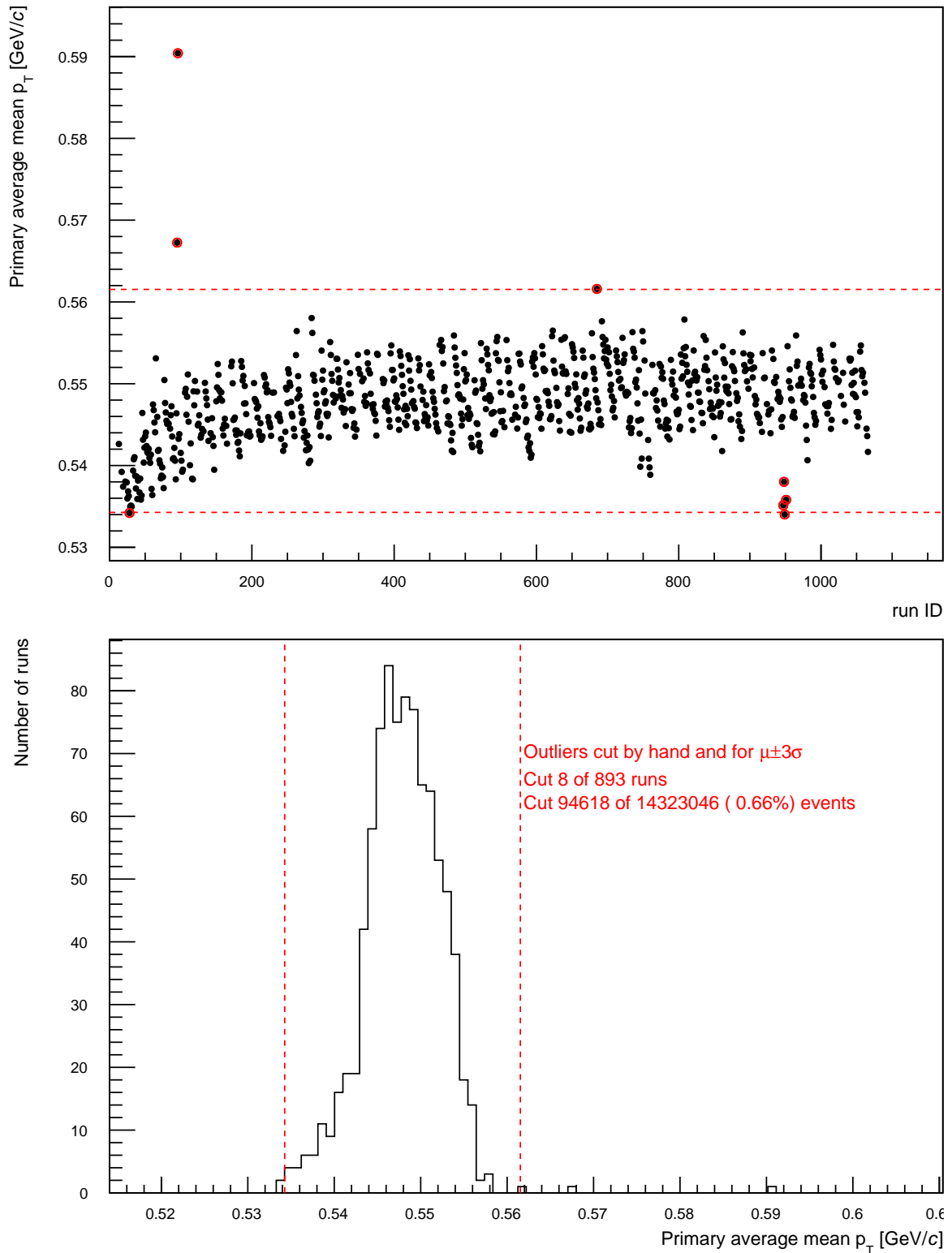
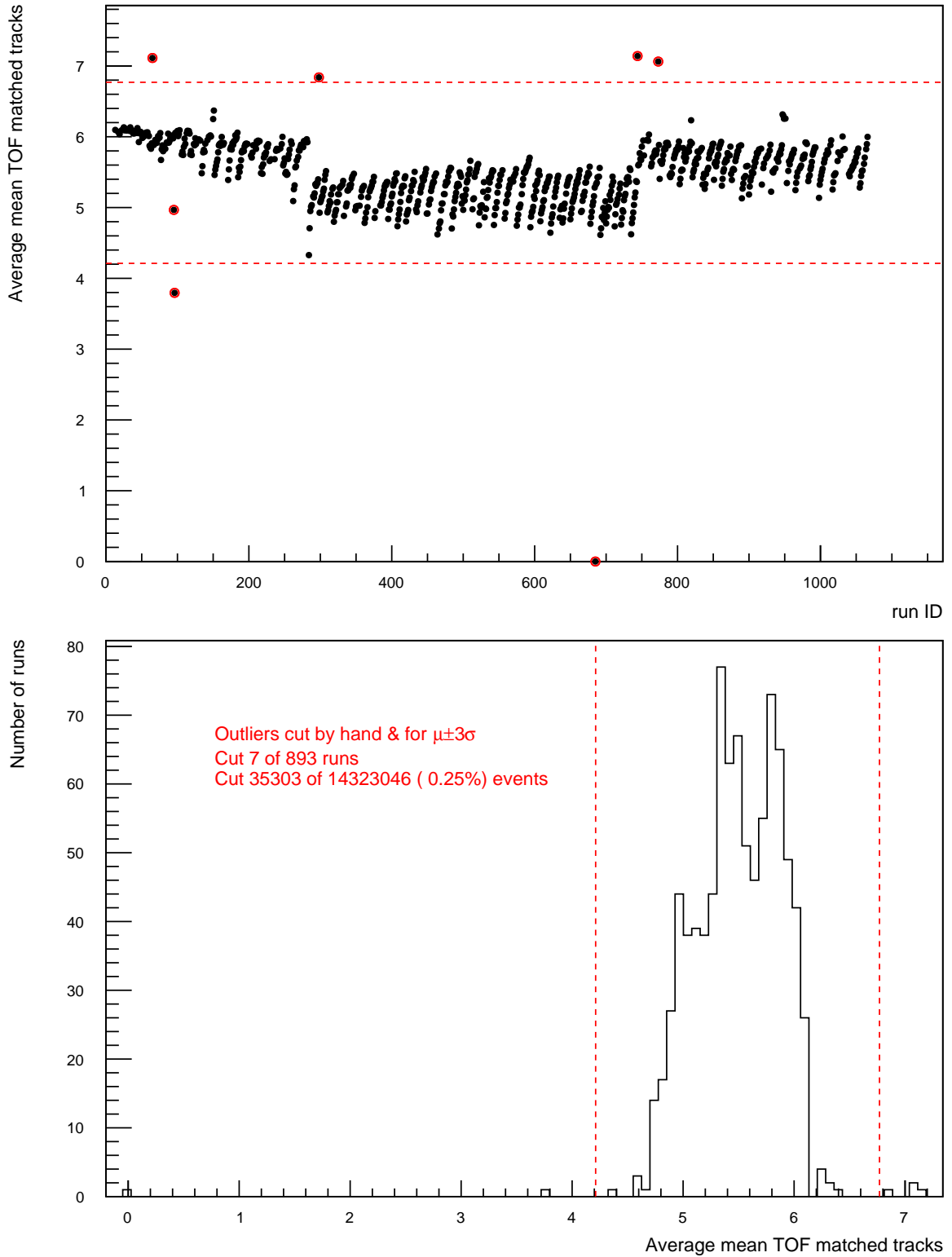Figure A.5: Event averaged $\langle p_{\mathrm{T,tracks}} \rangle$ per run (top), and distribution of run averages (bottom). Outliers cuts at $\pm 3\sigma$ of distribution (red dotted lines) and by hand. Runs circled in red (in top figure) are cut.
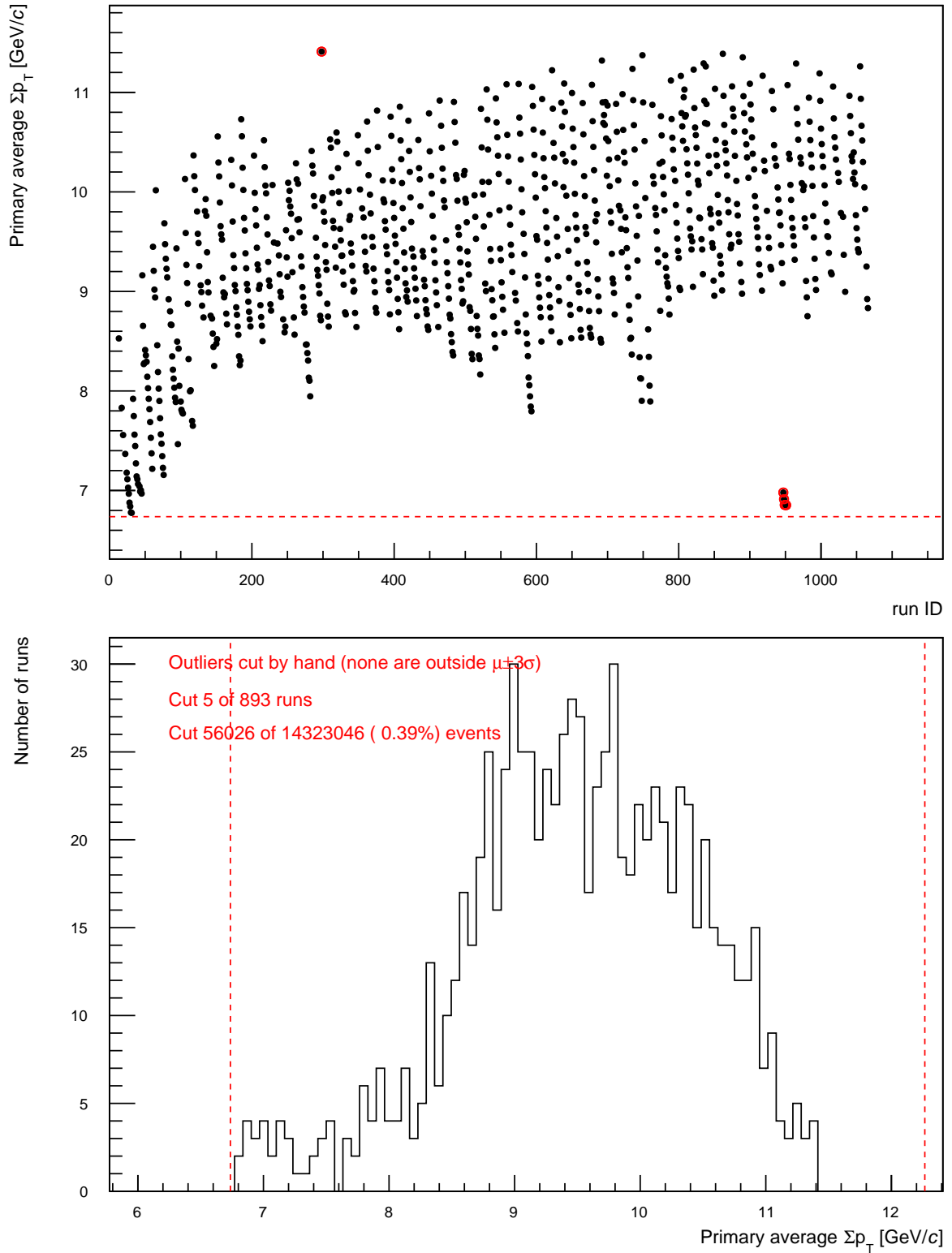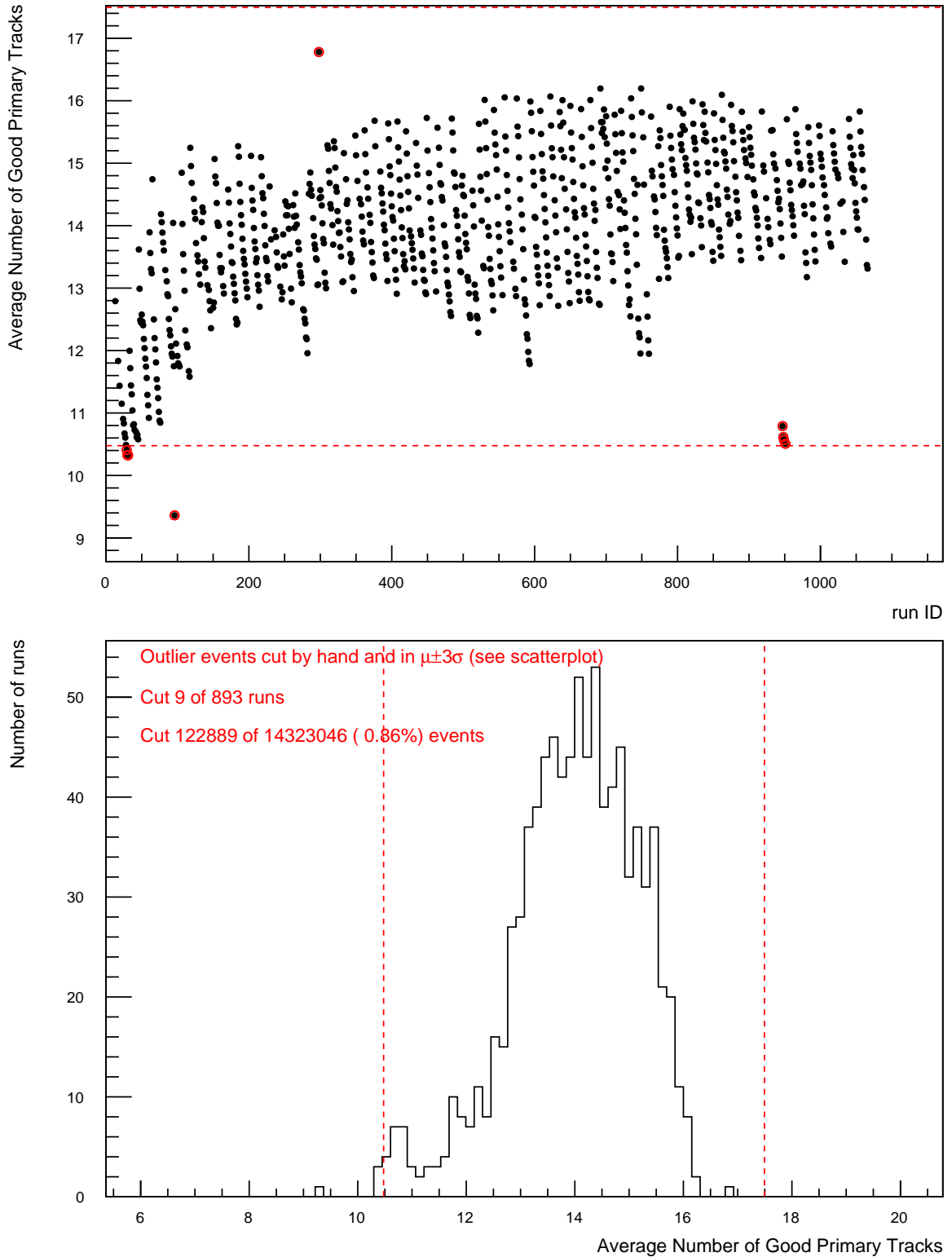
Figure A.6: Event averged $\Sigma p_{\mathrm{T,tracks}}$ per run (top), and distribution of run averages (bottom). Outliers cuts at $\pm 3\sigma$ of distribution (red dotted lines) and by hand. Runs circled in red (in top figure) are cut.
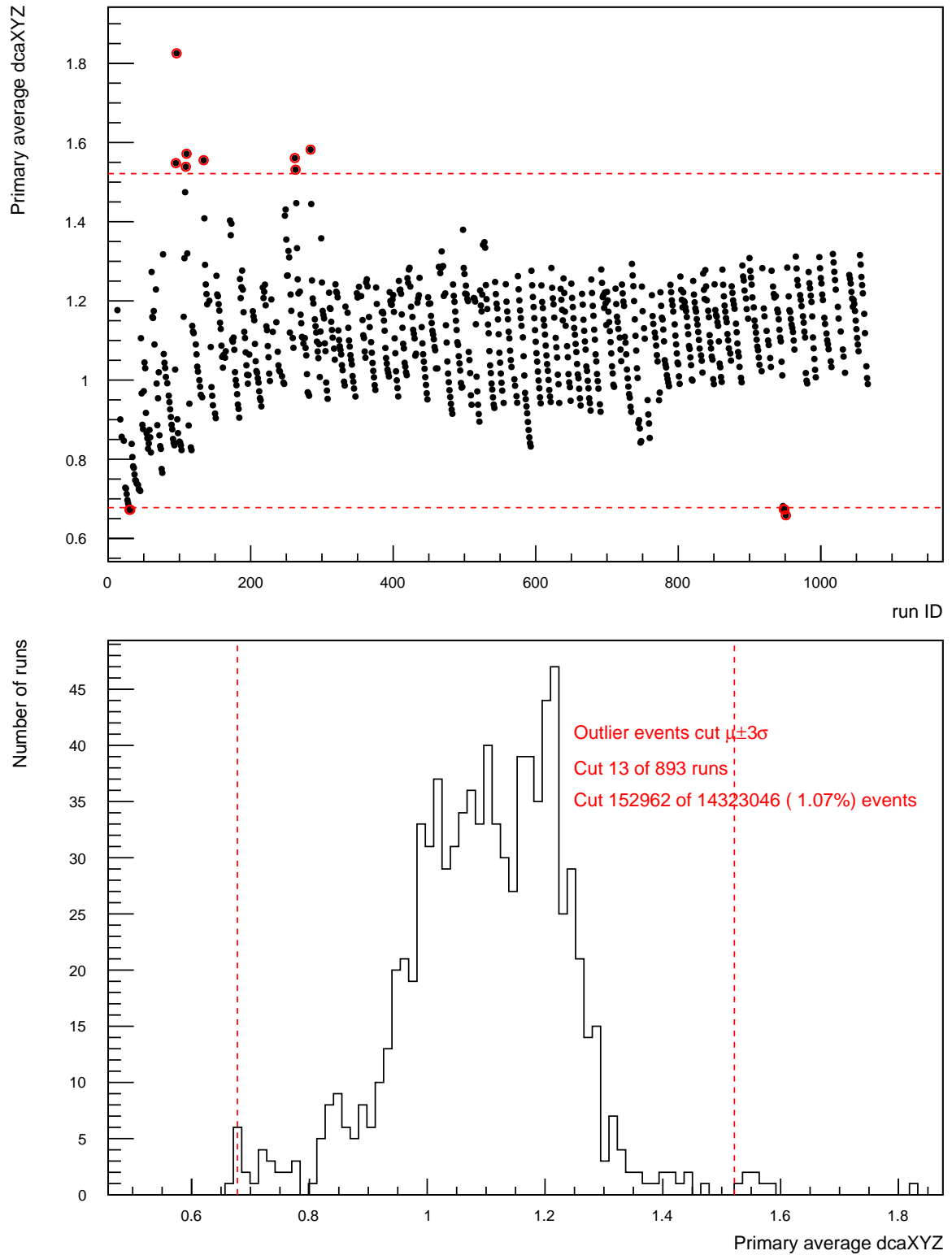
Figure A.7: Event averged DCA_{3D} per run (top), and distribution of run averages (bottom). Outliers cuts at $\pm 3\sigma$ of distribution (red dotted lines) and by hand. Runs circled in red (in top figure) are cut.
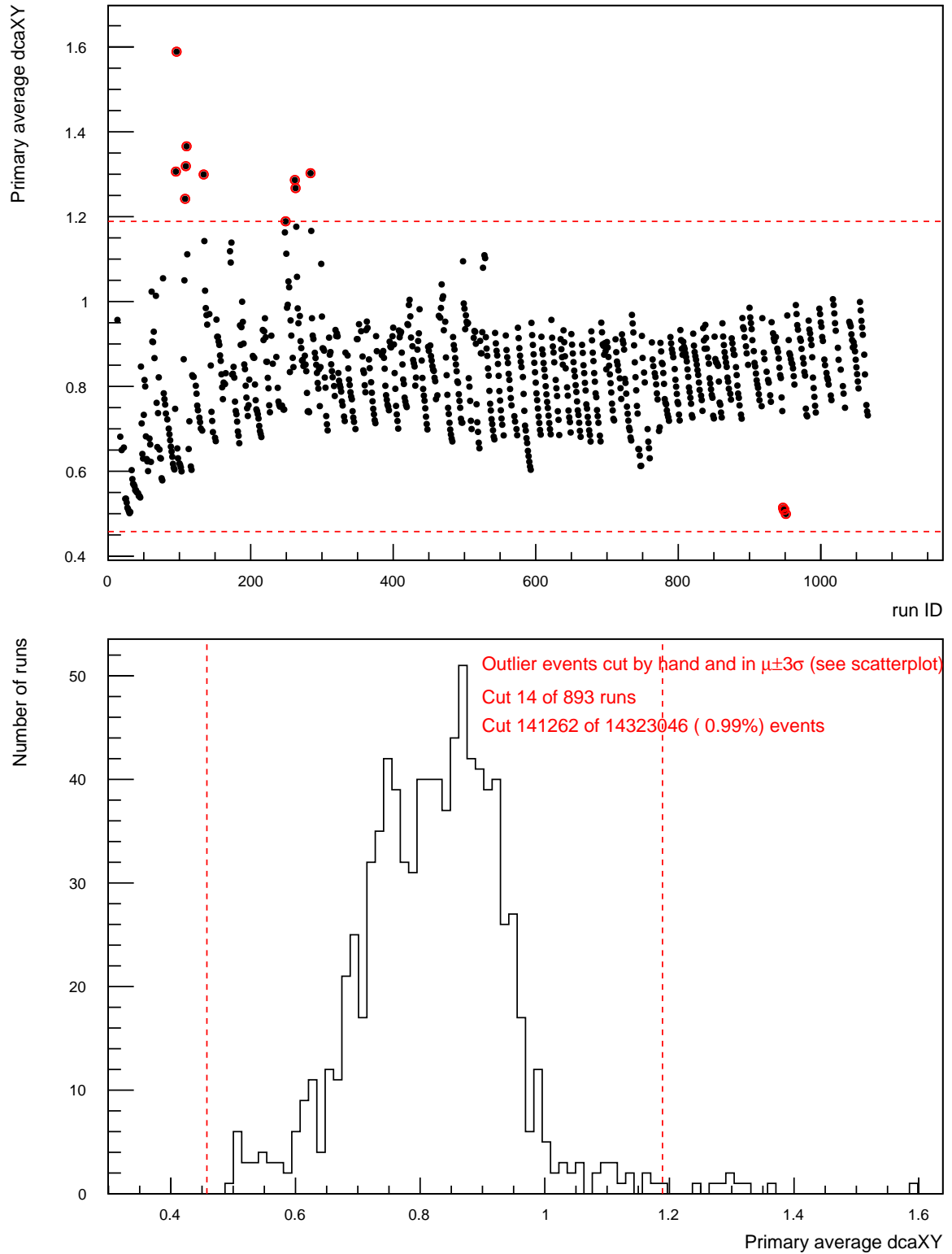
Figure A.8: Event averged DCA_{2D} per run (top), and distribution of run averages (bottom). Outliers cuts at $\pm 3\sigma$ of distribution (red dotted lines) and by hand. Runs circled in red (in top figure) are cut.
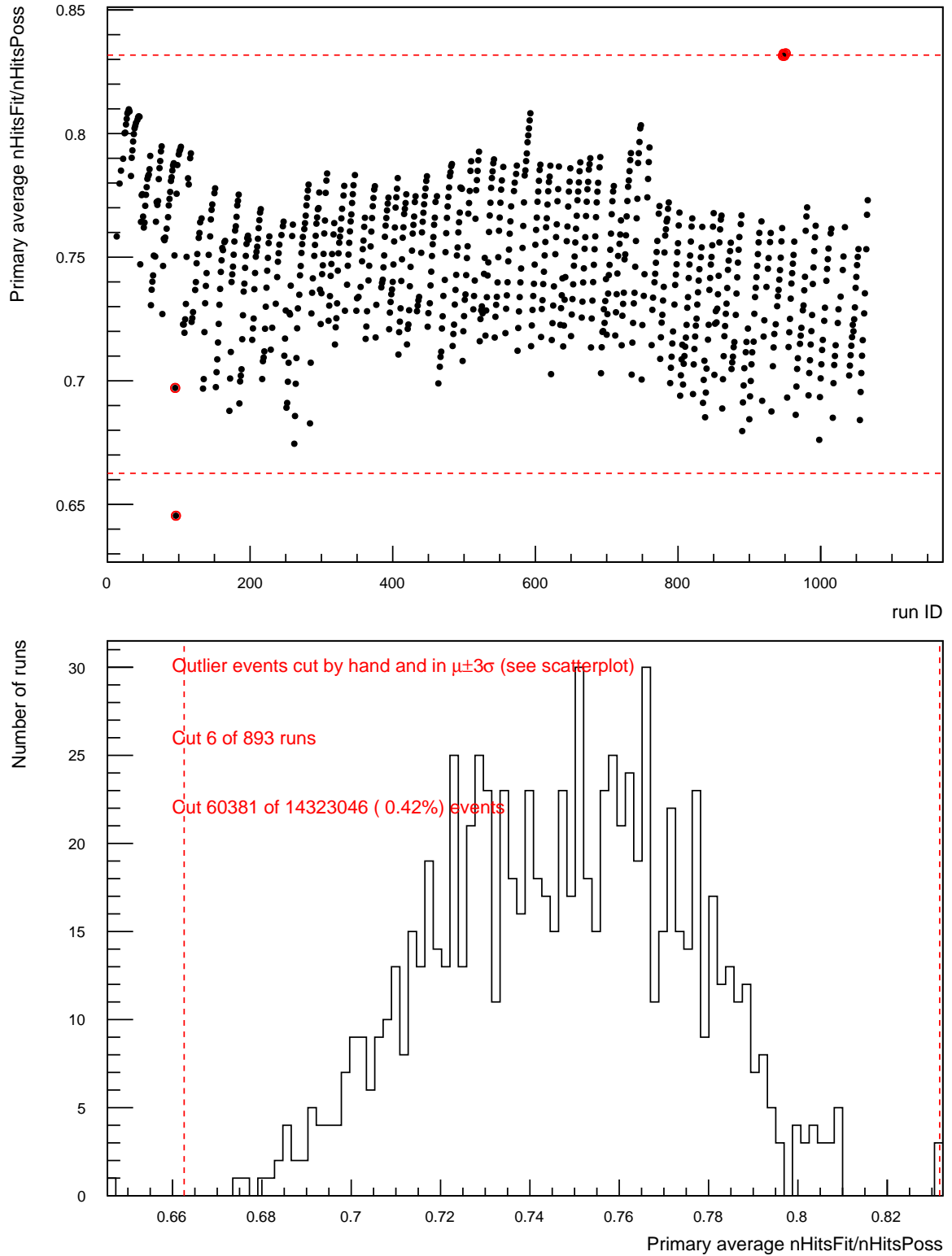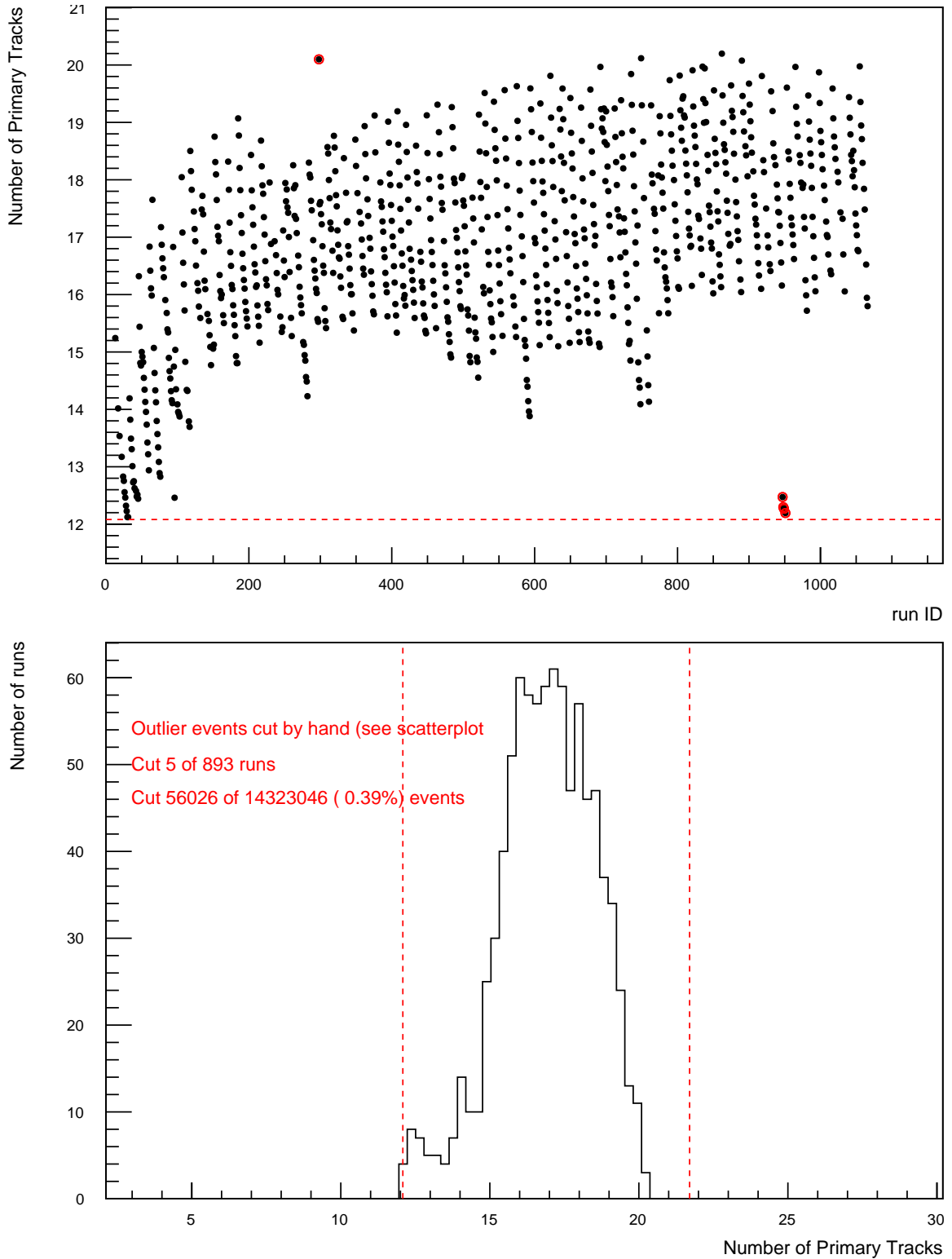
Figure A.9: Event averged N_{hits}/N_{poss} for primary tracks per run (top), and distribution of run averages (bottom). Outliers cuts at $\pm 3\sigma$ of distribution (red dotted lines) and by hand. Runs circled in red (in top figure) are cut.

127

Figure A.10: Event averged $\mathrm{N}_{\mathrm{tracks}}^{\mathrm{BEMC}}$ (primary tracks matched to hits in the BEMC) per run (top), and distribution of averages (bottom). Outliers cuts at $\pm 3\sigma$ of distribution (red dotted lines) and by hand. Runs circled in red (in top figure) are cut.
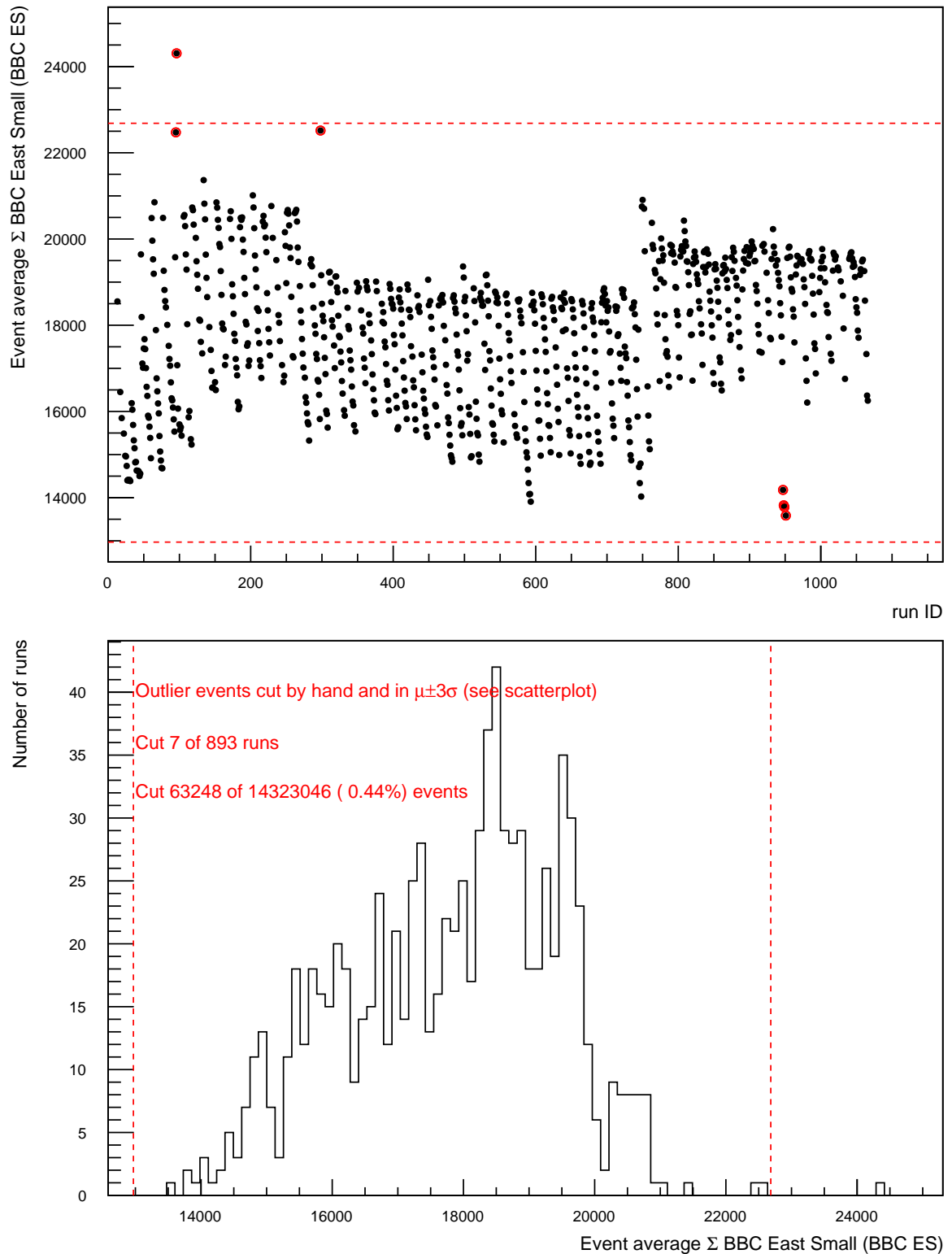
Figure A.11: Event averged N_{tracks}^{TOF} (primary tracks matched to hits in the TOF) per run (top), and distribution of averages (bottom). Outliers cuts at $\pm3\sigma$ of distribution (red dotted lines) and by hand. Runs circled in red (in top figure) are cut.

Figure A.12: Event averged $N_{\text{tracks,good}}^{\text{primary}}$ (number of primary tracks that pass cuts: $p_{\text{T}} \in [0.2, 30]\,\text{GeV}/c$, $|\eta| < 1$, at least 15 total and 52% of possible hits in TPC) per run (top), and distribution of averages (bottom). Outliers cuts at $\pm 3\sigma$ of distribution (red dotted lines) and by hand. Runs circled in red (in top figure) are cut.

Figure A.13: Event averged $N_{tracks}^{primary}$ (note: at this point in the STAR's data pipeline, there are already some cuts to the tracks applied, but not the ones listed in Figure A.12) per run (top), and distribution of averages (bottom). Outliers cuts at $\pm 3\sigma$ of distribution (red dotted lines) and by hand. Runs circled in red (in top figure) are cut.

Figure A.14: Event averged $\Sigma\text{BBC}_{\text{EastSmall}}$ (sum of inner tile signal in the BBC, see Section 3.2.4) per run (top), and distribution of averages (bottom). Outliers cuts at $\pm3\sigma$ of distribution (red dotted lines) and by hand. Runs circled in red (in top figure) are cut.

132
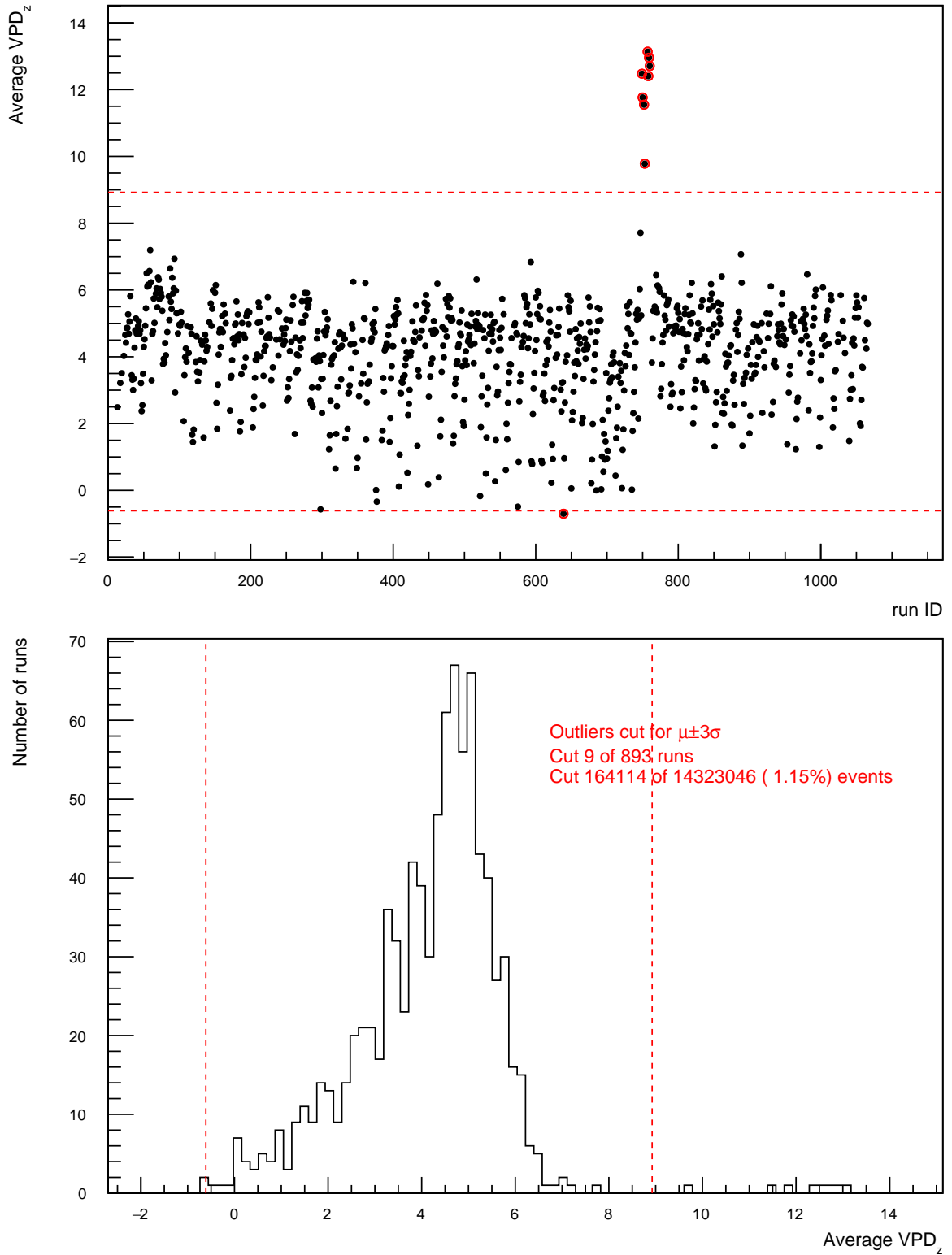
Figure A.15: Event averged $V_{z,\text{VPD}}$ (the Z-vertex distribution from the VPD, see Section 3.2.6) per run (top), and distribution of averages (bottom). Outliers cuts at $\pm 3\sigma$ of distribution (red dotted lines) and by hand. Runs circled in red (in top figure) are cut.

133
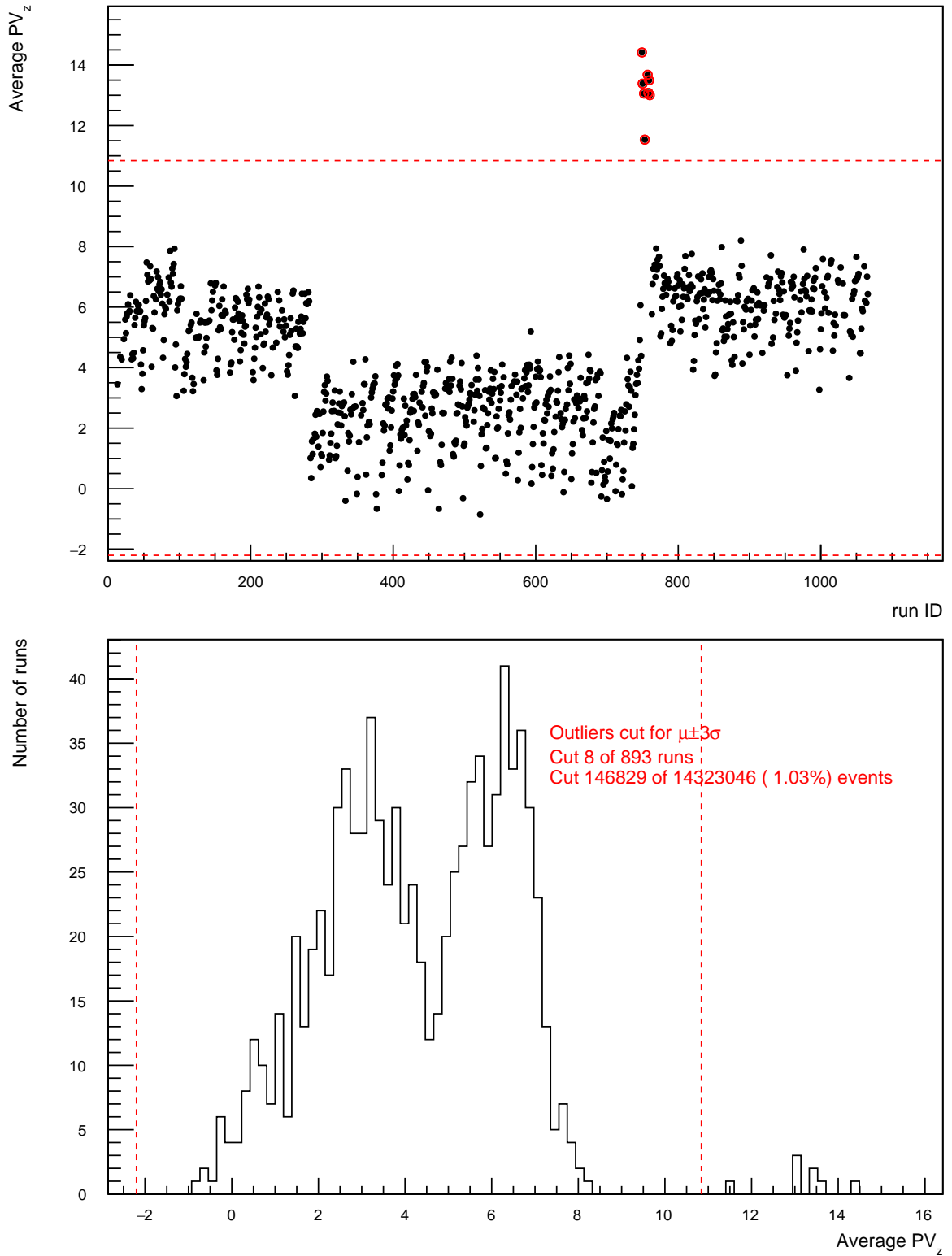
Figure A.16: Event averged $V_{z,\mathrm{TPC}}$ (the Z-vertex distribution from reconstructed tracks in the TPC, see Section 3.2.1) per run (top), and distribution of averages (bottom). Outliers cuts at $\pm 3\sigma$ of distribution (red dotted lines) and by hand. Runs circled in red (in top figure) are cut.
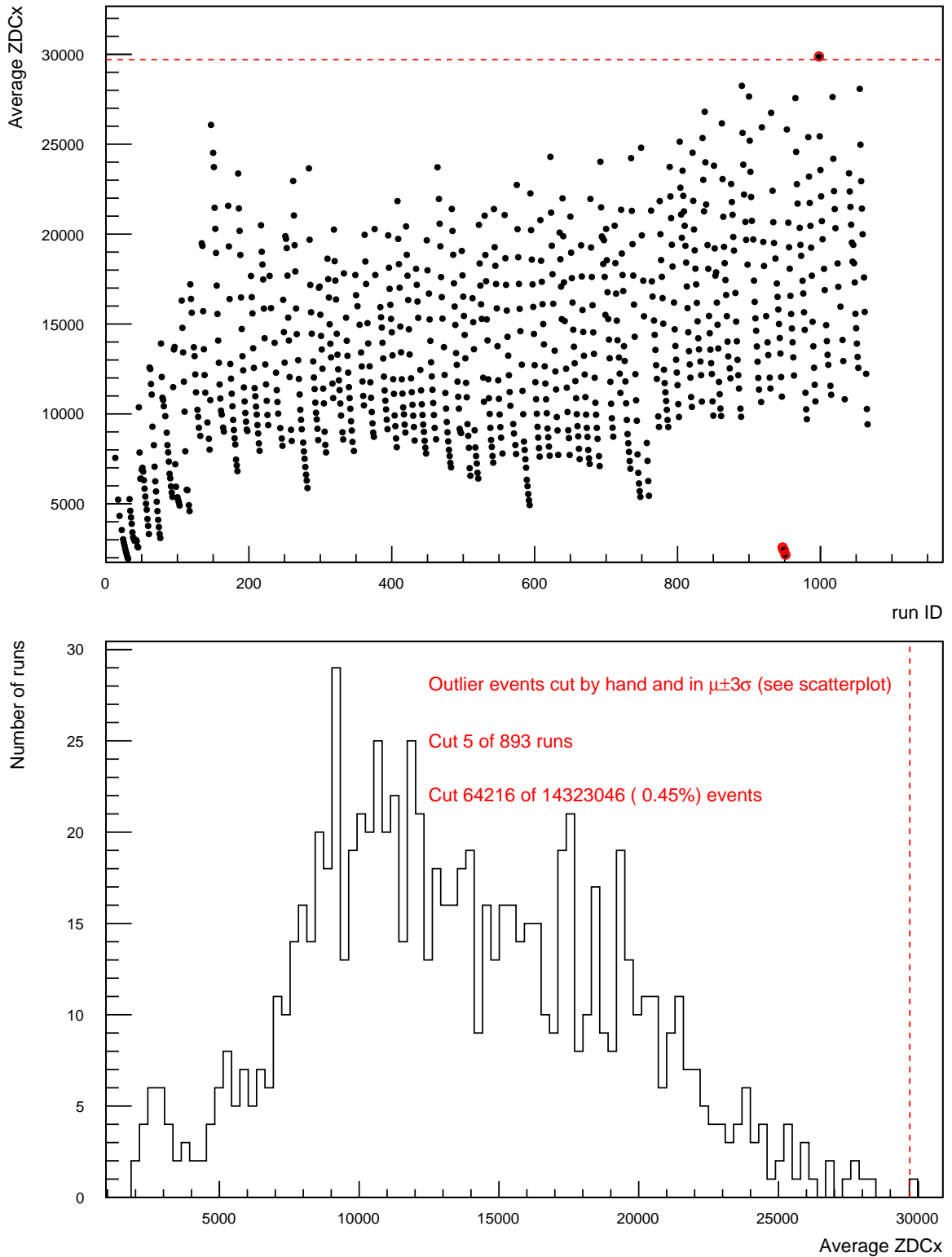
Figure A.17: Event averged ZDCx (the frequency of signal from ZDCx bits being occupied, see Section 3.2.5) per run (top), and distribution of averages (bottom). Outliers cuts at $\pm 3\sigma$ of distribution (red dotted lines) and by hand. Runs circled in red (in top figure) are cut.
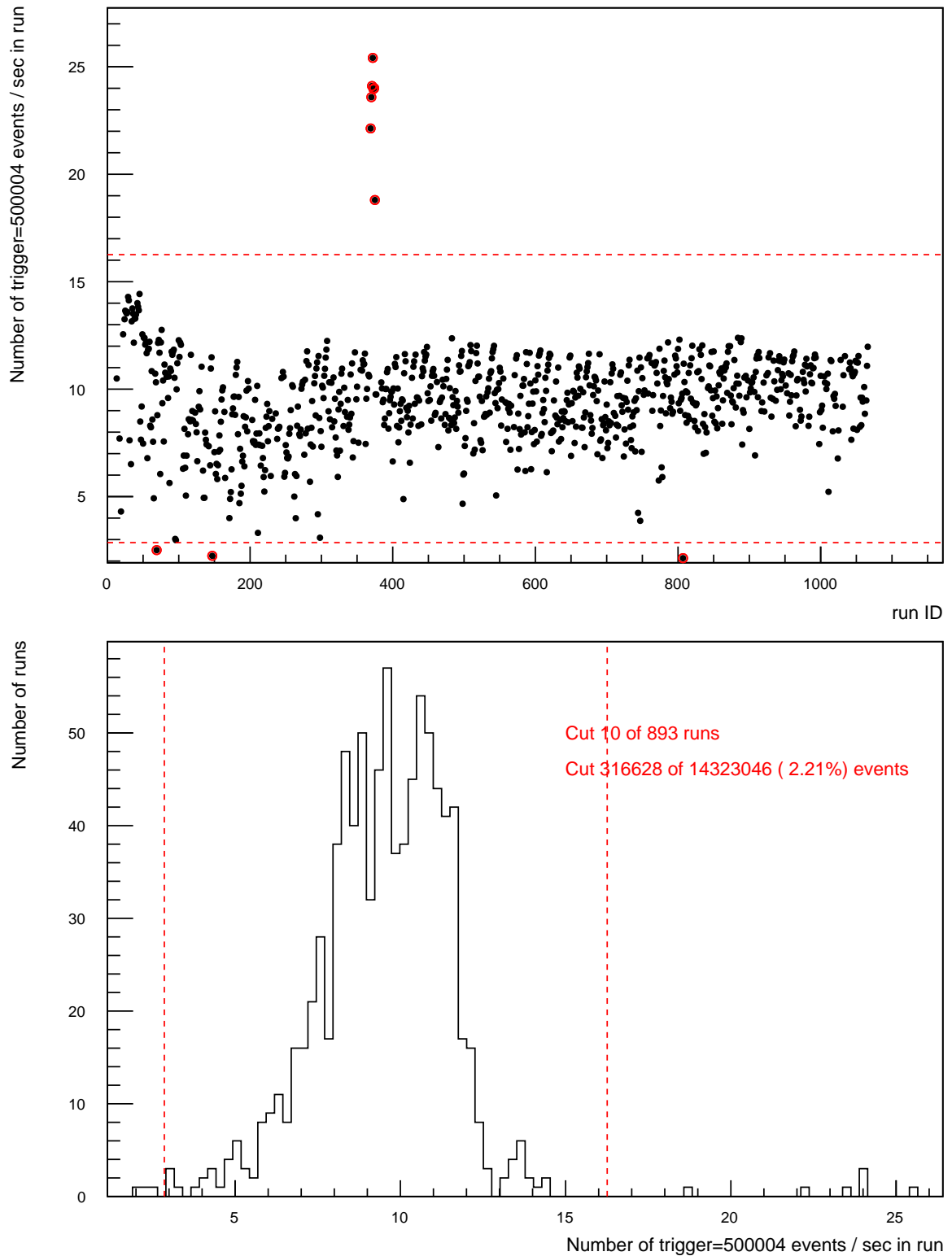
Figure A.18: Event averged events/sec (calculated at total 500004 events recorded per second of run duration) per run (top), and distribution of averages (bottom). Outliers cuts at $\pm 3\sigma$ of distribution (red dotted lines) and by hand. Runs circled in red (in top figure) are cut.

A.2 Semi-Inclusive Jet Spectra Binned in EA_TPC

The following charts are generated using the EA_TPC definition in the same way the charts in Section 6.3 were generated using the EA_BBC. They are placed here for reference because the physics conclusions are the same when combined with the equivalent results using EA_BBC in Section 6.3 and both EA_TPC and EA_BBC in Section 6.6.
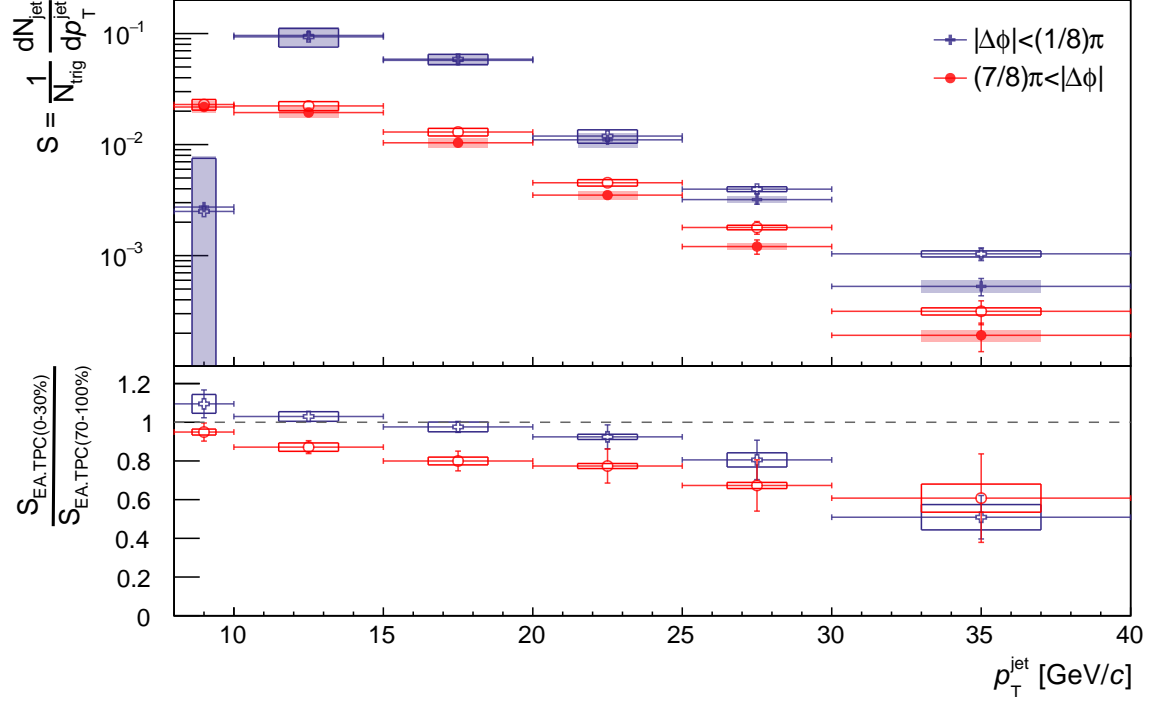
Figure A.19: Top panel: Full-jet, anti-k_T, $R = 0.4$, $|\eta_\text{jet}| < 0.6$ spectra per trigger (S) binned by $|\phi_\text{jet} - \phi_\text{trigger}|$ and highest and lowest 30% EA_TPC from all HT events with $E_\text{T}^\text{trig} > 8\,\text{GeV}$. Bottom panel: ratio of $S_{\text{EA}_\text{TPC}^\text{High}}$ to $S_{\text{EA}_\text{TPC}^\text{Low}}$. Systematic (statistical) uncertainties plotted as boxes (error bars).

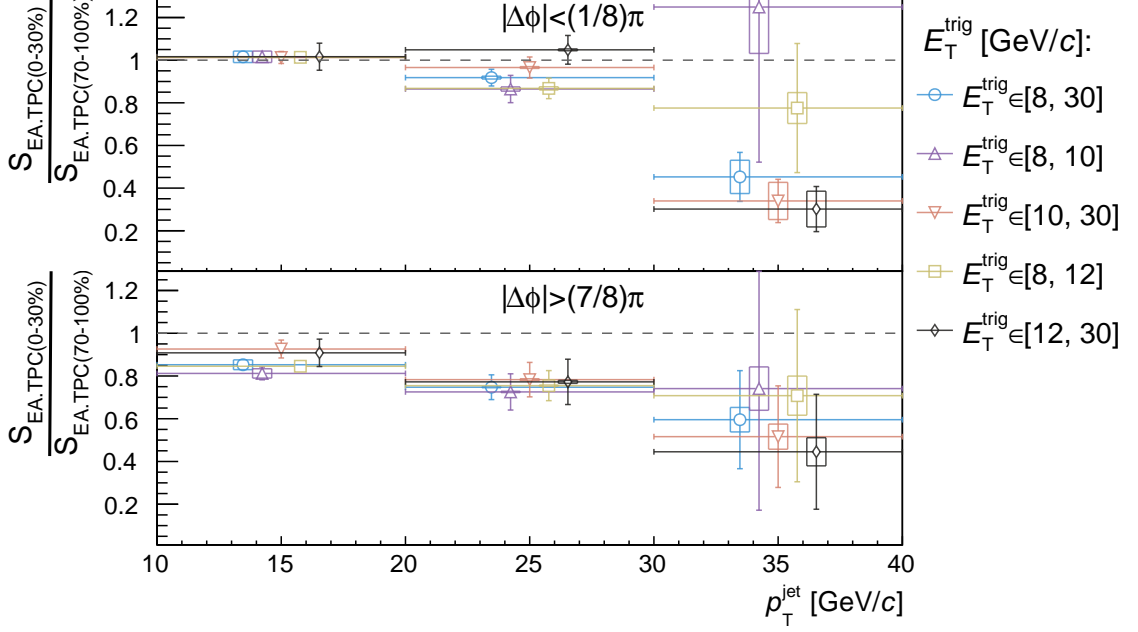Figure A.20: Ratios of $S_{\mathrm{EA_{TPC}^{High}}}/S_{\mathrm{EA_{TPC}^{Low}}}$ for events collected with various ranges of $E_{\mathrm{T}}^{\mathrm{trig}}$. Top: jets in trigger-side ($|\Delta\phi| < (1/8)\pi$) bin, bottom jets in recoil-side ($|\Delta\phi| > (7/8)\pi$) bin. Systematic (statistical) uncertainties plotted as boxes (error bars).

A.3   Jet Energy Scale and Resolution for High and Low Event Activity

This section contains the $p_{\mathrm{T,jet}}^{\mathrm{True}}$ to $p_{\mathrm{T,jet}}^{\mathrm{Measured}}$ plots used to calculate the JES and JER, along with the derived values. This uses the same process as documented in Section 4.7.1 repeated once each for the subsets of embedded events with $\mathrm{EA_{BBC}}$ less (more) than one σ below (above) the average $\mathrm{EA_{BBC}}$ of all embedded events.
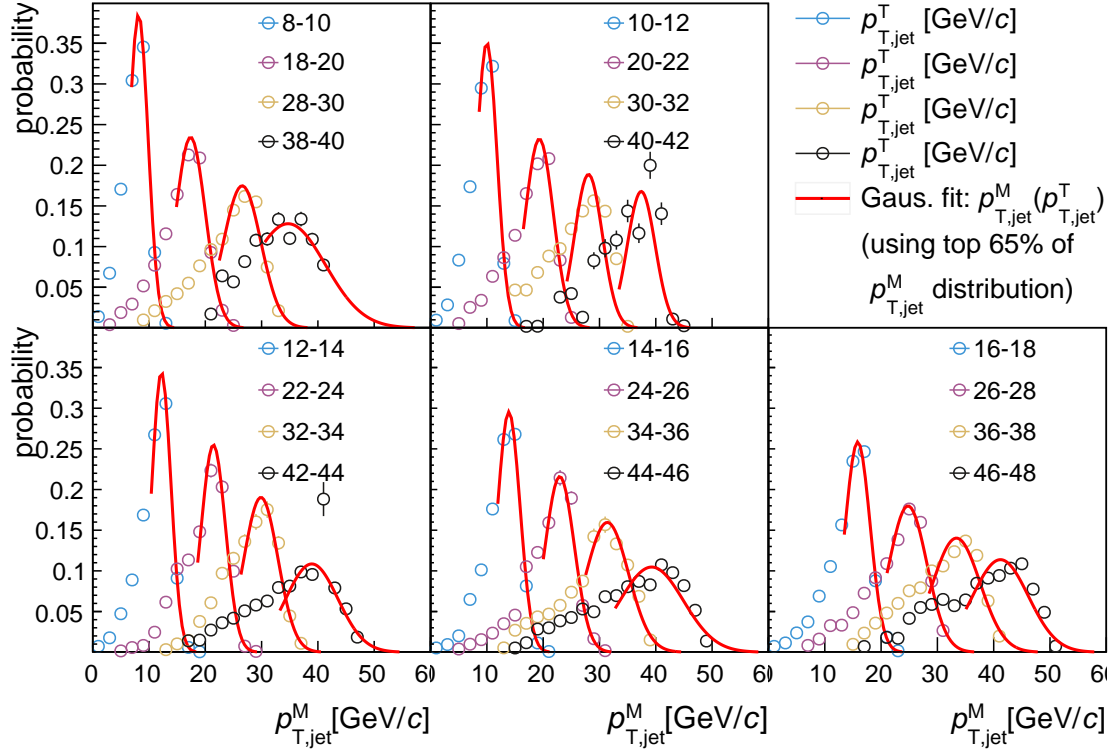
Figure A.21: Jet Energy Scale and Jet Energy Resolution for `PYTHIA6` jets embedded into p+Au $\sqrt{s_{\mathrm{NN}}} = 200\,\mathrm{GeV}$ MB events, using only events with $\mathrm{EA_{BBC}}$ less than one sigma below the mean of the $\mathrm{EA_{BBC}}$ distribution for all embedded jet events. Truth-level jets are divided into $p_{\mathrm{T}}^{\mathrm{T}}$ bins $2\,\mathrm{GeV}/c$ wide. The resulting matched measurement-level jet $p_{\mathrm{T}}^{\mathrm{M}}$ spectra for each $p_{\mathrm{T}}^{\mathrm{T}}$ is plotted. The 35th-100th percentile of each $p_{\mathrm{T}}^{\mathrm{M}}$ spectra is fit to a Gaussian; the offset of the Gaussian's mean to $p_{\mathrm{T}}^{\mathrm{T}}$ is the JES, and the σ is the JER.

Table A.1: Jet Energy Spectra and Resolution, $\mathrm{EA}_{\mathrm{BBC}}^{\mathrm{Low}}$ Events

$p_{\mathrm{T,full}}^{\mathrm{True}}$ [GeV/c]	JES [GeV/c]	JER [GeV/c]
[8, 10]	-0.72 ± 0.02	1.93 ± 0.02
[10, 12]	-0.78 ± 0.02	1.97 ± 0.02
[12, 14]	-0.83 ± 0.03	2.07 ± 0.02
[14, 16]	-0.92 ± 0.03	2.14 ± 0.03
[16, 18]	-1.16 ± 0.05	2.34 ± 0.04
[18, 20]	-1.64 ± 0.04	2.67 ± 0.03
[20, 22]	-1.70 ± 0.05	2.74 ± 0.04
[22, 24]	-1.63 ± 0.05	2.80 ± 0.04
[24, 26]	-1.80 ± 0.06	2.91 ± 0.05
[26, 28]	-2.31 ± 0.06	3.31 ± 0.04
[28, 30]	-2.52 ± 0.08	3.34 ± 0.05
[30, 32]	-2.61 ± 0.10	3.65 ± 0.07
[32, 34]	-3.60 ± 0.11	4.23 ± 0.08
[34, 36]	-3.49 ± 0.11	4.20 ± 0.09
[36, 38]	-3.47 ± 0.13	4.22 ± 0.09
[38, 40]	-4.64 ± 0.17	5.04 ± 0.13
[40, 42]	-4.74 ± 0.16	4.93 ± 0.11
[42, 44]	-4.86 ± 0.16	5.05 ± 0.11
[44, 46]	-5.65 ± 0.16	5.45 ± 0.10
[46, 48]	-5.84 ± 0.17	5.40 ± 0.11

JES and JER calculated from the mean (μ) and standard deviation (σ) values of Gaussians shown in Figure A.21. JES $= \mu - p_{\mathrm{T,full}}^{\mathrm{True}}$. JER $= \sigma$.
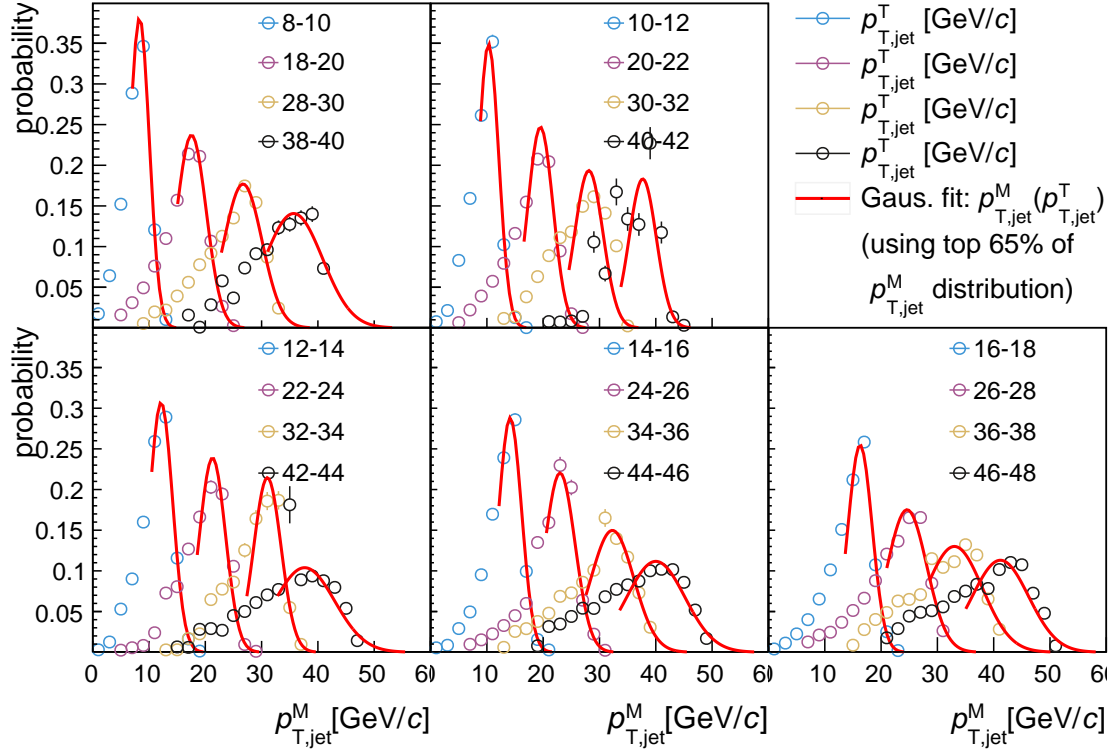
Figure A.22: Jet Energy Scale and Jet Energy Resolution for `PYTHIA6` jets embedded into p+Au $\sqrt{s_{NN}} = 200\,\text{GeV}$ MB events, using only events with EA_{BBC} greater than one sigma above the mean of the EA_{BBC} distribution for all embedded jet events. Truth-level jets are divided into p_T^T bins $2\,\text{GeV}/c$ wide. The resulting matched measurement-level jet p_T^M spectra for each p_T^T is plotted. The 35th-100th percentile of each p_T^M spectra is fit to a Gaussian; the offset of the Gaussian's mean to p_T^T is the JES, and the σ is the JER.

Table A.2: Jet Energy Spectra and Resolution, $\mathrm{EA_{BBC}^{High}}$ Events

$p_{\mathrm{T,full}}^{\mathrm{True}}$ [GeV/c]	JES [GeV/c]	JER [GeV/c]
$[8, 10]$	-0.58 ± 0.02	2.08 ± 0.02
$[10, 12]$	-0.64 ± 0.02	2.12 ± 0.02
$[12, 14]$	-0.74 ± 0.03	2.23 ± 0.02
$[14, 16]$	-0.84 ± 0.04	2.28 ± 0.03
$[16, 18]$	-0.89 ± 0.05	2.35 ± 0.04
$[18, 20]$	-1.47 ± 0.04	2.80 ± 0.03
$[20, 22]$	-1.58 ± 0.05	2.85 ± 0.04
$[22, 24]$	-1.65 ± 0.06	2.94 ± 0.04
$[24, 26]$	-1.70 ± 0.06	3.02 ± 0.04
$[26, 28]$	-2.40 ± 0.07	3.44 ± 0.05
$[28, 30]$	-2.30 ± 0.08	3.41 ± 0.06
$[30, 32]$	-2.51 ± 0.10	3.65 ± 0.07
$[32, 34]$	-2.43 ± 0.11	3.68 ± 0.08
$[34, 36]$	-3.33 ± 0.11	4.09 ± 0.07
$[36, 38]$	-3.79 ± 0.15	4.48 ± 0.10
$[38, 40]$	-3.77 ± 0.16	4.48 ± 0.11
$[40, 42]$	-4.87 ± 0.17	4.99 ± 0.12
$[42, 44]$	-5.04 ± 0.19	5.16 ± 0.12
$[44, 46]$	-5.58 ± 0.16	5.49 ± 0.11
$[46, 48]$	-5.71 ± 0.20	5.81 ± 0.15

JES and JER calculated from the mean (μ) and standard deviation (σ) values of Gaussians shown in Figure A.22. JES $= \mu - p_{\mathrm{T,full}}^{\mathrm{True}}$. JER $= \sigma$.

Bibliography

[1] R. N. Cahn, "The eighteen arbitrary parameters of the standard model in your everyday life", Reviews of Modern Physics **68**, 951–959 (1996) 10.1103/RevModPhys.68.951.

[2] Particle Data Group et al., "Review of Particle Physics", Physical Review D **98**, 030001 (2018) 10.1103/PhysRevD.98.030001.

[3] R. H. Dicke, P. J. E. Peebles, P. G. Roll, and D. T. Wilkinson, "Cosmic Black-Body Radiation.", The Astrophysical Journal **142**, 414–419 (1965) 10.1086/148306.

[4] A. A. Penzias and R. W. Wilson, "A Measurement of Excess Antenna Temperature at 4080 Mc/s.", The Astrophysical Journal **142**, 419–421 (1965) 10.1086/148307.

[5] H. D. Politzer, "Reliable Perturbative Results for Strong Interactions?", Physical Review Letters **30**, 1346–1349 (1973) 10.1103/PhysRevLett.30.1346.

[6] D. J. Gross and F. Wilczek, "Ultraviolet Behavior of Non-Abelian Gauge Theories", Physical Review Letters **30**, 1343–1346 (1973) 10.1103/PhysRevLett.30.1343.

[7] A. Deur, S. J. Brodsky, and G. F. de Teramond, "Connecting the hadron mass scale to the fundamental mass scale of quantum chromodynamics", Physics Letters B **750**, 528–532 (2015) 10.1016/j.physletb.2015.09.063.

[8] M. Gell-Mann and Y. Ne'eman, *The eightfold way: with new contributions from the authors*, 1st Perseus Pub. ed, Advanced Book Classics (Advanced Book Program, Perseus Pub, Cambridge, Mass, 2000), 388 pp.

[9] J. C. Collins and M. J. Perry, "Superdense Matter: neutrons or Asymptotically Free Quarks?", Physical Review Letters **34**, 1353–1356 (1975) 10.1103/PhysRevLett.34.1353.

[10]   N. Cabibbo and G. Parisi, "Exponential hadronic spectrum and quark liberation",
       Physics Letters B **59**, 67–69 (1975) 10.1016/0370-2693(75)90158-6.

[11]   K. Adcox, S. Adler, and (PHENIX), "Formation of dense partonic matter in rela-
       tivistic nucleus-nucleus collisions at RHIC: experimental evaluation by the PHENIX
       collaboration", Nuclear Physics A **757**, 184–283 (2005) 10.1016/j.nuclphysa.
       2005.03.086.

[12]   E. V. Shuryak, "Quantum chromodynamics and the theory of superdense matter",
       Physics Reports **61**, 71–158 (1980) 10.1016/0370-1573(80)90105-2.

[13]   L. R. Weih, M. Hanauske, and L. Rezzolla, "Postmerger Gravitational-Wave Signa-
       tures of Phase Transitions in Binary Mergers", Physical Review Letters **124**, 171103
       (2020) 10.1103/PhysRevLett.124.171103.

[14]   V. a. F. Sæl, s. v. 2. 0. O. N. M. a. P. O. b. 1. B. 0. O. N. Phone, and fax, *High Energy
       Physics - Department of Physics*, https://www.mn.uio.no/fysikk/english/
       research/groups/hep/index.html (visited on 07/13/2021).

[15]   F. Karsch, *Lattice QCD at High Temperature and Density*, (July 20, 2001) http:
       //arxiv.org/abs/hep-lat/0106019 (visited on 07/14/2021).

[16]   M. Csanad and T. Csorgo, *Initial energy density of p+p collisions at the LHC*,
       (Oct. 18, 2017) http://arxiv.org/abs/1307.2082 (visited on 07/14/2021).

[17]   T. Ludlam and L. McLerran, "What Have We Learned From the Relativistic Heavy
       Ion Collider?", Physics Today **56**, 48–54 (2003) 10.1063/1.1629004.

[18]   J. R. Alonso, "30 YEARS AT THE FOREFRONT - A PERSPECTIVE ON", 9.

[19]   G. E. Brown, "Heavy ion collisions at Bevalac energies", Comments Nucl. Part. Phys.
       19, 185–208 (1990).

[20]   A. Mocsy, director, *Smashing Matters: behind The Science Scene*, Oct. 27, 2017.

[21]   J. C. Collins, D. E. Soper, and G. Sterman, *Factorization of Hard Processes in QCD*,
       (Sept. 27, 2004) http://arxiv.org/abs/hep-ph/0409313 (visited on 07/30/2021).

[22]   *Fermilab Today*, https://www.fnal.gov/pub/today/archive/archive_2012/
       today12-09-14.html (visited on 07/09/2021).

[23]   B. Betz, "Jet Propagation and Mach-Cone Formation in (3+1)-dimensional Ideal
       Hydrodynamics", (2009).

[24] *Logo_full-plus-text-ver.png (PNG Image, 350 × 500 pixels)*, https://root.cern.ch/img/logos/ROOT_Logo/misc/logo_full-plus-text-ver.png (visited on 07/13/2021).

[25] P. Steinbrecher, "The QCD crossover at zero and non-zero baryon densities from Lattice QCD", Nuclear Physics A **982**, 847–850 (2019) 10.1016/j.nuclphysa.2018.08.025.

[26] T. D. N. S. A. Committee, *The Frontiers of Nuclear Science, A Long Range Plan*, (Sept. 17, 2008) http://arxiv.org/abs/0809.3137 (visited on 08/06/2021).

[27] S. A. Bass, J. Bernhard, and J. S. Moreland, "Determination of Quark-Gluon-Plasma Parameters from a Global Bayesian Analysis", Nuclear Physics A **967**, 67–73 (2017) 10.1016/j.nuclphysa.2017.05.052.

[28] Y.-L. Du et al., "Identifying the nature of the QCD transition in relativistic collision of heavy nuclei with deep learning", The European Physical Journal C **80**, 516 (2020) 10.1140/epjc/s10052-020-8030-7.

[29] U. Heinz, C. Shen, and H. Song, "The viscosity of quark-gluon plasma at RHIC and the LHC", in (2012), pp. 766–770, 10.1063/1.3700674.

[30] P. Kovtun, D. T. Son, and A. O. Starinets, "Holography and hydrodynamics: diffusion on stretched horizons", Journal of High Energy Physics **2003**, 064–064 (2003) 10.1088/1126-6708/2003/10/064.

[31] R. Nouicer, "New state of nuclear matter: nearly perfect fluid of quarks and gluons in heavy-ion collisions at RHIC energies: from charged particle density to jet quenching", The European Physical Journal Plus **131**, 70 (2016) 10.1140/epjp/i2016-16070-2.

[32] Z. Buthelezi, "Overview of recent results from heavy-ion collisions at ultra-relativistic energies".

[33] M. E. Peskin and D. V. Schroeder, *An introduction to quantum field theory*, 1. Indian ed (Levant Books, Kolkata, 2005), 842 pp.

[34] G. Aad et al., "Centrality and rapidity dependence of inclusive jet production in s NN = 5.02 TeV proton–lead collisions with the ATLAS detector", Physics Letters B **748**, 392–413 (2015) 10.1016/j.physletb.2015.07.023.

[35] *Hard scattering cross-sections at LHC in the Glauber approach: from pp to pA and AA collisions - INSPIRE*, https://inspirehep.net/literature/613386 (visited on 07/15/2021).

[36] J. Chauvin, D. Lebrun, A. Lounis, and M. Buenerd, "Low and intermediate energy nucleus-nucleus elastic scattering and the optical limit of Glauber theory", Physical Review C **28**, 1970–1974 (1983) 10.1103/PhysRevC.28.1970.

[37] *Klein-boesing_c_2013_habilitation.pdf*, https://www.uni-muenster.de/imperia/md/content/physik_kp/agwessels/thesis_db/ag_wessels/klein-boesing_c_2013_habilitation.pdf (visited on 04/02/2018).

[38] M. L. Miller, K. Reygers, S. J. Sanders, and P. Steinberg, "Glauber Modeling in High Energy Nuclear Collisions", Annual Review of Nuclear and Particle Science **57**, 205–243 (2007) 10.1146/annurev.nucl.57.090506.123020.

[39] J. L. Basdevant, J. Rich, and M. Spiro, *Fundamentals in nuclear physics: from nuclear structure to cosmology* (Springer, New York, 2005), 515 pp.

[40] Q. Y. Shou et al., "Parameterization of Deformed Nuclei for Glauber Modeling in Relativistic Heavy Ion Collisions", Physics Letters B **749**, 215–220 (2015) 10.1016/j.physletb.2015.07.078.

[41] *pPb-cartoon.jpg (JPEG Image, 640 × 480 pixels)*, https://bierlich.net/files/pPb-cartoon.jpg (visited on 07/15/2021).

[42] U. A. Wiedemann, "Heavy-ion collisions — selected topics", 30.

[43] W. Busza, K. Rajagopal, and W. van der Schee, *Heavy Ion Collisions: the Big Picture, and the Big Questions*, (Feb. 13, 2018) http://arxiv.org/abs/1802.04801 (visited on 04/13/2018).

[44] S. Basu, S. Thakur, T. K. Nayak, and C. A. Pruneau, "Multiplicity and pseudo-rapidity density distributions of charged particles produced in pp, pA and AA collisions at RHIC & LHC energies", Journal of Physics G: Nuclear and Particle Physics **48**, 025103 (2021) 10.1088/1361-6471/abc05c.

[45] G. Aad et al., "Measurement of Z Boson Production in Pb-Pb Collisions at s N N = 2.76 TeV with the ATLAS Detector", Physical Review Letters **110**, 022301 (2013) 10.1103/PhysRevLett.110.022301.

[46] R. Baier, "Jet Quenching", Nuclear Physics A **715**, 209c–218c (2003) 10.1016/S0375-9474(02)01429-X.

[47] J. Adams et al., "Experimental and theoretical challenges in the search for the quark–gluon plasma: the STAR Collaboration's critical assessment of the evidence from RHIC collisions", Nuclear Physics A **757**, 102–183 (2005) 10.1016/j.nuclphysa.2005.03.085.

[48] L. Adamczyk et al., "Dijet imbalance measurements in Au + Au and p p collisions at s N N = 200 GeV at STAR", Physical Review Letters **119**, 062301 (2017) 10.1103/PhysRevLett.119.062301.

[49] G. Aad et al., "Observation of a Centrality-Dependent Dijet Asymmetry in Lead-Lead Collisions at s NN = 2.76 TeV with the ATLAS Detector at the LHC", Physical Review Letters **105**, 252303 (2010) 10.1103/PhysRevLett.105.252303.

[50] S. Collaboration et al., "Measurements of jet quenching with semi-inclusive hadron+jet distributions in Au+Au collisions at $\sqrt{s_{NN}}$ = 200 GeV", Physical Review C **96**, 10.1103/PhysRevC.96.024905 (2017) 10.1103/PhysRevC.96.024905.

[51] *2020-05-31-DataPYTHIAComparison_R02_pt30to40.png (PNG Image, 1920 × 2204 pixels) — Scaled (41%)*, (Aug. 12, 2021) https://cds.cern.ch/record/2730824/files/2020-05-31-DataPYTHIAComparison_R02_pt30to40.png (visited on 08/12/2021).

[52] R. Singh, L. Kumar, P. K. Netrakanti, and B. Mohanty, "Selected Experimental Results from Heavy-Ion Collisions at LHC", Advances in High Energy Physics **2013**, 1–22 (2013) 10.1155/2013/761474.

[53] R. Debbe and ATLAS Collaboration, "Measurement of harmonic flow from heavy ion collisions in ATLAS", in (2013), pp. 666–668, 10.1063/1.4826866.

[54] A. Kurkela, U. A. Wiedemann, and B. Wu, "Opacity dependence of elliptic flow in kinetic theory", The European Physical Journal C **79**, 759 (2019) 10.1140/epjc/s10052-019-7262-x.

[55] F. Gelis, E. Iancu, J. Jalilian-Marian, and R. Venugopalan, "The Color Glass Condensate", Annual Review of Nuclear and Particle Science **60**, 463–489 (2010) 10.1146/annurev.nucl.010909.083629.

[56] B. Schenke, P. Tribedy, and R. Venugopalan, "Fluctuating Glasma initial conditions and flow in heavy ion collisions", Physical Review Letters **108**, 252301 (2012) `10.1103/PhysRevLett.108.252301`.

[57] M. Csanad et al., "Universal scaling of the elliptic flow data at RHIC", The European Physical Journal A **38**, 363–368 (2008) `10.1140/epja/i2008-10681-7`.

[58] A. Adare et al., "Scaling Properties of Azimuthal Anisotropy in Au + Au and Cu + Cu Collisions at s NN = 200 GeV", Physical Review Letters **98**, 162301 (2007) `10.1103/PhysRevLett.98.162301`.

[59] The CMS collaboration et al., "Observation of long-range, near-side angular correlations in proton-proton collisions at the LHC", Journal of High Energy Physics **2010**, 91 (2010) `10.1007/JHEP09(2010)091`.

[60] *Experimental overview on small collision systems at the LHC — Elsevier Enhanced Reader*, `10.1016/j.nuclphysa.2016.04.022`, `https://reader.elsevier.com/reader/sd/pii/S0375947416300732?token=6C62C51F7C604578F203F04C4BBFD96B2C80FE9F9351` `originRegion=us-east-1&originCreation=20210730194156` (visited on 07/30/2021).

[61] S. Marzani, G. Soyez, and M. Spannowsky, *Looking Inside Jets: an Introduction to Jet Substructure and Boosted-object Phenomenology*, Vol. 958, Lecture Notes in Physics (Springer International Publishing, Cham, 2019), `10.1007/978-3-030-15709-8`.

[62] *asymmetricDijetSketch.png (PNG Image, 295 × 311 pixels)*, `http://cds.cern.ch/record/2757389/files/asymmetricDijetSketch.png?version=1` (visited on 08/09/2021).

[63] *JetRAA_Fig1.png (PNG Image, 755 × 793 pixels)*, `https://www.star.bnl.gov/central/focus/JetRAA/JetRAA_Fig1.png` (visited on 08/09/2021).

[64] J. E. Huth et al., "Toward a Standardization of Jet Definitions ●", 7.

[65] M. Cacciari, G. P. Salam, and G. Soyez, "FastJet user manual", The European Physical Journal C **72**, `10.1140/epjc/s10052-012-1896-2` (2012) `10.1140/epjc/s10052-012-1896-2`.

[66] M. Cacciari, G. P. Salam, and G. Soyez, "The anti-k_t jet clustering algorithm", Journal of High Energy Physics **2008**, 063–063 (2008) `10.1088/1126-6708/2008/04/063`.

[67] S. Catani, Y. Dokshitzer, M. Seymour, and B. Webber, "Longitudinally-invariant kT-clustering algorithms for hadron-hadron collisions", Nuclear Physics B **406**, 187–224 (1993) 10.1016/0550-3213(93)90166-M.

[68] S. D. Ellis and D. E. Soper, "Successive combination jet algorithm for hadron collisions", Physical Review D **48**, 3160–3166 (1993) 10.1103/PhysRevD.48.3160.

[69] Y. Dokshitzer, G. Leder, S. Moretti, and B. Webber, "Better jet clustering algorithms", Journal of High Energy Physics **1997**, 001–001 (1997) 10.1088/1126-6708/1997/08/001.

[70] M. Wobisch and T. Wengler, *Hadronization Corrections to Jet Cross Sections in Deep-Inelastic Scattering*, (July 8, 1999) http://arxiv.org/abs/hep-ph/9907280 (visited on 08/13/2021).

[71] R. Atkin, "Review of jet reconstruction algorithms", Journal of Physics: Conference Series **645**, 012008 (2015) 10.1088/1742-6596/645/1/012008.

[72] A. Adare et al., "Centrality-Dependent Modification of Jet-Production Rates in Deuteron-Gold Collisions at s N N = 200 GeV", Physical Review Letters **116**, 122301 (2016) 10.1103/PhysRevLett.116.122301.

[73] J. Adam et al., "Measurement of charged jet production cross sections and nuclear modification in p–Pb collisions at s NN = 5.02 TeV", Physics Letters B **749**, 68–81 (2015) 10.1016/j.physletb.2015.07.054.

[74] C. Collaboration, "Measurement of inclusive jet production and nuclear modifications in pPb collisions at sqrt(s[NN]) = 5.02 TeV", The European Physical Journal C **76**, 372 (2016) 10.1140/epjc/s10052-016-4205-7.

[75] S. Acharya et al., "Constraints on jet quenching in p–Pb collisions at s NN = 5.02 TeV measured by the event-activity dependence of semi-inclusive hadron-jet distributions", Physics Letters B **783**, 95–113 (2018) 10.1016/j.physletb.2018.05.059.

[76] Alice Collaboration et al., "Centrality dependence of charged jet production in p–Pb collisions at $$\sqrt{s_\mathrm{NN}}$$ s NN = 5.02 TeV", The European Physical Journal C **76**, 271 (2016) 10.1140/epjc/s10052-016-4107-8.

[77] J. Lajoie, "Recent Reconstructed Jet Results from PHENIX", Moriond QCD 2021 (https://moriond.in2p3.fr/QCD/2021/FridayAfternoon/Lajoie.pdf), 2021.

149

[78] M. Anerella et al., "The RHIC magnet system", Nucl.Instrum.Meth.A **499**, 280–315 (2003) `10.1016/S0168-9002(02)01940-X`.

[79] H. Hahn et al., "The RHIC design overview", Nuclear Instruments and Methods in Physics Research Section A: Accelerators, Spectrometers, Detectors and Associated Equipment, The Relativistic Heavy Ion Collider Project: RHIC and Its Detectors **499**, 245–263 (2003) `10.1016/S0168-9002(02)01938-1`.

[80] Y. Luo, W. Fischer, and S. White, *Beam-beam observations in the Relativistic Heavy Ion Collider*, BNL–108394-2015-IR, 1222607 (June 24, 2015), BNL–108394-2015-IR, 1222607, `10.2172/1222607`.

[81] A. G. Ruggiero, "Tandems as injectors for synchrotrons", Nuclear Instruments and Methods in Physics Research Section A: Accelerators, Spectrometers, Detectors and Associated Equipment **328**, 3–9 (1993) `10.1016/0168-9002(93)90592-6`.

[82] W. MacKay et al., "Spin dynamics in AGS and RHIC", in Proceedings of the 2003 Bipolar/BiCMOS Circuits and Technology Meeting (IEEE Cat. No.03CH37440) (2003), pp. 405–409, `10.1109/PAC.2003.1288936`.

[83] J. Adam et al., "Results on total and elastic cross sections in proton–proton collisions at s = 200 GeV", Physics Letters B **808**, 135663 (2020) `10.1016/j.physletb.2020.135663`.

[84] W. Fischer et al., "Measurement of the total cross section of gold-gold collisions at square root [sNN] = 200 GeV", 5.

[85] C. Liu et al., *RHIC operation with asymmetric collisions in 2015*, BNL–108367-2015-IR, 1214539 (Aug. 7, 2015), BNL–108367-2015-IR, 1214539, `10.2172/1214539`.

[86] *RHIC Run Overview*, `https://www.agsrhichome.bnl.gov/RHIC/Runs/index.html#Run-15` (visited on 07/20/2021).

[87] W. B. Christie, "Overview and Status of the Star Detector at Rhic", in *Advances in Nuclear Dynamics 5*, edited by W. Bauer and G. D. Westfall (Springer US, Boston, MA, 1999), pp. 321–328, `10.1007/978-1-4615-4719-8_33`.

[88] R. Brown, A. Etkin, W. Leonhardt, and J. Mills, "The STAR Detector Magnet Subsystem", in (May 7, 1997).

[89] T. S. Collaboration et al., *Longitudinal and transverse spin asymmetries for inclusive jet production at mid-rapidity in polarized p+p collisions at sqrt{s}=200 GeV,* (May 11, 2012) http://arxiv.org/abs/1205.2735 (visited on 07/26/2021).

[90] M. Anderson et al., "The STAR Time Projection Chamber: a Unique Tool for Studying High Multiplicity Events at RHIC", Nuclear Instruments and Methods in Physics Research Section A: Accelerators, Spectrometers, Detectors and Associated Equipment **499**, 659–678 (2003) 10.1016/S0168-9002(02)01964-2.

[91] M. Beddo et al., "The STAR Barrel Electromagnetic Calorimeter", Nuclear Instruments and Methods in Physics Research Section A: Accelerators, Spectrometers, Detectors and Associated Equipment **499**, 725–739 (2003) 10.1016/S0168-9002(02)01970-8.

[92] T. Cormier et al., "STAR barrel electromagnetic calorimeter absolute calibration using "minimum ionizing particles" from collisions at RHIC", Nuclear Instruments and Methods in Physics Research Section A: Accelerators, Spectrometers, Detectors and Associated Equipment **483**, 734–746 (2002) 10.1016/S0168-9002(01)01951-9.

[93] Y. Wang et al., "Production and quality control of STAR-TOF MRPC", Nuclear Instruments and Methods in Physics Research Section A: Accelerators, Spectrometers, Detectors and Associated Equipment **613**, 200–206 (2010) 10.1016/j.nima.2009.11.045.

[94] W. Llope, "Multigap RPCs in the STAR experiment at RHIC", Nuclear Instruments and Methods in Physics Research Section A: Accelerators, Spectrometers, Detectors and Associated Equipment **661**, S110–S113 (2012) 10.1016/j.nima.2010.07.086.

[95] *STAR BBC,* https://www.star.bnl.gov/public/bbc/geom/small_hex_triplet.html (visited on 07/27/2021).

[96] *STAR BBC,* https://www.star.bnl.gov/public/bbc/geom/front_view.html (visited on 07/27/2021).

[97] E. Judd et al., "The evolution of the STAR Trigger System", Nuclear Instruments and Methods in Physics Research Section A: Accelerators, Spectrometers, Detectors and Associated Equipment **902**, 228–237 (2018) 10.1016/j.nima.2018.03.070.

[98]   *Bbc.gif (GIF Image, 612 × 792 pixels)*, `https://www.star.bnl.gov/public/trg/` `.introduction/bbc.gif` (visited on 07/26/2021).

[99]   Y.-F. Xu et al., "Physics performance of the STAR zero degree calorimeter at relativistic heavy ion collider", Nuclear Science and Techniques **27**, 126 (2016) `10.1007/` `s41365-016-0129-z`.

[100] Y.-F. Xu et al., "Physics performance of the STAR zero degree calorimeter at relativistic heavy ion collider", Nuclear Science and Techniques **27**, 126 (2016) `10.1007/` `s41365-016-0129-z`.

[101] R. Reed et al., "Vertex finding in pile-up rich events for p+p and d+Au collisions at STAR", Journal of Physics: Conference Series **219**, 032020 (2010) `10.1088/1742-` `6596/219/3/032020`.

[102] W. Llope et al., "The STAR Vertex Position Detector", Nuclear Instruments and Methods in Physics Research Section A: Accelerators, Spectrometers, Detectors and Associated Equipment **759**, 23–28 (2014) `10.1016/j.nima.2014.04.080`.

[103] J. Landgraf et al., "An overview of the STAR DAQ system", Nuclear Instruments and Methods in Physics Research Section A: Accelerators, Spectrometers, Detectors and Associated Equipment **499**, 762–765 (2003) `10.1016/S0168-9002(02)01973-3`.

[104] M. Calderon et al., *STAR Integrated Tracker Guide*.

[105] R. Reed et al., "Vertex finding in pile-up rich events for p+p and d+Au collisions at STAR", Journal of Physics: Conference Series **219**, 032020 (2010) `10.1088/1742-` `6596/219/3/032020`.

[106] *BEMC*, `https://drupal.star.bnl.gov/STAR/book/export/html/649` (visited on 08/19/2021).

[107] L. Adamczyk et al., "Precision Measurement of the Longitudinal Double-Spin Asymmetry for Inclusive Jet Production in Polarized Proton Collisions at s = 200 GeV", Physical Review Letters **115**, 092002 (2015) `10.1103/PhysRevLett.115.092002`.

[108] R. Brun et al., *GEANT 3 : user's guide Geant 3.10, Geant 3.11*, CERN-DD-EE-84-01 (CERN, 1987).

[109] K. Olive, "Review of Particle Physics", Chinese Physics C **38**, 090001 (2014) `10.` `1088/1674-1137/38/9/090001`.

[110] J. Adams et al., "Identified hadron spectra at large transverse momentum in p+p and d+Au collisions at sNN=200 GeV", Physics Letters B **637**, 161–169 (2006) 10.1016/j.physletb.2006.04.032.

[111] B. I. Abelev et al., "Strange particle production in p + p collisions at s = 200 GeV", Physical Review C **75**, 064901 (2007) 10.1103/PhysRevC.75.064901.

[112] A. Adare et al., "Spectra and ratios of identified particles in Au+Au and d +Au collisions at s N N = 200 GeV", Physical Review C **88**, 024906 (2013) 10.1103/PhysRevC.88.024906.

[113] J. Adams et al., "K (892) * resonance production in Au+Au and p + p collisions at s NN = 200 GeV", Physical Review C **71**, 064902 (2005) 10.1103/PhysRevC.71.064902.

[114] *The Computational Geometry Algorithms Library*, https://www.cgal.org/index.html (visited on 09/11/2021).

[115] *FastJet: INSTALL Source File*, http://fastjet.fr/repo/doxygen-3.4.0/INSTALL_source.html (visited on 09/11/2021).

[116] G. D'Agostini, "A multidimensional unfolding method based on Bayes' theorem", Nuclear Instruments and Methods in Physics Research Section A: Accelerators, Spectrometers, Detectors and Associated Equipment **362**, 487–498 (1995) 10.1016/0168-9002(95)00274-X.

[117] T. Adye, "Proceedings of the PHYSTAT 2011 Workshop on Statistical Issues Related to Discovery Claims in Search Experiments and Unfolding: CERN, Geneva, Switzerland 17 - 20 Jan 2011", in (2011), pp. 313–318.

[118] *RooUnfold / RooUnfold*, GitLab, https://gitlab.cern.ch/RooUnfold/RooUnfold (visited on 09/14/2021).

[119] P. Jacobs, "Search for jet quenching effects in high multiplicity pp collisions at s = 13 TeV", Nuclear Physics A **1005**, 121924 (2021) 10.1016/j.nuclphysa.2020.121924.

[120] J. Adam et al., "Centrality dependence of particle production in p – Pb collisions at s NN = 5.02 TeV", Physical Review C **91**, 064905 (2015) 10.1103/PhysRevC.91.064905.

[121] O. Lubynets, I. Selyuzhenkov, and V. Klochkov, "Centrality estimation with MC Glauber model", 10.

[122] F. D'Eramo, K. Rajagopal, and Y. Yin, "Molière scattering in quark-gluon plasma: finding point-like scatterers in a liquid", Journal of High Energy Physics **2019**, 172 (2019) 10.1007/JHEP01(2019)172.

[123] D. V. Perepelitsa, "Hard processes in small systems", Nuclear Physics A **967**, 113–120 (2017) 10.1016/j.nuclphysa.2017.06.043.

[124] S. Schlichting and B. Schenke, "The shape of the proton at high energies", Physics Letters B **739**, 313–319 (2014) 10.1016/j.physletb.2014.10.068.

[125] D. McGlinchey, J. L. Nagle, and D. V. Perepelitsa, "Consequences of high- x proton size fluctuations in small collision systems at s N N = 200 GeV", Physical Review C **94**, 024915 (2016) 10.1103/PhysRevC.94.024915.

[126] M. Kordell and A. Majumder, "Jets in d (p) – A collisions: color transparency or energy conservation", Physical Review C **97**, 054904 (2018) 10.1103/PhysRevC.97.054904.

[127] M. S. Abdallah et al., "Invariant jet mass measurements in p p collisions at s = 200 GeV at RHIC", Physical Review D **104**, 052007 (2021) 10.1103/PhysRevD.104.052007.

[128] I. Mooney, *Jet substructure in p+p and p+Au collisions at $\sqrt{s_{\text{NN}}} = 200$ GeV at STAR*, (Sept. 10, 2020) http://arxiv.org/abs/2009.04962 (visited on 08/12/2021).